



This work is protected by copyright and other intellectual property rights and duplication or sale of all or part is not permitted, except that material may be duplicated by you for research, private study, criticism/review or educational purposes. Electronic or print copies are for your own personal, non-commercial use and shall not be passed to any other individual. No quotation may be published without proper acknowledgement. For any other use, or to quote extensively from the work, permission must be obtained from the copyright holder/s.

A *Suzaku* survey of iron lines in type 1 Active Galactic Nuclei

Adam Patrick
BSc Hons

Doctor of Philosophy

Department of Astrophysics, University of Keele.

July 2013

Abstract

Active galactic nuclei (AGN) are some of the most energetic objects which have ever been observed and each of these harbour a supermassive black hole at its centre. By looking at the X-ray emission from these nuclei, information can be gathered regarding their inner workings. Emission from regions which are very close to the central black hole can be subject to strong relativistic effects and the examination of this emission can lead to the placing of estimates upon the rate at which the black hole is spinning.

Within this thesis, I make an analysis of all Seyfert 1 observations which have been observed with *Suzaku* to date, although using selection criteria such that broad features in the Fe K region can be observed if they are indeed present. Models are constructed of the time-averaged broadband spectra over 0.6-60.0 keV, which accurately describe these complex AGN and allow the measurement of the impact relativistic effects have upon the X-ray spectrum. There are a total of 46 different objects and 84 observations used within this analysis.

By conducting a full broadband analysis of these AGN, supermassive black hole spin constraints are placed upon 11 objects, 7 of which are unique to this analysis with the remaining 4 either confirming or improving upon previous analyses. In general, it is found that 50% of the objects in this sample show evidence for emission from the inner regions of the nucleus although none of the AGN require a maximally spinning black hole, which is in contrast to the results in alternative analyses. The data within this thesis are best described with emission originating from no further in than a few tens of R_g .

Acknowledgements

Firstly I would like to thank my supervisor James Reeves for all his patience, enthusiasm and help in completing this thesis. Without his good advice and energy I have no doubt that much of the enclosed work would not have been possible. There have been many high intensity debates which we have both been involved in which have proven to be fun as well as intellectually stimulating. Throughout the last 3 years I have also had the welcome advice and encouragement from Delphine Porquet, for which I am grateful. I would also like to thank the astrophysics department at Keele University for providing me with the opportunities and the feeling of being a part of something.

On a less scientific note, none of this would have been possible without the support of my friends and family who have helped me to finish this thesis, providing words of encouragement and the much need distractions when working until the early hours. A very special thanks goes to my Mum and Dad who have always listened to me throughout whatever difficulties I came across, I have always been safe in the knowledge that I had their unconditional love and support throughout my life.

I would also particularly like to thank Rach, Kev, Dan and Aaron (last but certainly not least!) who have all put up with me over the last three years and longer and who I've shared many hours of fun with, whether it be the endless games of pool (and drinking!) at the KPA, tearing my body to shreds playing squash a little too competitively or generally just chatting the night away. I know I've made some very special friends.

Contents

Abstract	iii
Acknowledgements	iv
1 Introduction	1
1.1 Overview	1
1.2 The central engine	2
1.3 AGN taxonomy	6
1.4 Unification schemes	9
1.4.1 Seyfert unification	9
1.4.2 Radio-loud and radio-quiet unification	10
1.4.3 AGN structure	11
1.5 SED and the X-ray spectra of Seyfert 1 AGN	13
1.5.1 Important processes in AGN spectra	14
1.5.1.1 Blackbody radiation	14
1.5.1.2 Compton scattering	16
1.5.1.3 Photoelectric absorption	16
1.5.1.4 Line emission	17
1.5.2 Intrinsic X-ray continuum	17
1.5.3 X-ray reflection	18
1.5.4 The soft excess	20
1.5.5 Absorption in X-ray spectra	22
1.6 Broad emission and the Fe K region	25
1.6.1 Broad emission and the inner regions	25
1.6.2 Distant narrow emission	28
1.6.3 Highly ionised absorption in the Fe K region	30
1.7 Supermassive black hole spin	31
1.7.1 What SMBH spin can tell us	31
1.7.2 Fe K lines, spin in the literature and motivation	32
1.7.3 Thesis outline	36
2 Instrumentation and data analysis	37
2.1 Types of X-ray detectors	38
2.1.1 Proportional counters	38
2.1.2 CCD detectors	38
2.1.3 Scintillators	40
2.1.4 Microcalorimeters	40
2.2 Previous X-ray observatories	41
2.3 Current X-ray observatories	42
2.3.1 <i>XMM-Newton</i>	42

2.3.2	<i>Chandra</i>	43
2.3.3	<i>Suzaku</i>	44
2.3.4	<i>Swift</i>	48
2.4	Data reduction and analysis	49
2.4.1	Screening the data	49
2.4.2	Data reduction	52
2.4.3	Model fitting and statistics	55
2.5	Common models used within this work	57
2.5.1	Modelling of the soft excess	57
2.5.2	Compton reflection	58
2.5.3	Warm absorption	60
2.5.4	Highly ionised absorption	61
2.5.5	Partial covering	62
2.5.6	Asymmetric line profiles and diskline-type models	65
2.5.7	Convolution models	69
3	Analysis of ‘bare’ Seyfert sample	71
3.1	The importance of broadband data and a clean spectrum	73
3.2	Bare Seyfert sample	73
3.3	Bare Seyfert results	75
3.3.1	Model A – Parameterisation of spectra	78
3.3.2	Model B – Self consistent distant reflection	84
3.3.3	Model C – Laor profile	86
3.3.4	Model D – Kerrdisk profile	89
3.3.5	Model E – Blurred reflector (1)	93
3.3.6	Model F – Blurred reflector (2)	95
3.4	Discussion of iron K emission in ‘bare’ Seyferts	96
3.4.1	Accretion disc parameters and SMBH spin	98
3.4.2	Towards the origin of the soft excess	99
4	Analysis of deep <i>Suzaku</i> observations	103
4.1	The deep observation sample	105
4.2	Deep observation results	108
4.2.1	Initial parameterisation and baseline model	108
4.2.1.1	Fairall 9	110
4.2.1.2	MCG–6-30-15	112
4.2.1.3	NGC 3516	115
4.2.1.4	NGC 3783	117
4.2.1.5	NGC 4051	118
4.2.2	The Fe K region and disc parameters	120
4.2.2.1	The effect of partial covering	125
4.2.2.2	Testing for retrograde SMBH spin	129

4.2.3	Dual reflector	130
4.3	Discussion of deep observation results	133
4.3.1	Average parameters of the disc	135
4.3.2	The affect of absorption in complex sources	136
4.3.3	Is MCG–6-30-15 not maximal?	137
4.3.4	A retrograde SMBH spin in NGC 3783?	138
5	Analysis of the full <i>Suzaku</i> sample	141
5.1	The <i>Suzaku</i> sample	143
5.2	Model construction and the implied geometries	146
5.2.1	Modelling of the soft excess	147
5.2.2	Compton reflection	148
5.2.3	Emission lines from distant material	149
5.2.4	Warm absorption	150
5.2.5	Highly ionised absorption	151
5.2.6	Partial covering	151
5.2.7	Relativistic line emission	151
5.3	Full <i>Suzaku</i> sample results	152
5.3.1	Baseline model	152
5.3.2	Prevalence of typical features in X-ray spectra	153
5.3.2.1	Absorbed Seyfert spectra – fully covering	154
5.3.2.2	Absorbed Seyfert spectra – partially covering	158
5.3.2.3	Soft excess and reflector properties	159
5.3.3	The Fe K region	161
5.3.3.1	Additional distant ionised emission	161
5.3.3.2	Highly ionised absorption and outflows	162
5.3.3.3	Broad residuals in the Fe K region	171
5.3.4	Dual reflector fits	176
5.4	Selected individual objects	180
5.4.1	Fairall 9	181
5.4.2	Mrk 205	181
5.4.3	NGC 3227	181
5.4.4	NGC 3516	182
5.4.5	NGC 3783 - High or low spin?	184
5.4.6	NGC 4051	189
5.5	Conclusions	191
6	Discussion	194
6.1	Typical broadband Seyfert 1 spectra	195
6.1.1	Soft and hard excesses	195
6.1.2	Soft X-ray absorption and partial covering	196
6.2	Relativistic emission and black hole spin in Seyfert 1 AGN	200

6.2.1	Broad Fe K line statistics	200
6.2.2	Ionised emission in the Fe K region	201
6.2.3	Highly ionised absorption and outflows	202
6.2.4	Typical parameters of the disc	203
6.2.5	Shape of the line profile	205
6.2.6	Distribution of SMBH spin, disc parameters and the implications	208
6.2.6.1	Comparison with stellar mass BHs	211
6.3	Alternative mechanisms and scenarios	213
6.3.1	An atomic origin of the soft excess?	213
6.3.2	Disc winds	215
6.3.3	A truncated disc	217
6.3.4	Inner reflection versus partial covering	218
6.4	Future prospects	220
A	Observation details	224
B	Bare Seyfert sample tables	232
C	Deep observation sample tables	239
D	Full sample tables	245
	Publications	261
	Bibliography	262

List of Figures

1.1	Schematic of an AGN.	11
1.2	Broadband spectral energy distribution of an AGN.	13
1.3	X-ray spectral energy distribution.	15
1.4	Reflection spectra for a range of ionisations.	19
1.5	Comparison of soft excess mechanisms.	21
1.6	Warm absorber examples for NGC 3516.	23
1.7	Narrow absorption lines observed with <i>Chandra</i>	24
1.8	Line profiles generated with DISKLINE and the effect of changing parameters.	27
1.9	Ratio plot of red wing in the Miniutti et al. (2007) analysis of MCG–06-30-15.	28
1.10	Examples of Fe K regions in an <i>XMM-Newton</i> analysis of Seyfert 1 AGN.	29
1.11	Spin constrain in Fairall 9 by Schmoll et al. (2009).	33
2.1	Example of quantum efficiency curves for CCDs.	39
2.2	<i>XMM-Newton</i> schematic.	43
2.3	<i>Suzaku</i> schematic.	45
2.4	Schematic of HXD counters onboard <i>Suzaku</i>	46
2.5	Effective area curves for modern X-ray observatories.	47
2.6	Example source regions during data reduction.	51
2.7	Example of warm absorbing zone with changing column density.	59
2.8	Example of warm absorbing zone with changing ionisation.	60
2.9	Example of highly ionised zone with changing ionisation.	62
2.10	Example of partial covering with changing covering fraction.	63
2.11	Example of partial covering with changing column density.	64
2.12	Line profiles generated with RELLINE with changing emissivity.	65
2.13	Line profiles generated with RELLINE with changing inclination.	66
2.14	Line profiles generated with RELLINE with changing spin.	67
2.15	Relativistic blurring of the reflection continuum.	70
3.1	Broadband residuals with the Fe K region unmodelled.	79
3.2	Bare Seyfert ratios to a powerlaw.	81
3.3	Fe K region residuals with reflection and diskline emission unmodelled.	82
3.4	Fe K region residuals with inner emission unmodelled.	85
3.5	$\nu F\nu$ plots of the full broadband model.	90
3.6	Contour plot of SMBH spin for Mrk 335, NGC 7469 and SWIFT J2127.4+5654.	92
3.7	$\nu F\nu$ plots of blurred reflector models for Mrk 335.	97
4.1	Fe K region residuals without modelling of the reflection component.	107
4.2	Fe K region residuals without modelling of emission from the inner disc.	111

4.3	$\nu F\nu$ plots of the baseline model.	116
4.4	Contour plot of SMBH spin for Fairall 9, MCG–06-30-15 and NGC 3783.	120
4.5	FeK region residuals to the full model.	124
4.6	$\nu F\nu$ plots of the full broadband model.	126
4.7	Comparison of the effects of partial covering in MCG–06-30-15.	127
4.8	Spin contour plots using RELLINE for NCG 3783.	131
5.1	Examples of hard excesses which may require a partial covering geometry.	159
5.2	FeK region residuals without modelling of the reflection component.	163
5.3	$\nu F\nu$ plots of the full broadband model.	176
5.4	$\nu F\nu$ plots to demonstrate the significant spectral variability in some objects.	183
5.5	High and low spin comparisons of NGC 3783.	188
6.1	Distribution of covering fractions.	197
6.2	Distribution of broad iron line parameters when fit with a Gaussian.	201
6.3	Distribution of highly ionised outflow parameters.	202
6.4	Distribution of iron line profile parameters.	206
6.5	Predicted iron line widths.	207
6.6	Reflection dominated spin distribution from Walton et al. (2013).	210
6.7	Comparison of stellar mass black hole models.	214
6.8	Example wind spectrum from Sim et al. (2008)	216
6.9	<i>Nustar</i> observation of NGC 1365.	222

List of Tables

1.1	AGN taxonomy.	7
1.2	Spin estimates in the literature	35
2.1	Summary of screening criteria.	50
3.1	The <i>Suzaku</i> bare Seyfert sample.	74
3.2	Summary of model components for Models A-F.	77
4.1	The <i>Suzaku</i> Seyfert sample.	106
4.2	Table of KERRDISK parameters for objects in the deep <i>Suzaku</i> sample.	122
4.3	Table of KERRDISK parameters when using only a fully covering absorbing geometry.	128
4.4	Table of RELLINE parameters for NGC 3783 allowing for $-0.998 < a < 0.998$	129
5.1	The full <i>Suzaku</i> Seyfert sample.	144
5.2	Summary of the models used to fit the AGN in the full <i>Suzaku</i> sample.	155
5.3	Broad Gaussian parameters for the full <i>Suzaku</i> sample.	168
5.4	Summary of the line profiles using RELLINE fit to the full <i>Suzaku</i> sample.	173
6.1	Summary of percentage of objects featuring particular components.	199
6.2	Average iron line parameters.	204
A.1	Summary of observations for the objects in the full <i>Suzaku</i> sample.	224
B.1	Model A parameters for the ‘bare’ <i>Suzaku</i> sample.	232
B.2	Model B parameters for the ‘bare’ <i>Suzaku</i> sample.	234
B.3	Model C parameters for the ‘bare’ <i>Suzaku</i> sample.	235
B.4	Model D parameters for the ‘bare’ <i>Suzaku</i> sample.	236
B.5	Model E parameters for the ‘bare’ <i>Suzaku</i> sample.	237
B.6	Model F parameters for the ‘bare’ <i>Suzaku</i> sample.	238
C.1	Initial parameterisation of objects in the deep <i>Suzaku</i> observations.	239
C.2	Baseline model parameters for objects in the deep <i>Suzaku</i> sample.	241
C.3	Soft X-ray emission lines in the baseline model.	242
C.4	Parameters for a dual reflector fit to objects in the deep <i>Suzaku</i> sample.	243
D.1	Baseline model parameters for objects in the full <i>Suzaku</i> sample.	245
D.2	Fe K region properties in the full <i>Suzaku</i> sample.	252
D.3	Dual reflector parameters in the full <i>Suzaku</i> sample.	256
D.4	Hard and soft X-ray fluxes in the full <i>Suzaku</i> sample.	258

1 Introduction

1.1 Overview

A galaxy can be described as a very large gravitationally bound system with in the region of $10^7 - 10^{11}$ stars, many of which feature a central super massive black hole with a mass of $10^6 - 10^9 M_{\odot}$. In addition to stars, galaxies contain a wide range of interesting features such as nebulae (e.g. star forming regions or supernova remnants), open or globular clusters, dark matter, stellar mass black holes and other stellar remnants. Indeed, galaxies themselves are often (but not exclusively) found in clusters of other galaxies and can be seen to be merging with other nearby galaxies or have further systems of stars orbiting them (i.e. globular clusters). Of course, galaxies themselves come in a very wide range of shapes and sizes, from large elliptical galaxies to the perhaps more familiar disc or spiral shape galaxies. Galaxies make up the oldest objects in the Universe, for example, Zheng et al. (2012) claim to have observed the oldest galaxy to date at a redshift of $z = 9.6 \pm 0.2$, which they estimate puts the formation of the galaxy just 200 million years after the big bang (i.e. $z < 14$).

Galaxies emit huge amounts of energy through electromagnetic radiation, however, it was discovered that a small proportion of galaxies are especially energetic or bright; these are called ‘active’ galaxies. The luminosity of a ‘normal’ (i.e. in-active) galaxy can be thought of as the combined output of all the stars in the galaxy itself ($\sim 10^{11} L_{\odot}$), whereas an ‘active’ galaxy has a total luminosity much higher than simply adding together each individual star’s emitted electromagnetic radiation, for example, up to 10^4 times the luminosity of a typical galaxy. Instead, at the centre of these galaxies massive amounts of energy are emitted from what appears to be a point source, i.e. from the inner regions (or nucleus, within $r < 100$ pc since it is unresolved by observations) of the galaxy; hence Active Galactic Nuclei (AGN). In addition to this, AGN emit over a very wide range in energies rather than just a narrow section of the electromagnetic spectrum and in some cases with emission or absorption lines with

a total flux which is a reasonable percentage of the continuum flux. Seyfert (1943) discovered that not only is this subset of galaxies more luminous than other galaxies but they also display properties such as rapid variability and broadened emission lines from emitting material orbiting the nucleus at relatively high velocity.

The variability of AGN can place limits upon the size of the central emitting region due to an estimation of the light crossing time. Since many AGN are seen to be variable on timescales of months and in some cases even a few days or hours (e.g. Lira et al. 2010; Abdo et al. 2011), the speed with which emitted light can vary is limited to the distance from either side of the emitting region, therefore, from these calculations it is apparent that in some AGN a region approximately the size of the solar system is emitting hundreds of times more radiation than the entire galaxy.

1.2 The central engine

A supermassive black hole (SMBH) can power an active nucleus through the gravitational in-fall of matter onto a central object via a hot accretion disc, allowing the extraction of energy. Accreting matter forms a disc since matter travelling along inclined orbits collide and over time all orbits will form in a single plane. Matter orbiting an object following a Keplerian orbit possesses angular momentum l and this must be lost before the matter can fall inwards (see Equation 1.1).

$$l = Rv_\phi = \sqrt{GM_{\text{BH}}R} \quad (1.1)$$

Since the total amount of angular momentum must be conserved, in order for matter to move from one orbit to another (closer in) orbit, angular momentum must be transported outwards. Viscosity within the disc aids the transport of angular momentum outwards as an outer, slower ring brakes the inner, faster ring through friction, therefore decreasing the inner ring's angular momentum and increasing the outer ring's, thereby transporting angular momentum outwards and allowing matter to fall further inwards through the accretion disc towards the SMBH.

Matter continues to fall inwards until it reaches the innermost stable circular orbit (R_{ISCO} , also R_{ms} the radius of marginal stability). This radius is dependent upon the rate of spin of the central black hole: for a non-rotating (Schwarzschild) black hole this is $6 R_g$ and for a maximally rotating (Kerr) black hole this is $1.235 R_g$ where $R_g = GM/c^2$. These refer to the spin parameter $a = 0$ and $a = 0.998$ respectively, where the spin parameter a is given by Equation 1.2.

$$a = \frac{cJ}{GM^2} \quad (1.2)$$

The spin parameter is bounded above at $a = 0.998$ rather than at $a = 1$ due to photon capture, that is, photons on retrograde orbits around the black hole are preferentially captured and because of their ‘negative’ angular momentum, they have the effect of ‘spinning down’ the black hole, hence reducing the maximum possible spin of the black hole and increasing the innermost stable circular orbit to $R_{\text{ISCO}} = 1.235$ from $R_{\text{ISCO}} = 1$ (Thorne 1974).

The efficiency of the accretion process is dependent upon R_{ISCO} and hence the spin of the black hole. The maximum efficiency for an accreting object can be deduced from the binding energy at R_{ISCO} which is the difference between the rest mass of the particle and the energy of the particle at infinity.

$$\eta = 1 - \sqrt{1 - \frac{2R_g}{3R_{\text{ISCO}}}} \quad (1.3)$$

For the case of a Schwarzschild black hole, the maximum radiative efficiency is $\sim 5.7\%$ and $\sim 42\%$ for a Kerr black hole, however, due to the limit imposed by photon capture as stated above, the efficiency decreases to $\sim 30\%$ for a maximally rotating black hole (Thorne 1974). Even for the case of the less efficient non-rotating black hole, the efficiency of turning rest-mass energy into radiation is very high compared to nuclear fusion inside our Sun ($\eta \sim 0.7\%$).

We can express the power generated by the accretion of a mass ΔM over a time Δt (i.e. $\dot{M} = \Delta M / \Delta t$) as seen in Equation 1.4 where $U = GM_{\text{BH}}M/R$ and the factor of $1/2$ is because half heats the surrounding gas and half is radiated away.

$$L = -\frac{1}{2} \frac{dU}{dt} = \frac{GM_{\text{BH}}\dot{M}}{2R} \quad (1.4)$$

This can also be written as the conversion of rest mass into energy with some efficiency η , giving Equation 1.5.

$$L = \eta \dot{M} c^2 \quad (1.5)$$

Comparing the above two equations and rearranging for η we can then roughly calculate the accretion efficiency of the black hole in a Newtonian geometry. For example, in the Schwarzschild case the innermost stable circular orbit is at $R = 6R_{\text{g}} = 6GM/c^2$ which after substituting into Equation 1.6 gives an efficiency of $\eta = 1/12$.

$$\eta = \frac{GM}{2R c^2} \quad (1.6)$$

Of course, for an increasingly high accretion rate we get an increasing luminosity (Equation 1.5), however, this does not hold for an arbitrarily high accretion rate, i.e. the maximum rate of accretion is limited to the Eddington rate (\dot{M}_{E}) which therefore limits the maximum luminosity called the Eddington luminosity (L_{E}). The Eddington luminosity is given in Equation 1.7 where σ_{T} is the Thomson cross-section, working under the assumption that photons are emitted isotropically:

$$L_{\text{E}} = \frac{4\pi GM_{\text{BH}}m_{\text{p}}c}{\sigma_{\text{T}}} \quad (1.7)$$

This can be calculated by resolving the force due to the gravity of the central object and the force due to the radiation pressure exerted by outward photons, giving the maximum luminosity the source can continuously maintain. For luminosities higher than this, the in-falling gas will be blown away due to the radiation pressure exceeding the gravitational pull of the SMBH.

Efficiency can also be stated in terms of the Eddington Luminosity (L_{E}) and the Eddington mass accretion rate (\dot{M}_{E} , i.e. the mass accretion rate required to sustain L_{E}), see Equation 1.8.

$$\dot{M}_E = \frac{L_E}{\eta c^2} = \frac{4\pi G M_{\text{BH}} m_p}{\sigma_T \eta c} \quad (1.8)$$

However, this value of the accretion rate is valid only under the assumption of spherically symmetric accretion and can in fact be exceeded by models featuring accretion through a disc.

We can also express the luminosity of an optically thick disc in terms of the temperature, taking a thin disc emitting as a blackbody according to the Stefan Boltzmann law ($L = \sigma_B T^4$) per unit area where the surface area of an annulus is given by $2\pi R \Delta R$ which has two sides giving an extra factor of two and subsequently Equation 1.9:

$$\Delta L = 4\pi R \Delta R \sigma_B T(R)^4 \quad (1.9)$$

Combining this with $\Delta L = G \dot{M} M_{\text{BH}} \Delta R / 2 R^2$ we get an expression for the temperature of the accretion disc as a function of the radius (Equation 1.10).

$$T = \left(\frac{G M_{\text{BH}} \dot{M}}{8\pi \sigma_B R^3} \right)^{1/4} \quad (1.10)$$

However, this does not take into account any energy which may be lost through the viscous dissipation of energy in the accretion disc, i.e. as a consequence of the outward transport of momentum from material on interior orbits.

A more complete analysis of the temperature of an optically thick but geometrically thin accretion disc as a function of radius can be derived from the heat release per unit disc area whereby the potential energy lost by the inward fall of matter is partly used to heat the disc if the torque is viscous and partly in the transport of angular momentum outwards. This leads us to Equation 1.11, e.g. see Peterson (1997).

$$T(r) = \left[\frac{3GM\dot{M}}{8\pi\sigma_B R_S^3} \right]^{1/4} \left(\frac{R}{R_S} \right)^{-3/4} \left[1 - \left(\frac{R_{\text{in}}}{R} \right)^{1/2} \right]^{1/4} \quad (1.11)$$

For $R \gg R_{\text{in}}$, this can be expressed in terms the Eddington accretion rate (Equation 1.8) and Solar masses gives the final equation for the temperature of a

geometrically thin but optically thick accretion disc taking energy dissipation through viscous forces into account (Equation 1.12).

$$T(r) = \left[\frac{3c^5 m_p}{16\sigma_B \sigma_T G M_\odot \eta} \right]^{1/4} \left(\frac{M}{M_\odot} \right)^{-1/4} \left(\frac{\dot{M}}{\dot{M}_E} \right)^{1/4} \left(\frac{R}{R_S} \right)^{-3/4} \quad (1.12)$$

From this equation we can see that the temperature of the accretion disc can be modelled as a series of blackbody radiators at successive annuli of radius R scaling as $T \propto R^{-3/4}$, i.e., the temperature of the emitted spectrum from the disc decreases further from the central black hole. We can also see that the temperature of the disc increases with higher accretion rates and in fact decreases with the mass of the central SMBH, for example, for $10^9 M_\odot$ the maximum disc temperature is typically $T \sim 10^5$ K, whereas for tens of M_\odot $T \sim 10^7$ K.

1.3 AGN taxonomy

The many different types of AGN can be divided into separate sub-classes according to their luminosity, variability and radio emission.

Quasi-stellar radio sources (Quasars) make up the most luminous subclass of AGN and form the very luminous and compact centres of galaxies, so luminous in fact that they outshine their host galaxies such that only the core is visible (10^{45} - 10^{49} erg s $^{-1}$). Quasars have a relatively featureless spectrum, spanning from radio wavelengths to hard X-rays. Despite the origin of the name, the term quasar now refers to a generic AGN with only 5-10% of quasars having strong radio emission. Sky surveys have detected traces of a low surface brightness halo surrounding some quasars ('quasar fuzz') which appears to suggest that in some cases starlight from the host galaxy may just be visible, adding weight to the theory that quasars are just very luminous Seyferts. This has recently been further investigated by the Hubble Space Telescope, revealing the presence of the host galaxy in some quasars (Bahcall et al. 1995).

Type	Point like	Broad lines	Narrow lines	Radio	Variable
Radio loud quasar	Yes	Yes	Yes	Yes	Some
Radio quiet quasar	Yes	Yes	Yes	Weak	Weak
Broad line radio galaxy (FR2 only)	Yes	Yes	Yes	Yes	Weak
Narrow line radio galaxy (FR1 and FR2)	No	No	Yes	Yes	No
OVV Quasars	Yes	Yes	Yes	Yes	Yes
BL Lac objects	Yes	No	No	Yes	Yes
Seyfert Type 1	Yes	Yes	Yes	Weak	Some
Seyfert Type 2	No	No	Yes	Weak	No
LINERs	No	No	Yes	Some	No

Table 1.1: Comparison of different types of AGN. Radio implies that a reasonably large fraction ($\sim 10^{-3}$) of the object's bolometric luminosity is emitted at radio frequencies ($\nu \sim 10$ GHz). Pointlike refers to whether an optical point source can be seen, variability refers to an object which varies by an order of magnitude or more in the optical band over a timescale comparable to the human lifetime. Table adapted from Krolik (1999).

Seyfert galaxies are typically lower luminosity AGN (10^{43} - 10^{45} erg s $^{-1}$) showing line emission of highly ionised atoms. Seyferts bear similarity to quasars in their properties (see Table 1.1) with the exception that the host galaxy of the AGN is clearly visible as a spiral galaxy and the brightest Seyferts are often of comparable luminosity to the least luminous quasars. Also in contrast to some quasars (especially radio-loud), Seyferts show features in their X-ray spectra indicative of emission and absorption. Seyferts are divided into two distinct classes: Seyfert 1 (S1) and Seyfert 2 (S2). Seyfert 1 AGN display a combination of permitted and forbidden narrow lines and permitted broad optical emission lines. The narrow lines have velocity widths of a few hundred km s $^{-1}$ (still broad compared to non-AGN, but narrow in terms of active galaxies). The widths of the broad emission lines can be up to 10^4 km s $^{-1}$. Seyfert 2 AGN differ in that they do not show broad emission lines (Osterbrock 1989).

Radio galaxies can be viewed as giant elliptical galaxies at optical wavelengths but they produce large amounts of radio emission ($L_{\text{Radio}} > 10^8 L_{\odot}$), usually from a pair of lobes fed by jets emanating from the nucleus. The distinction between FR1 and FR2 (*Fanaroff-Riley*; Fanaroff & Riley 1974) is well defined: FR1 objects are brightest close to the centre of the nucleus, becoming fainter towards the edges of the lobes; in FR2s the jet is relatively weak compared to the lobes and is often only on one side of the nucleus. It is thought that the differences between FR1 and FR2 may be due to the velocity of the jet, i.e. the faster FR2 jets are travelling supersonically through an intervening medium causing shocks.

Low ionisation Nuclear Emission line Region galaxies (LINERs) are very common and could be detectable in as many as up to half of all spiral galaxies, they are similar to Seyfert 2s with the addition that the low ionisation lines (such as O[III] and N[II]) are particularly strong in comparison to those found in Seyferts (Baldwin, Phillips and Terlevich 1981). It is thought that some LINERs may in fact be very low luminosity Seyfert galaxies which can therefore make it difficult to distinguish between Seyferts and LINERs in a quantitative manner (e.g. NGC 7213, Lobban et al. 2010; NGC 4278, Younes et al. 2010). Often low flux ratios of O[III]/H β and N[II]/H α are a good indication of a LINER rather than a low luminosity Seyfert (Veilleux & Osterbrock 1987).

Optically violently variables (OVV) are radio loud AGN which show abnormally large variations at optical wavelengths on timescales as short as 24 hours. These objects also have high polarization compared to most AGN. BL Lac objects share some of the properties of (the more luminous) OVVs showing no emission or absorption features (although weak features have been detected in high S/N spectra). For this reason, OVVs and BL Lacs have been referred to as ‘Blazars’ which have a strongly relativistically beamed component close to the line of sight, i.e., as if viewed down the beam, therefore resulting in the observed variability and dilution of the emission line features.

1.4 Unification schemes

1.4.1 Seyfert unification

The main difference between Seyferts 1 and 2 is that S2s do not feature broad emission lines and the continuum is weaker. There have been a number of attempts to unify S1 and S2s; an initial idea suggested that S1 and S2 were the same except that S2s were viewed through a dusty medium which partially extinguishes the continuum and the broad lines (Allen 1976). The main flaw with this idea is that despite their weaker continuum, some S2s still appear to have a powerlaw-like spectrum whereas if the continuum is indeed obscured by dust, the spectrum should be heavily reddened, i.e. no longer a powerlaw. In addition, S2s are approximately only one magnitude fainter, yet the broad lines are completely extinguished. Some have also suggested that S2s are simply S1s but in a low state (Peterson & Wilkes 2000), however, there are few highly variable Seyferts and even in these cases the broad lines have not totally disappeared. The currently accepted point of view (suggested by Osterbrock 1978) poses that S1s and S2s are actually the same object but viewed from a different angle with the broad line region in S2s being obscured from view by a dusty torus around the central region. Based upon the populations of Seyferts, the torus must cover $\sim 75\%$ of the central source. This model works around the problems encountered by the original dust-obscuration theory by including a further electron scattering medium located above the source and torus, scattering (and therefore polarizing) light from the nucleus to any observer lying in the same plane as the torus without the spectrum being reddened.

There have been some confirmed cases of Seyfert 2s being Seyfert 1s simply viewed from a different angle, given that the narrow emission line features of S1s and S2s are statistically identical. In some cases the S1 spectrum has been observed in the scattered component of the S2 spectrum (Antonucci & Miller 1985). Evidence against the unification of Seyferts in this way stems from the general lack of polarization in the majority of S2s, whereas, for example, in the extreme case of the galaxy being viewed totally edge-on the continuum polarization should be as high as 50% - far higher than

any currently known source. In addition, most higher luminosity objects all appear to have S1-like spectra and not S2-like. If differences in the spectra were mainly due to the viewing angle, there should be a similar distribution of S1 and S2-like spectra in higher luminosity sources. A counter-argument suggests that in higher luminosity AGN the torus has been destroyed (or made thinner), for example by radiation pressure or outflows (e.g. Krolik & Begelman 1988; Hill, Goodrich & Depoy 1996).

1.4.2 Radio-loud and radio-quiet unification

Radio-loud AGN only make up a small proportion of AGN except for particularly high luminosity sources where up to 50% can be radio-loud. Statistically, the UV spectra of radio-loud and radio-quiet AGN are indistinguishable (Steidel & Sargent 1991), however, there are subtle differences in their optical spectra. For example, radio-quiet AGN show stronger Fe[II] emission and weaker narrow lines (Boroson and Green 1992) with radio-loud objects showing smoother line profiles (Miley and Miller 1979). Unification schemes have been proposed, however, in most cases they fail to sufficiently match source properties with statistics. In this case, therefore, it may be that radio emission is a fundamental parameter to AGN, in as much a way as luminosity is.

It has been suggested that it is black hole spin which powers the jets (and hence the radio emission) as mechanical energy is extracted from the black hole (Blandford & Znajek 1977; Wilson and Colbert 1995). This theory operates around the assumption that black hole spin is determined by galaxy mergers and mergers of SMBHs within the parent galaxies, rather than related to the actual accretion process. For example, a merger of two high mass SMBHs could result in a single high mass and high spin black hole (presumably a rare occurrence) which would produce a high luminosity radio-loud AGN. However, a merger of a pair of low mass ($\sim 10^5 M_{\odot}$) black holes would result in a single low mass but high spin black hole, resulting in a relatively faint but radio-loud source. If mergers are the dominant method of determining the spin of SMBHs, the spin distribution can be compared to the fraction of radio-loud AGN, i.e., radio-loud AGN should occupy only the high spin region of the spin distribution whereas only

radio-quiet AGN feature slowly spinning SMBHs.

1.4.3 AGN structure

The standard model of an AGN consists of a central SMBH surrounded by an accretion disc, a broad permitted emission line region orbiting above the disc (e.g. Mg[II], C[IV]) followed by a dusty torus (Antonucci 1993; the candidate for the obscuration of the broad line region as suggested by Seyfert unification theories) and further out is the narrow forbidden line (e.g. O[III]) emission region (see Figure 1.1).

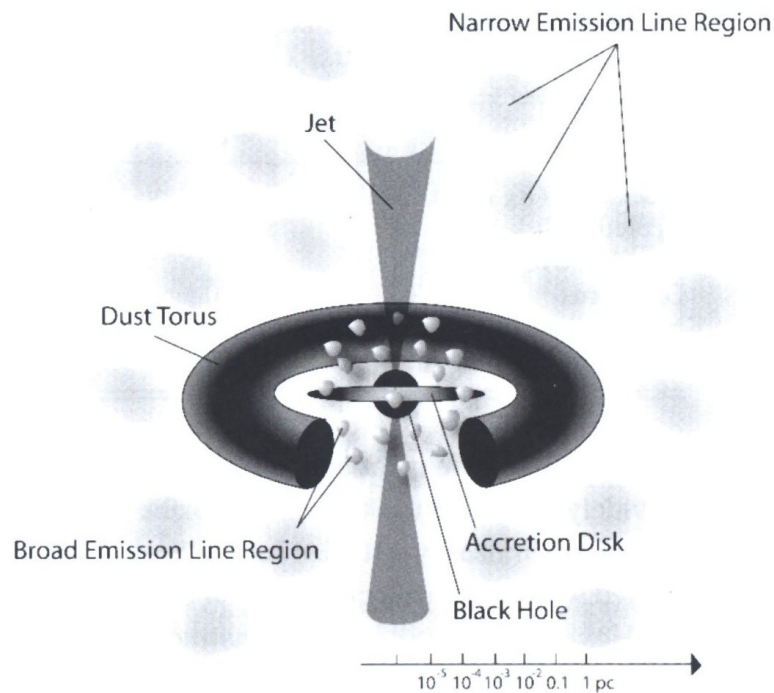


Figure 1.1: Schematic of the central region of a radio-loud AGN displaying the proposed components of an AGN including the dusty torus which may be the distant material responsible for observed narrow emission such as neutral He-like and H-like Fe. Dimensions are logarithmic. Figure taken from Rosswog & Bruggen (2007).

The accretion disc is not isothermal and therefore its spectrum does not follow a single Plank spectrum. The emission of the disc can then be represented as the sum of a

series of blackbody spectra for increasing radii throughout the disc (see Equation 1.11). As a result, the peak emission from the disc occurs at a photon energy of $kT \sim 10$ eV (for a $\sim 10^8 M_\odot$ SMBH accreting at \dot{M}_E occurring at a radius of $\sim 20 R_g$) which lies in the UV and EUV bands. The rise in the continuum spectra of AGN caused by this is often referred to as the Big Blue Bump. A hot corona above the disc in which soft photons are Comptonised by thermal electron-positron pairs could be a source of hard photons observed at higher X-ray energies (Czerny & Elvis 1987, Haardt & Maraschi 1993, Tsuruta & Kellen 1995).

The broad line region is an area of fast moving, high density ($n_e > 10^9 \text{ cm}^{-3}$) clouds of gas responsible for emission lines at optical and UV wavelengths. As a consequence of its high density, only permitted emission lines are seen since forbidden lines produced by non-electric dipole transitions are collisionally suppressed. Observed correlations between variations in broad lines and the continuum suggest that photoionisation from the central source is a likely explanation for the excitation of the region (Peterson 1994). The broad line widths of emission lines from this region are due to broadening via the Doppler effect of the rapidly orbiting clouds. The high velocities required by this explanation ($\sim 10^4 \text{ km s}^{-1}$) indicate that the broad line region must be close to the central SMBH.

The intervening torus blocks broad optical and UV spectral lines emitted from the broad line region whereas the absorbed high energy radiation is re-emitted as a blackbody spectrum at infrared wavelengths. The inner radius of the torus is ~ 1 pc from the central source, extending to $\sim 50 - 100$ pc.

The narrow line region (lying beyond the dusty torus) is a region of low density ionised gas ($n_e \approx 10^3 - 10^6 \text{ cm}^{-3}$), i.e. electron densities are sufficiently low such that forbidden transitions are not collisionally suppressed. Due to its size the narrow line region can be spatially resolved at optical wavelengths, extending from $50 - 200$ pc.

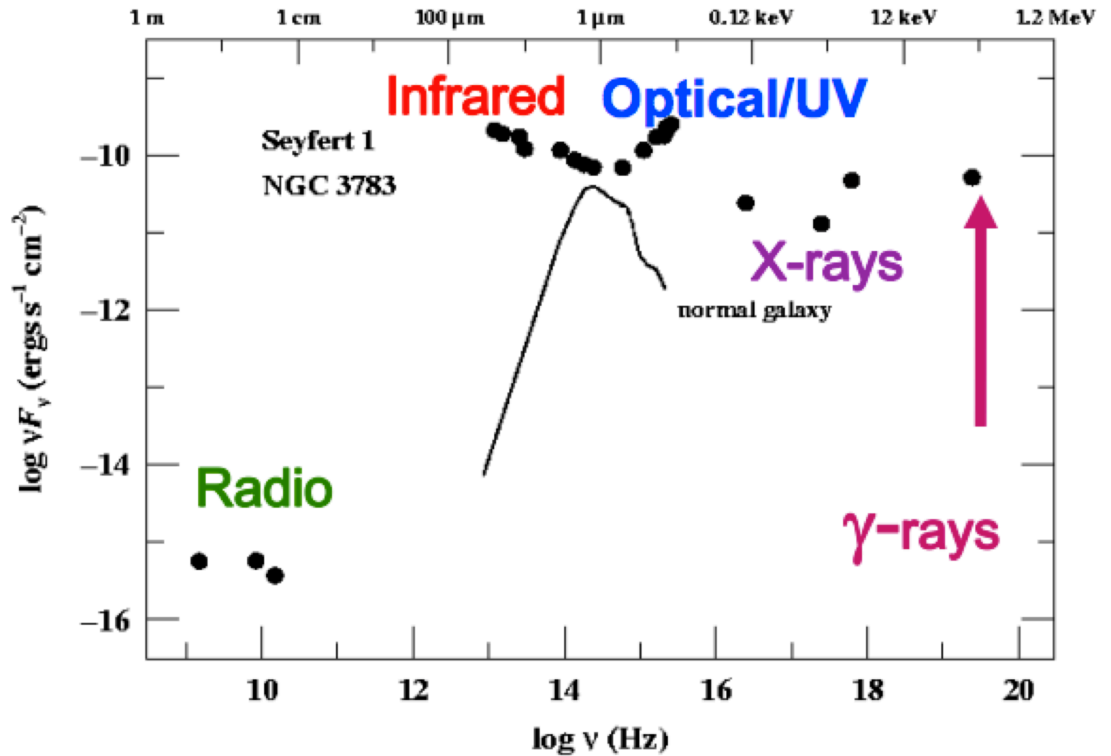


Figure 1.2: Spectral energy distribution (SED) of the Seyfert 1 AGN NGC 3783 covering radio up to gamma rays, note the flux relative to that for a normal (i.e. non AGN) galaxy. Figure taken from <http://ned.ipac.caltech.edu/level5/March11/Peterson/peterson1.pdf> and adapted from Alloin et al. (1995).

1.5 SED and the X-ray spectra of Seyfert 1 AGN

The spectral energy distribution (SED) of AGN is their defining feature and what makes them different from other galaxies, being more luminous at every wavelength in comparison. Indeed, non-thermal emission is required to describe the SED of AGN. In general the whole broadband spectrum can be described as a power-law $F_\nu \propto \nu^{-\alpha}$ where $0 < \alpha < 1$ (note that examining each energy band in isolation will yield differing spectral indices). Plotting as $\log \nu F_\nu$ versus $\log \nu$ (i.e. $\nu F_\nu \propto \nu^{-\alpha+1}$), $\alpha = 1$ would

give a flat slope with equal energy per decade. Figure 1.2 shows the spectral energy distribution for the Seyfert 1 AGN NGC 3783 plotted in this manner.

A significant fraction of the bolometric luminosity of AGN is in the form of X-rays ($\sim 10\%$). The widespread nature of X-ray emission from Seyferts (Elvis et al. 1978) was established by the *Ariel-V* sky survey (Cooke et al. 1978), in which the general power-law shape of the X-ray spectrum was recognised (Mushotzky 1978a, 1978b, 1980; Ives, Sanford & Penston 1976; Stark et al. 1976; Barr et al. 1977). Initial spectral analysis revealed 6.4 keV Fe K α line emission and curvature at soft X-ray energies due to photoelectric absorption. *EXOSAT* observations revealed rapid variations in some AGN (McHardy 1990, Pounds & McHardy 1988) and the existence of the soft excess in $\sim 50\%$ of Seyferts (Arnaud et al. 1985, Turner & Pounds 1989). A basic representation of the X-ray spectrum at 2-50 keV can take the form of a simple power-law with photon index $\Gamma \sim 2.0$ with a high-energy photoelectric cut-off at approximately > 100 keV (Risaliti 2002).

With data from more advanced X-ray observatories with higher resolution and greater band-pass, much more of the X-ray spectrum of AGN has been revealed by telescopes such as *Chandra*, *XMM-Newton* and *Suzaku*. For example, a very basic representation of the continuum can be seen in Figure 1.3, which features Galactic absorption, the intrinsic powerlaw, soft excess, reflection component, narrow FeK α emission, broad emission in the FeK region and warm absorption.

1.5.1 Important processes in AGN spectra

1.5.1.1 Blackbody radiation

A blackbody is an object which emits and absorbs at the same rate and is therefore in thermal equilibrium with intensity given by Equation 1.13:

$$I(T) = \frac{2h\nu^3}{c^2(e^{h\nu/k_B T} - 1)} \quad (1.13)$$

In the above equation I is the intensity of the output spectrum given a temper-

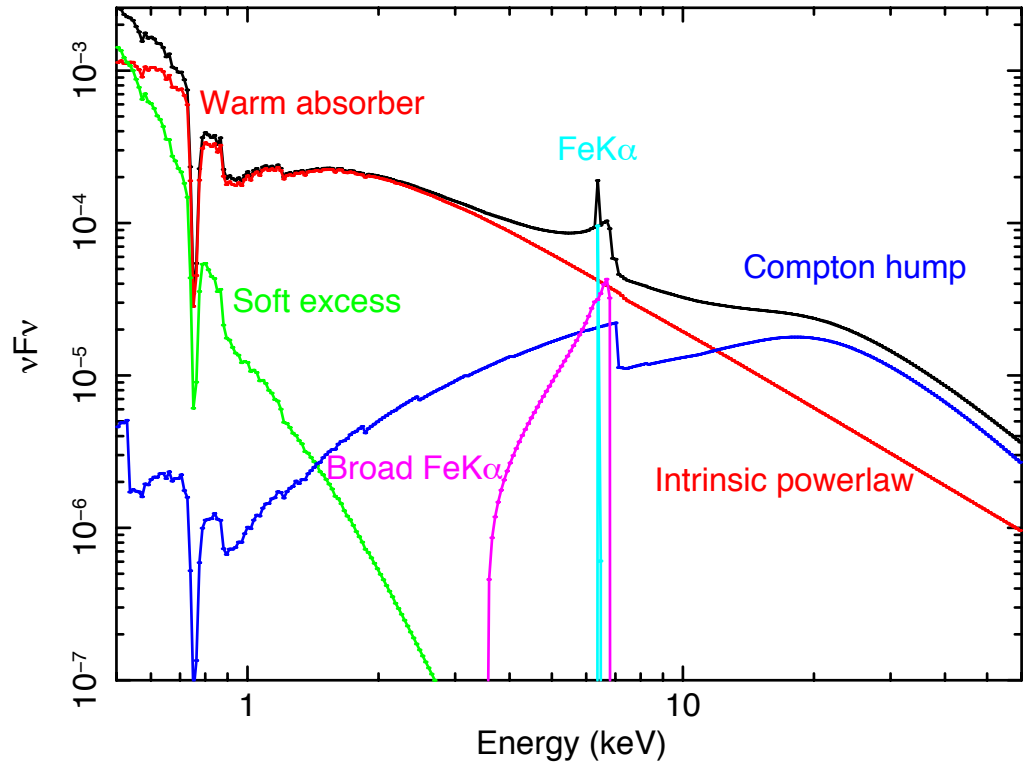


Figure 1.3: The main components found in AGN X-ray spectra. The spectrum consists of a power-law at $\Gamma = 2.0$ (red component), Comptonisation of soft photons in a hot plasma at low energies (Titarchuk 1994, green component), narrow emission from the FeK region ($\sim 6 - 7$ keV, light blue component), broad emission from the FeK region (pink component) and a Compton hump at high energies due to Compton scattered photons produced from X-ray reflection (dark blue component). Note that all components are attenuated by a warm absorbing zone as can be seen at low X-ray energies.

ature T at a frequency ν , h is Planck's constant, c the speed of light in a vacuum and k_B is the Boltzmann constant. While being a relatively simple concept, a blackbody radiator can provide a reasonable explanation for a number of astrophysical scenarios, e.g. thermal emission from an optically thick accretion disc through the summation of annuli of different kT .

1.5.1.2 Compton scattering

Compton scattering is the process whereby photons (e.g. X-rays) inelastically scatter off matter such that the energy of the photon is decreased. Some of the energy from the incoming photon is transferred to the scattering electron and the photon (with decreased energy) is then scattered at an angle θ to the original photon trajectory. Note that it is referred to as inelastic since the energy of the photon is decreased through this process, however, the interaction as a whole including the electron *can* be considered to be elastic due to conservation of energy. The change in the photon's wavelength can be expressed in Equation 1.14, where λ' and λ are the final and initial wavelengths respectively and m_e is the rest mass of an electron.

$$\lambda' - \lambda = \frac{h}{m_e c}(1 - \cos\theta) \quad (1.14)$$

Particularly important in high energy astrophysics is a scenario known as inverse Compton scattering whereby the energy of the incident photon is actually increased as a result of scattering off a relativistic electron. This process is thought to be responsible for the non-thermal power-law shape typical of X-ray spectra in AGN, see also Section 1.5.2.

1.5.1.3 Photoelectric absorption

Photoelectric absorption is the absorption of a photon of a specific energy by an electron inside an atom. This can either result in the electron remaining bound to the atom but existing in an excited state or the electron can be ejected from the atom (known as a bound-free transition) and the atom becomes ionised.

The probability of a photon being absorbed by an atom is a function of energy and is given by the photoelectric cross-section $\sigma(E)$. The probability of absorption of the photon is at its highest at the energy required to just eject the electron, producing an absorption edge (see Section 1.5.5). The output spectrum F_{out} after the input spectrum F_{in} has been absorbed by a column density of N_{H} is typically given by Equation 1.15.

$$F_{\text{out}} = F_{\text{in}} \times e^{-N_{\text{H}}\sigma(E)} \quad (1.15)$$

1.5.1.4 Line emission

Photons which are incident upon an atom can excite bound electrons to higher energy levels, leaving a gap in the inner energy levels. The atom can de-excite by the excited electron dropping down to fill the energy gap while emitting a photon with an energy equal to the energy gap; this is known as fluorescence. An example of such an emission line is the Fe K α line at 6.4 keV which is the energy of the photon produced when an electron from the L shell drops to the innermost K shell, this line is very common in the X-ray spectra of AGN (Nandra & Pounds 1994). The K α line is actually a doublet with the line energies differing due to the electron's spin-orbit interaction, i.e. the $1s - 2p_{1/2}$ and $1s - 2p_{3/2}$ transitions. Similarly the Fe K β emission line at 7.056 keV occurs when an electron drops from the M shell to the K shell.

1.5.2 Intrinsic X-ray continuum

The intrinsic power-law shape of the X-ray spectrum of AGN is thought to originate from the Compton up-scattering of UV photons emitted from the accretion disc itself. The heat generated from the accretion disc due to the viscosity of the disc and the resultant transfer of angular momentum to the outer regions of the disc causes the geometrically thin but optically thick accretion disc to emit as a blackbody (i.e. see Section 1.2 and Equations 1.10 & 1.12). Given that the temperature of the emitted spectrum varies according to the radius of the orbit, the resultant spectrum of the accretion disc is the summation of a series of blackbody emitters for each successive annulus (i.e. a thermal origin, Malkan & Sargent 1982; Czerny & Elvis 1987). The primary component of the emitted spectrum is at UV energies and forms what is commonly known as the 'big blue bump'. Note that that true origin of the big blue bump is as yet unknown and there have been alternatives to an optically thick origin

suggested (e.g. Barvainis 1993) whereby it originates from material which is optically thin to free-free absorption.

The thermal UV emission from the accretion disc peaks at temperatures $kT \sim 20$ eV and these act as seed photons for the production of the actual X-ray continuum itself which is formed by the inverse Compton scattering of UV photons in a hot corona of relativistic electrons surrounding the disc ($kT \sim 100$ keV,) to create a non-thermal power-law spectrum ($F_\nu \propto \nu^{-\Gamma}$). This forms the basis of the intrinsic X-ray spectrum of Seyfert Type AGN with Mushotzky et al. (1980) finding that early X-ray observations of AGN could be fitted with a power-law of slope $\Gamma \sim 1.7$.

1.5.3 X-ray reflection

X-rays seen at high energies are thought to originate from the reflection of primary X-rays off a cold ($T < 10^6$ K; George & Fabian 1991), optically thick gas which could be the accretion disc (Guilbert & Rees 1988; Lightman & White 1988). Due to Compton down-scattering of photons at high energies and photoelectric absorption at lower energies reducing the number of photons reflected, a feature called a ‘Compton-hump’ is produced at energies peaking at ~ 30 keV.

Iron is the last element with a high abundance which can significantly affect the amount of reflection/ absorption of the incident X-rays, resulting in an Fe K edge absorption feature from $\sim 7 - 9$ keV and an Fe K α fluorescence line from neutral Fe which is observed in nearly all AGN spectra. The Compton reflection model is therefore dependent upon the fraction of photons which are reflected (i.e. the solid angle covered by the scattering medium), the inclination of the medium to the line of sight, the abundances of elements (notably Fe) and the ionisation of the scattering medium. As the ionisation of the scattering medium increases elements such as carbon, oxygen and then iron reach complete ionisation such that the reflection spectrum resembles the smooth incident power-law spectrum at soft energies (see Figure 1.4). The ‘Compton hump’ therefore becomes less pronounced at higher ionisations, however, there is still a drop off above 30 keV due to the decrease in the Compton scattering cross-section

with increasing energy.

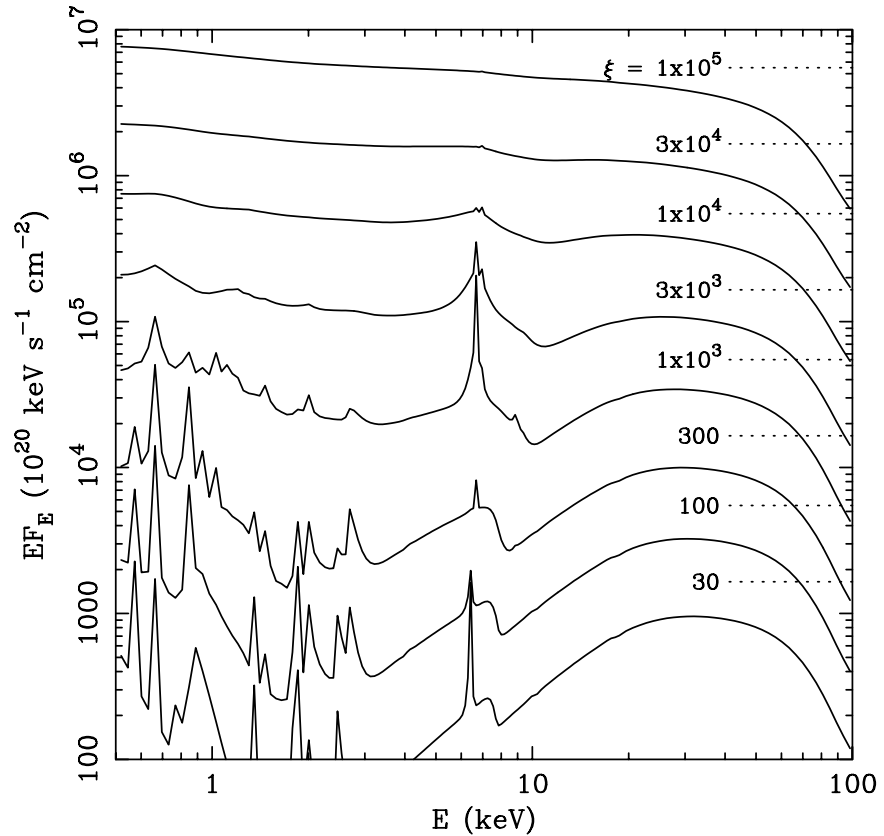


Figure 1.4: Reflection spectra for illumination of a uniform slab with varying values of the ionisation parameter $\xi = 4\pi F/n_H$ in units erg cm s^{-1} , where F is the total illuminating flux (from 0.01-100 keV) and n_H is the hydrogen number density. Figure taken from Ross, Fabian & Young 1999.

Alternative explanations of the Fe K edge and observed high energy excess includes a partial covering of the primary X-ray source by low ionisation, dense material of with column density ($N_H > 10^{23} \text{ cm}^{-2}$) with a covering fraction of up to $\sim 98\%$, i.e. some proportion of the continuum emission is covered by thick absorbing gas while some of the intrinsic power-law leaks through the absorbing zone unattenuated (Matsuoka et al. 1990, Piro et al. 1990). The large column density produces the Fe K edge and since the covering material is transparent to Thomson scattering but the

Fe K line emission cross section is greater than the electron scattering cross section, line emission can still be seen in models using partial covering unless $N_H > 10^{24} \text{ cm}^{-2}$ where Thomson/ Compton scattering is not negligible. Partially covering material with particularly high column densities ($N_H > 10^{24} \text{ cm}^{-2}$) can absorb the incident X-ray photons to the extent that only the hard X-rays ‘leak’ through, thereby accentuating an excess at hard X-ray energies which can be an alternative to or even be supplementary to the reflection component.

1.5.4 The soft excess

In many X-ray spectra, there is often an observed excess towards the lower X-ray energies (i.e. at soft X-rays, typically $< 2.0 \text{ keV}$). The precise origin of the soft excess is unknown, however, there are a number of competing theories. A basic interpretation is simple black-body radiation from the accretion disc or the resultant spectral shape representative of the thermal emission of the disc from the sum of the Wien tails from consecutive annuli throughout the disc (see Figure 1.5). This hypothesis would, however, suggest a relatively constant temperature of the soft excess component which is inconsistent with the observed data for AGN, i.e. the inferred disc temperature of $kT \sim 0.1 \text{ keV}$ is too high for AGN, whereas we would expect a temperature of typically tens of eV (Gierliński & Done 2004). Since the temperature of the direct emission from the disc scales as $T_{\text{disc}} \propto M^{-1/4}$, what we observe as the soft excess component in the X-ray spectra of AGN would be more appropriate for discs surrounding intermediate size black holes, i.e. $10^4 - 10^5 M_{\odot}$.

A variation upon this concept is the Compton up-scattering of EUV photons from the disc (i.e. of seed photons with a temperature appropriate for an accretion disc in an AGN) in a warm corona above the disc with temperatures of a few keV. The resultant powerlaw-like spectrum is then consistent with the observed soft X-ray data. Note that this mechanism is similar to the production of the intrinsic power-law component seen in all AGN, differing only in the temperature and optical depth of the surrounding corona (e.g. see Figure 1.5). In comparison, the hot corona which is

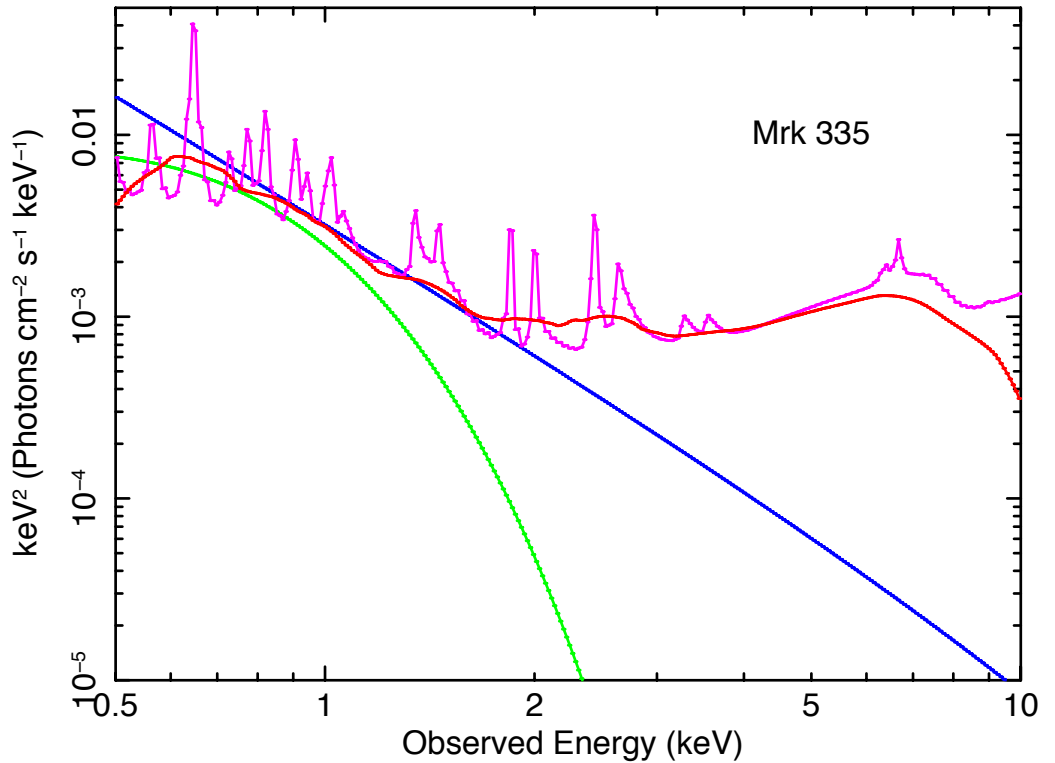


Figure 1.5: Examples of the varying interpretations of the soft excess component applied to the Seyfert 1 AGN Mrk 335. Green represents a simple disc blackbody, blue results from the Compton up-scattering of EUV photons from the disc, i.e. powerlaw-like, red represents blurred reflection from the inner regions of the accretion disc which when smeared into a continuum may be used to model the soft excess whereas the pink (spiked) line represents this reflection component prior to relativistic blurring.

responsible for the intrinsic power-law component has $kT \sim 100$ keV.

The soft excess in AGN has also been hypothesised to have an atomic origin whereby soft X-ray emission lines in the reflection spectrum from the inner regions of the accretion disc are subject to extreme relativistic blurring such that the discrete emission line features are smeared into a smooth continuum (see Figure 1.5; also see Section 1.7.2 for more on blurred reflection interpretations). Due to the significant amount of blurring required to form such a smooth spectrum, emission from the disc must be very centrally concentrated and the central black hole must be rotating rapidly

(i.e. near maximal) in order to remove the discrete nature of the soft X-ray emission lines.

1.5.5 Absorption in X-ray spectra

While ‘clean’ AGN X-ray sources do exist, the vast majority of AGN X-ray spectra feature at least some degree of absorption in addition to the typical Galactic absorption which is a line-of-sight effect due to dust in our own Galaxy. The nucleus of the AGN is surrounded by one or more zones of absorbing gas in which photoionisation is the primary process for the ejection of electrons from an ion due to the intensity of the radiation from AGN, i.e., photoionisation is dominant over collisional ionisation whereby free electrons collide with the ions and eject further electrons. Electrons are ejected from ions via interactions with UV/ X-ray photons provided that the incident photon carries sufficient energy to match or exceed that required to eject an electron from its shell; this threshold is called the ionisation energy. Since bound-free transitions can be produced by any incident photon which has an energy exceeding the ionisation energy, the bound-free edge or ‘gap’ in the resulting spectrum features a sharp drop at the ionisation energy followed by a gradual drop off in the amount of absorption towards higher energies.

These absorption zones can impart spectral curvature upon the X-ray continuum at soft X-ray energies due to the superposition of bound-free edges from different ions. The column density of the absorbing gas and its ionisation can therefore drastically affect the degree of spectral curvature and the energies at which it most affects the reprocessed X-ray spectrum. With sufficiently high column densities the soft X-ray spectrum is almost totally absorbed, i.e. there are enough ions such that all incident photons are absorbed, although the remaining photons at high energies are due to scattering of the photons. With increasing ionisation of the absorber it is intuitive that bound-free edges occur at higher and higher energies as the ionisation energy of ions increases and hence the effects of a warm absorber can have a more important effect further up the X-ray spectrum. The cumulative effect of these absorption edges

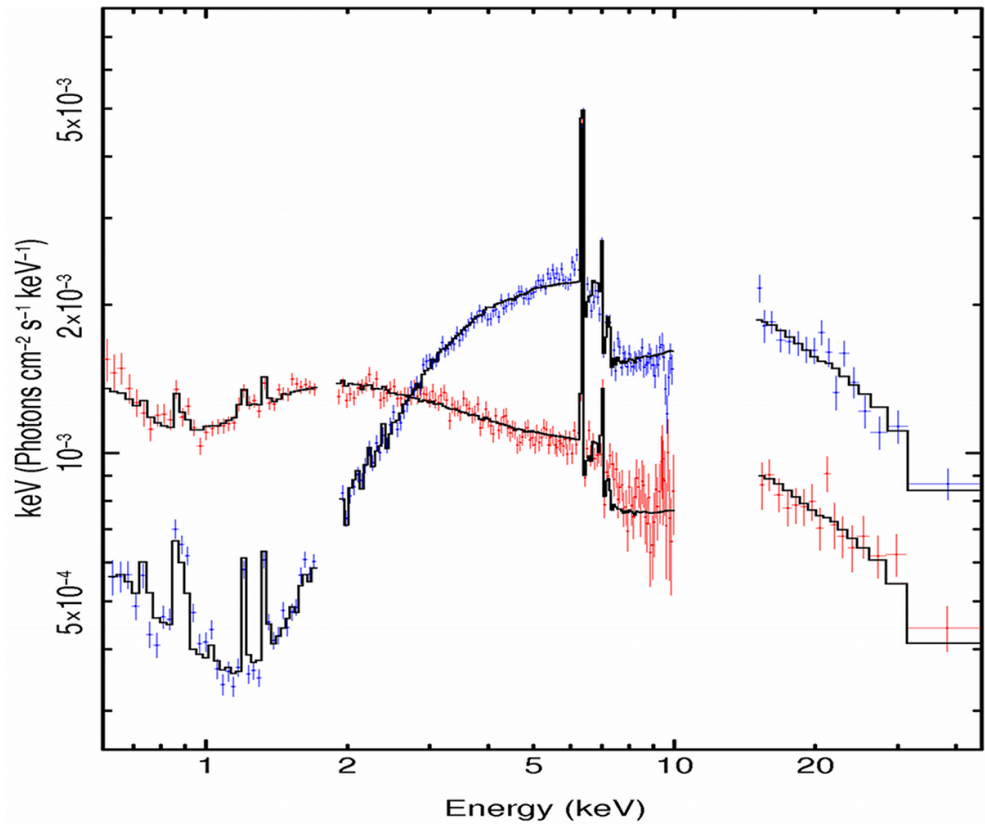


Figure 1.6: Example of the effect a warm absorber can have on the X-ray spectrum of AGN. In this case changes in the warm absorber have altered the shape of the spectrum of NGC 3516 between the 2005 (blue) and 2009 (red) observations with *Suzaku*. Figure taken from Turner et al. (2011).

can result in significant spectral curvature, e.g. see Figure 1.6.

The presence of a warm absorbing component was first invoked to explain flux-correlated spectral changes in the line-of-sight of AGN. For example, Halpern (1984) and Pan, Stewart & Pounds (1990) found that in an analysis of 15 observations of MR2251-178 with *EXOSAT*, luminosity changes were correlated with changes in the column density or ionisation of the warm absorber. Similarly, Nandra et al. (1991) found that changes in the ionisation of the absorbing material cause variations in the relative amplitudes of the soft and hard X-ray variability.

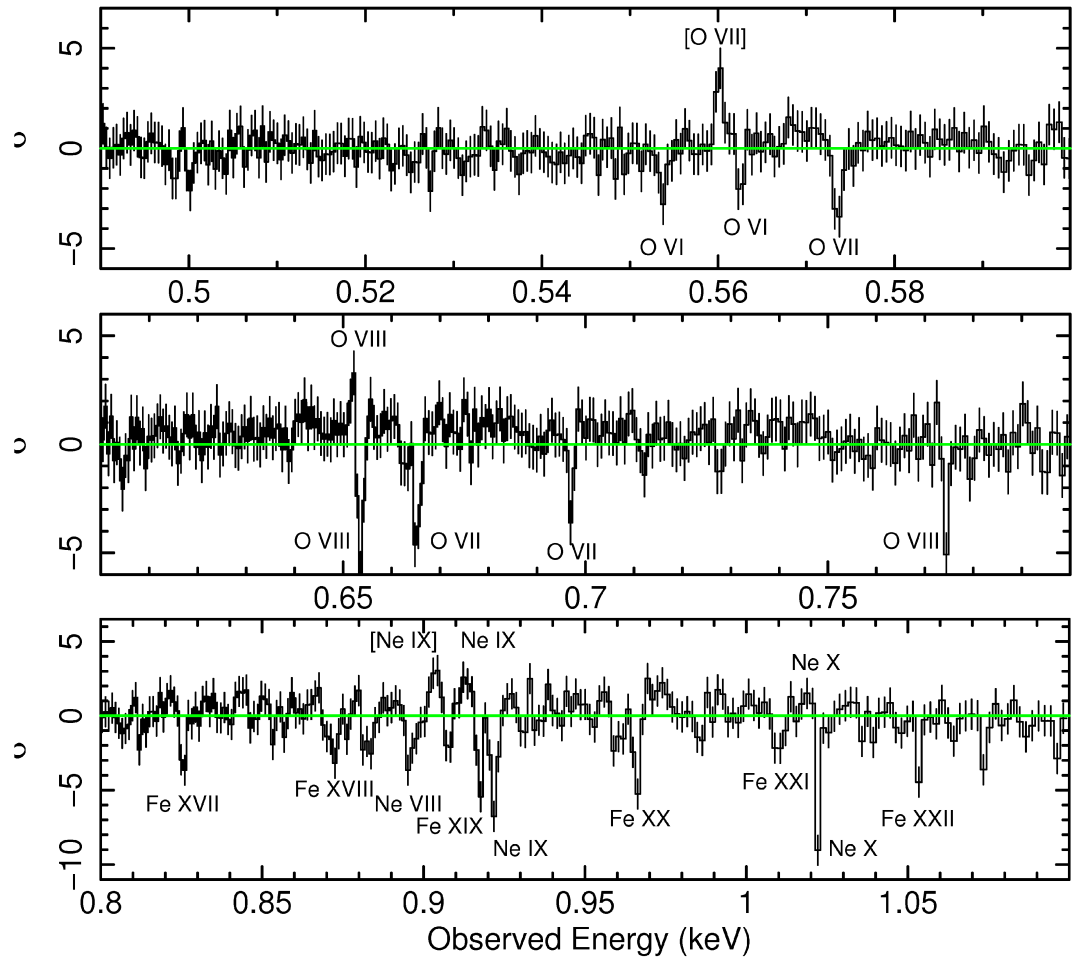


Figure 1.7: Examples of narrow absorption lines observed in Seyfert 1 AGN in HETG *Chandra* data. Plots taken from Lobban et al. (2011) in an analysis of *Chandra* and *Suzaku* observations of NGC 4051.

In addition to bound-free edges we also see strong evidence for resonance absorption lines in the X-ray spectra of AGN, which are particularly prominent in grating spectra taken during *Chandra* observations (e.g. see Figure 1.7). Indeed, Matt (1994) suggested that if ionised matter is in the line of sight (i.e. the warm absorber) then in the optically-thin regime the equivalent width of any FeK absorption line would be sufficiently strong to be detected in the X-ray spectra of AGN, for example, with equivalent widths of tens of eV for column densities of around 10^{23} cm^{-2} . Narrow ab-

sorption lines were detected in the first high resolution X-ray spectrum of a Seyfert with the Low Energy Transmission Grating (LETG) onboard *Chandra* in an observation of NGC 5548, finding highly ionised species of C, N, O, Ne, Na, Mg, Si and moderately ionised species of Fe (Kaastra et al. 2000; also see Figure 1.7), noting that the corresponding absorption edges are absent. These narrow absorption lines were also found to be blue-shifted by a few hundred km s^{-1} , suggesting the material may be outflowing. Subsequent to this initial observation of absorption lines in AGN, there have been many observations and detections of similar absorption zones with outflow velocities ranging from hundreds to thousands of km s^{-1} , e.g. Kaspi et al. (2002) in NGC 3783; Blustin et al. (2005); Lobban et al. (2011). In addition to soft X-ray absorption lines, absorption due to highly ionised species of iron have been detected in a number of AGN, also outflowing, e.g. Reeves et al. (2004) and Tombesi et al. (2010a), see Section 1.6.3.

1.6 Broad emission and the Fe K region

The Fe K region ($\sim 6 - 7 \text{ keV}$), despite being a relatively small part of the X-ray spectrum, features a large number of components which can allow a great deal of information to be obtained regarding the inner regions of AGN. This region can contain indications of relativistically broadened emission from the very inner regions of the accretion disc, distant emission lines from the outer disc, NLR, BLR or torus; and highly ionised absorption which may result from outflows due to disc winds.

1.6.1 Broad emission and the inner regions

After modelling the above mentioned X-ray continuum components, some AGN have shown evidence for a small bump or excess at energies $\sim 5 - 6.4 \text{ keV}$. One of the first instances of this excess being modelled with relativistic emission from reflection of the inner regions of the accretion disc is presented by Fabian et al. (1989) in an

analysis of the X-ray spectrum of the high-mass X-ray binary Cygnus X-1. This paper led to the development of the DISKLINE relativistic line emission model assuming a Schwarzschild black hole (i.e. non-rotating). This model allows the inner radius of emission, disc emissivity (the radial dependence of the disc emission, parameterised by a power-law of the form R^{-q}) and inclination of the accretion disc to be estimated given a sufficient number of counts at FeK energies. These models can produce asymmetric line profiles with both red and blue wings of varying strengths due to transverse Doppler shift, i.e. from the approaching and receding sides of the disc and its inclination to the observer's line of sight.

For example, if the emission arises from the very inner regions of the accretion disc the photons will be subject to much greater orbital velocities and subsequently the receding edge of the disc will appear to be reddened or highly redshifted. In extreme cases FeK α emission at 6.4 keV in the rest frame can be redshifted down to soft X-ray energies as low as 1-2 keV. The overall line profile will be subjected to gravitational redshift, producing a net redshift of the whole profile relative to the rest-frame energy. The blue-wing of an asymmetric line profile therefore arises from the approaching edge of the disc whereby photons of 6.4 keV in the rest frame are blue shifted up to ~ 7 keV, e.g. see Figure 1.8. Indeed, in the majority of cases the blue-wing is stronger relative to the red-wing when the disc is viewed at an angle since material in the inner disc is travelling at relativistic velocities and is enhanced when travelling towards the observer due to Doppler boosting. More details regarding the shape of line profiles originating from the inner regions of the accretion disc can be found in Section 2.5.6.

With more sensitive X-ray telescopes and higher quality data, evidence for broadened FeK α lines became more common, perhaps the most well known being the iron line in MCG-06-30-15, in which the first detection of a 'diskline' type line profile in an AGN was made by Tanaka et al. (1995) in data from ASCA. Although this was initially under the assumption of a Schwarzschild black hole. The line profile in MCG-06-30-15 has since been claimed to be sufficiently broad as to require a rapidly rotating (i.e. Kerr) SMBH at its centre (e.g. Miniutti et al. 2007, see Figure 1.9). Some surveys such as that by Nandra et al. (2007) using *XMM-Newton* data have suggested that

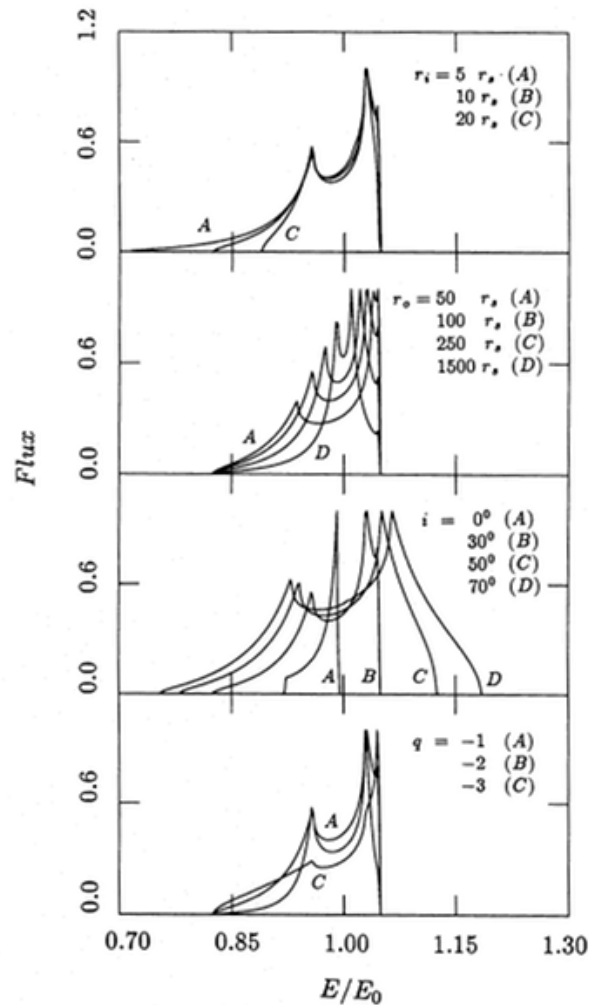


Figure 1.8: Line profiles generated with the DISKLINE model from Fabian et al. (1989) under the assumption of a non-rotating Schwarzschild black hole. When not specified, other parameters are specified with $R_{\text{in}} = 10 R_S$, $q = -2$ and $i = 30^\circ$, where R_{in} is the radius of the inner edge of emission from the accretion disc. Note that the convention used in this figure for the emissivity index is of the form R^q as opposed to R^{-q} . Figure taken from Fabian et al. (1989).

the majority of AGN feature some form of broad emission in the Fe K region from reflection off inner disc material (see Figure 1.10 for examples). Broad emission lines are therefore relatively common and can be used as an important diagnostic of the inner

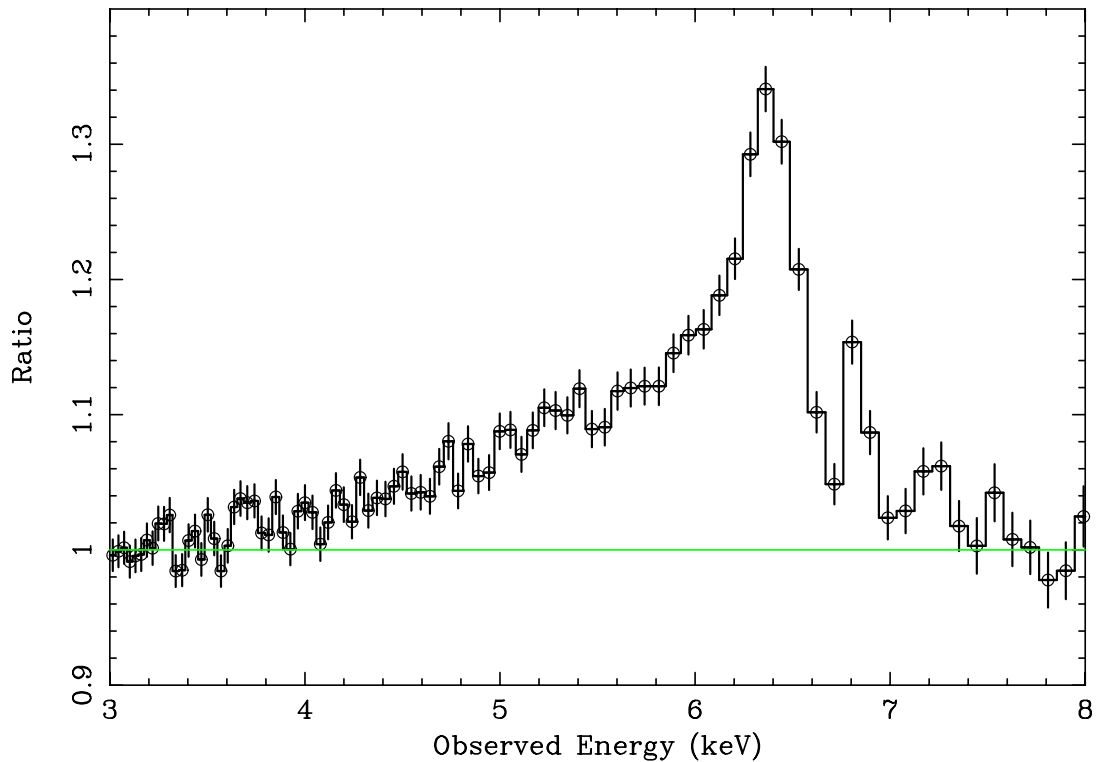


Figure 1.9: Ratio plot displaying an example of a broad red-wing claimed to have been observed by some authors. Data from a 2006 *Suzaku* observation of MCG–06-30-15 are fit to a simple power-law over 2.5-10 keV. Figure taken from Miniutti et al. (2007). See Chapter 4 for a more comprehensive analysis of this data set.

regions of the accretion disc, allowing the estimation of the disc inclination, central concentration of emission and in some cases SMBH spin.

1.6.2 Distant narrow emission

The FeK region can also feature strong emission from material more distant from the central object, in regions such as the outer accretion disc (i.e. hundreds of R_g), the broad line region or the torus (see Matt et al. 1996). In comparison to emission lines from the inner region of the disc, these more distant lines are relatively narrow and any width is as a result of velocity broadening rather than due to gravitational redshift

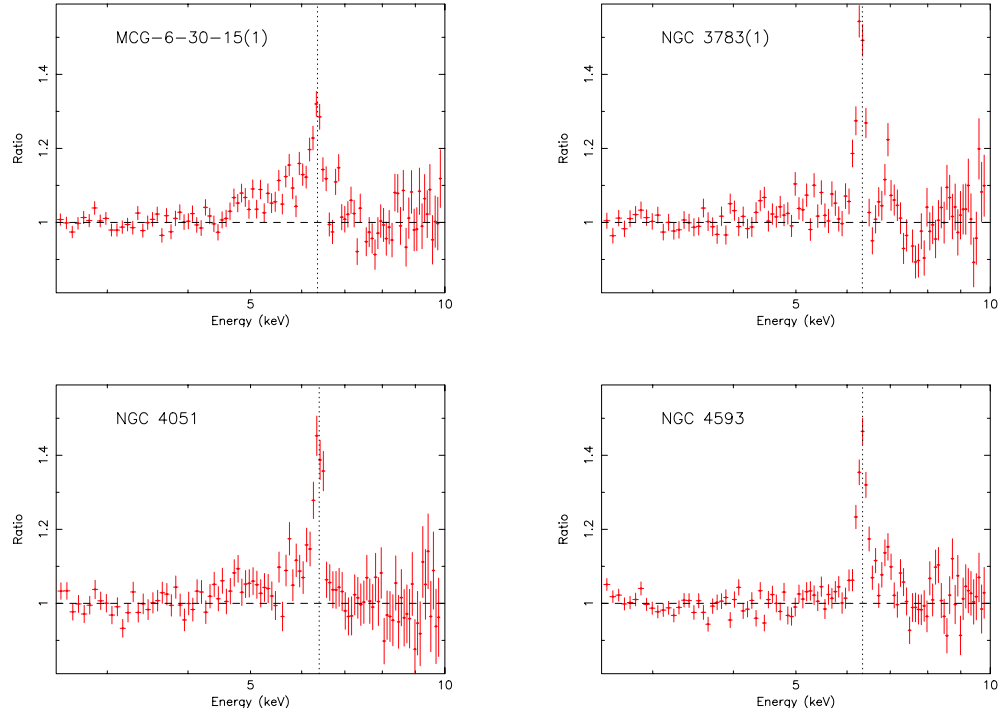


Figure 1.10: Ratios of Fe K regions to a power-law spectrum of AGN. Note the presence of narrow emission or absorptions lines at 6.7 keV and 6.97 keV in some objects. Plots taken from Nandra et al. (2007), which conducts an analysis of *XMM-Newton* observations over the 2.5-10.0 keV range.

or other relativistic effects. Also common in the Fe K region are emission lines from highly ionised species of iron at energies of 6.7 keV and 6.97 keV from Fe XXV and Fe XXVI respectively (1s-2p resonance transitions, see Nandra & Pounds 1994 and Figure 1.10 for examples). These emission lines were initially thought to be rare in the X-ray spectra of Seyfert 1 AGN. If ionised emission lines originate from circumnuclear gas such as the torus they can be more readily observed in Compton thick Seyfert 2 spectra of AGN since they are not subject to heavy dilution due to photons from an unobscured nucleus.

Since the launch of X-ray observatories with greater energy resolution at Fe K energies (such as *XMM-Newton*, *Chandra* and *Suzaku*) the Fe K α narrow emission line

has been observed in a number of nearby Seyfert 1 AGN, e.g. Kaspi et al. (2001); Yaqoob et al. (2001); Reeves et al. (2001); Pounds et al. (2001). The first detection of narrow ionised emission lines due to FeXXV and FeXXVI was made by Matt et al. (2001) in NGC 5506 (also see Bianchi & Matt 2002), however, recently there have been more detections of these lines in nearby Seyfert 1 AGN (e.g. Nandra et al. 2007; Bianchi et al. 2009).

It should be noted that the detection of emission lines from highly ionised species of iron could be influenced by the presence of a blue wing of an asymmetric line profile from emission near the inner regions of an accretion disc. If a blue wing of a line profile peaks at a similar energy to the FeXXV or FeXXVI energies, it cannot be certain that a peak in the X-ray spectrum is indeed either the blue wing of a relativistic line or the relatively narrow 6.7 keV or 6.97 keV photoionised emission lines.

1.6.3 Highly ionised absorption in the Fe K region

In addition to emission lines from highly ionised species of iron in the Fe K region (FeXXV and FeXXVI), some authors have found strong evidence for highly ionised absorption zones in the X-ray spectra of AGN (Reeves et al. 2004; Miller, Turner & Reeves et al. 2008; Tombesi et al. 2010a, 2010b; Lobban et al. 2011; see Figure 1.10). A large proportion of these absorption zones have been found to be outflowing, i.e. the absorption lines are found to be *blueshifted* with respect to their rest-frame energies of 6.7 keV and 6.97 keV at velocities of up to a reasonable fraction of c ($v_{\text{out}} < 10^5 \text{ km s}^{-1}$; Chartas et al. 2002, 2003; Pounds et al. 2003; Dadina et al. 2005; Markowitz et al. 2006; Braitto et al. 2007; Cappi et al. 2009; Reeves et al. 2009; Tombesi et al. 2010a, 2010b; Gofford et al. 2013). These blue-shifted absorption lines are thought to be a signature of high velocity outflows and accretion disc winds, likely due to radiation pressure (Proga et al. 2000) and a high degree of ionisation by intense nuclear radiation with potentially large velocities (e.g. King & Pounds 2003).

Subtle spectral curvature due to highly ionised absorption in the Fe K region can also mimic what would otherwise be described as broadened *emission* from the inner

regions of the disc (see NGC 3783 Reeves et al. 2004). Depending upon the velocity of the absorbing zone, the strength of the absorption could effect the detection of narrow distant emission lines if both the emission and absorption lines occur at similar energies. Both of these factors mean that highly ionised absorption zones in the X-ray spectra of AGN are very important and a key component when modelling the Fe K region.

1.7 Supermassive black hole spin

Black holes can primarily be characterised by two properties: their mass and their spin (the so called ‘No hair theorem’). While a number of methods exist for determining the mass of a central supermassive black hole, e.g., from reverberation (see for example Blandford & McKee 1982; Peterson 1993), masers (e.g. Miyoshi et al. 1995; Greenhill, Moran & Herrnstein 1997); the spin can be somewhat harder to constrain.

1.7.1 What SMBH spin can tell us

The spin of a SMBH can reveal information regarding the evolution of the galaxy and the general distribution of SMBH spins can be used to discriminate between varying accretion methods. For example, the spin of a SMBH could shed light on the merger history of a galaxy, whereby a high spin could only be the result of the merger if both members of the binary are of equal mass. In many other instances however, the resultant BH spin would likely decrease if the mass of the secondary SMBH is less than the primary (Hughes & Blandford 2003; Gammie et al. 2004). Given that mergers with mass ratios approximately equal to one are unlikely, it is therefore suggested that maximally rotating SMBHs are not a consequence of merger events and must be due to some other factor. Information regarding the distribution of spins could place constraints upon the frequency with which merger events might occur. Volonteri et al. (2005), however, suggest that repeated captures of smaller mass black holes favours neither an increase nor decrease in the overall spin; instead the primary (i.e. more

massive counterpart) typically retains its initial spin. This would therefore suggest that the dominant factor in giving SMBHs their spin is either due to the way in which they are formed or through their method of accretion.

The general accretion method which grows or ‘feeds’ the black hole can also be estimated by measuring the distribution of spins. If an increasingly high number of AGN are found with a near maximal or a rapidly rotating black hole at its centre, this would tend to suggest that AGN typically feature prolonged accretion via a geometrically thin disc (Volonteri et al. 2005). If, however, a low to intermediate spin distribution is found then periods of chaotic accretion may be more suitable, whereby the feeding of the black hole proceeds via small-scale, randomly-oriented accretion events (King & Pringle 2007). Indeed, King et al. (2008) find that in the event of these episodes of accretion, SMBHs should have intermediate spins with spin decreasing as the mass of the SMBH increases.

1.7.2 Fe K lines, spin in the literature and motivation

The detection of relativistically broadened emission lines from the inner regions of the accretion disc in the X-ray spectra of AGN is a somewhat contentious issue. To date there have been many observations of Seyfert AGN with apparent broadening in the FeK region, however, it is the origin of this which is the subject of some debate. In light of analyses by Fabian et al. (1989); Mushotzky et al. (1995); Tanaka et al. (1995); Nandra et al. (1997); Miniutti et al. (2007) and others, the inner regions of the accretion disc are thought to be the origin of broadening in the FeK region and aspects of spectral variability. The light bending model of Miniutti et al. (2003) proposes that a ring-like X-ray source could exist at a height above the disc and variations in this height are responsible for changes in the observed X-ray flux. Subsequently, this geometry requires emission from very close to the central black hole and therefore predicts a very strong relativistic red-wing in the Fe K region (see Figures 2.15, 1.9 and 1.8). However, some authors have noted that a full analysis of any warm absorbing zones which may be present can either reduce or eliminate the need for a broad relativistic emission

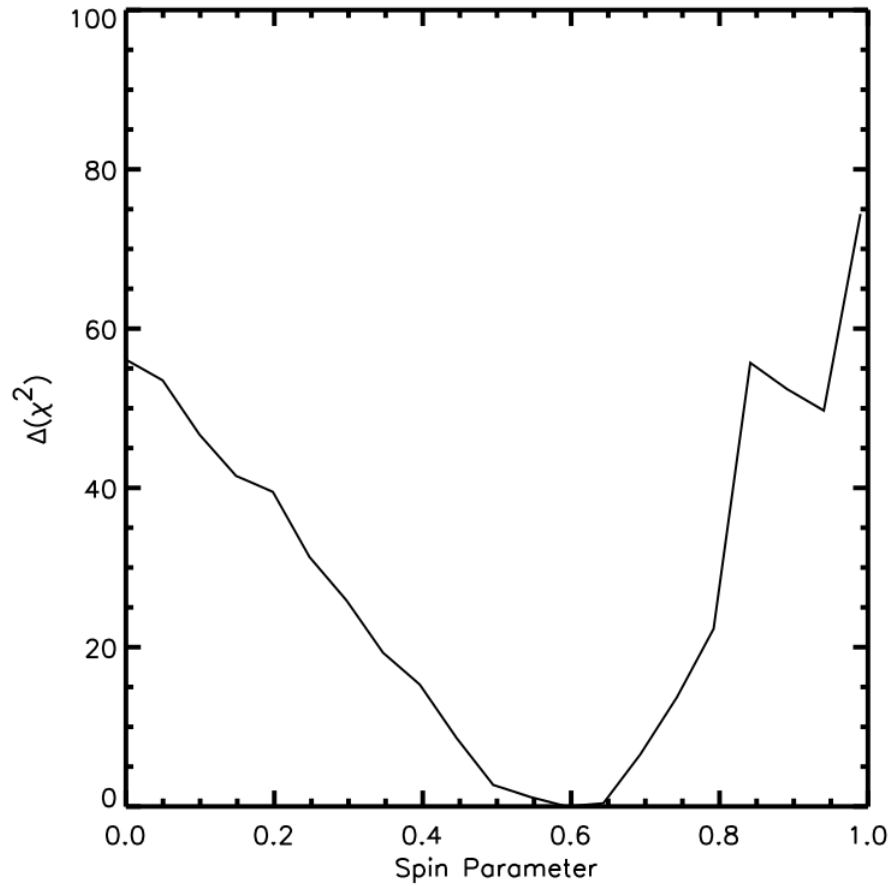


Figure 1.11: Contour plot of spin parameter a versus $\Delta\chi^2$ for Fairall 9 suggesting an intermediate SMBH spin, figure taken from Schmoll et al. (2009).

component (due to the introduction of bound-free curvature) and can explain observed spectral variability through the use of partially covering absorbing components (e.g. Zycki et al. 2010).

Indeed, Miller, Turner & Reeves (2008) noted that in an analysis of all the available MCG-06-30-15 data (*Chandra*, *XMM-Newton* & *Suzaku*), a model composed of a simple power-law covered by a complex warm absorber with both fully and partially covering components provided a good fit to all flux states without the requirement for any further component from the inner regions of the accretion disc (see also Zycki et

al. 2010). This is in stark contrast to the analyses of Miniutti et al. (2003, 2007) and Brenneman & Reynolds (2006), which suggest that highly relativistically blurred reflection from the very inner regions of the disc (i.e. within $6 R_g$) is required to explain the observed spectral variability.

Data provided by *XMM-Newton* have been used in surveys of Seyfert 1 AGN to determine how commonplace broad iron lines are and their typical strength (e.g. Porquet et al. 2004; Guainazzi et al. 2006; Nandra et al. 2007; Brenneman & Reynolds 2009; de la Calle Pérez 2010; Walton et al. 2013). For example, Nandra et al. (2007) find that as high as 69% of objects show evidence for broad line emission whereas de la Calle Pérez (2010) find only 36%. Similarly, Brenneman & Reynolds (2009) suggest that most sources required relativistic smearing in order to produce a good fit to the data, which would indicate that there is strong emission from the inner regions of the accretion disc. Suggesting that, in some analyses, a spinning black hole (i.e. non-Schwarzschild) is relatively common in Seyfert 1 AGN.

With a sufficient number of X-ray counts, tentative estimates can be placed on the spin of the central SMBH. This can be through modelling the broad iron line itself, or through the implication of a blurred reflection component which models the continuum/ soft excess (e.g. Nardini et al. 2012). Few estimates have been placed upon the spin of SMBHs to date and exist in only some of the longest and highest quality data sets. The majority of spin constraints result from the application of a highly relativistically blurred reflection component, one of the first (and perhaps one of the most well known) AGN with a spin estimate is MCG–06-30-15 which has been suggested to harbour a near maximally rotating SMBH ($a > 0.93$, $a > 0.98$ and $a > 0.92$; Reynolds et al. 2005; Brenneman & Reynolds 2006; Miniutti et al. 2007 respectively). Further spin constraints in the literature can be seen in Table 1.2.

The main issue with placing estimates on SMBH spin in AGN is essentially determining the strength of any emission from the inner regions of the disc and therefore the robustness with which we can present our results. With various analyses coming to differing conclusions and indeed opposite extremes for the same objects, it is important that each aspect is considered and a complete analysis is made in order to assess if there

Table 1.2: List of SMBH spin estimates in the literature.

Object	Spin parameter a	Reference
1H0707-495	$a > 0.98$	Zoghbi et al. (2010)
Ark 120	$a = 0.74^{+0.19}_{-0.50}$	Nardini et al. (2011)
Fairall 9	$a = 0.65^{+0.05}_{-0.05}$	Schmoll et al. (2009, see Figure 1.11)
	$a > 0.93$	Reynolds et al. (2005)
MCG-06-30-15	$a > 0.98$	Brenneman & Reynolds (2006)
	$a > 0.92$	Miniutti et al. (2007)
Mrk 79	$a = 0.7^{+0.1}_{-0.1}$	Gallo et al. (2011)
NGC 3783	$a > 0.98$	Brenneman et al. (2011)
RBS 1124	$a > 0.74$	Miniutti et al. (2010)
SWIFT J2127.4+5654	$a = 0.6^{+0.2}_{-0.2}$	Miniutti et al. (2009)
TON S180	$a = 0.85^{+0.07}_{-0.05}$	Nardini et al. (2012)

is indeed a broad wing indicative of emission from the inner regions. Using data from *Suzaku* we can form models which are consistent over a broad bandpass which will allow for the measurement of the hard X-ray component and therefore the influence of both absorption dominated and reflection dominated models. With simultaneous high energy data, distinctions can be made between the two scenarios and complex models can be formed to account for any intrinsic absorption which may be present in the soft X-ray spectrum. This can account for the accompanying spectral curvature prior to examining for the presence of a broad Fe K α line. Within this thesis, models for each of the interpretations are formed to give estimates of the strength of the inner disc emission. These models are consistent over the full X-ray bandpass with *Suzaku* with the eventual aim of making robust estimates of SMBH spin in AGN, determining what percentage of Seyfert 1 AGN do show emission from the inner regions of the disc and other principle components of X-ray spectra. If constraints can be placed on the typical inner radius of emission of the accretion disc or the distribution of SMBH spin, information can in principle be gained regarding the way in which galaxies evolve giving an insight into the history of these AGN, e.g., method of accretion or indeed merger history.

1.7.3 Thesis outline

Within this thesis, an analysis is made of the Seyfert 1 AGN observed by *Suzaku* prior to September 2011. Complex models are formed in a step-by-step process and are assessed for their statistical ability to fit the data and their physical plausibility. Details regarding some of the frequently used models can be found towards the end of Chapter 2 in Section 2.5. In order to build up the full sample of AGN, Chapter 3 first conducts an analysis of the more simple to model AGN, namely 6 ‘bare’ X-ray spectra which feature very little or no intrinsic warm absorption. These provide a good basis for determining the properties of the Fe K region without complications such as additional curvature due to single or multiple absorbing zones. The next step is to include some of the best available data sets in the archive, primarily those with the longest exposures and highest number of counts. These 5 AGN, namely Fairall 9, MCG–06-30-15, NGC 3516, NGC 3783 and NGC 4051, which are analysed in Chapter 4, feature some of the most complex X-ray spectra. Previous analyses in the literature point towards multiple warm absorbing zones in these objects which can be both fully and partially covering. Chapter 5 then contains the remaining AGN which are publicly available in the *Suzaku* archive to achieve a total sample of 46 AGN and 84 observations, an analysis of this sample allows us to begin to estimate how common particular components of the X-ray spectrum are and approximately how many AGN feature signs of emission from the inner regions of the accretion disc. The results included within Chapters 3-5 are discussed in Chapter 6 with a view to Seyfert 1 AGN as a whole and the conclusions which are formed throughout.

2 Instrumentation and data analysis

In order to observe the X-ray spectra of galaxies, we must launch X-ray telescopes into space due to the fact that cosmic X-rays do not penetrate the Earth's atmosphere as a result of photoelectric absorption. Since X-rays are high energy photons, an incident X-ray is often absorbed by the majority of materials, hence focussing X-rays onto a detector can be a difficult process. Therefore, materials which are not transparent to X-rays must be used in X-ray telescopes, for example, gold is used in the construction of the *Suzaku* observatory through the use of 'grazing angle incidence' mirrors which help to focus the incoming X-ray photons towards the detector. In addition to the X-rays emanating from the X-ray source we are interested in, there are other factors such as the Cosmic X-ray background (CXB) and other X-ray sources to consider before we can examine the data we are interested in. To help exclude these background photons which bear no information regarding the object of interest, collimators and baffles are used throughout the focal length of the telescope. Although these can restrict the field of view of the telescope, they can help to ensure that X-rays reaching the detector originate from the direction in which the telescope is pointed.

Despite ensuring that only X-rays originating from the field of view of the telescope are measured, there are still background X-rays which may be due to other extragalactic or Galactic sources, e.g., noise generated by the telescope itself (e.g. the power sources) and high energy particles from the Sun. All of these can contribute to background noise. For example, the Cosmic X-ray background may be due to emission from the pre-cursors to present epoch Seyfert AGN, i.e., those which are more compact and of smaller mass than a typical AGN. Assuming these accrete at Eddington for a Hubble time the mass of the central object will increase and perhaps evolve into something representative of a Seyfert AGN (Boldt & Leiter 1986). In these young objects non-thermal emission is suppressed (Cavaliere & Morrison 1980) therefore yielding a flattened Comptonised thermal spectrum which forms a possible component of the CXB (Boldt 1987).

2.1 Types of X-ray detectors

The following section describes some of the X-ray detectors commonly used onboard X-ray observatories.

2.1.1 Proportional counters

A proportional counter consists of a tube of gas which produces an electric charge upon the absorption of an X-ray. Applying a voltage to the tube propels the electrons to the end of the tube where they can be measured and the energy of the incident X-ray can be estimated. Due to the potentially large surface area of proportional counters, mirrors are not required to focus X-rays onto them.

2.1.2 CCD detectors

A Charged-Coupled Device (CCD) is a solid state detector composed of silicon which allows for the measurement of the energy of incident photons. CCDs sensitive to X-rays measure the incident photon as it is absorbed in the middle of the CCD chip, photons without sufficient energy will be absorbed before reaching the detecting region of the CCD and photons with higher energies (i.e. tens of keV) will pass straight through and not be absorbed. The absorption of an X-ray photon in the detection region creates a number of electron-hole pairs and voltages are applied to move these photo-electrons to the edge of the chip where their electric charge can be measured and hence the energy of the incident photon can be estimated. The probability of an incident photon being absorbed and therefore detected is determined by the quantum efficiency of the detector, e.g. see Figure 2.1 (note that a front-illuminated X-ray CCD detector is less sensitive to soft X-rays than a back-illuminated CCD). This is due to the electrode structure on the surface of the CCD strongly attenuating photons < 0.6 keV, a back-illuminated CCD thereby resolves this issue by allowing the incident soft X-ray photons to more easily reach the detection region. While the energy of the

incident photon can be accurately estimated, CCDs typically have a small collecting area resulting in fewer collected photons and therefore poorer timing measurements. An arrangement of mirrors is therefore regularly used to focus more X-rays onto the CCD. The first X-ray telescope to use CCDs was *ASCA* with the Solid-state Imaging Spectrometer (SIS; Tanaka et al. 1994).

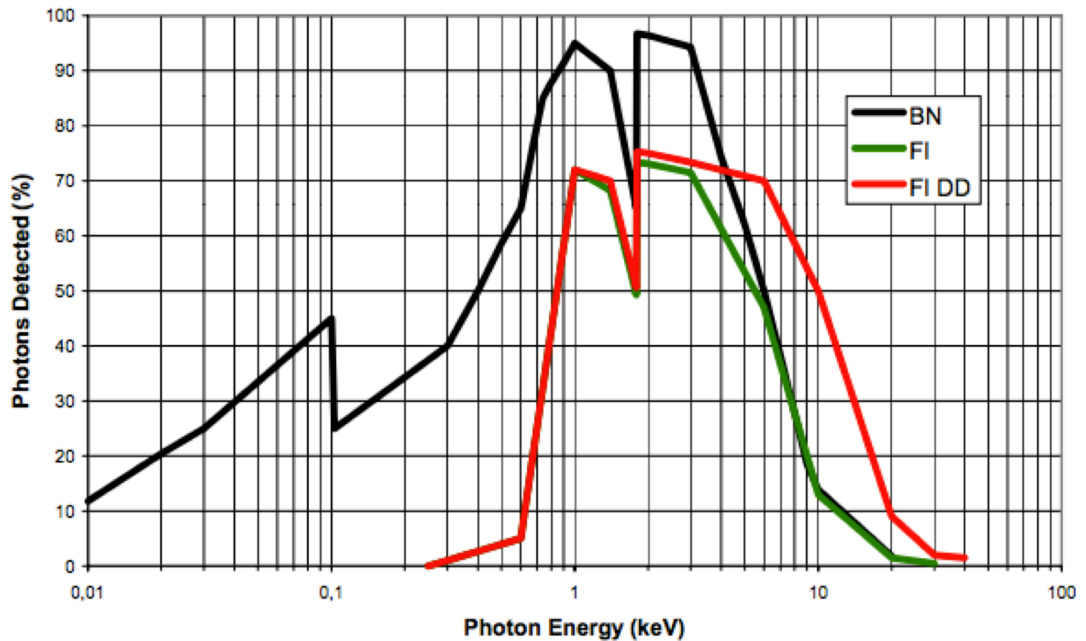


Figure 2.1: An illustration of quantum efficiency curves for Back Illuminated (BN in the plot above), Front Illuminated (FI) and Front Illuminated Deep Depletion (FI DD) Devices. The discontinuities are due to the L and K absorption edges in Silicon. Figure taken from http://www.lot-qd.de/files/downloads/andor/en/cc_notesxray_deen.pdf

2.1.3 Scintillators

In order to measure hard X-rays with a traditional proportional counter, either a large column of gas or a gas under high pressure must be used in order to absorb the higher energy photons. Since this can quickly become impractical for space based missions, scintillators provide a good alternative for the measurement of hard X-rays above 20 keV. Scintillators consist of a crystal which, upon absorption of an X-ray photon, emits photons in the optical band which can then be collected by a photomultiplier tube to convert into a voltage, this can then give an estimate of the original X-ray photon energy. Using a second crystal, estimates can be placed upon the X-ray background allowing hard X-ray photons from the rear and the sides of the scintillator to be rejected. If the crystals are made of different materials the optical emission will have different decay times allowing the background and source X-rays to be distinguished, for example, the GSO instrument onboard *Suzaku* uses Gd_2SiO_5 crystals for X-ray detection and $\text{Bi}_4\text{Ge}_3\text{O}_{12}$ crystals for rejection of the background.

2.1.4 Microcalorimeters

Calorimeters operate at very low temperatures (i.e. near zero Kelvin) based upon the principle that an incident X-ray photon will be absorbed and increase the temperature of the detecting material, allowing very accurate estimates to be made of the energy of the X-ray photon, e.g., with an energy resolution of ~ 7 eV across a bandpass of 0.3-12 keV. This material is then connected to a heat sink to allow for the dissipation of heat, allowing for another measurement. Calorimeters provide a much higher energy resolution than CCD detectors due to the accuracy to which the temperature can be measured. The main drawback of calorimeters, however, is that only a limited amount of coolant can be stored and used to cool the instrument to near zero Kelvin, indeed the XRS instrument onboard *Suzaku* had the first space based calorimeter, however, the liquid Helium required to cool the instrument was lost prematurely. A calorimeter will next be launched on the *Astro-H* satellite (Takahashi et al. 2010).

2.2 Previous X-ray observatories

There have been a number of X-ray satellites launched into space to examine the spectra of AGN. Some of the first being *UHURU* and *Ariel-V* (Giacconi et al. 1971; Holt 1976), which performed some of the first all-sky surveys and confirmed the widespread nature of X-ray emission from Seyfert galaxies (Elvis et al. 1978). *Ariel-V* also made the first discovery of iron line emission in extragalactic sources and indications that variability on scales of days to months is a characteristic of Seyfert AGN (Ives, Sanford & Penston 1976; Ward et al. 1977).

Subsequent to these initial X-ray observatories, in the late 1970s and early 1980s further telescopes were launched: *EINSTEIN*, *EXOSAT* and *GINGA* (Giacconi et al. 1979; Taylor et al. 1981; Makino 1987). These observatories made further progress in obtaining information regarding the X-ray spectra of AGN, including some of the first high resolution low energy data sets, in-depth variability studies, observations of warm absorption, ionised emission lines and suggestions of redshifted iron lines in the Fe K region (e.g. Halpern 1984; Arnaud et al. 1985; McHardy & Czerny 1987; Turner et al. 1989; Ghosh & Soundararajaperumal 1991, Nandra & Pounds 1995).

More recent notable observatories include *ROSAT*, *ASCA* and *BeppoSAX* which served to provide X-ray spectra through the 1990s. *ROSAT* conducted the first all-sky survey using an imaging telescope with an X-ray sensitivity approximately 1000 times greater than the first survey by *UHURU* (Voges et al. 1999). *ASCA* was the first X-ray observatory to be launched with a Charge-Coupled Device (CCD) detector and provided the first detections of broadened iron lines in AGN, leading to investigations into the very central regions of AGN and the accretion disc (Mushotzky et al. 1995; Tanaka et al. 1995; Iwasawa et al. 1996).

2.3 Current X-ray observatories

The majority of the work presented in this thesis is based upon data obtained with the broad-band X-ray telescope *Suzaku*. The following sections detail the current space based X-ray observatories in popular use for the analysis of AGN; namely *XMM-Newton*, *Chandra* and *Suzaku*.

2.3.1 *XMM-Newton*

The X-ray Multi-Mirror Mission *XMM-Newton* (Jansen et al. 2001) was launched by the European Space Agency in December 1999 featuring a very large collecting area (e.g. 731cm^2 at 6 keV for the EPIC-PN) and the ability to simultaneously obtain X-ray and optical data. *XMM-Newton* features three mirror assemblies, one of which feeds the EPIC-PN detector (Strüder et al. 2001) with the remaining two assigned to the EPIC-MOS (Turner et al. 2001) and RGS detectors (den Herder et al. 2001). An optical monitor (Mason et al. 2001) can also provide optical/ ultra-violet photometry.

Moderate resolution spectra (130 eV at 6.0 keV, compared to 240 eV at 6.0 keV with *ASCA*) can be obtained with the EPIC-PN detector, which is an array of 12 CCDs with a 0.2-12 keV bandpass (European Photon Imaging Camera; Strüder et al. 2001). *XMM-Newton* can also conduct high-resolution spectroscopy with its Reflection Grating Spectrometer (RGS), while featuring a somewhat limited bandpass of 0.4-2.5 keV, its resolving power is much improved over the EPIC CCD detectors. For example, the RGS can resolve down to a full width at half maximum (FWHM) resolution of 2.9 eV at 1.0 keV whereas EPIC-PN has a FWHM resolution of 55 eV at 1.0 keV. The drawback of the RGS detector is that the reflected photons are only $\sim 40\%$ of the collected photons, these then proceed to reach an array of 9 MOS CCDs (Metal Oxide Silicon; Turner et al. 2001) which make up the RGS detector, leading to a smaller collecting area. The unattenuated photons, i.e., those which are not reflected, but pass straight through the grating, however, are not wasted and reach an array of *EPIC-MOS* CCDs in the focal plane of the telescope (see Figure 2.2).

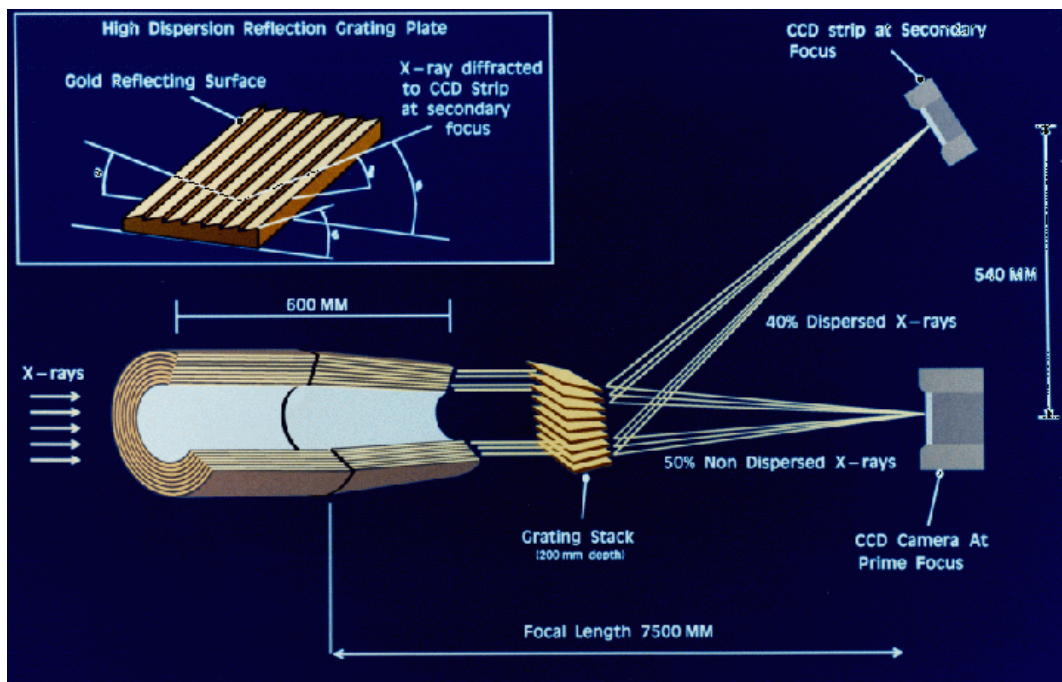


Figure 2.2: Schematic of a mirror assembly onboard *XMM-Newton* detailing the RGS and EPIC-MOS detectors. Figure taken from <http://heasarc.gsfc.nasa.gov>

2.3.2 *Chandra*

Chandra was launched in 1999 by NASA as the direct follow-on to the *EINSTEIN* observatory with the aim of obtaining high resolution X-ray imaging and spectroscopy. The High Resolution Mirror Assembly (HMRC; Schwartz et al. 2000) differs from some previous observatories such as *XMM-Newton* by using iridium to coat the grazing angle mirrors rather than gold. There are two primary instruments lying in the focal plane: the High Resolution Camera (HRC; Murray et al. 2000) and the Advanced CCD Imaging Spectrometer (ACIS; see Garmire et al. 2003), only one of these can be used at any one time. Two transmission grating spectrometers can be placed behind the mirror assembly, the Low Energy Transmission Grating (LETG; Brinkman et al. 2000) and the High Energy Transmission Grating (HETG; Canizares et al. 2005). The resultant spectrum is then detected by either ACIS or HRC and either can be

used for high resolution spectroscopy.

The HETG is best suited to high resolution spectroscopy of X-rays in the 0.6-10.0 keV energy band, able to resolve down to a FWHM resolution of 29 eV at 6.0 keV and can be particularly useful for determining the presence of ionised narrow emission lines such as Fe XXV and Fe XXVI. Details regarding highly ionised absorption zones in the Fe K region and estimating the outflow velocity to high accuracy are some of the HETG's primary achievements. In addition to this, the HETG has a higher spectral resolution compared to the RGS instrument onboard *XMM-Newton* being able to resolve down to a FWHM of 1.0 eV at 1.0 keV compared to a FWHM of 2.9 eV at 1.0 keV. The LETG provides high resolution spectroscopy at very soft X-ray and EUV energies (0.1-6.0 keV) which is particularly useful for determining the presence of warm absorbing zones in the X-ray spectra of AGN and is the highest resolution instrument onboard *Chandra* at soft X-ray energies.

2.3.3 *Suzaku*

Suzaku (or *Astro-E2*) is the result of a collaborative effort between the Japanese space agency (JAXA) and NASA to study the broad-band X-ray spectrum of AGN and was launched in June 2005 (see Mitsuda et al. 2007). It is the follow on mission from *Astro-E* which was due to be active in 2000, however, it failed to achieve orbit during launch and was subsequently lost. There are three instruments onboard *Suzaku*: the X-ray Spectrometer (XRS; Kelley et al. 2007), X-ray Imaging Spectrometer (XIS; Koyama et al. 2007) and the Hard X-ray Detector (HXD; Takahashi et al. 2007) - see Figure 2.3. At launch the primary instrument was the XRS which is an X-ray microcalorimeter designed to perform very high resolution X-ray spectroscopy in the 0.2-12.0 keV energy band with the ability to resolve down to a FWHM resolution of 6.5 eV at 6.0 keV and the rest of its bandpass. The XRS, however, prematurely lost its liquid helium cryogen which cooled the instrument and effectively rendered it inoperable towards the

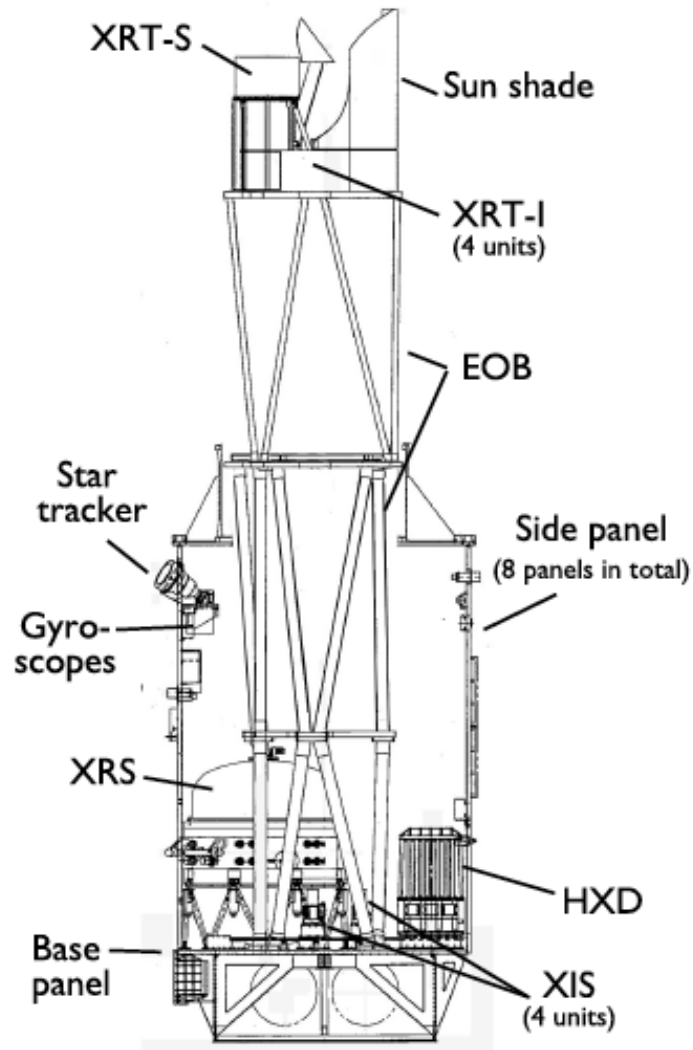


Figure 2.3: A schematic diagram of the X-ray telescope *Suzaku*, figure taken from Mitsuda et al. (2007).

beginning of the mission¹.

The X-ray Imaging Spectrometer (XIS) consists of four CCD detectors (XIS 0-3) which sit at the end of four dedicated X-ray Telescopes (XRT-I; Serlemitsos et

¹<http://heasarc.gsfc.nasa.gov/docs/suzaku/news/xrsend.html>

al. 2007), three of which are front-illuminated (XIS 0, 2, 3) whereas XIS 1 is back illuminated. The back illuminated XIS 1 is more sensitive to soft X-rays, however, the quantum efficiency of the CCD at high energies is reduced due to imperfect charge collection at the back of the silicon detector. That is, the front illuminated CCDs are more suited to parameterising the Fe K region and feature a lower background at higher X-ray energies (Koyama et al. 2007). The XIS covers the 0.2-12.0 keV energy band with the ability to resolve down to 120 eV at 6.0 keV which is more or less comparable to the EPIC-PN detector onboard *XMM-Newton*. In November 2006, XIS 2 suffered a micro-meteoroid impact which has since resulted in it being left inoperable².

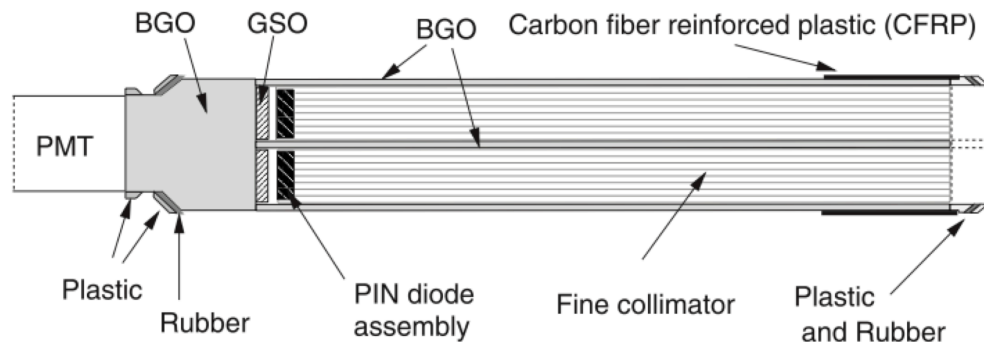


Figure 2.4: Schematic of the counter unit for GSO and PIN detectors onboard *Suzaku*. The silicon PIN diode is placed inside the well just above the GSO scintillator while the BGO forms a shield from off-axis hard X-ray photons. Figure taken from Takahashi et al. (2007).

²<http://www.astro.isas.ac.jp/suzaku/doc/suzakumemo/suzakumemo-2007-08.pdf>

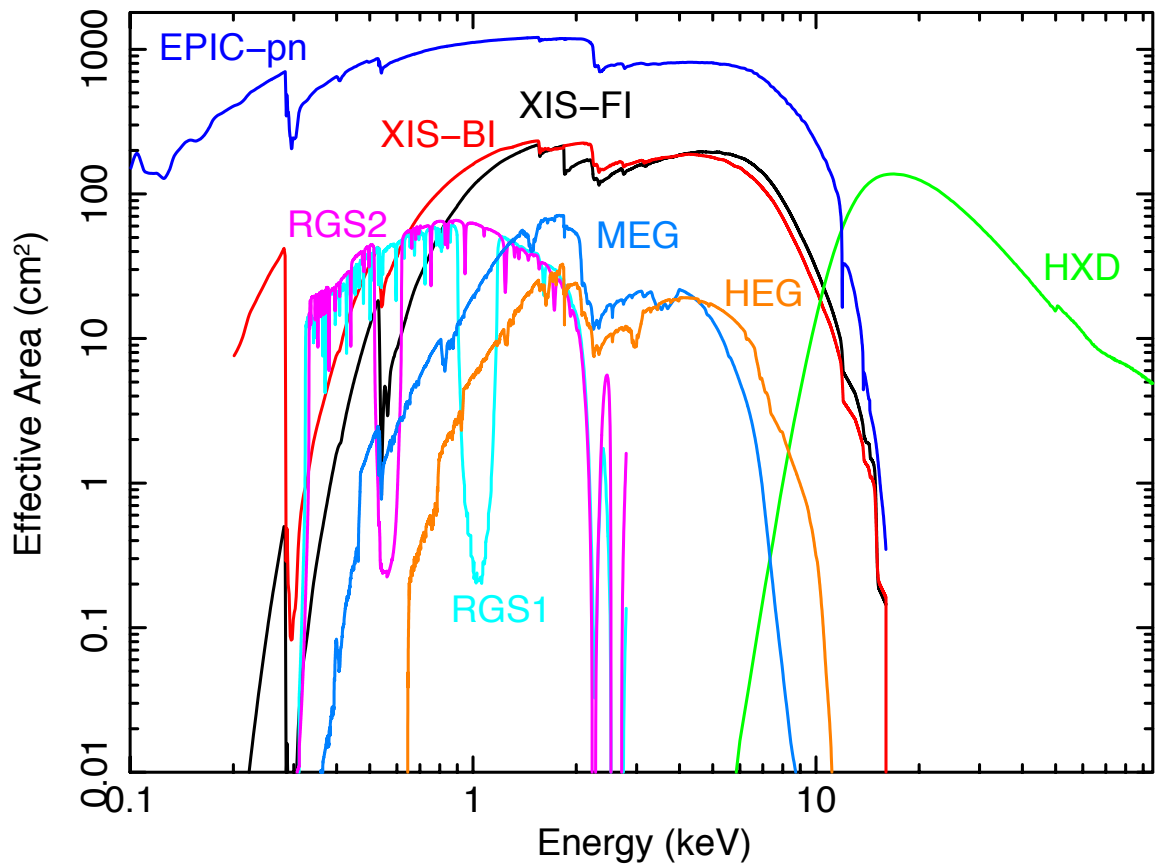


Figure 2.5: Comparison of the effective area (i.e. the efficiency) of modern X-ray telescope instruments. Note that the effective area curve plotted here for the front-illuminated XIS is for a single CCD, in many observations this can be increased by up to a factor of 3 since there are 3 front-illuminated XIS detectors on board *Suzaku*.

The main advantage *Suzaku* has over other X-ray telescopes is its ability to simultaneously gather hard X-ray data above 10 keV with the Hard X-ray Detector (HXD), which is non-imaging but extends the *Suzaku* bandpass to ~ 600 keV (although ~ 50 keV is the upper limit in practice for most extragalactic X-ray sources; Takahashi et al. 2007). There are two sensors which make up the HXD instrument: the Positive Intrinsic Negative (PIN) silicon diodes and the gadolinium silicate (GSO) crystal scintillators, operable in the 10-70 keV and 40-600 keV ranges respectively with a resolution of 3 keV across the PIN bandpass. The GSO detector consists of gadolinium silicate crystal scintillators, each of which are buried in a bismuth germanate crystal

(BGO) which acts as a rejection mechanism for non-forward pointing photons. The GSO itself has a large collecting area and FOV of $4.5^\circ \times 4.5^\circ$, all of the scintillators feed into a single photomultiplier. The silicon PIN diodes are also placed inside the well (just above the GSO scintillators to form a PIN-GSO pair, see Figure 2.4) and these provide the low energy response of the HXD, i.e. below ~ 70 keV. The PIN detectors have a smaller FOV of $34' \times 34'$ than the GSO.

2.3.4 *Swift*

The *Swift* telescope is the result of a collaboration between the USA, the UK and Italy and was launched in November 2004 into a low Earth orbit. The Burst Alert Telescope (BAT; Barthelmy et al. 2005) operates in the 15-150 keV range and was primarily designed to be used to detect Gamma-ray bursts (GRBs), hence featuring a very wide field-of-view. While searching the sky for a new GRB, the BAT instrument also performs an all-sky hard X-ray survey, resulting in time averaged hard X-ray spectra of a large number of AGN over a period of many months. This has formed one of the most sensitive catalogues of hard X-ray sources to date, e.g, see Markwardt et al. (2005); Tueller et al. (2008); Baumgartner et al (2010).

These data can then be used simultaneously with softer X-ray data to give a picture of the general shape of the hard X-ray continuum. *Swift* also features two further detectors, the X-ray telescope (XRT) which focusses X-rays onto a CCD and the UV/ Optical Telescope (UVOT). Both of these instruments are used to follow up any GRBs which may have been detected in order to provide both 0.5-10.0 keV X-ray data and optical data. In this thesis I primarily make use of the time averaged *Swift* BAT spectra from the 58 month survey (Baumgartner et al. 2010) in order to supplement the HXD/ PIN data above 10 keV.

2.4 Data reduction and analysis

As noted above in Section 2.1, modern X-ray detectors operate through the detection of individual photons, this is in part due to the relatively low count-rate of typical X-ray sources and their the relatively high energy of each photon. The raw data resulting from an observation (such as a list of detections, the time of detection, its raw energy and position on the CCD) are compiled and contained in a FITS file (Flexible Image Transport System). Since the raw data aren't appropriate for scientific analysis, the data must first be screened according to some of the criteria in the following section.

2.4.1 Screening the data

In CCD detectors, when the charge (or pulse height) of an individual pixel exceeds a threshold amount, a so called 'event' is registered. The 'grade' of the event is assigned a value and is dependent upon the charges registered in the surrounding pixels, forming either a 3x3 or a 5x5 grid. These correspond to grades 0, 2, 3, 4, 6 according to the convention established with *ASCA*³ where grade 7 events are deemed to be particle events. The grade of an event gives an initial indication of the quality of the event and whether it is appropriate for analysis. For example, a high quality event (i.e. from the cosmic source of interest) may be an event in which only one pixel registers a charge above a threshold energy (e.g. a grade 0 event), whereas a low quality event may be an event in which the surrounding 3x3 or 5x5 pixels all register a charge above the threshold energy. In addition to this, events of particular pulse heights may be due to the Fe 55 calibration sources in the case of the XIS CCD detectors onboard *Suzaku* which are present in the corners of the CCD image (e.g. see Figure 2.6). Some pixels in CCD detectors can also produce a registered pulse height without the external influence of an incident photon, these are known as bad pixels or hot spots and can be easily filtered out due to the small size of the pixels compared to the telescope point

³http://www2.astro.psu.edu/xray/docs/TARA/TARA_users_guide/node12.html

spread function (PSF). Such flickering pixels can be dependent upon the operating temperature of the instrument, subsequently if the detector is sufficiently cooled this becomes less of an issue.

The raw data must also be screened according to times during which the telescope passes through the South Atlantic Anomaly (SAA), i.e., the area in which the inner Van Allen radiation belt passes closest to the Earth’s surface. In this region there is an increased flux of high energy particles which may register as an event or even damage the detectors themselves. During these periods, the time since passage through the SAA (i.e. T_SAA) is used to screen the data ensuring that data are not used during the telescope’s passage through the SAA. The *cut-off rigidity* of an instrument also gives a measurement of how charged particles interact with the telescope. The rigidity of a charged particle is a measure of how magnetic fields influence the momentum of the particle, i.e. a particle with a higher momentum (or ‘rigidity’) will have a greater resistance to deflection by a magnetic field. In terms of scientific observations, if the rigidity of a charged particle exceeds a threshold value, the particle will be detected by the instrument; otherwise the Earth’s magnetosphere will shield the telescope from such charged particles. For the XIS detector onboard *Suzaku*, regions with a cut-off rigidity below ~ 6 GV are filtered out and regions with < 8 GV are filtered for the HXD.

Table 2.1: Summary of the data screening and selection criteria for the XIS and HXD onboard *Suzaku*.

Criteria	XIS	HXD
XIS Grade	0, 2, 3, 4, 6	N/A
Telemetry bit rate	Superhigh, high & medium	
Flickering pixels	Removed	N/A
ANG_DIST	$< 1.5'$	$< 1.5'$
ELV	$> 5^\circ$	$> 5^\circ$
DYE_ELV	$> 20^\circ$	$> 20^\circ$
SAA_HXD	0 or excluded	0 or excluded
T_SAA_HXD	> 436 s	> 500 s
TN_SAA_HXD	> 180 s	> 180 s
COR	> 6 GV	> 8 GV

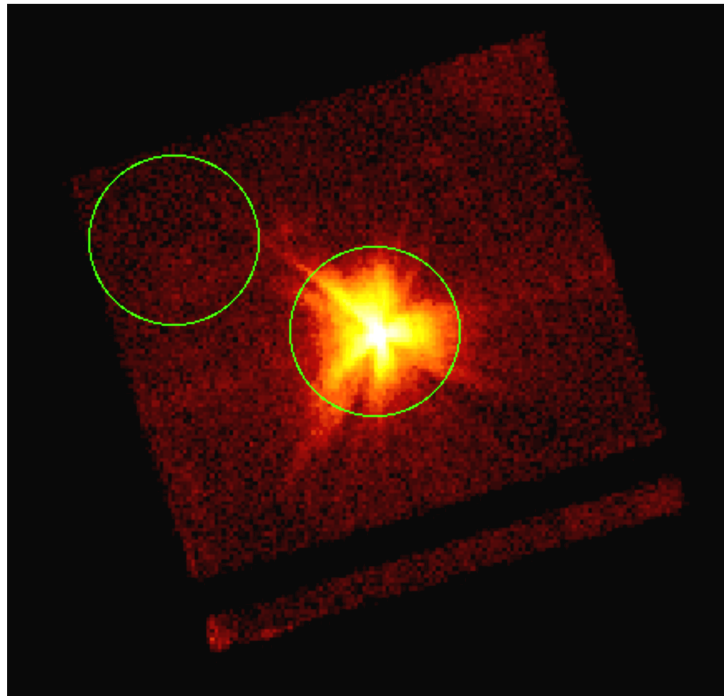


Figure 2.6: An example of appropriate regions of radius $3'$ for source and background selection using an image generated using the XSELECT ftool as part of the HEASoft software package. Note that the source and background regions are the same size and avoid the Fe 55 calibration source in the top right-hand corner. The CCD image shown is from XIS 0 onboard *Suzaku*.

It is intuitive that the pointing direction of the telescope will affect the suitability of data for scientific analysis. For instance at angles close to Earth's limb, soft X-rays may be absorbed due to a thicker observed column of the Earth's atmosphere. At points

above sunlit regions of the Earth (or bright Earth), X-rays may be scattered in the atmosphere and directed towards the telescope. It is therefore important that the pointing angle of the telescope relative to these positions is recorded and that the data are filtered appropriately. For example, only data taken with a telescope elevation of $> 5^\circ$ should be used, however, when the softer end of the X-ray spectrum is ignored during analysis (i.e. below 0.6 keV) this restriction upon on the elevation angle may be relaxed. A summary of the screening criteria for *Suzaku's* XIS and HXD is shown in Table 2.1.

2.4.2 Data reduction

‘Cleaned’ event files which have already undergone screening can be downloaded from the *HEASARC Data Archive*⁴ in which the data has been filtered according to the above criteria. For detectors featuring spatial resolution such as the XIS onboard *Suzaku*, the XSELECT program (Arnaud 2006) within the HEASoft⁵ software package can be used to extract source and background regions. Figure 2.6 shows how one might select appropriate source and background regions from a cleaned event file, note that the source and background regions are circles of radius 3'. Within XSELECT an event file can be filtered for particular regions, time intervals or periods in which the source exceeds a particular count rate, also allowing light curves to be produced. The cleaned events files are filtered according to the regions selected (i.e. source or background, see Figure 2.6) and the subsequent spectrum is extracted. This is repeated for both the source and background spectra. Once given the required selection criteria, the charge for each X-ray is measured and stored in the PHA file (Pulse Height Amplitude) which is then corrected for time and position on the detector which leads to the production of the PI file (PHA Invariant). The instrumental response then converts directly from the PI file to give the energy.

⁴<http://heasarc.gsfc.nasa.gov/>

⁵<http://heasarc.nasa.gov/docs/software/lheasoft/>

The actual observed X-ray photon count spectrum results in the convolution of the total source plus background spectrum with the instrumental response files. For detectors such as the XIS onboard *Suzaku* these are often split into two components: the unit-less *Redistribution Matrix File* (RMF) and the *Ancillary Response File* (ARF, with units cm^2). The RMF gives the probability of a photon of a particular energy being detected in a specific energy bin, this takes into account the fact that the energy response of a detector has a spread such that a count instead may be detected in adjacent bins due to the energy resolution of the instrument. The ARF makes use of the effective area of the telescope and the quantum efficiency of the detector to give the collecting area as a function of energy.

In the case of reducing data from the XIS detectors, these response files must be generated outside of XSELECT; the *Redistribution Matrix File* (RMF) using XISRMFGEN and the *Ancillary Response File* (ARF) using XISSIMARFGEN. This is a ray-tracing tool which is used to generate the telescope effective area as a function of position and energy, e.g., by simulating X-ray photons through *Suzaku's* X-ray telescope and the XIS detector and then counting the number of events in the extracting regions which have been defined by the user, i.e., the same regions as used to extract the source in XSELECT. A high number of events must be simulated to reduce the statistical errors, for example, in this thesis the ancillary response files have all been generated with 10^5 photons per bin.

These four components (source, background, RMF, ARF) can then be grouped together using GRPPHA which allows the keywords of the PI file to be changed and the appropriate instrumental response files and observational background file to be assigned. Within GRPPHA the binning of the PI file can be set to determine which channels start each new bin, for example the user can specify a minimum number of counts per bin. Typically here this is $N > 50$ counts per bin so that Gaussian statistics are applicable. Once a grouped and binned PI file has been produced this forms a reduced spectrum which can then be analysed using the XSPEC package, ready for comparison with model spectra.

The high energy HXD detector on-board *Suzaku* is non-imaging and as such

the source and background spectra cannot be separated in this way. Instead, the background data can be obtained from a pre-calculated database of the time-variable particle background provided by the HXD team. The tool `MGTIME` merges the ‘good time intervals’ (GTIs) for the background FITS file with the cleaned PIN source GTIs to create a list of GTIs which are the intervals during the observation which are appropriate for analysis. The program `XSELECT` can then be used to filter the PIN source events file with the newly generated good time intervals from which a source spectrum can be extracted (i.e. the PI file). The same can then be done for the downloaded background events file to produce a background PI file. The source PI file must then be corrected for HXD dead-time (which is typically $\sim 5\%$ of the observation) using the tool `HXDDTCOR` and is achieved through editing the ‘Exposure’ keyword in the source PI file. Next the tool `GRPPHA` is used to edit the ‘Exposure’ keyword of the background PI file which is increased by a factor of 10 in order to suppress Poisson errors as the model background files are generated with $10\times$ the actual rate.

Once the source and background spectra have been extracted and the relevant corrections to the exposure have been made, the response files for the observation must be downloaded according to the date and the pointing direction of the detector relative to its axis. The Cosmic X-ray Background (CXB - the unresolved sum of all the extragalactic X-ray sources in the field of view) must also be calculated from a standard model since it is not included in the background event file. The background events file available from the online database only includes the non-X-ray background and since the CXB flux is $\sim 5\%$ of this it must be taken into account. The model proposed by Boldt (1987) is generally used with the form of a power-law of slope $\Gamma = 1.29$ and a high-energy cut-off at 40 keV. This model is then used to estimate the CXB and is generated with the instrumental flat field file with an exposure equal to that in the exposure keyword of the background PI file to produce a second background (CXB) PI file. The count rate for the CXB is typically 0.025 counts per second. The background files for the non-X-ray background and the simulated Cosmic X-ray background must then be combined using `MATHPHA`, again setting the exposure equal to the source PI file. The final step is to edit the keywords of the source PI file to group the total

background and the instrumental response file together using GRPPHA with the source data binned in order to have a typical S/N per bin above the background.

2.4.3 Model fitting and statistics

XSPEC is a detector-independent, command-driven, X-ray spectral fitting package (Arnaud 1996). After building a suitable model and inputting appropriate parameters within the XSPEC program, a predicted count spectrum is calculated through convolution of the model spectrum with the detector's response files and this is then compared to the observed count rate spectrum obtained with the detector (e.g. *Suzaku* XIS data). The model spectrum can then be compared with the detected spectrum to produce a χ^2 'goodness of fit' statistic. The complexity of the model depends upon the complexity of the source, ranging from a simple power-law plus Galactic absorption up to multiple warm absorption zones, diskline models, reflection models etc (see Section 2.5). Some model parameters are kept 'frozen', i.e., do not vary. For example, an object's redshift is frozen, whilst some are 'free' which the program varies with each iteration of a specified step size. The fit statistic is then recalculated until the best fit to the observational data is found. It is noted, however, that the fitting algorithm often obtains a local best fit rather than a global best fit, meaning that it is possible for the fitting process to get stuck at a local minimum, especially if the χ^2 space is complex (e.g. when using complex models). This can be worked around in some cases by the user setting appropriate initial parameters or by stepping through a wider range in parameter space and calculating the χ^2 at each parameter value.

Within X-ray astronomy the Gaussian and Poisson distributions are primarily used to determine the 'goodness of fit'. Which of these are used depends upon the number of counts in the observed spectrum per energy bin. If, for example, the number of counts per bin is sufficiently high enough (e.g. typically $N > 25$ per bin) then the Gaussian distribution and the χ^2 statistic may be used, below this the Poisson distribution and the C-statistic is appropriate. The χ^2 statistic is defined as follows, where σ_i^2 is the variance:

$$\chi^2 = \sum_i^N \frac{(X_i - M_i)^2}{\sigma_i^2} \quad (2.1)$$

χ^2 is a statistic which characterises the dispersion of the observed data points (X_i) from the theoretical points (M_i), for example, if the theoretical model matches the data exactly at a point, then $\chi^2 = 0$ for that point. Through repeated iterations the value of χ^2 is minimised and the quality of the fit can be determined by comparison with the number of degrees of freedom (ν) which is equal to the number of data points minus the number of free parameters. The reduced chi-squared can then be calculated using:

$$\chi_\nu^2 = \frac{\chi^2}{\nu} \quad (2.2)$$

A good fit has been obtained when $\chi_\nu^2 \approx 1$, values significantly greater than this indicate that the model is not a good fit to the data while values less than this do not necessarily indicate a better fit. This may instead indicate that the error bars on the observational data are too large to be appropriately fit with a model of this complexity, or perhaps through over-estimation of the error bars on the data. Of course, if a particular model achieves a reduced χ^2 value of 1 or close to 1, this does not necessarily mean that this is the correct or the only model which could fit the data. There may be alternative theoretical models which will achieve a similar reduced chi-squared but differ significantly in their physical implications or geometries. It is the role of the user to determine the physical appropriateness of a suggested model.

Errors upon the free parameters produced by the spectral fitting process can be calculated using the `ERROR` or `STEPPAR` (stepping through χ^2 space) command within `XSPEC`. Usually quoted at the 90% confidence level, these are calculated by varying the parameter in question until a deviation of $\Delta\chi^2 \sim 2.71$ (for one interesting parameter) from the best fit is found. All of the data sets analysed subsequently here have relatively high photon statistics (i.e. $N > 25$ per bin), therefore, the χ^2 minimisation technique is appropriate.

2.5 Common models used within this work

Within this section is a description of the frequently used models in the analysis of data in Chapters 3, 4 & 5.

2.5.1 Modelling of the soft excess

There are a number of possible origins of the soft excess observed in AGN X-ray spectra. A simple method of modelling the soft excess is as a black body to replicate direct thermal emission from the accretion disc (Malkan & Sargent 1982). However, the relatively constant temperature of the soft excess is in disagreement with the typical accretion disc properties for a SMBH which should scale with $M_{\text{BH}}^{-1/4}$ - more typical of an intermediate mass black hole, e.g., of $M_{\text{BH}} \sim 10^3 - 10^4 M_{\odot}$ with $kT \sim 100 - 200$ eV (Gierliński & Done 2004). A variation upon this concept is that the soft excess originates from the inverse-Compton scattering of the EUV photons from the accretion disc off electrons in a thermal plasma above the disc in a corona or a disc atmosphere (with kT of a few keV). Such a model would allow for a large variation in photon seed temperature, yet it could still produce a relatively constant output photon temperature. Here the COMPTT model is adopted (Titarchuk 1994) which produces a Comptonised output spectrum from a corona above the disc with UV photons from the disc acting as seed photons. Such a model has been successful in modelling the soft excess in a sample of PG quasars (see Porquet et al. 2004).

Departing from an origin of the soft excess due to emission from the accretion disc, an alternative explanation is an atomic origin. In this scenario soft X-ray emission lines are responsible for the soft excess, however, since these are discrete features and the observed soft excess is typically smooth, the reflection continuum must be highly relativistically blurred and hence originate from the inner regions of the accretion disc (Ross, Fabian & Ballantyne 2002). Such a model can be achieved by convolving a reflection continuum with a relativistic smearing kernel such as those used to generate the line shape in a relativistic diskline type model, e.g. KERRCONV or RELCONV. This

interpretation of the soft excess has also proved successful in statistical terms in some AGN such as Ark 120, Fairall 9 and MCG–6-30-15 (Ballantyne, Vaughan & Fabian 2003; Crummy et al. 2006; Schmoll et al. 2009; Nardini et al. 2010).

2.5.2 Compton reflection

Following the availability of hard X-ray data from *Suzaku*'s HXD and *Swift*'s BAT detectors features such as the Compton reflection hump at ~ 30 keV can be measured in the spectra of these AGN which may originate via reflection off the outer disc or a parsec scale torus. Using an ionised reflection model such as REFLIONX (Ross & Fabian 2005) allows properties such as the ionisation state, the iron abundance (Z_{Fe}) of the disc and the strength of the reflection component to be measured.

To account for the distant reflection component in these AGN, in the forthcoming work, PEXRAV is used (Magdziarz & Zdziarski 1995) to model reflection off a neutral slab, but this does not include any line emission, hence, the narrow FeK α and FeK β lines must be modelled using additional Gaussians with the appropriate K β /K α branching ratio of ~ 0.13 . This allows the strength of the broad line emission to be measured independently prior to modelling with a more physical diskline-type model and without a contribution from the Compton shoulder. PEXRAV is then replaced in later models with an unblurred REFLIONX ionised reflection model with the input photon index Γ tied to that of the intrinsic power-law with a built-in cut-off fixed at $E_c = 300$ keV. The advantage of the REFLIONX model is that it includes the reflected continuum and the soft narrow emission lines in addition to narrow FeK α emission lines and allows for a range in ionisations. Note that the ionisation parameter in REFLIONX is defined by Equation 2.3 in units of erg cm s^{-1} where F_{tot} is the total illuminating flux incident upon the reflector and n_{H} is the hydrogen number density ($n_{\text{H}} = 10^{15} \text{ cm}^{-3}$). The ionisation parameter here has a lower limit of $\xi = 1 \text{ erg cm s}^{-1}$. Another advantage of REFLIONX in preference to PEXMON (Nadra et al. 2007) is that as it is a pre-computed table of models, it is faster to run than the analytical PEXRAV model, this is of extreme importance during the later convolution models which are

very time consuming to run. However, $\text{FeK}\beta$ emission with flux $F_{\text{K}\beta} = 0.13 \times F_{\text{K}\alpha}$ is not included self-consistently in REFLIONX and as such is modelled using a narrow Gaussian of fixed width $\sigma = 0.01$ keV and with flux fixed at the value obtained during an initial parametrisation with PEXRAV plus Gaussians. Additional narrow ionised emission lines, e.g. at 6.7 keV and 6.97 keV from photoionised gas from the BLR or NLR may also be required and are modelled using a narrow Gaussian with width fixed as above.

$$\xi = \frac{4\pi F_{\text{tot}}}{n_{\text{H}}} \quad (2.3)$$

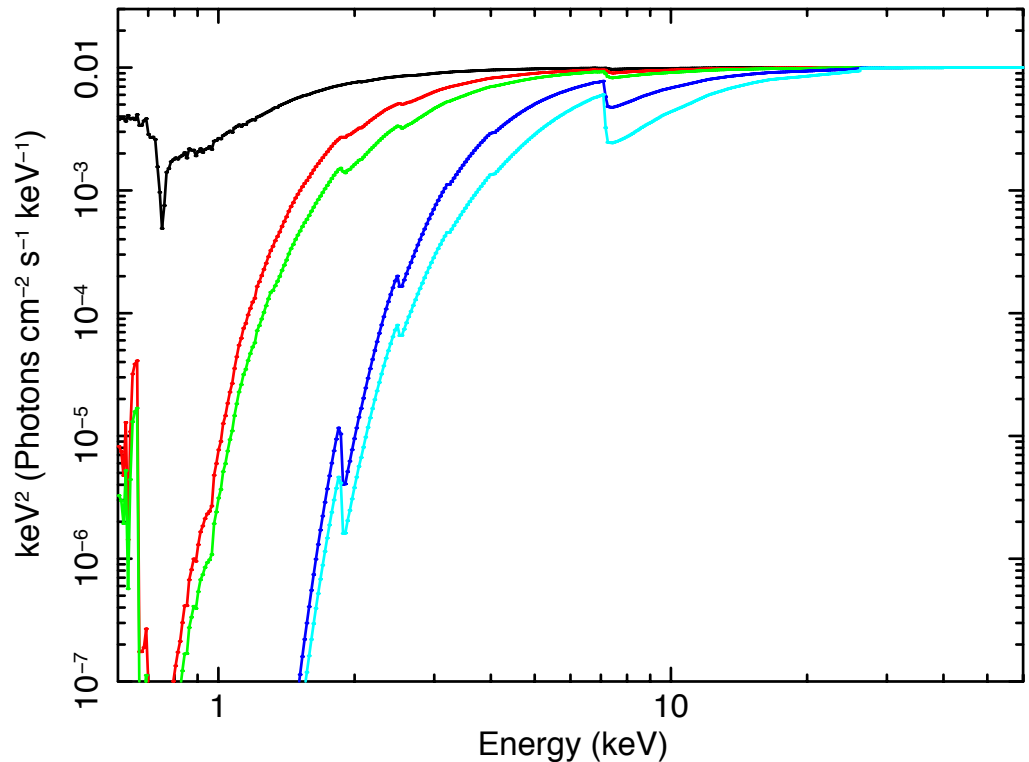


Figure 2.7: Examples of how a fully covering warm absorbing zone varies with changing column density. All plots are generated with an input photon index of $\Gamma = 2.0$ and ionisation $\log \xi = 1$. Black has a column density of $N_{\text{H}} = 10^{22} \text{ cm}^{-2}$, red $N_{\text{H}} = 5 \times 10^{22} \text{ cm}^{-2}$, green $N_{\text{H}} = 10^{23} \text{ cm}^{-2}$, dark blue $N_{\text{H}} = 5 \times 10^{23} \text{ cm}^{-2}$ and light blue $N_{\text{H}} = 10^{24} \text{ cm}^{-2}$.

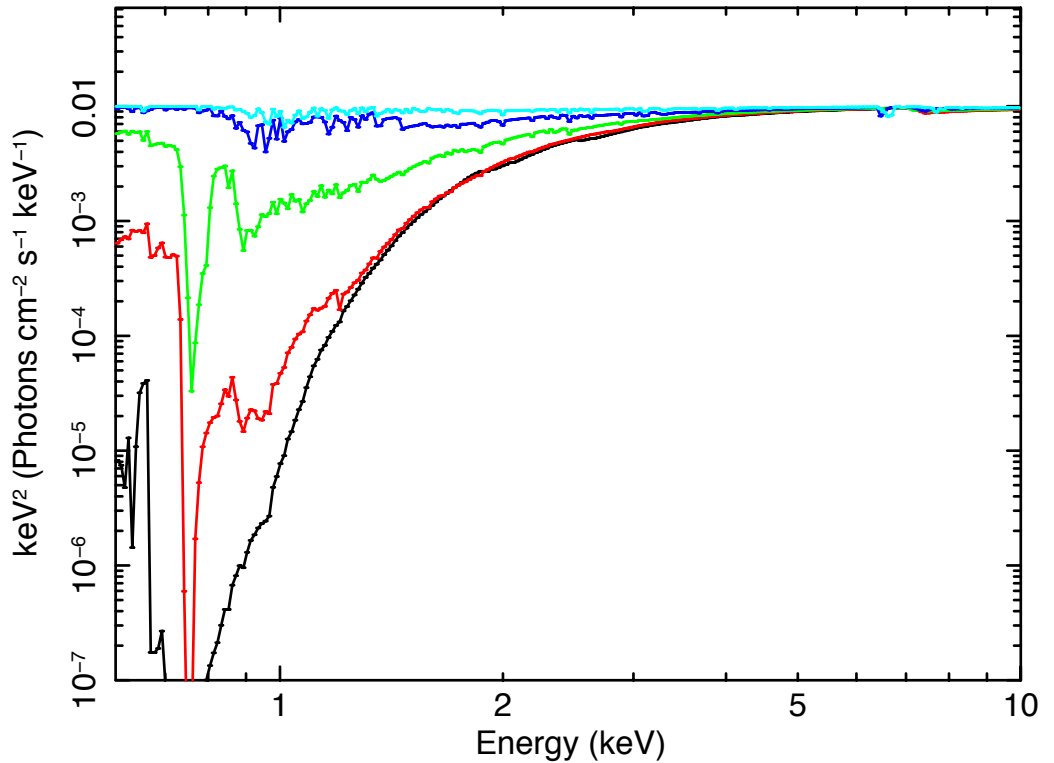


Figure 2.8: Examples of how a warm absorbing zone varies with changing ionisation. All plots are generated with an input photon index of $\Gamma = 2.0$ and a column density of $N_{\text{H}} = 5 \times 10^{22} \text{ cm}^{-2}$. Black has an ionisation of $\log \xi = 1.0$, red $\log \xi = 1.5$, green $\log \xi = 2.0$, dark blue $\log \xi = 2.5$ and light blue $\log \xi = 3.0$.

2.5.3 Warm absorption

The presence of an X-ray absorber primarily affects the X-ray spectrum of soft energies, however, with higher column densities the warm absorber may add subtle spectral curvature to the spectrum above 2.5 keV, see Figure 2.7. In particular, highly ionised absorption zones can affect the measured line parameters and strength of the observed broad red-wing in the FeK region (e.g. Reeves et al. 2004; Turner et al. 2005; see Figure 2.8). In previous observations of these objects (bar those ‘bare’ objects such as Ark 120, Fairall 9 etc) the presence of complex absorption zones has been well documented (Kaspi et al. 2000; Yaqoob et al. 2005; McKernan et al. 2007; Markowitz

et al. 2008; Miller, Turner & Reeves 2008; Lobban et al. 2011).

$$\xi = \frac{L_{\text{ion}}}{n_e R^2} \quad (2.4)$$

To model the soft X-ray warm absorber components in this work, an XSTAR generated (Kallman et al. 2004) grid is used which is illuminated by a photon index of $\Gamma = 2$, abundances fixed at solar values (except Ni, which was set to zero) and with a turbulent velocity of 200 km s^{-1} . This grid is well suited to accounting for typical absorption zones due to its wide range in column density ($5 \times 10^{18} \text{ cm}^{-2} < N_{\text{H}} < 5 \times 10^{24} \text{ cm}^{-2}$) and ionisation parameter ($0 < \log \xi < 5$) with units erg cm s^{-1} which is defined in Equation 2.4 where L_{ion} is the ionising luminosity in the range 1-1000 Ryd in units of erg s^{-1} , n_e is the electron density in cm^{-3} and R the distance from the source in cm. From Figure 2.7 it is clear that with increasing column density there is more spectral curvature added to the model and at higher columns there is a measurable impact from iron K absorption. Figure 2.8 shows that with increasing ionisation the obscuring material becomes more transparent to the soft X-ray continuum. During the fitting process absorption zones are added as required, in some objects more than one zone may be statistically required.

2.5.4 Highly ionised absorption

In the event that absorption features in the FeK region are found (such as 1s-2p resonance lines from FeXXV or FeXXVI), these are accounted for using a model representative of a highly ionised absorption zone. An XSTAR generated grid is used with a turbulent velocity of 1000 km s^{-1} (to better model the observed equivalent widths of the lines which will tend to saturate for lower turbulent velocities and hence line widths), an input continuum of $\Gamma = 2.0$ and range in column density and ionisation parameter of $1 \times 10^{20} \text{ cm}^{-2} < N_{\text{H}} < 1 \times 10^{24} \text{ cm}^{-2}$ and $0 < \log \xi < 6$ respectively, see Figure 2.9.

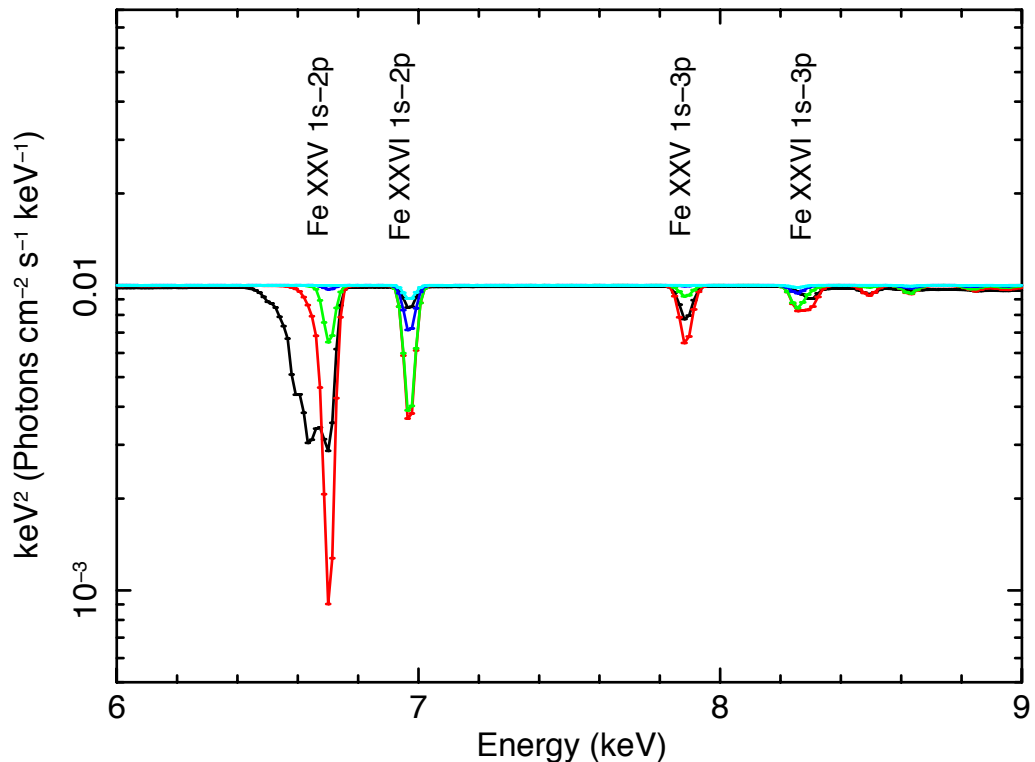


Figure 2.9: Examples of highly ionised absorption in the Fe K region. All plots are generated with an input photon index of $\Gamma = 2.0$ and a column density of $N_{\text{H}} = 5 \times 10^{22} \text{ cm}^{-2}$. Black has an ionisation of $\log \xi = 3.0$, red $\log \xi = 3.5$, green $\log \xi = 4.0$, dark blue $\log \xi = 4.5$ and light blue $\log \xi = 5.0$. Note that with increasing ionisation the iron ions become increasingly stripped of electrons until all electrons are removed and a smooth continuum is revealed, i.e. no electrons remain to attenuate incident photons and hence produce an absorption line.

2.5.5 Partial covering

Some models used in the analysis of these AGN use partial covering geometries whereby a fraction of the observed X-rays are absorbed by a surrounding gas in the line-of-sight (in addition to typical fully-covering absorbers), while some fraction of the continuum ‘leaks’ through and is unaffected by the partially covering material. The partial coverer used here takes the form of (powerlaw + WA*powerlaw), where WA represents the partially ionised warm absorber modelled by an additional XSTAR grid with the

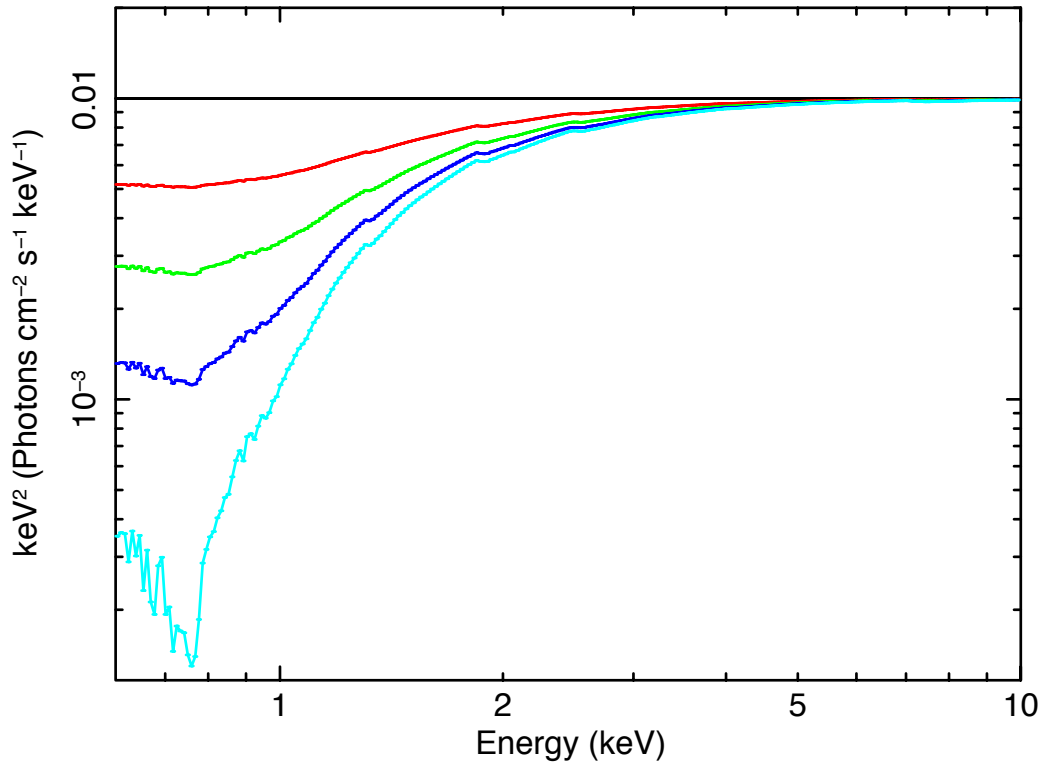


Figure 2.10: Examples of how a partial covering model can vary significantly according to the covering fraction of the absorbing zone. All plots are generated with an input photon index of $\Gamma = 2.0$ and column density $N_{\text{H}} = 10^{22} \text{ cm}^{-2}$ with a simple neutral absorber. Black has a covering fraction of $C_{\text{frac}} = 0$, red $C_{\text{frac}} = 0.5$, green $C_{\text{frac}} = 0.75$, dark blue $C_{\text{frac}} = 0.9$ and light blue $C_{\text{frac}} = 1.0$.

photon index of both the absorbed and unabsorbed power-law components tied and normalisation free to vary, giving the covering fraction as $C_{\text{frac}} = N_{\text{abs}} / (N_{\text{abs}} + N_{\text{unabs}})$ where N_{abs} represents the normalisation of the absorbed power-law component. The parameters of the warm absorber (ionisation and column density) are also allowed to vary, see Figures 2.10 and 2.11.

The column density of the partially covering medium can have a significant affect upon the spectrum. For example, high column partial coverers ($N_{\text{H}} \sim 10^{24} \text{ cm}^{-2}$) predominantly affect the hard X-ray energies producing an apparent hard excess and are used here to supplement the distant reflection component in cases where a hard

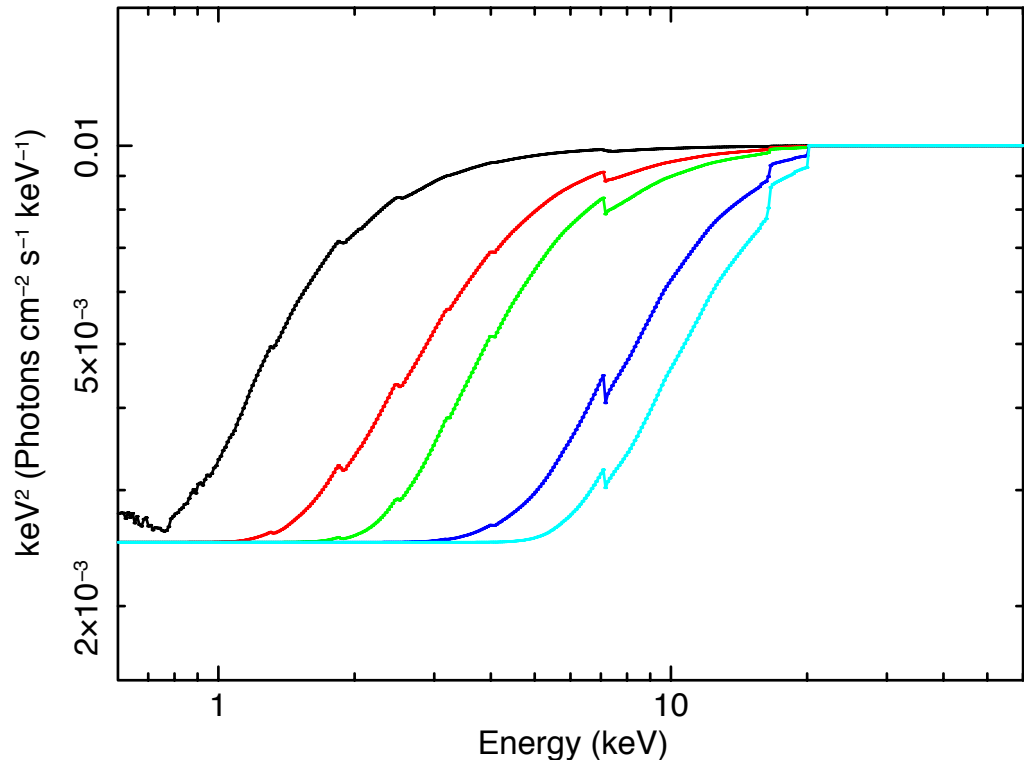


Figure 2.11: Examples of how a partial covering model can vary significantly according to the column density of the absorbing zone. All plots generated with an input photon index of $\Gamma = 2.0$ and with a simple neutral absorber and $C_{frac} = 0.75$. Black has a column density of $N_{\text{H}} = 10^{22} \text{ cm}^{-2}$, red $N_{\text{H}} = 5 \times 10^{22} \text{ cm}^{-2}$, green $N_{\text{H}} = 10^{23} \text{ cm}^{-2}$, dark blue $N_{\text{H}} = 5 \times 10^{23} \text{ cm}^{-2}$ and light blue $N_{\text{H}} = 10^{24} \text{ cm}^{-2}$.

excess remains unmodelled, e.g. see Figure 2.11. Lower column density partial coverers may greatly affect spectral curvature at lower X-ray energies below 10 keV and in some cases can entirely remove any ‘broad’ residuals in the FeK region (Miller, Turner & Reeves 2009). For example, typical partial coverer column densities of $N_{\text{H}} \sim 10^{23} \text{ cm}^{-2}$ can impart spectral curvature in the FeK band. Subsequently up to one partially covering absorbing zone is allowed to fit the data here, however, the use of multiple partially covering zones can lead to models which are highly degenerate with a wide range of disc line parameters therefore significantly reducing the ability to estimate accretion disc properties.

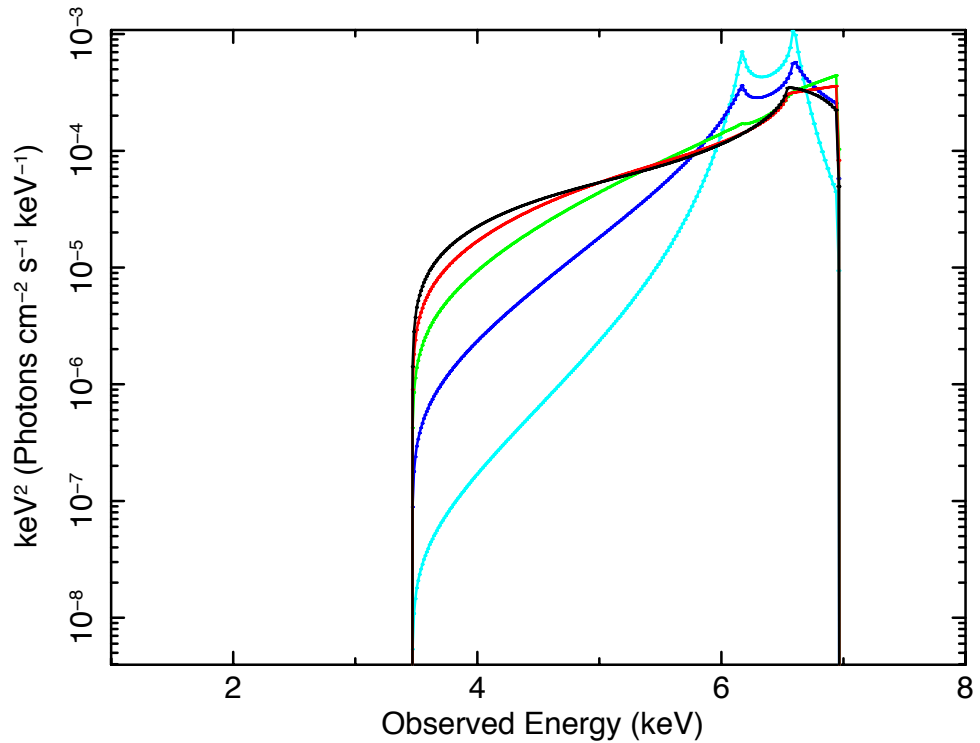


Figure 2.12: Line profiles using RELLINE with rest energy 6.4 keV and parameters spin $a = 0$, inclination $i = 40^\circ$, $R_{\text{in}} = R_{\text{isco}}$ and varying emissivity $q = 5$ (black), $q = 4$ (red), $q = 3$ (green), $q = 2$ (dark blue) and $q = 1$ (light blue).

2.5.6 Asymmetric line profiles and diskline-type models

With higher quality data there has been a need for a more physical method of modelling the broad emission which is sometimes observed in the FeK regions of AGN. While the strength or presence of broad emission can be assessed with a simple Gaussian, asymmetric line profile models are required to sufficiently model emission from the very inner regions of the accretion disc. A variety of relativistic line models are available, e.g. DISKLINE (Fabian et al. 1989), LAOR (Laor 1991), KYRLINE (Dovčiak et al. 2004), KERRDISK (Brenneman & Reynolds 2006) and RELLINE (Dauser et al. 2010). With good data, these models can potentially allow information regarding the inclination, emissivity and inner radius of the disc to be estimated according to the shape of the

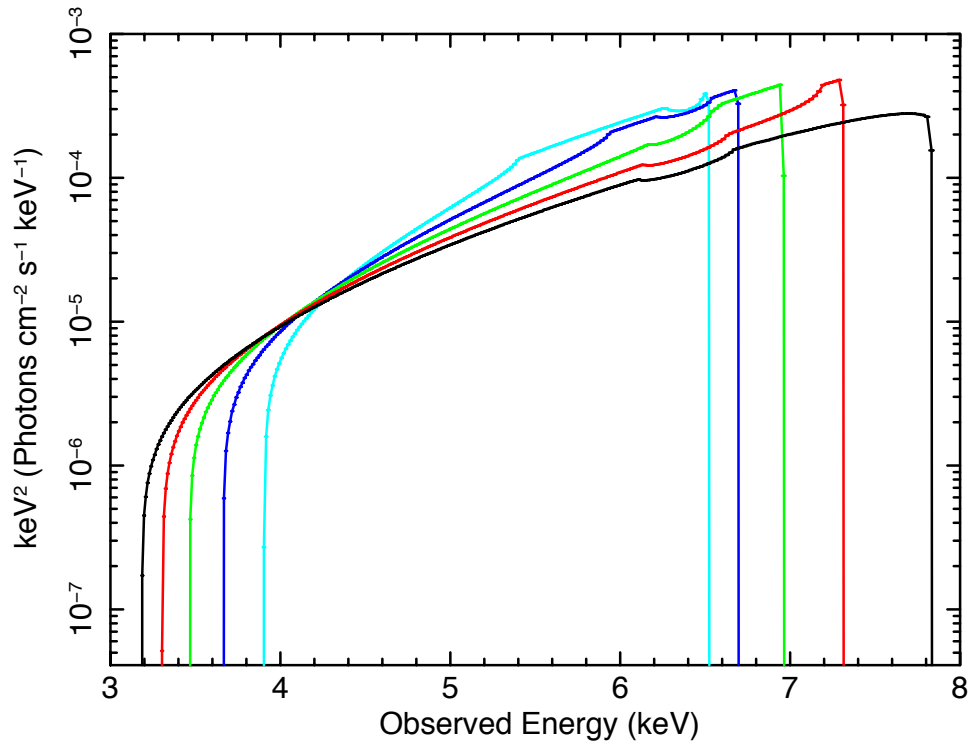


Figure 2.13: Line profiles using RELLINE with rest energy 6.4 keV and parameters $q = 3.0$, $a = 0$, $R_{\text{in}} = R_{\text{isco}}$ and inclination $i = 60^\circ$ (black), $i = 50^\circ$ (red), $i = 40^\circ$ (green), $i = 30^\circ$ (dark blue) and $i = 20^\circ$ (light blue).

line profile.

Fabian et al. (1989) developed the DISKLINE model for non-rotating BHs with $a = 0$ and the inner radius of emission free to vary and later Laor (1991) developed a similar model (called LAOR) this time for a Kerr BH with $a = 0.998$. Until the advent of higher quality data with better S/N from X-ray telescopes such as *Suzaku* it was only possible to distinguish between these two opposite scenarios in a few objects. Dovčiak et al. (2004) produced the KYRLINE model which then allowed the spin of the BH to be estimated as mentioned above. Similar models were also produced by Beckwith & Done (2004; KDLINe) and Brenneman & Reynolds (2006; KERRDISK).

These models all assume that the SMBH rotates in a prograde fashion, i.e., in the same direction as the surrounding accretion disc. Dauser et al. (2010; see also

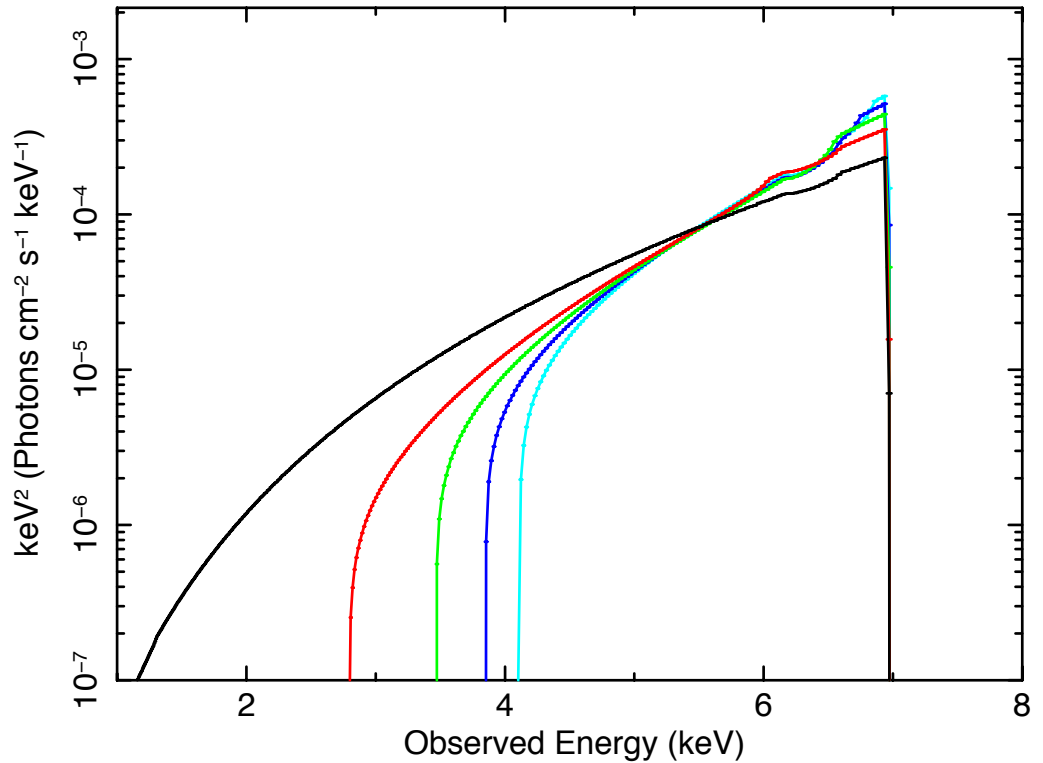


Figure 2.14: Line profiles using RELLINE with rest energy 6.4 keV and parameters $q = 3.0$, $i = 40^\circ$, $R_{\text{in}} = R_{\text{isco}}$ and spin increasing left to right $a = +0.998$ (black), $a = +0.5$ (red), $a = 0.0$ (green), $a = -0.5$ (dark blue) and $a = -0.998$ (light blue). Note that even in the case of a maximally rotating retrograde BH (furthest out R_{ISCO}), there is still a significantly broadened line profile.

Dovčiak et al. 2004) developed the RELLINE model which accounts for the scenario of a retrogradely spinning BH in which the SMBH rotates in the opposite direction to the accretion disc with the spin parameter then ranging between $-0.998 < a < +0.998$. The effect is to force R_{ISCO} further out beyond that for a Schwarzschild BH to $\sim 9 R_g$, therefore producing narrower line profiles than for progradely rotating BHs (Dauser et al. 2010; also see Figure 2.14).

The emissivity index (q) of the disc is a measure of the extent to which emission from the disc is centrally concentrated, scaling with radius as R^{-q} . A high emissivity index would suggest that emission is very centrally concentrated with strong relativistic

effects such as light bending having an influence (Miniutti & Fabian 2004), whereas a low index would suggest the opposite and relativistic effects are weaker as emission originates from the outer regions of the disc, see Figure 2.12 whereby the relativistic effects upon the line profile become less pronounced with lower emissivities although the ‘horned’ profile shape becomes more obvious. The inner radius of emission can also determine the degree to which photons from an emitting region are redshifted, i.e. the closer the disc extends towards the central SMBH, the stronger the red-wing of the line profile. Under the assumption that the accretion disc is not truncated by some factor, if it is assumed that the disc extends all the way down to the innermost stable circular orbit (R_{ISCO}), the measurement of this then becomes synonymous with the measurement of the spin of the SMBH. As noted in Section 1.2, $R_{\text{ISCO}} = 6 R_g$ and $R_{\text{ISCO}} = 1.235 R_g$ for non-rotating and maximally rotating SMBHs respectively (i.e. Schwarzschild and maximal Kerr black holes).

It should be noted that for moderate to high inclinations ($i > 20^\circ$) the blue-wing of the line profile peaks at a higher flux than the red-wing peak due to a boosting effect from material travelling at relativistic velocities in orbit ‘close’ to the central black hole. This effect is accentuated with lower emissivities since with increasing q (and hence more centrally concentrated emission) a greater proportion of the emitted photons are present in the red-wing of the line profile due to their proximity to the very inner regions and increased gravitational broadening. Figure 2.13 also shows that with higher inclinations the blue-wing of the line profile is shifted to higher energies. At particularly high emissivities, the blue-wing diminishes and the majority of the flux is contained within the red-wing of the line profile, forming a single peaked profile and an increasingly strong red-wing below 6.4 keV (Fabian et al. 1989; Laor 1991; Dauser et al. 2010). Further still, at near maximal spin and high q the entire line profile can produce an asymmetric featureless hump which simply creates additional curvature in the $\sim 1 - 7$ keV region.

2.5.7 Convolution models

A variation upon the diskline-type models described above in Section 2.5.6 is to convolve a particular model with a relativistic smearing kernel such as those used in typical relativistic line emission models. Convoluting a reflection continuum with such a kernel would subject the entire reflection continuum to relativistic effects such as Doppler broadening/ boosting and gravitational broadening which would be representative of reflection from the very inner regions of the accretion disc. For example, if a narrow Gaussian at 6.4 keV (i.e. $\text{FeK}\alpha$) were to be convolved with the RELCONV convolution model (Dauser et al. 2010), the output model would be exactly the same as that produced by the RELLINE line emission model. There are a wide range of convolution models available, similarly to LAOR, KERRDISK, RELLINE etc above: KDBLUR, KERRCONV, RELCONV (Laor 1991; Brenneman & Reynolds 2006; Dauser et al. 2010).

As noted in Sections 1.7.2 and 1.5.4, the soft excess can be modelled by the application of strong relativistic effects to discrete soft X-ray emission lines. Such a scenario can be constructed by convolving the reflection continuum from the REFLIONX model (Ross & Fabian 2005) with a relativistic smearing kernel, in this thesis two kernels are used; KERRCONV (Brenneman & Reynolds 2006) in Chapters 3 & 4 and RELCONV (Dauser et al. 2010) in Chapter 5. Aside from uses as a possible interpretation of the soft excess, any relativistic blurring applied to an $\text{FeK}\alpha$ emission line from the inner regions of the accretion disc can also be self-consistently applied the remainder of the reflection continuum to represent the reflection component also originating from the inner regions of the accretion disc. Figure 2.15 shows a comparison of the reflection components which may arise from the accretion disc, e.g. the unblurred case represents reflection off material which is distant from the central SMBH whereas the relativistically blurred cases represent emission from the inner regions of the accretion disc. Only in the scenario in which there is reflection off material from the extreme inner regions of the disc (i.e. a maximally spinning SMBH and highly centrally concentrated emission) can the convolved reflection continuum begin to represent a smooth continuum which may prove as an alternative mechanism for modelling the soft excess (also see Figure

1.5 in Section 1.5.4).

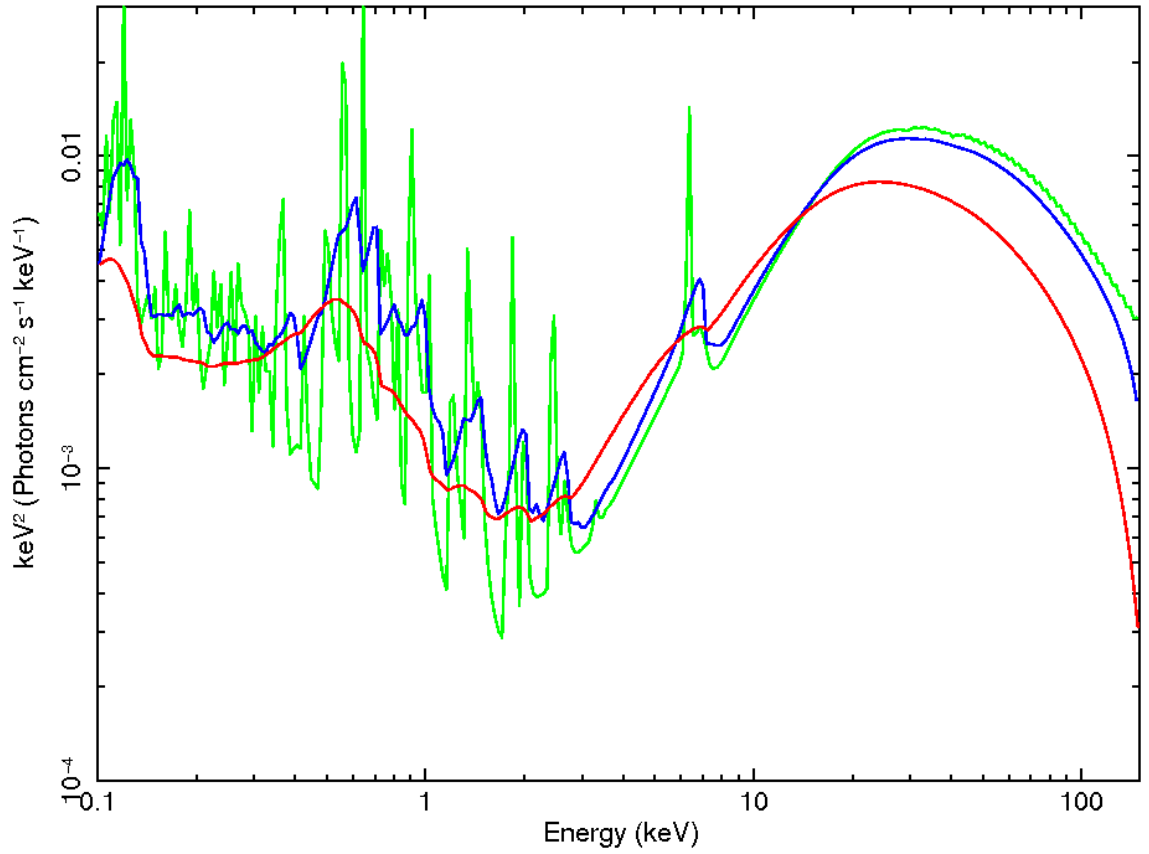


Figure 2.15: Convolution of REFLIONX reflection model (Ross & Fabian 2005) with a KERRDISK kernel (Brenneman & Reynolds 2006). Significant blurring (red), moderate blurring (blue), no blurring (green).

3 Analysis of ‘bare’ Seyfert sample

Analysis of the Fe K line profile can help us determine some of the intrinsic properties of the central black hole in AGN and its accretion disc (e.g. Fabian et al. 1989; Laor 1991). Foremost in the current climate is the determination of black hole (BH) spin, for example recent observations by Miniutti et al. (2007 & 2009) and Schmoll et al. (2009) have analysed the broad Fe K α region in order to constrain the spin of the central BH. A black hole can be characterised simply by its mass and its spin. Many objects have now been classified in terms of their mass into three categories: Galactic BH, Intermediate Mass BH and Supermassive BH. The spin of the black hole determines the nature of the space-time metric in the regions close to it. The spin parameter $a = cJ/GM^2$ (where J =angular momentum and $0 < a < 0.998$) is used to describe the spin of the BH, where a is limited to a maximum value of $a = 0.998$ at the Thorne limit. This is due to photon capture in which photons travelling on ‘negative’ angular momentum orbits are preferentially captured by the black hole therefore producing an upper bound to the spin parameter a and hence limiting the innermost stable circular orbit to a minimum of $R_{\text{ISCO}} = 1.235 R_g$ (Thorne 1974). Constraining the spin of SMBHs in AGN and studying the distribution of black hole spin can aid our understanding of the evolution of AGN and the black holes themselves, e.g. mergers, relativistic jets and variability (Blandford & Znajek 1977; Volonteri et al. 2007; King, Pringle & Hofmann 2008).

Line emission from the inner regions of the accretion disc can become broadened due to relativistic effects and Doppler motions (Fabian et al. 1989) resulting in an asymmetric profile. Evidence for such broadening was found using the X-ray CCD detectors onboard *ASCA* by Mushotzky et al. (1995), Tanaka et al. (1995) and Nandra et al. (1997) typically over the 0.5–10.0 keV range. Now with X-ray spectra of increasing quality and over wider energy ranges such as that obtained with the XIS and high energy HXD detectors onboard *Suzaku* (0.5–60.0 keV, Mitsuda et al. 2007), the Fe K region of AGN can be examined in detail. High energy X-ray data are important since it allows the reflection component and its strength to be properly fit, assessing

its contribution to the continuum and FeK region (e.g. Reeves et al. 2007). Fitting features such as the Compton hump at ~ 30 keV allows, for example, the ionisation state of the reflecting material to be determined (Ross & Fabian 2005). With the aim of measuring properties of the accretion disc and the central black hole itself, broadband data allows us to start making constraints on parameters in these regions based upon the shape of the FeK line profile.

Previous studies of iron lines have been made using data from *XMM-Newton* over the 2.5–10.0 keV (Nandra et al. 2007) and 0.6–10.0 keV energy ranges (Brenneman & Reynolds 2009), finding complex emission in the FeK band in the majority of Type 1 Seyfert AGN over and above narrow line components originating from distant material. In a sample of 26 objects Nandra et al. (2007) found that narrow 6.4 keV emission is ubiquitous amongst AGN and broad FeK lines feature in ~ 40 – 50% of AGN and ionised emission due to FeXXVI and FeXXV is relatively rare amongst AGN. Brenneman & Reynolds (2009) found that 4/8 AGN were best fit by a model consisting of relativistically blurred reflection from the inner regions of the accretion disc with 2/8 objects suggesting non-zero spin, however, noting that the 10.0 keV cut-off with the EPIC-PN camera limits their findings of the reflection continuum.

In order to make robust measurements of the FeK region as a pre-cursor to determining the spin of a central SMBH, it is essential that there is a self consistent description of the broadband X-ray spectrum. The X-ray spectra of AGN are, in general, very complex and hence robust measurements of black hole spin are difficult to obtain. This chapter tackles this initial hurdle by conducting an analysis of a sample of objects which are simple to model and provide a relatively ‘clean’ spectrum. To give the best possible opportunity of understanding the broadband spectrum, data from observations with the X-ray satellite *Suzaku* are used which, with its HXD detector, is able to provide measurements of the hard X-ray continuum in addition to the soft X-ray data provided by the XIS. The work within this chapter takes advantage of medium to long observations of so called ‘bare’ Seyferts which are notable in their lack of intrinsic absorption, therefore significantly reducing the possible complications and degeneracies typically involved in an analysis targeted at the FeK region, e.g. bound-free absorption

leading to spectral curvature due to warm absorbing zones.

The results and analysis in this chapter are based upon those presented in a lead-author paper Patrick et al. (2011a).

3.1 The importance of broadband data and a clean spectrum

This small sample features predominantly bare Seyferts, i.e., either with no or a very weak warm absorber. This is in an attempt to simplify the modelling of the broadband spectrum and therefore provide a basic understanding of the properties of the FeK region and any accompanying broad red-wing without the need for debate over differing interpretations of the origin of various absorption components in the spectrum (Turner & Miller 2009). Using data from *Suzaku's* XIS (Koyama et al. 2007) and HXD (Takahashi et al. 2007) spanning a total of 0.5–60.0 keV and BAT data (from the *Swift* 22 month all sky survey available at the time of analysis, Tueller et al. 2010) over 20.0–100.0 keV provides the broadband spectra necessary for a detailed modelling and measurement of the FeK region and the associated Compton reflection hump. This approach ensures that a robust model of the FeK line region (and broadband spectrum) can be made with the aim of establishing the degree to which narrow ionised emission lines and relativistically broadened components are required in this small sample of ‘bare’ Seyferts.

3.2 Bare Seyfert sample

The objects in this sample are described in Table 3.1 and are the Seyfert 1, radio quiet AGN with low intrinsic absorption available in the public *Suzaku* data archive with spectra from the XIS and HXD detectors at the time of analysis (i.e. 2010), namely Ark 120, Fairall 9, MCG-02-14-009, Mrk 335, NGC 7469 and SWIFT J2127.4+5654.

Table 3.1: The *Suzaku* bare Seyfert sample. Galactic column density is given in units 10^{22}cm^{-2} .

Object	RA (J2000)	Dec (J2000)	Redshift	N_{H} (Gal)	Date	Exposure
Ark 120	05 16 11.4	-00 09 00	0.033	0.0978	01/04/07	101 ks
Fairall 9	01 23 45.8	-58 48 21	0.047	0.0316	07/06/07	168 ks
MCG-02-14-009	05 16 21.2	-10 33 41	0.028	0.0924	28/08/08	142 ks
Mrk 335	00 06 19.5	+20 12 10	0.026	0.0356	21/08/06	151 ks
NGC 7469	23 00 44.4	+08 36 17	0.016	0.0445	24/06/08	112 ks
SWIFT J2127.4+5654	21 27 45.0	+56 56 40	0.014	0.7650	09/12/07	92 ks

All objects are detected above 15 keV and are relatively nearby with redshift $z < 0.05$. Hard X-ray data from the 22 month BAT catalogue from *Swift* are used in addition to the HXD data in all observations other than MCG-02-14-009, for which no BAT spectrum was publically available (it was, however, later detected by BAT in the 39 month version of the survey with a 14–150 keV flux of $1.5 \times 10^{-11} \text{ erg cm}^{-2} \text{ s}^{-1}$, Cusumano et al. 2010). The *Suzaku* data sets of the six objects detailed in Table 3.1 are analysed here, note that only the 2007 data for Fairall 9 is used here (Obs. ID: 702043010), at the time of this work the later 2010 observation was not publicly available. Further details of the observations used in this analysis are given in Table A.1 on page 224. Note that the non-simultaneous BAT hard X-ray data was given a cross-normalisation of approximately 1.0 but allowed to vary in all observations.

The objects featured in this sample are all objects with a very low degree of warm absorption (see Figure 3.1), however, three objects in this analysis have been noted as having some additional absorption in previous observations: MCG-02-14-009, Mrk 335 and NGC 7469. Gallo et al. (2006) found a small neutral absorber ($N_{\text{H}} < 10^{21} \text{ cm}^{-2}$) and an O VII edge in a re-analysis of a very short (~ 5 ks net exposure) observation of MCG-02-14-009 with *XMM-Newton*. However, including these components in the *Suzaku* data used here makes no improvement ($N_{\text{H}} < 3 \times 10^{20} \text{ cm}^{-2}$) and the optical depth of the O VII edge can only be constrained to $\tau < 0.04$. Therefore MCG-02-14-009

can be considered as ‘bare’ for the purposes of this analysis.

Mrk 335 has also shown evidence for a warm emitter whilst in a low state when observed with *XMM-Newton* (Grupe et al. 2008), however, in the *Suzaku* data used here Mrk 335 has a 0.5 – 2.0 keV flux 14× higher than in the low state observation and as such any warm absorption or emission features are entirely dominated by the continuum. As a result of this Mrk 335 is also suitable for inclusion within this sample. Previous observations of NGC 7469 have noted some degree of X-ray and UV absorption ($N_{\text{H}} \sim 10^{20} - 10^{21} \text{ cm}^{-2}$, Scott et al. 2005; Blustin et al. 2007). The *Suzaku* data used here is consistent with the previous work using data from *XMM-Newton*, requiring an O VII edge depth of $\tau < 0.1$, however, there is no effect upon the Fe K parameters and NGC 7469 has also been included within this sample. The broadband *Suzaku* spectrum plotted in Figure 3.1 shows no significant additional absorption features below 2 keV within the *Suzaku* data in this AGN.

3.3 Bare Seyfert results

All the *Suzaku* data in this analysis were reduced using the HEASOFT reduction and analysis package (version 6.8). XIS source spectra were extracted from circular regions of 3.0′ within XSELECT centred upon the source at the on-axis pointing position, in accordance with Section 2.4.2. Similarly, background spectra were extracted from 3.0′ circular regions, taking care not to include the source or the Fe 55 calibration sources in the corners of the CCD’s field of view. Only data from the front-illuminated XIS cameras were used, i.e. the XIS 0 and XIS 3 cameras – due to their greater sensitivity at Fe K energies, however, the observation of Mrk 335 (Obs. ID: 701031010) also includes the now non-operational front-illuminated XIS 2. It should be noted that only data from the XIS 3 camera was available for the *Suzaku* observation of SWIFT J2127.4+5654 (Obs. ID: 702122010) since the XIS 0 camera was non-operational during this observation.

All XIS data below 0.5 keV, above 10.0 keV are ignored and between 1.7–1.95 keV

due to uncertainties in the calibration of the detectors around the Si K edge. In the analysis of the HXD/PIN spectra data is typically considered between 15.0–60.0 keV however, in some cases such as Mrk 335 the data was also ignored below 20.0 keV due to thermal noise. Hard X-ray data also obtained from the *Swift* 22-month BAT catalogue was included for all objects (other than MCG-02-14-009) over the energy range 20.0–100.0 keV.

Table 3.2: Summary of models and components used for each feature in the construction of Models A-F in the analysis of bare Seyferts.

Model	Continuum	Distant Reflection	Soft Excess	6.4keV Core	6.4keV Broad
Model A	POWERLAW	PEXRAV	COMPTT	Gaussian	Gaussian
Model B	POWERLAW	REFLIONX	COMPTT	within REFLIONX	None
Model C	POWERLAW	REFLIONX	COMPTT	within REFLIONX	LAOR
Model D	POWERLAW	REFLIONX	COMPTT	within REFLIONX	KERRDISK
Model E	POWERLAW	REFLIONX	Blurred REFLIONX	within REFLIONX	Blurred REFLIONX
Model F	POWERLAW	–	COMPTT	Gaussian	Blurred REFLIONX

3.3.1 Model A – Parameterisation of spectra

The continua of the six bare Seyferts were initially parameterised as described below, hereafter Model A, see also Table 3.2. Model A is intended to provide a simple parameterisation of the spectra and give an insight into the presence of basic components in the spectra and the extent to which a possibly relativistically broadened component is required to model the Fe K line region. None of the spectra required any significant warm absorber (see Section 3.3), thereby simplifying the modelling of the soft X-ray spectrum. Additionally, the COMP_{TT} model representing Comptonisation of soft disc photons in a hot plasma above the disc (Titarchuk 1994; as discussed in Section 2.5.1) with a soft input photon temperature of 0.02 keV, is employed to account for the soft excess if present in the spectra (see Figure 3.2). Porquet et al. (2004) also found that in a sample of PG quasars the soft excess was better modelled in this way, rather than by direct thermal emission from the accretion disc. Adopting a second soft POWERLAW component instead of COMP_{TT} also gives a similar parametrisation of the soft excess. The narrow 6.4 keV Fe K α core due to reflection off distant material is present in all six objects and has been modelled with a narrow Gaussian with width $\sigma_{K\alpha}$ free to vary. The narrow component is not resolved in any of the spectra and as such the width is subsequently fixed at $\sigma_{K\alpha} = 0.01$ keV, i.e., less than the XIS energy resolution. Emission resulting from Fe K β is also accounted for with the line energy fixed at 7.056 keV, width fixed to that of the narrow K α and flux tied to 13% of the K α component from the K β /K α branching ratio.

To be consistent with the narrow Fe K α emission lines, emission from neutral distant Compton reflection is accounted for using the PEXRAV model (Magdziarz & Zdziarski 1995) applied to the broadband 0.5–100 keV spectra which models the reflection continuum off a neutral slab. This model requires the input of a photon index Γ which is tied to the continuum powerlaw, the normalisation of the PEXRAV component is also tied to that of the powerlaw, abundances are assumed to be Solar (Anders & Grevesse 1989) and the inclination with respect to the observer is fixed at $\cos i = 0.87$ throughout (i.e. consistent with Seyfert 1s being relatively face-on). The reflection

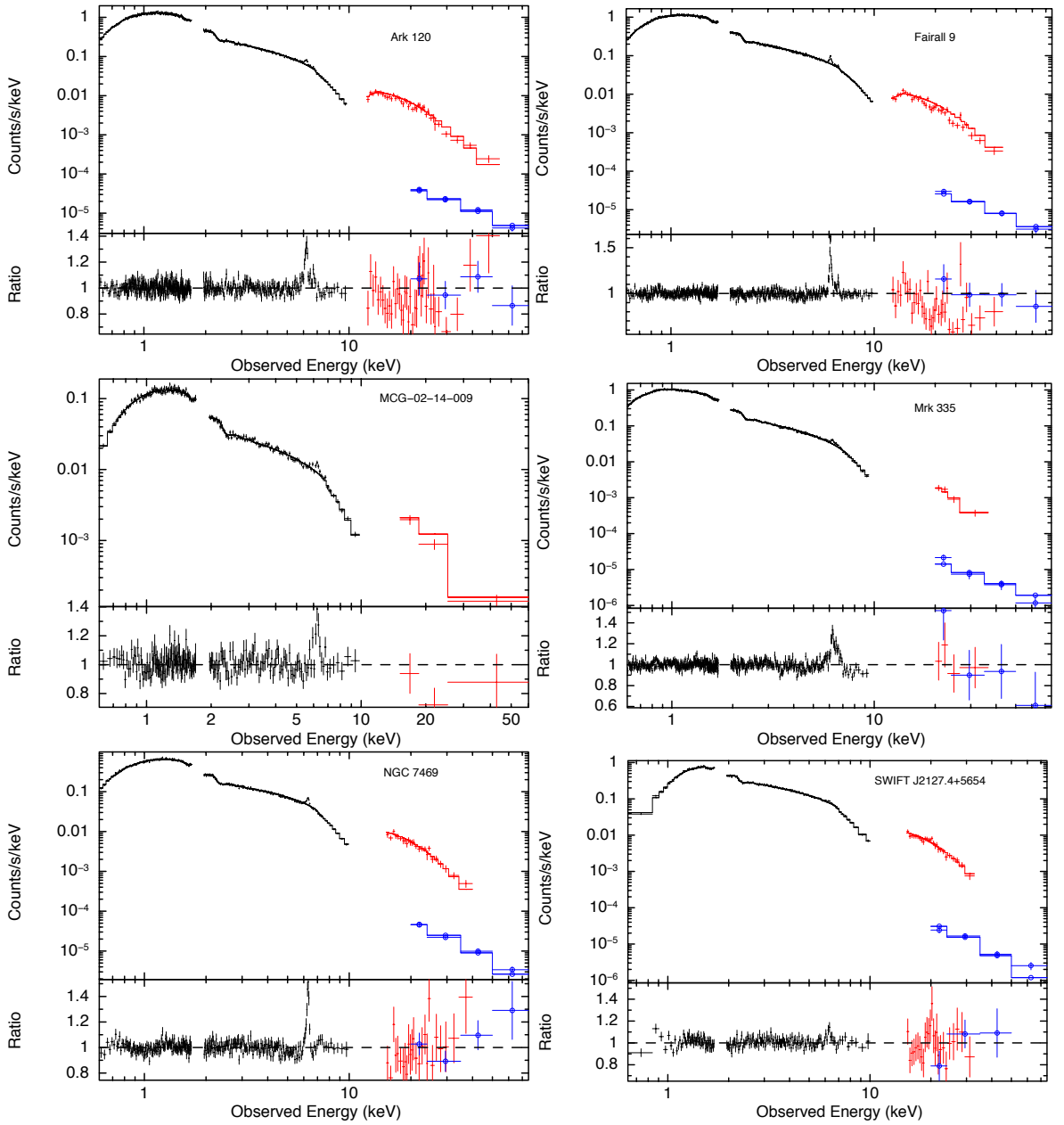


Figure 3.1: The 0.5–70.0 keV spectra and residuals of the six bare Seyferts. The data/model ratio residuals (lower panels) are plotted after modelling of the continuum with a POWERLAW, neutral reflection from the PEXRAV model, COMPTT to model the soft excess and WABS to account for Galactic absorption, the entire FeK region is left unmodelled. XIS data is in black, HXD in red and BAT data is represented by blue circles.

fraction $R = \Omega/2\pi$ is left as a free parameter (where $R = 1$ denotes reflection from material subtending 2π sr). The exponential cut-off energy for the PEXRAV component is fixed at 1000 keV, except for NGC 7469 and SWIFT J2127.4+5654 which show indications of a roll-over at high energies, occurring at $E_c = 119_{-31}^{+65}$ keV and $E_c = 49_{-14}^{+43}$ keV respectively. Such a roll-over was found in SWIFT J2127.4+5654 previously by Malizia et al. (2008) at $E_c = 33_{-10}^{+19}$ keV.

Examining the residuals after the application of these components, some objects have more complex features such as excess emission around energies of 6.7 keV and 6.97 keV relating to narrow ionised emission from Fe XXV and Fe XXVI respectively, again due to distant photoionised gas (see Figure 3.1 and Figure 3.3). Similarly to the modelling of the narrow 6.4 keV core, the energies of these lines are free to vary as is the normalisation, however, the width remains fixed to $\sigma = 0.01$ keV. A broad Gaussian is also added to the model to account for a red-wing in the spectra with energy, normalisation and σ_{Broad} as free parameters. In this case the energy is allowed to drop below 6.4 keV in the rest frame as this model is only intended as a simple parametrisation of the Fe K region and a test of the significance of the components used to model the region. This could represent either gravitational redshift if the line originates from the inner disc or the presence of a strong Compton shoulder.

A good fit is obtained by Model A in all objects, particularly Fairall 9, NGC 7469 and SWIFT J2127.4+5654, see Table B.1 on page 232. No significant soft excess is found in MCG-02-14-009 and SWIFT J2127.4+5654, the latter (if present) is likely to be mostly absorbed due to the relatively high column of Galactic absorption ($N_{\text{H}} \approx 7.65 \times 10^{21} \text{ cm}^{-2}$). In SWIFT J2127.4+5654 there is some indication of the presence of an intrinsic neutral absorber, albeit of relatively low column density (as found in Miniutti et al. 2009). Instead modelling the spectrum with an absorbed POWERLAW using the ZPHABS model at the redshift of the source improves the fit by $\Delta\chi^2 \sim 59$ for one additional free parameter with intrinsic column density $N_{\text{H}} \approx 8.2_{-0.6}^{+0.6} \times 10^{20} \text{ cm}^{-2}$ and photon index $\Gamma = 2.19_{-0.05}^{+0.05}$.

Statistically significant narrow ionised emission is found in most objects, with only SWIFT J2127.4+5654 and MCG-02-14-009 having very little requirement for these

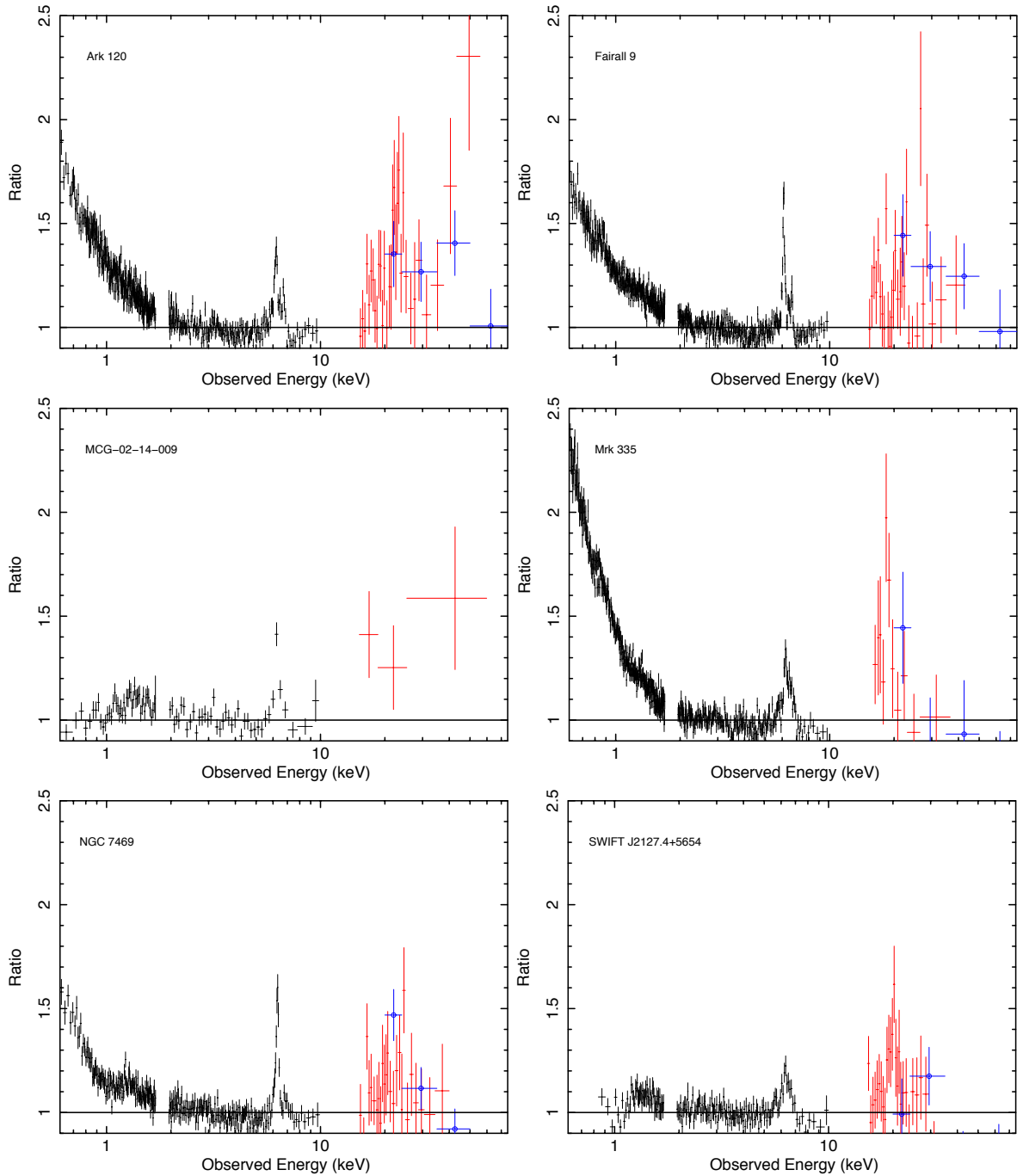


Figure 3.2: The 0.5–70.0 keV data/model residuals after modelling of the continuum with a simple POWERLAW and WABS to account for Galactic absorption, the entire Fe K region and any soft excess is left unmodelled. The soft excess is particularly prominent in Ark 120, Fairall 9, Mrk 335 and NGC 7469. XIS data is in black, HXD in red and BAT data is represented by blue circles.

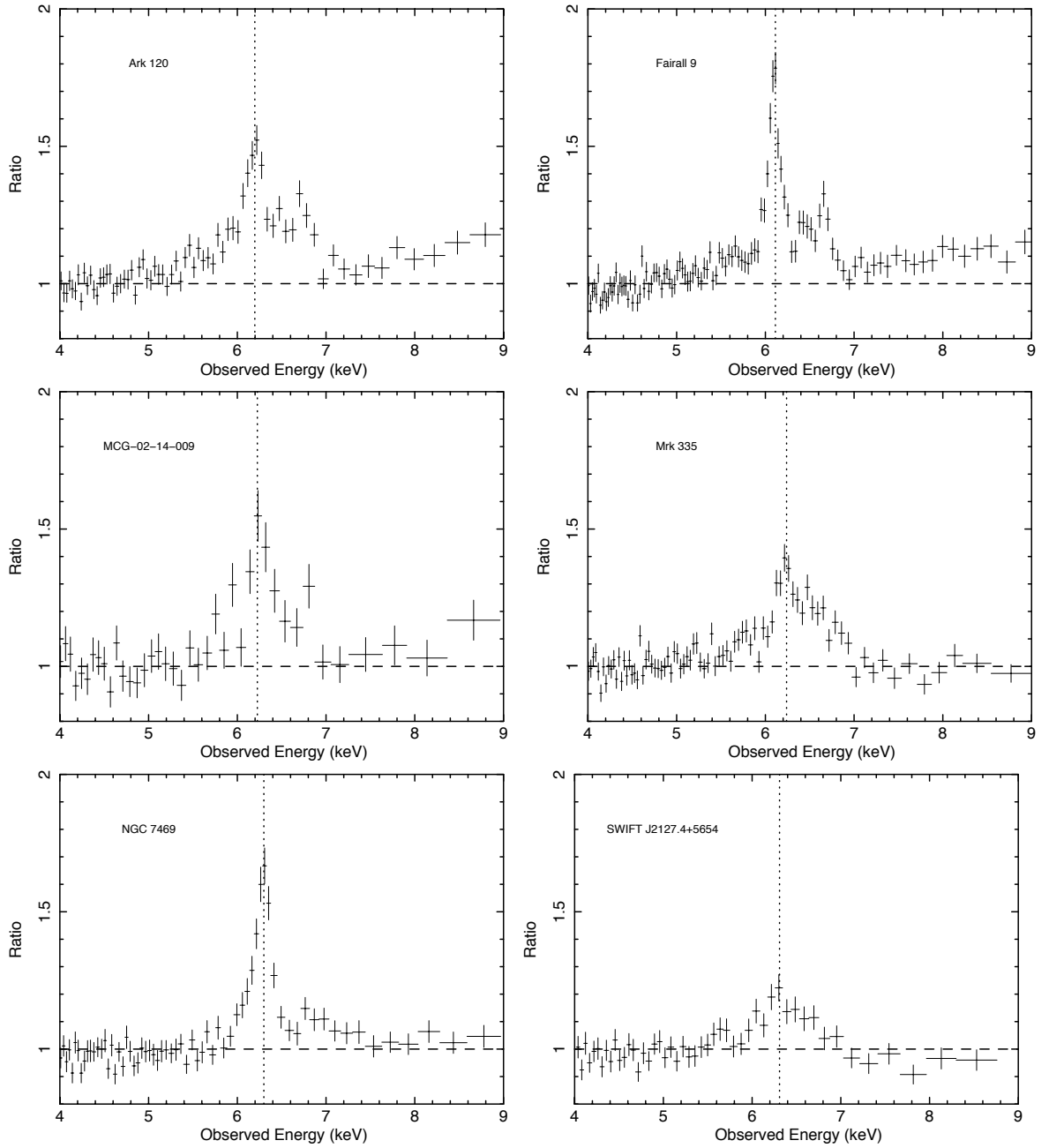


Figure 3.3: The 4–9 keV residuals after modelling of the continuum with a powerlaw, COMPTT to model the soft excess and Galactic photoelectric absorption. The dashed vertical line represents 6.4 keV in the rest frame.

features. These lines occur at energies likely originating from FeXXV and FeXXVI with emission at ~ 6.97 keV being particularly evident in the spectra, proving strong in Fairall 9 for which the fit improves by $\Delta\chi^2 \sim 24$ with the introduction of a narrow Gaussian (and therefore two additional free parameters) at $6.98_{-0.02}^{+0.02}$ keV and to a lesser extent in Ark 120 ($\Delta\chi^2 \sim 12$ at $6.96_{-0.04}^{+0.04}$ keV). The only objects not showing residuals at ~ 6.7 keV or ~ 6.97 keV are NGC 7469 and SWIFT J2127.4+5654, also in agreement with Miniutti et al. (2009). Residuals at ~ 6.7 keV are only found to be significant in two objects: Fairall 9 and Mrk 335 with improvements of $\Delta\chi^2 \sim 7$ and ~ 14 respectively.

With the aim of determining the extent to which emission from further in to the black hole is required, a broad component significantly improves the quality of the fit for most objects, typically $\Delta\chi^2 > 20$ for three additional free parameters and with line widths of the order $\sigma_{\text{Broad}} \sim 0.3$ keV. Only in MCG-02-14-009 does the addition of a broad Gaussian not make a particularly significant improvement ($\Delta\chi^2 \sim 3$). This is surprising given evidence to the contrary by Porquet (2006) in which a prominent broad and statistically significant iron line was found in a short 5 ks *XMM-Newton* observation with an equivalent width of $EW \sim 527_{-248}^{+277}$ eV whereas only $EW \sim 92_{-56}^{+59}$ eV is found here. However, the *XMM-Newton* observation was only 5 ks net exposure and as a result the Fe K line parameters are poorly constrained, while the *Suzaku* data also allow the broadband continuum to be better constrained (however, some variability between these two observations cannot be ruled out). In SWIFT J2127.4+5654, the lower equivalent width of the broad line may be due to the relatively high best-fitting value of the reflection component with $R = 2.5_{-0.8}^{+1.1}$ which may reduce the significance of a broad component. Mrk 335 features a relatively broad Gaussian with $\sigma_{\text{Broad}} = 0.50_{-0.11}^{+0.13}$ keV and $EW = 134_{-38}^{+42}$ eV, however, this feature is not as strong as the one found by Larsson et al. (2008) with $\sigma = 0.45_{-0.06}^{+0.10}$ keV and $EW = 250_{-39}^{+40}$ eV. Larsson et al. (2008) also find that the FeXXVI emission line does not improve the fit, however, an improvement of $\Delta\chi^2 \sim 8$ for three additional free parameters is found here with the introduction of a line at $6.98_{-0.14}^{+0.06}$ keV.

In general, the broad emission found in these objects is typically too strong

to be modelled as purely a Compton shoulder to the narrow 6.4 keV emission line despite the similarity of the line energy of the broad Gaussian with the first order Compton shoulder peak energy of ~ 6.24 keV (see Table B.1 on page 232). However, the possibility of a contribution from a Compton shoulder cannot be ruled out. Given the relatively high EW of the broad line component (mean $EW \sim 86$ eV) compared to the narrow core, the majority of the emission is likely to arise from a broadened component. Indeed the Compton shoulder is unlikely to contribute more than $\sim 20\%$ of the 6.4 keV core flux (e.g. George & Fabian 1991; Matt 2002). Note that the Compton shoulder is included in subsequent models through the use of a REFLIONX reflection component.

3.3.2 Model B – Self consistent distant reflection

In an attempt to build a more self-consistent model the PEXRAV and narrow 6.4 keV core are replaced with the REFLIONX ionised reflection model from Ross & Fabian (2005) which self-consistently includes emission lines in addition to the reflection continuum, see Table 3.2. Model B provides fits of a reasonable quality to all six spectra, however, it is not expected to improve upon Model A since it doesn't include a broad Gaussian to parameterise the red-wing of the $K\alpha$ line in an attempt to retain self-consistency and begin the construction of a more physically motivated model. Model B therefore acts as a 'null hypothesis' model in that all emission and reflection originates from distant matter. In most cases the fit statistic is somewhat worse than in Model A, except for Fairall 9, in which the quality of the fit is actually improved to $\chi^2_{\nu} = 864.7/834$, fit parameters for Model B are quoted in Table B.2 on page 234. The COMPTT model is still used here to model the soft excess in the four objects requiring it, however, the COMPTT parameters are not quoted in Table B.2 on page 234 and in subsequent table in Appendix B since the parameters obtained are consistent with those in Model A.

The narrow ionised emission lines at 6.7 keV and 6.97 keV found in Model A remain in Model B and following the removal of the broad component the significance

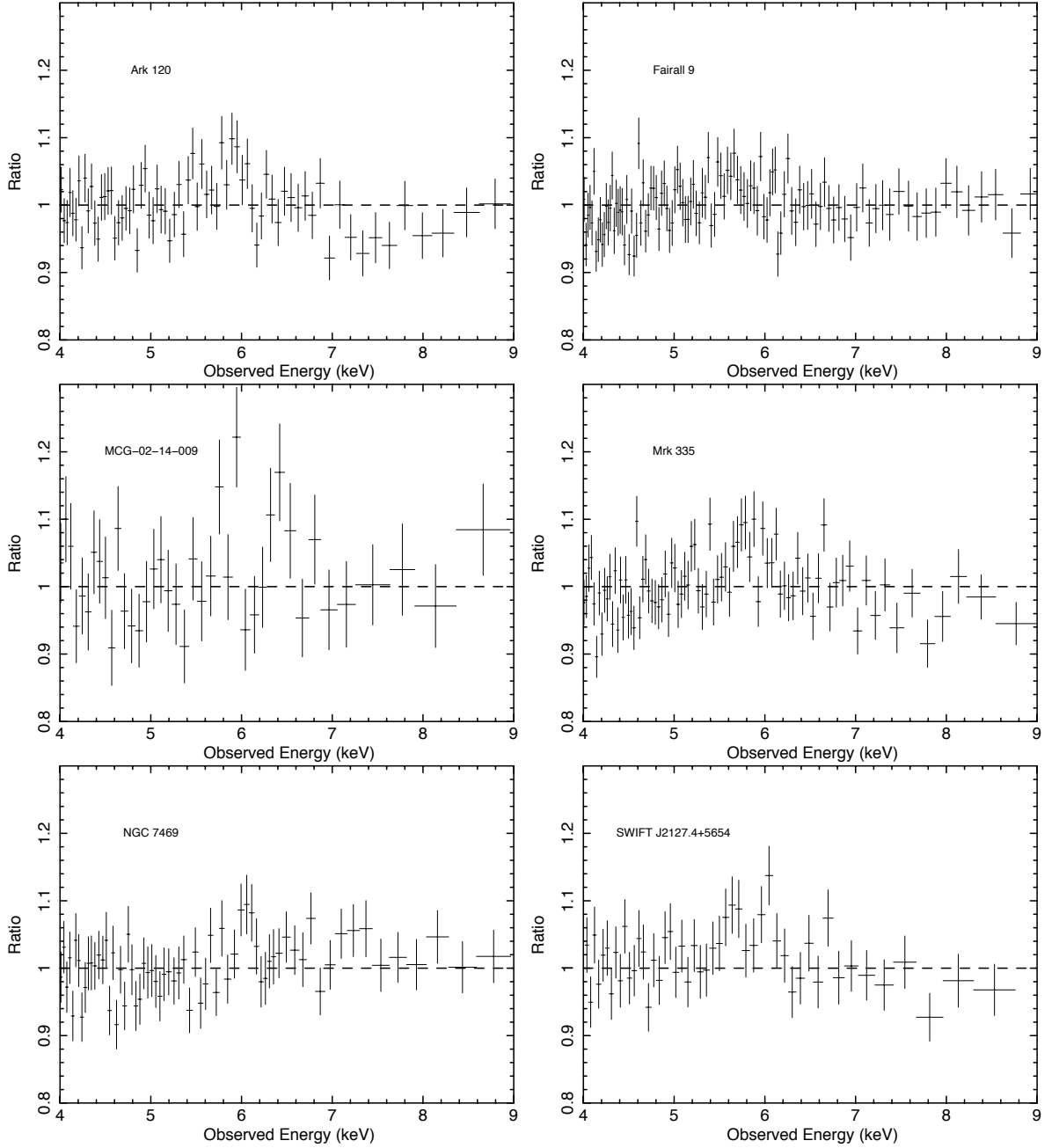


Figure 3.4: Ratio plots of Model B (i.e. without including a broad $\text{FeK}\alpha$ line) to the ‘bare’ Seyfert sample revealing excesses at energies red-ward of 6.4 keV in some objects. Model B consists of a POWERLAW + COMPTT (where required) + unblurred REFLIONX + narrow ionised lines as required, see Table 3.2.

of these lines is increased. In the case of SWIFT J2127.4+5654, for which there are no statistically significant ionised emission lines in Model A, there are small excesses at these energies, indeed suggesting the possible presence of these lines. Emission lines of high significance in Model A are also similarly significant in Model B, e.g. the FeXXVI in Fairall 9 is particularly prominent in both A & B. This is contrary to the analysis of Fairall 9 by Schmoll et al. (2009) in which they did not detect the FeXXVI line in the same *Suzaku* data, but they did however, detect the He-like FeXXV emission line which is also seen here in Models A and B.

All objects show some indication of at least a small red-wing (see Figure 3.4), noting that in MCG-02-14-009 this feature is not particularly strong and in all objects the red-wing does not extend below ~ 5 keV. A smaller than expected excess at energies red-ward of 6.4 keV is seen in Fairall 9, given the statistical significance of the broad Gaussian in Model A. This could be due in part to a relatively high Fe abundance as measured by the Fe/Solar parameter within REFLIONX at approximately twice the solar value. Some objects in the sample indicate a super-solar Fe abundance according to the REFLIONX component (see Table B.2 on page 234), however, the true abundance may in fact be lower than this measured value if part of the FeK α emission additionally arises from Compton-thin matter such as the BLR or NLR, i.e. in addition to the reflection component. A summary of the results obtained with Model B can be found in Table B.2 on page 234.

3.3.3 Model C – Laor profile

The possible presence of emission from close-in to the black hole has been indicated in the previous two models. In accordance with this, emission from the Fe K line region can be modelled with a relativistic component representing line emission from the accretion disc in addition to any appropriate emission from distant material (see Figure 3.4). As can be seen in Table 3.2, Model C advances upon Model B by remodelling the Fe K region with the addition of a LAOR line profile operating under the assumption of a maximally spinning black hole (Laor 1991; see also Section 2.5.6 in Chapter 2). This

model therefore allows for relativistic blurring and asymmetric line profiles from the inner regions of the accretion disc. The line energy was restricted to 6.4–6.97 keV in the rest frame, with emissivity, inclination and the inner radius of emission allowed to vary. The outer radius of emission was fixed at $400 R_g$ throughout. In the cases where the line emission reaches its lower limit it is fixed at 6.4 keV in the rest frame. Whilst giving a more feasible interpretation of the broad emission in the Fe K region it does not provide us with the most physically accurate representation given the assumption of a maximally rotating central black hole with $a = 0.998$ within the LAOR model, although allowing R_{in} to vary does relax this assumption and gives an estimate of the inner radius responsible for any broad Fe K α emission.

Not all of the objects in the sample will feature a maximally rotating black hole, indeed Fairall 9 and SWIFT J2127.4+5654 have previously been found to have intermediate spin values (see Schmoll et al. 2009; Miniutti et al. 2009). The presence of narrow ionised emission lines was reassessed after accounting for the blue-wing of the LAOR line profile. Employment of this model therefore seeks to further parameterise the broad emission in the Fe K region, providing suitable and plausible parameters for use in the later KERRDISK models.

The fit to all objects is improved over the purely distant emission in Model B. The 6.97 keV line is found to be present in all but NGC 7469 and SWIFT J2127.4+5654 whilst the 6.7 keV line is only found in Mrk 335 (although not formally required). Model C improves the fit to MCG-02-14-009 the least with only $\Delta\chi^2 \sim 14$ for three additional free parameters whereas the introduction of a LAOR profile offers a significant improvement for most other objects, particularly Fairall 9, Mrk 335 and SWIFT J2127.4+5654 ($\Delta\chi^2 \sim 33, 37$ & 34 respectively), see Table B.3 on page 235 for full model parameters.

None of the objects in the sample *require* emission from within $6 GM/c^2$ indicating that a rotating black hole, whilst possible, is not required to model the spectra. According to the fit parameters obtained with LAOR, the inner radius of emission lies at tens of R_g for all six AGN. In most cases the accretion disc is unlikely to be truncated at these distances from the black hole and it is likely that these values arise from the

assumption of a maximally rotating black hole within the LAOR model. The emissivity indices also indicate that a high concentration of emission from very close to the black hole is absent in the spectra from these AGN. An emissivity index of $q > 5$ would suggest that the emission from the accretion disc is very centrally concentrated (e.g. Miniutti et al. 2003), while for objects such as Mrk 335 and Fairall 9 this is within the error bars, one would also expect the inner radius of emission to be much closer to the black hole if this interpretation were suitable for the spectra. For the cases where the emissivity index cannot be constrained, it is fixed to $q = 3.0$ which is consistent with the other objects in the sample.

Mrk 335 appears to have one of the strongest relativistic lines in the sample with a LAOR profile equivalent width of $EW = 126_{-35}^{+33}$ eV, and an improvement of $\Delta\chi^2 \sim 37$. However, this is not particularly strong in comparison with previous studies of this AGN, for example Longinotti et al. (2007) find an $EW = 320_{-100}^{+170}$ eV at a line energy of $E = 6.93_{-0.27}^{+0.77}$ keV in a 40 ks *XMM-Newton* observation of Mrk 335 in 2000, also using a LAOR profile. The width of the iron line emission from the disc and its suggested high ionisation state could be due to the lack of a FeXXVI line in the Longinotti spectra (possibly due to low S/N), which has been accounted for in this analysis and is noted by O’Neill et al. (2007) in an analysis of an *XMM-Newton* observation use. Also in agreement with the results here, O’Neill et al. (2007) found the equivalent width of the broad line in Mrk 335 to be $EW = 115_{-14}^{+14}$ eV in comparison with $EW = 126_{-35}^{+33}$ eV for the LAOR profile and $EW = 113_{-52}^{+46}$ eV for the broad Gaussian employed in Model A.

The results obtained here are consistent with a recent analysis of Ark 120 by Nardini et al. (2011) who initially fit the features in the FeK region with a LAOR profile. In the Nardini et al. (2011) analysis, both the inclination of the accretion disk and emissivity are frozen at typical values of $i = 40^\circ$ and $q = 3.0$ respectively, finding an inner radius of emission of $r_{\text{in}} = 13_{-7}^{+19} r_g$. These values are consistent with those obtained here with Model C, finding $i^\circ = 34_{-5}^{+7}$, $q = 3.0_{-1.0}^{+1.6}$ and $r_{\text{in}} = 25_{-7}^{+19} r_g$. Also detected is the FeXXVI narrow ionised emission line, again consistent with Nardini et al. (2011).

As in Model A, there are no narrow ionised emission lines found in SWIFT

J2127.4+5654 corresponding to Fe XXV and Fe XXVI. This implies that the excesses modelled as narrow components in Model B may instead be due to relativistically broadened Fe K α emission. When modelled as a single LAOR profile all significant excesses in the Fe K band are removed with the profile centroid rest frame energy at 6.4 keV and the blue-wing peaking at ~ 6.7 keV in the rest frame. Consequently the observed excess at 6.7 keV observed in Model A and more significantly in Model B is more convincingly described as a blue-wing. Additionally, the observed intermediate feature in MCG-02-14-009 ($E \sim 6.6$ keV) is modelled well by the blue-wing of the LAOR profile which occurs at ~ 6.58 keV, prompting the removal of the previously employed narrow Gaussian. Thus, there is some degeneracy between the blue-wing of the LAOR diskline profile and narrow ionised emission above 6.4 keV.

3.3.4 Model D – Kerrdisk profile

Replacing the LAOR model with a KERRDISK line profile (Brenneman & Reynolds 2006) further allows a more physically motivated fit to the data. The KERRDISK model allows the spin parameter to be varied between $0 < a < 0.998$ with the aim of determining the extent to which a non-rotating or maximally spinning black hole is required. Similarly to Model C, the outer radius of the disc is fixed at $400 R_{\text{ms}}$ (i.e. the radius of marginal stability, $R_{\text{ms}} = R_{\text{ISCO}}$), while assuming a disc of a uniform emissivity profile. Throughout the fits using Model D the inner radius of emission is assumed to extend down to the innermost stable circular orbit (R_{ISCO}). The line energy is again confined to 6.4–6.97 keV in the rest frame, being frozen at 6.4 keV if it reaches its lower limit.

Model D provides good fits to all six objects, producing the best fitting physically motivated model for Mrk 335 and NGC 7469 prior to considering a blurred reflection component from the inner regions of the accretion disc (i.e. Models E & F), see Table B.4 on page 236 and Figure 3.5. The presence of ionised emission lines is entirely consistent with Model C, adding weight to the possibility that these lines are present in the spectra. Further to this, the inclinations of the accretion discs to the observer are all comparable to those obtained in Model C, as are the equivalent widths of the

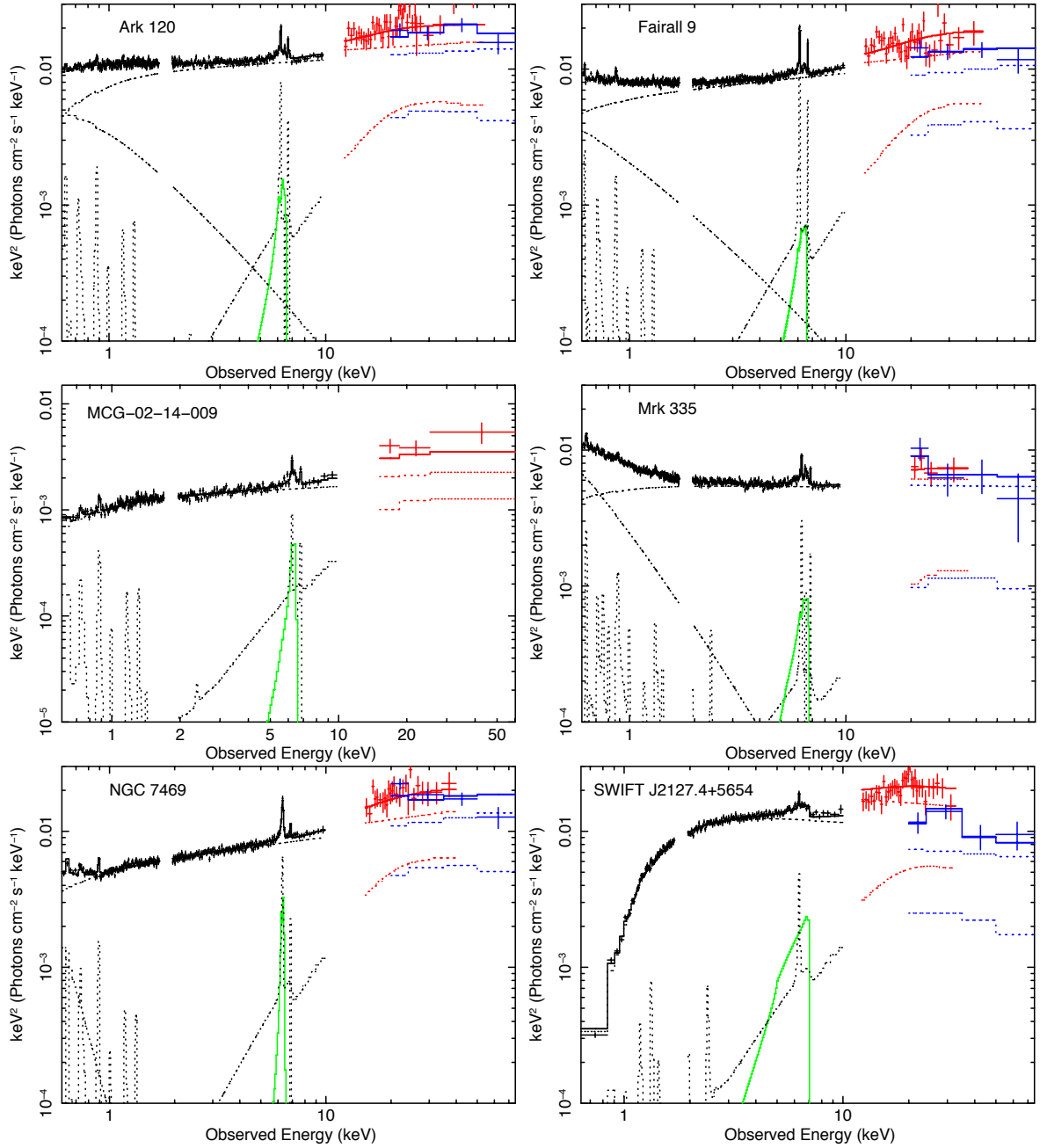


Figure 3.5: $\nu F\nu$ plots of Model D indicating the strength of any soft excess and relativistic line emission from the KERRDISK models. Consisting of POWERLAW + COMPTT (where required) + unblurred REFLIONX + KERRDISK + narrow ionised lines as required. XIS data is in black, HXD in red and BAT data is represented by blue circles. The solid green line represents the contribution to the model from the KERRDISK components.

relativistic line profiles. Given that the spin of the central black hole is a free parameter and the assumptions within this model, the emissivity indices are expected to vary from those obtained with the LAOR profile since the measured emissivity is degenerate to some extent with the inner radius of emission. Therefore, as the spin parameter varies so does R_{ISCO} , consequently affecting the measured q .

The results obtained from the spin parameter a for these six objects suggest that a maximally spinning central black hole can be ruled out at the 90% confidence level in some AGN, however, for some objects such as Ark 120 and MCG-02-14-009 the spin is unconstrained and only an upper limit can be measured ($a < 0.94$ and $a < 0.88$, suggesting that emission does not occur within $2.02 R_g$ and $2.45 R_g$ respectively, consistent with the Nardini et al. 2011 analysis of Ark 120).

Here, for Fairall 9, the best fitting model gives a measured spin value of $a = 0.44^{+0.04}_{-0.11}$. A previous spin constraint for Fairall 9 by Schmoll et al. (2009) found $a = 0.65^{+0.05}_{-0.05}$ using a blurred reflector model (KERRCONV, Brenneman & Reynolds (2006), convolved with REFLIONX). The measurement here also gives an intermediate value, however, it is only consistent with their findings when they ignore the spectra below 2 keV to ensure that the soft excess is not the component driving the main part of the fit. Schmoll et al. (2009) quote a worse spin constraint when these conditions are upheld $a = 0.5^{+0.1}_{-0.3}$. Within error bars at the 90% level these results are consistent with the value of the spin parameter found here. However, here the emissivity index is constrained to $q = 2.7^{+0.7}_{-0.4}$ whereas Schmoll et al. only constrain this to $q > 4.9$.

Mrk 335 has been noted previously as an object with a broad relativistic FeK line (Gondoin et al. 2002). Here an intermediate spin $a = 0.70^{+0.12}_{-0.01}$ is measured, ruling out maximally spinning and non-rotating black holes at the 95% confidence level. The emissivity index is measured at a moderate value of $q = 2.6^{+0.5}_{-0.3}$ in agreement with previous studies of this object, for example by Longinotti et al. (2007). In agreement with Model C, the KERRDISK component also features a relatively broad equivalent width $EW = 146^{+39}_{-39}$ with an improvement of $\Delta\chi^2 \sim 40$ (for four additional free parameters) over purely distant emission.

In NGC 7469 a broad Fe line is found featuring a low emissivity index of $q =$

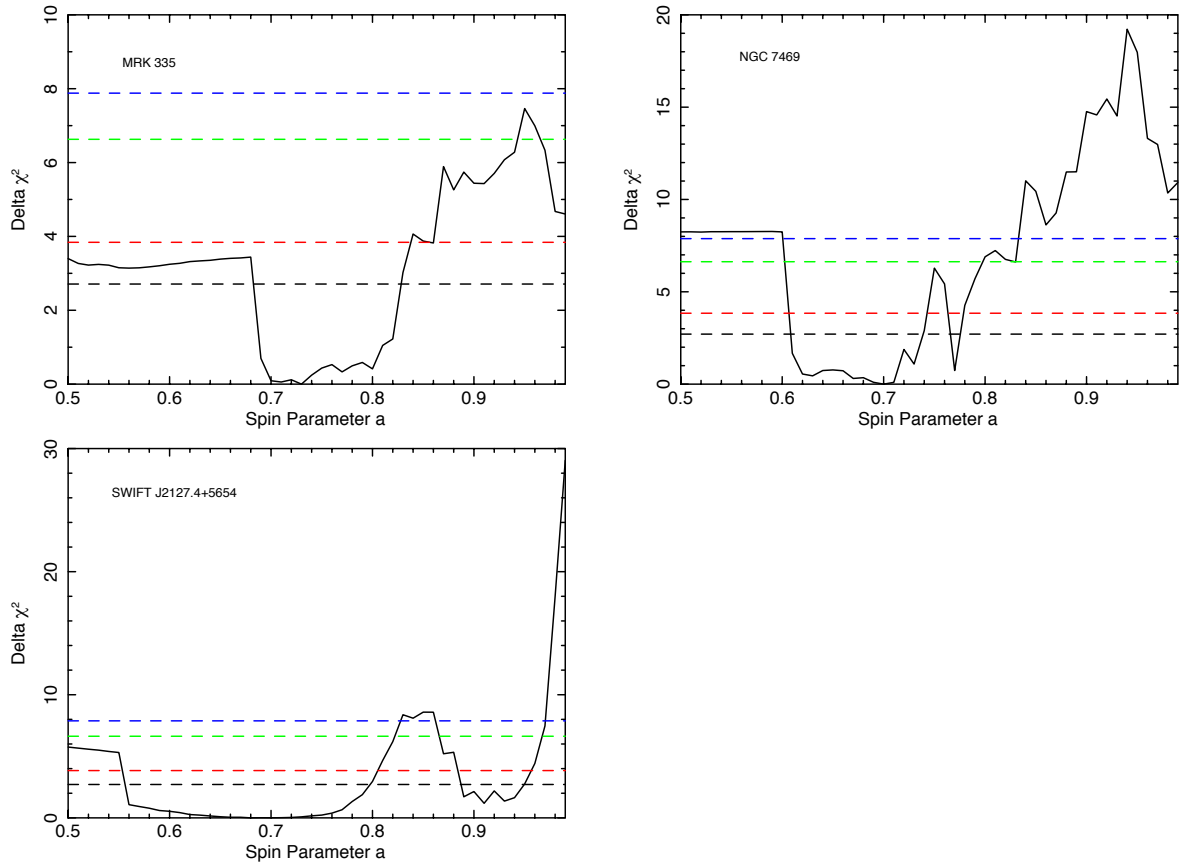


Figure 3.6: Confidence plots from Model D of $\Delta\chi^2$ versus the spin parameter a for those objects in which it could be constrained. Dashed lines representing 90% (black), 95% (red), 99% (green) and 99.5% (blue) confidence levels. Note that the emissivity index q is a free parameter.

$1.7_{-0.6}^{+0.4}$, an inclination of $i^\circ = 23_{-7}^{+15}$ and $EW = 91_{-8}^{+9}$ eV, providing good agreement with the previous measurements made within Model C. Subsequently a black hole spin of $a = 0.69_{-0.09}^{+0.09}$ is obtained, ruling out a Schwarzschild black hole with 95% confidence and a maximally rotating black hole at the 99% confidence level.

SWIFT J2127.4+5654 also shows a broad and statistically significant component, $EW = 178_{-69}^{+82}$ eV, improving the fit by $\Delta\chi^2 \sim 37$ (similarly to Model C) for four additional free parameters. The emissivity and the inclination of the accretion disc are typical of the objects in this sample. The spin parameter measured here is consistent

with that measured by Miniutti et al. (2009), $0.70_{-0.14}^{+0.10}$ compared to $0.6_{-0.2}^{+0.2}$ found using a blurred reflection model. Here a maximally rotating central black hole is rejected at greater than 99% confidence and a non-rotating black hole with 95% confidence. The spin constraints obtained with Model D for Mrk 335, NGC 7469 and SWIFT J2127.4+5654 can be seen in Figure 3.6.

3.3.5 Model E – Blurred reflector (1)

In contrast to the previous models, Model E does not include a contribution from the Comptonisation of soft photons (i.e. the COMPTT model). Alternatively, the excess seen at soft X-ray energies is modelled using a blurred reflector in addition to reflection consistent with distant emission. The ionised reflection model REFLIONX is convolved with a KERRDISK kernel, modelling a relativistically blurred reflection spectrum from the accretion disc originating from very near to the black hole instead of just the iron line via the KERRDISK model, i.e. the KERRCONV model (Brenneman & Reynolds 2006). The reflection components consist of: (REFLIONX + KERRCONV*REFLIONX). The assumptions in using this convolution model are consistent with those used in Model D, the inner radius of the accretion is assumed to extend down to R_{ISCO} and outer radius fixed at $400 R_{\text{ms}}$ for a disc of uniform emissivity. Narrow emission lines from ionised matter are also included where required, while the narrow 6.4 keV core is accounted for by the second unblurred REFLIONX component.

Model E is a significantly worse fit in all 4 AGN with a soft excess (by an average of $\Delta\chi^2 \sim 23$ compared to Model D), requiring a significant amount of blurring to account for the excess at low energies (see Table B.5 on page 237). Given the amount of blurring required, parameters such as the emissivity index and the spin parameter approach more extreme values for all objects with a soft excess (e.g. $q > 4$ and $a > 0.9$). Whilst Model E is a good fit to the data for Mrk 335 and NGC 7469, Model D provides a better fit and without the use of such extreme parameters.

In addition, the best-fit obtained with Model E for Ark 120 requires an inclination of $i = 48^\circ$, whilst not unreasonable, differs from the inclinations measured using Models

C & D. However, freezing the inclination at $i = 35^\circ$ worsens the fit further ($\chi^2_\nu = 824.6/648$ compared to $\chi^2_\nu = 770.2/647$). A similar dual-reflector fit as used here is considered by Nardini et al. (2011) in which the emissivity index is frozen at $q = 5.0$ compared to $q = 4.1^{+0.9}_{-0.9}$ measured here. Nardini et al. (2010) also note a relatively high inclination of $i^\circ = 57^{+5}_{-12}$ obtained in their analysis is likely too large for an object such as Ark 120 although it possible for the accretion disc and obscuring material to be misaligned. One area of disagreement between the results obtained with Model E and the Nardini et al. (2011) fit is the determination of the spin parameter. Nardini et al. finding $0.24 < a < 0.93$ whereas here only a lower limit of $a > 0.97$ is found, this may be due to the degeneracies between the spin and emissivity index which are both allowed to vary in Model E.

Similarly, NGC 7469 is best fit with a KERRCONV inclination parameter of $i^\circ = 70^{+4}_{-3}$ whereas Models C & D suggest that the disc is inclined at $i \sim 23^\circ$ to the observer, worsening the fit by $\Delta\chi^2 \sim 80$. These high inclinations are likely to be driven by the need to model the relatively smooth soft excess.

For the case of MCG-02-14-009, Model E provides an approximately equal quality of fit compared to Models C & D. No significant amount of blurring is required to model the spectrum, obtaining parameters similar to those previously, i.e. low emissivity and an unconstrained spin parameter. The narrow FeXXVI ionised emission line is also present, in line with findings from Models C & D. The SWIFT J2127.4+5654 spectrum is fitted very well with Model E ($\chi^2_\nu = 830.4/865$). Extreme parameters are not required to fit the data, which is in agreement with results from the previous diskline models. This may be due to the lack of any notable soft excess in these two objects. Since a significantly blurred spectrum simulates an excess at lower energies, a high emissivity and near maximally rotating black hole would provide an over-excess at soft energies, inappropriate for objects such as MCG-02-14-009 and SWIFT J2127.4+5654. Nonetheless Miniutti et al. (2009) find $q = 5.3^{+1.7}_{-1.4}$ in SWIFT J2127.4+5654 compared to $q = 2.2^{+0.6}_{-0.4}$ here, this may be due to the high level of Galactic absorption and the additional small amount of intrinsic absorption at the redshift of the source. An increase in the emissivity index could be compensated for by increased absorption

which is found in the Miniutti et al. (2009) analysis.

3.3.6 Model F – Blurred reflector (2)

Model F starts with Model B as the base model but instead blurring the single REFLIONX reflection spectrum with the KERRCONV convolution model to model any broad residuals present in the spectra, see Table 3.2. The Fe K line complex can still be modelled in this way since the REFLIONX model includes Fe K α emission and blurring the spectrum emulates the resulting profile from a KERRDISK model. Since the narrow Fe K α core included within REFLIONX is now relativistically blurred, a narrow Gaussian of fixed width 10 eV was added to ensure that the narrow 6.4 keV is still modelled. This may represent the case where the 6.4 keV line is observed from Compton-thin matter, such as the BLR or NLR. Contrary to Model E, the soft excess (where present) is modelled using the COMPTT soft photon Comptonisation model.

Any ionised emission due to FeXXV and FeXXVI required in Model D with KERRDISK is also found to be required in this model. In general a good fit to all objects is obtained, with Model F clearly providing a better fit to the data compared to Model E for Fairall 9, NGC 7469 and SWIFT J2127.4+5654, see Table B.6 on page 238. The KERRCONV parameters are also consistent within error bars with the emissivity index, inclination and spin parameter found using the KERRDISK line profile previously, yielding typically slightly lower emissivity indices.

Note that the best-fitting spin parameter value with Model F for Fairall 9 is $a = 0.40_{-0.40}^{+0.33}$ (quoted at the 75% confidence level and is unconstrained at the 90% confidence level) in agreement with $a = 0.44_{-0.11}^{+0.04}$ found in Model D (at the 90% confidence level) and with $a = 0.5_{-0.3}^{+0.1}$ found by Schmoll et al. (2009).

Given the independent modelling of the soft excess within this model, it is interesting to note that $a = 0.72_{-0.17}^{+0.18}$ is obtained for NGC 7469 at the 90% confidence level. This value of the spin parameter is in agreement with that found in Model D, although providing a slightly worse constraint.

3.4 Discussion of iron K emission in ‘bare’ Seyferts

This small sample of six AGN includes typically bare Seyfert 1 galaxies featuring little or no intrinsic absorption. This property of these AGN is important since the spectra of these objects is simpler to model without complicating factors (such as absorption) allowing the observer to draw conclusions about the fundamentals of accretion disc properties and basic features of the FeK region. These conclusions will therefore be less model dependent up on how the warm absorber is modelled (Turner & Miller 2009). It is important to effectively model the spectra of these AGN and assess the likely origin of various components of the spectrum before conclusions regarding more complicated AGN can be drawn. Modelling of the broadband continuum is also essential prior to analysis of the FeK region, this has been achieved using data from both HXD and BAT hard X-ray detectors onboard *Suzaku* and *Swift* respectively. Allowing the spectrum spanning 0.5–100.0 keV to be modelled with better constraints upon distant reflection components modelled by PEXRAV and REFLIONX, whilst maintaining effective modelling of the soft excess. This approach furthers that taken by Nandra et al. (2007) in which EPIC-pn data from *XMM-Newton* is analysed only in the 2.5–10.0 keV range.

The presence of narrow ionised emission lines due to FeXXV and FeXXVI assessed prior to modelling any broad residuals in the FeK region has an important effect upon the parameters obtained with broad diskline profiles. In some spectra neglecting to model these lines (if present) can accentuate any apparent broad FeK line, particularly those resulting from ionised species of Fe. Most commonly occurring in the objects analysed here is the 6.97 keV line from H-like Fe which is observed in all objects, except NGC 7469 and SWIFT J2127.4+5654. This is a surprising result given the rarity of such lines found by Nandra et al. (2007) in which only 2/26 sources showed evidence for these lines (although more common in work by Bianchi et al. 2009). This may be due to higher quality (longer exposure) data obtained with *Suzaku* allowing these lines to be more easily distinguished from broad residuals at these energies. Similarly, neglecting to include a narrow 6.97 keV emission line where present forces the relativistic line profile to have the emissivity index increased to particularly large values ($q > 6$)

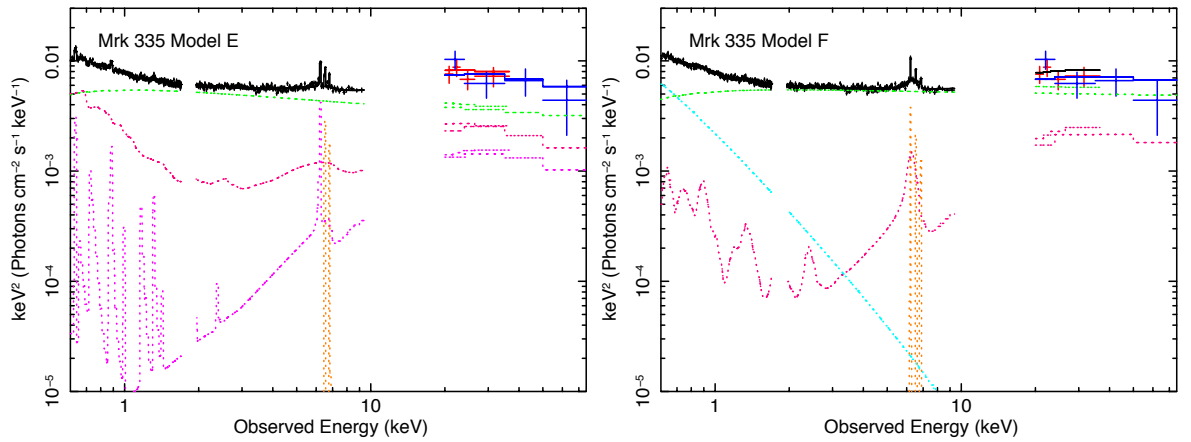


Figure 3.7: $\nu F\nu$ plots of Models E & F for Mrk 335 showing to degree to which relativistic blurring of the reflection component is required according to differing interpretations of the soft excess. Note that the significant blurring required in Model E to account for the soft excess reduces the accuracy of the fit to the Fe K region features. XIS data is in black, HXD in red and BAT is represented by blue circles. Components are as follows: power-law (green), COMPTT (light blue), REFLIONX (purple), relativistically blurred reflection (i.e. $\text{KERRCONV} \times \text{REFLIONX}$; pink), additional Fe K lines (orange).

and the inclination is slightly increased to $\sim 45^\circ - 55^\circ$ whereby the blue-wing of the profile is forced to model the narrow excess at ~ 6.97 keV.

In agreement with Nandra et al. (2007), however, is the rarity of the 6.7 keV line from He-like Fe which only features significantly here in Mrk 335. Models A & B earlier suggested the possible presence of Fe XXV in Fairall 9 and SWIFT J2127.4+5654, however, it was found that excesses at these energies coincided with the peak in the blue-wing of the relativistic line profile. This suggests that high (i.e. calorimeter) resolution data is necessary to determine the presence of this emission line particularly when employing a relativistic line profile, such as that which would be obtained with *Astro-H* (see Kelley et al. 2010).

The introduction of the KERRDISK model over a model considering emission purely from distant material (i.e. Model B) improves the fit to the six objects by an average of $\Delta\chi^2 \sim 20$. This implies that broad residuals are a statistically significant feature in all of these objects (although less so in MCG-02-14-009).

3.4.1 Accretion disc parameters and SMBH spin

The average inclination of the accretion disc to the observer as inferred by the KERRDISK line profiles in Model D is $i = 33^\circ \pm 4^\circ$, this is consistent with Nandra et al. (2007) who find $i = 38^\circ \pm 6^\circ$. Also from Model D, an average emissivity index of $q = 2.3 \pm 0.2$ is found, much lower than those used in previous work for some of these objects, e.g. Fairall 9 (Schmoll et al. 2009) and SWIFT J2127.4+5654 (Miniutti et al. 2009), particularly when using blurred reflection models to model the whole continuum. The line profile produced within Model D also suggests a broad line profile with an average equivalent width $EW = 119 \pm 19$ eV consistent with an average $EW = 91.3 \pm 12.8$ eV found by Nandra et al. (2007) using a Gaussian to model the broad residuals. Whilst here for Models C & D the centroid rest energy of the diskline profile is not allowed to extend below 6.4 keV in the rest frame, the basic parametrisation within Model A suggests an average broad component line energy of 6.29 ± 0.03 keV with $\sigma = 0.34 \pm 0.04$ keV compared to $E_{K\alpha} = 6.27 \pm 0.07$ keV and $\sigma = 0.34 \pm 0.05$ keV according to Nandra et al. (2007).

The low average emissivity index of the objects in this small sample may be due to a number of factors: independent modelling of the soft excess through a Comptonisation of soft photons; modelling of ionised emission lines where present in the data and the assumption that emission extends down to R_{ISCO} (the KERRDISK model). In accordance with this, within Models E & F facilitating the use of a blurred reflector, the average emissivity index is also dependent upon the way in which the soft excess is modelled. Model F (in which the soft excess is modelled with a COMPTT component, as in Models A–D) suggests an average $q = 2.0 \pm 0.1$ in general agreement with Model D. However, Model E (in which purely the blurred reflection component is tasked with modelling the soft excess) suggests an average $q = 5.0 \pm 0.7$ for those objects featuring a soft excess and an average $q = 2.0 \pm 0.4$ for those without, namely MCG-02-14-009 and SWIFT J2127.4+5654. Thus the high emissivity in Model E for some objects is driven by the need to fit a featureless soft excess, e.g. see Figure 3.7. A blurred reflection model with high emissivity therefore appears to be ruled out given Model E

produces a significantly worse fit in all 4 AGN with a soft excess. The high emissivity indices due to the treatment of the soft excess are evident in analyses by other groups, e.g. Mrk 335 (Gallo et al. 2013), Mrk 79 (Gallo et al. 2011), Ton S180 (Nardini et al. 2012 and in a sample of ‘bare’ AGN by Walton et al. 2013). Walton et al. (2013) also conducted an analysis of a sample of ‘bare’ Seyfert 1 AGN with results consistent with the conclusion drawn from Model E here, i.e. a reflection dominated approach resulting in highly centrally concentrated emission (high q) and SMBH spin distribution heavily skewed towards $a \sim 0.998$. This is discussed further in Section 6.2.6.

Model C alternatively models reflection off a relativistic accretion disc under the assumption of a maximally rotating central black hole, without the inner radius of emission fixed at the ISCO. This approach also suggests a similarly relatively small equivalent width of $EW = 102 \pm 14 \text{ eV}$ and an average emissivity $q = 3.2 \pm 0.4$ (for those objects for which the emissivity could be constrained), higher than that derived from Model D and likely due to the fact that R_{in} is not fixed at R_{ISCO} . The average inclination of the accretion disc is also very similar to Model D above with $i = 34^\circ \pm 3^\circ$. Given the assumptions made within this model, the inner radius of emission is found to originate at tens of R_g rather than $< 6 R_g$ at an average $R_{\text{in}} = 39 \pm 8 R_g$. Indeed, in Ark 120, Fairall 9 and MCG-02-14-009 Model C and this interpretation of the accretion disc and SMBH provides a marginally better fit. However, given the degeneracies between q , a and R_{in} it would be impossible to reasonably constrain any of these values without assumptions similar to those mentioned above. Nonetheless, generally the results tend to suggest that the iron K emission is not extremely centrally concentrated, suggesting either that broad emission occurs from typically tens of R_g or that emissivity profiles are flat.

3.4.2 Towards the origin of the soft excess

The results for determining the spin of the central black holes of the AGN in this sample suggest that the spin derived is very much dependent upon which interpretation of the FeK line region is followed. Modelling the soft excess through an independent model

such as COMPTT tends to yield low to intermediate spin constraints for the objects in this sample, the exceptions being Ark 120 and MCG-02-14-009 in which only an upper limit could be placed. The employment of this interpretation also yields low to intermediate emissivity indices for the accretion discs (i.e. $q \sim 2$). Modelling the 0.5–100.0 keV spectrum with a blurred reflection component and no other modelling of the soft excess (i.e. Model E) gives particularly high values of both emissivity index and spin parameter, typically $q >$ and $a > 0.9$, but these fits are ruled out here on statistical grounds.

This is, however, only in objects featuring a soft excess. In MCG-02-14-009, which has no obvious excess over a power-law at low energies, the derived parameters are very similar throughout Models D, E & F. Similarly for SWIFT J2127.4+5654, the parameters obtained with these three models are all consistent and indeed the resulting spin parameter is also consistent with previous findings by Miniutti et al. (2009) although they find a much higher emissivity index is required ($q = 5.3_{-1.4}^{+1.7}$ compared to $q = 2.2_{-0.9}^{+0.3}$ from Model E).

As discussed previously, the spin constraint obtained here for Fairall 9 agrees with that found by Schmoll et al. (2009), but only in the case where they ignore the spectrum below 2 keV ($a = 0.5_{-0.3}^{+0.1}$ compared to $a = 0.44_{-0.11}^{+0.04}$ found here in Model D). According to Model D, an intermediate spin of the central black hole within NGC 7469 is found, with $a = 0.69_{-0.09}^{+0.09}$. This is also consistent with that found within Model F $a = 0.72_{-0.17}^{+0.18}$, suggesting that the spin of this object is indeed $a \sim 0.7$.

The relatively constant temperature of the soft excess versus BH mass from studies of various AGN (e.g. Gierliński & Done 2004) suggests that it may not arise from direct thermal emission from the accretion disc, since the accretion temperature properties should scale with $M_{\text{BH}}^{-1/4}$ in a standard accretion disc (see Section 1.2) for direct disc emission although this does not take into account the Comptonisation of disc seed photons. An atomic origin of the soft excess has been suggested, however, no obvious spectral features are seen in high resolution data (e.g. Gondoin et al. 2001; Emmanoulopoulos et al. 2011) meaning that if atomic emission is responsible it must be significantly relativistically blurred such as here in Model E (Ross, Fabian &

Ballantyne 2002; Fiore, Matt & Nicastro 1997). Although if this is the case it must be to the extent that the spin estimates made with a blurred reflector (to model the soft excess) are inconsistent with those obtained from a broadened line profile in the Fe K region, e.g. KERRDISK fits from Model D suggest low/ flat emissivity profiles. Whilst in this Chapter the aim is not to determine the physical origin of the soft excess, a simple parameterisation of the soft excess continuum through a model such as a Comptonised disc spectrum via COMPTT provides a better fit to the spectra than an atomic origin from a highly blurred reflection component.

A recent publication by Walton et al. (2013) conducts an analysis of 26 ‘bare’ Seyferts which have been observed with *Suzaku*, although they note that six of these objects do show evidence for ionised absorption at soft X-ray energies which is modelled with an appropriate XSTAR grid, therefore they are not *strictly* ‘bare’. The authors note that a purely reflection origin for the soft excess is assumed throughout while also requiring that the emissivity is $q > 3$ which is justified by the assumption that emission is centrally concentrated, noting that if emission arises from the very inner regions of the accretion disc it will be subjected to general relativistic light bending and time dilation (Miniutti & Fabian 2004; Wilkins & Fabian 2011).

Walton et al. (2013) find that in the vast majority of these AGN rapidly spinning SMBHs are found resulting in a highly skewed spin distribution towards $a \sim 0.998$. However, based upon the results in Chapter 3, this is to be expected when assuming a blurred atomic origin of the soft excess, see Section 1.5.4. The high disc ionisations, steep emissivity profiles, maximal spin and high inclinations all point towards a blurred reflector geometry which is being forced into a smooth soft X-ray continuum to model the strength of the soft excess. It should be noted that of the objects in the Walton et al. (2013) sample, the objects which do not feature a soft excess typically do not have spin estimates placed upon them, i.e., the Fe K region is not being fitted such that a relativistically broadened line profile does not facilitate the estimation of accretion disc and SMBH spin parameters. The SMBH spin estimates made by Walton et al. (2013) are therefore only valid if blurred reflection alone is responsible for the soft excess. If there is any contribution from a reprocessed thermal component in a corona above the

disc, as is popularly believed (see Porquet et al. 2004; Dewangan et al. 2007; Lohfink et al. 2013; Noda et al. 2013 etc), then the high spin estimates and accretion disc properties presented in Walton et al. (2013) will be significantly altered, leading to results which may then be consistent with the work presented in Chapter 3 and Patrick et al. (2011a).

4 Analysis of deep *Suzaku* observations

Gaining information regarding the spin of supermassive black holes (SMBHs) in active galactic nuclei (AGN) is essential in order to understand some of the fundamental mechanisms for powering radio jets, galaxy evolution and AGN merger histories. For example, it is thought that the spin of the SMBH may be related to powering relativistic jets and it is therefore important to begin to assess the differences between radio-loud and radio-quiet AGN (e.g. Wilson & Colbert 1995) and the intrinsic properties of the SMBH and its accretion disc. Similarly, the distribution of SMBH spin or the 'average' spin could be an essential tool for distinguishing between various galaxy evolution models (Hughes & Blandford 2003; Volonteri et al. 2005; King & Pringle 2007; Rezzolla et al. 2008). Prolonged accretion could result in a large fraction of BHs having a high degree of spin, however, if the majority of AGN have more intermediate or low BH spin then spin-alignment during mergers could be the mechanism responsible for spin-ups or the Blandford-Znajek effect (the magnetic extraction of BH rotational energy; Blandford & Znajek 1977) could cause the reduction of BH spin in many AGN (Berti & Volonteri 2008).

The properties of the SMBH and the surrounding accretion disc can be measured through the analysis of the X-ray spectrum of AGN since line emission occurring from close to the black hole can become relativistically broadened (Fabian et al. 1989; Laor 1991). The shape of such a line profile allows properties such as the emissivity and the inclination of the disc to be determined, in addition to the typical inner radius of emission and the spin of the central black hole (Dovčiak et al. 2004; Brenneman & Reynolds 2006; Dauser et al. 2010). These signatures of emission from close to the black hole are most prominent in the neutral FeK α line at 6.4 keV due to the high abundance and fluorescent yield of iron. In order to make the required measurements (particularly BH spin), a robust broad-band spectral model must be formed in order to assess the contribution (if any) of relativistically broadened line emission.

Recent publications have gone some way towards making tentative spin measure-

ments in AGN through the analysis of Seyferts lacking significant amounts of intrinsic absorption (Miniutti et al. 2009; Schmoll et al. 2009; Patrick et al. 2011), or the analysis of deep observations of more complex AGN (Brenneman & Reynolds 2006; Brenneman et al. 2011; Gallo et al. 2011). As noted in Patrick et al. (2011), the interpretation as to the origin of the soft excess can influence the obtained accretion disc parameters and BH spin. Employing a relativistically smeared reflection spectrum from the inner regions of the accretion disc (e.g. an ionized disc reflection spectrum convolved with a Kerr metric; Ross & Fabian 2005; Brenneman & Reynolds 2006) to model both the soft excess and broadening in the Fe K region yields results in which the measured parameters differ significantly when they are obtained from either the soft excess or Fe K region. This is particularly notable in AGN with a strong soft excess, in which case the soft excess is the driving force behind the fit, often leading to typically high spin and emissivity values, i.e. $a > 0.90$ and $q > 4.5$. As the soft excess is often smooth or featureless, a very high degree of blurring is required.

Alternatively employing a Comptonisation origin of the soft excess (Titarchuk 1994) and separately measuring these parameters purely from the observed line profile in the Fe K region yields a more moderate emissivity index and a range of spin values akin to the results found in objects without an observed soft excess, i.e. $0 < a < 0.998$ and $q \sim 2.3$ (Patrick et al. 2011a). It is therefore essential that high quality data sets and deep exposures are used in order to distinguish between these scenarios and measure the true accretion disc parameters independently.

Having conducted an analysis of the ‘bare’ Seyfert 1 AGN in Chapter 3 and Patrick et al. (2011a), it is intuitive that the deep observations of AGN will provide the next best opportunity to place estimates upon SMBH spin and the origin of the soft excess. Since the X-ray spectra of those AGN which feature intrinsic absorption are complex, long observations of these AGN provide the high number of counts required in order to examine the broadband spectrum in detail. That is, the X-ray continuum and any warm absorption or partial covering geometries which may be present in these AGN can be modelled as accurately as possible with the data currently available from the archive. In combination with the results from Chapter 3, the vast majority of the

Seyfert 1 AGN with a reasonable opportunity for estimating SMBH spin will have been analysed.

The results and analysis in this chapter are based upon those presented in a lead-author paper Patrick et al. (2011b).

4.1 The deep observation sample

The objects included within this sample are listed in Table 4.1 and are all the Seyfert 1, radio quiet AGN with exposures > 200 ks which have been observed with *Suzaku* with data publicly available in the *Suzaku* data archive¹ as of September 2010. The objects in this sample are also all nearby with redshift $z < 0.05$. High energy X-ray data from the 58 month *Swift*/BAT catalogue (Baumgartner et al. 2010) is also used in addition to that obtained from the HXD detector onboard *Suzaku* (allowing the cross-normalisation to vary), therefore the total energy range covered is 0.6-100.0 keV. Further details of the observations included are listed in Table A.1 on page 224. The following observations are analysed: the 2010 observation of Fairall 9 (Obs. ID: 705062010), 2006 observations of MCG-06-30-15 (Obs. IDs: 700007010, 700007020, 700007030), 2009 observation of NGC 3516 (Obs. ID: 704062010), 2009 observation of NGC 3783 (Obs. ID: 704063010) and 2008 observation of NGC 4051 (Obs. ID: 703023010). NGC 4051 has been observed on three occasions with *Suzaku*, only the long November 2008 observation is included here, however, Lobban et al. (2011) conducted an analysis of all three simultaneously. The long 2010 *Suzaku* observation of NGC 1365 is excluded from this sample due to its similarities with Seyfert 2 AGN, i.e., due to its high degree of obscuration (Maiolino et al. 2010).

In this analysis, the spectrum is first fitted at soft X-ray energies and include any absorbing components which may be required by the data prior to assessing the remaining residuals in the FeK region which may be representative of diskline emission. By

¹<http://heasarc.gsfc.nasa.gov/>

Table 4.1: The *Suzaku* Seyfert sample. Galactic column density is given in units 10^{22}cm^{-2} . Note that the exposure time listed for MGC–06-30-15 is the total exposure for the three January 2006 observations, for more details see Table A.1 on page 224.

Object	RA (J2000)	Dec (J2000)	Redshift	N_H (Gal)	Date	Exposure
Fairall 9	01 23 45.8	−58 48 21	0.0470	0.0316	26/08/10	229 ks
MGC–6-30-15	13 35 53.8	−34 17 44	0.0077	0.0392	09/01/06	338 ks
NGC 3516	11 06 47.5	+72 34 07	0.0088	0.0345	29/10/09	251 ks
NGC 3783	11 39 01.7	−37 44 19	0.0097	0.0991	10/07/09	210 ks
NGC 4051	12 03 09.6	+44 31 53	0.0023	0.0115	06/11/08	274 ks

taking a balanced approach over a broad bandpass the effects of warm absorbers upon the FeK region can be determined in an attempt to discover if these broad residuals remain. Only after modelling for absorbers are any models which may be representative of emission from the inner regions of the accretion disc included.

This analysis of the deep observations sample therefore aims to assess the strength or indeed even the presence of diskline emission in the FeK regions of these objects. Through modelling of absorption zones where they are required and the application of a variety of models and interpretations, the degeneracies involved with measuring such parameters can be investigated and hence estimates can be placed upon BH spin and accretion disc properties where possible. An analysis of these objects is performed by testing models both with and without a partial covering absorption component in order to assess the effect of the partial covering absorber on the iron line parameters. In later analysis (Section 4.2.3), only after modelling the absorption, are dual reflector models used, i.e., an inner (blurred) and outer (unblurred) reflector from distant material in an attempt to estimate accretion disc and SMBH parameters.

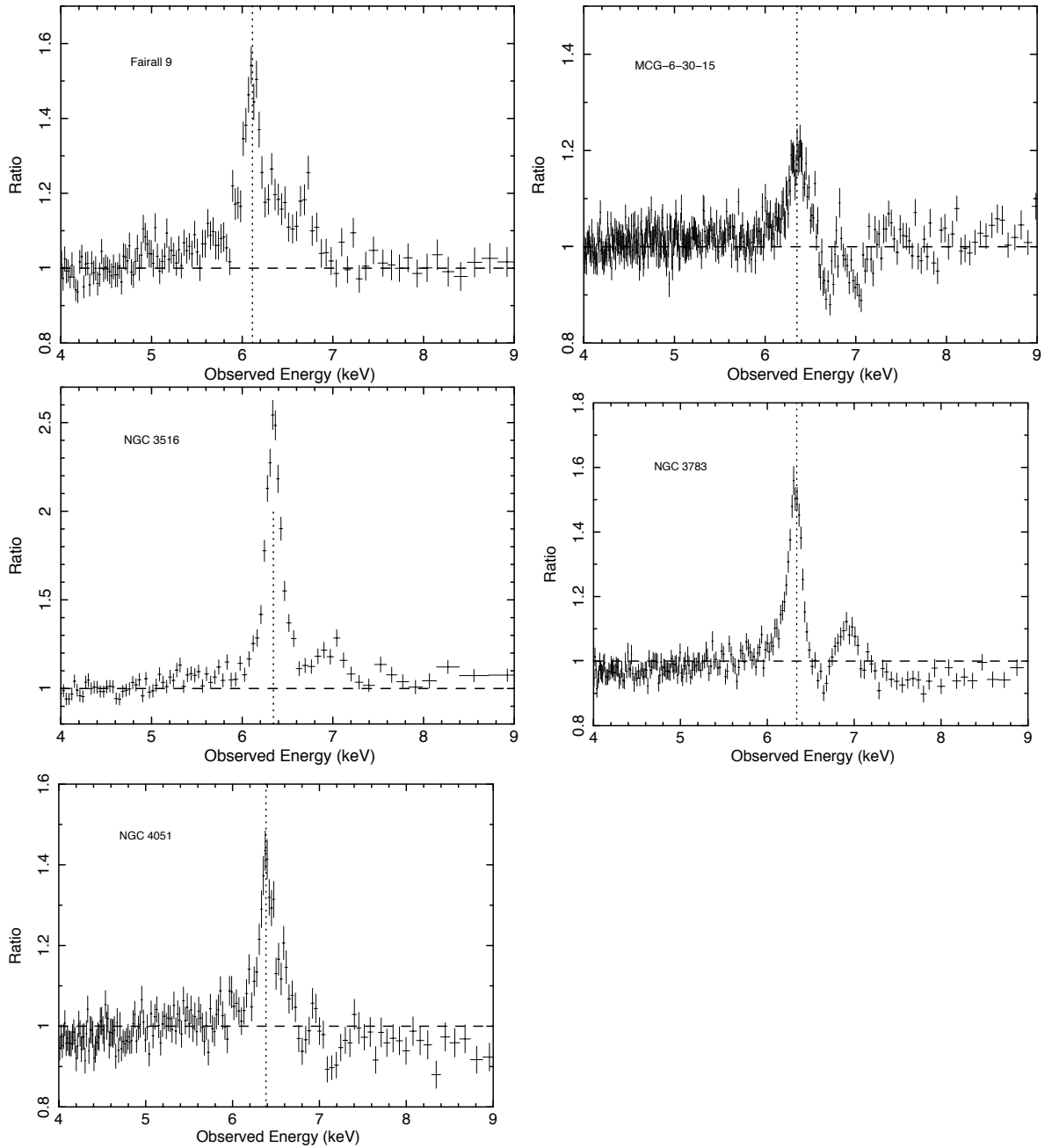


Figure 4.1: Data/ model ratio plots of the 4-9 keV residuals for the five deep observations without any modelling of the reflection component, i.e. the Fe K region is left totally unmodelled. The 0.6-100 keV continuum is modelled with a power-law and including warm absorption at soft X-ray energies with the soft excess taken into account through COMPTT (where required). The vertical dashed lines represent 6.4 keV in the observed frames.

4.2 Deep observation results

4.2.1 Initial parameterisation and baseline model

An initial parameterisation of the spectra is made in order to assess properties such as the strength of the reflection continuum and the strength of any emission or absorption features which may be present in the FeK region. It should be noted that all objects in this sample (with the exception of Fairall 9, the shorter observation discussed in Chapter 3) feature complex intrinsic absorption components. Once these basic components have been established, resulting in a reasonable fit to the data, the FeK region can then be assessed as to the presence of any additional features such as the broad iron line. For example, narrow emission lines such as neutral FeK α , He and H-like FeXXV and FeXXVI or indeed the need for a highly ionised absorption zone at FeK energies (see Reeves et al. 2004 for FeXXV absorption in an *XMM-Newton* observation of NGC 3783) which may be required to model the FeK region. A Comptonisation origin of the soft excess is again assumed unless stated otherwise, using COMP_{TT} with a soft photon input temperature fixed at 0.02 keV, see Sections 1.5.4 and 3.3.1 for more details on the modelling of the soft excess.

The broadband spectra are first parameterised in a similar manner as per the ‘bare’ Seyferts in Chapter 3 with a power-law component adopted to account for the underlying X-ray continuum. The strength of the reflection component is initially measured using the PEXRAV neutral reflection model (Magdziarz & Zdziarski 1995) with the reflection fraction $R = \Omega/2\pi$ left free to vary. The cut-off energy for the PEXRAV component is fixed at 300 keV for consistency with the built-in cut-off in the later used REFLIONX model (similarly the power-law cut-off is fixed at 300 keV) and $\cos i = 0.87$ throughout. Narrow Gaussians of fixed width (10 eV) are added where appropriate to model neutral and ionised emission or absorption features. FeK β emission at 7.056 keV is accounted for with fixed line energy and flux $F_{K\beta} = 0.13 \times F_{K\alpha}$. The flux of the FeK β component measured was later fixed and carried forward into later models since it is not included within the REFLIONX model (Ross & Fabian 2005).

Any broad residuals in the FeK region are initially modelled using a broad Gaussian with σ width free to vary.

Additional narrow soft X-ray emission lines (such as O VII, O VIII etc from distant photoionised gas as frequently detected in high resolution observations of Seyferts, e.g. see Krongold et al. 2007; Lobban et al. 2011) are added on an ad-hoc basis where required, again with fixed width $\sigma = 0.01$ keV. The warm absorber component is treated with successive zones of an XSTAR grid added as statistically required, see Section 2.5.3 more for details. As expected from previous studies of these objects, MCG–6-30-15, NGC 3516, NGC 3783 and NGC 4051 all require at least one ionised soft X-ray absorption zone (e.g. Reeves et al. 2004; Markowitz et al. 2008; Miller, Turner & Reeves 2009; Lobban et al. 2011). In Fairall 9, however, the Galactic line-of-sight absorption is sufficient to describe the total absorption at soft X-ray energies as discussed in Chapter 3. The warm absorber in these objects (with the exception of Fairall 9) may indeed be more complex than modelled here in higher resolution grating data, although the main aim is to derive and measure black hole and accretion disc properties from the FeK region, given a consistent model to the broadband *Suzaku* data. The parameters obtained during this initial parameterisation are listed in Table C.1 on page 239.

Subsequently, the baseline model is intended to model the entire 0.6-100.0 keV range in full to account for features such as any soft or hard excess which may be present in a more self consistent manner than in the initial parameterisation. For example, by replacing PEXRAV with REFLIONX to model reflection and using high ionisation XSTAR grids to model absorption in the FeK region instead of Gaussians. This baseline model does not, however, include any components which may be representative of emission occurring from regions close to the central black hole, i.e. any broadened lines or observed red-wing are left unmodelled for the purposes of this first step. This represents a null hypothesis whereby all emission and absorption is distant from the central SMBH. Once the baseline model has been parameterised next step is to examine the nature of the residuals in the FeK region and the strength of any broad red-wing indicative of emission from the inner regions of the accretion disc.

Initially the modelling of these individual AGN is discussed before discussing

these deep observations in a broader context:-

4.2.1.1 Fairall 9

Fairall 9 is well modelled using an approach similar to that used in Patrick et al. (2011a) and Chapter 3, consisting of COMPTT to model the soft excess plus power-law and an unblurred REFLIONX to account for distant reflection without the need for any intrinsic absorption. The broadband spectral properties in this long observation are very similar to those in the shorter 2007 observation, however, the initial parameterisation measures a reflection fraction of $R = 1.55_{-0.24}^{+0.26}$ compared to $R = 0.52_{-0.18}^{+0.20}$ in the previous 2007 observation. A broad Gaussian improves the fit to the FeK region by $\Delta\chi^2 \sim 13$ and with parameters which are consistent with Patrick et al. (2011a), see Table C.1 on page 239 and Figure 4.2. As a consistency check, fitting both the 2010 and 2007 observations simultaneously and allowing the reflection fraction and intrinsic power-law to vary gives consistent results with both analyses and a smaller difference between the reflection fractions for each observation. Forcing the power-law slope Γ to be the same in both observations provides a good fit to the XIS spectra of both observations with the majority of the residuals remaining in the fit to the HXD/PIN data.

Due to the increased signal-to-noise in this observation, an additional narrow emission line due to O VIII Ly α is observed at $0.66_{-0.02}^{+0.01}$ keV with an improvement to the fit by $\Delta\chi^2 \sim 35$ for a further two free parameters. However, since the REFLIONX model includes some soft X-ray emission lines, in this high quality data it is these lines which appear to determine the obtained reflection parameters and are therefore detrimental to the overall fit. In particular the hard X-ray data from the HXD is poorly fit. In order to resolve this issue, a neutral absorber at the redshift of the source ($z = 0.047$) is included to only absorb the soft X-ray emission lines included within REFLIONX. This results in an improvement of $\Delta\chi^2 \sim 109$ in the overall fit with column density $N_{\text{H}} = 39.59_{-6.19}^{+8.11} \times 10^{22} \text{ cm}^{-2}$. Whilst this combination of ZPHABS*REFLIONX may not be entirely physical in its origin, it is consistent with being an artifact due to the nature of the publically available REFLIONX model not extending down to neutral ionisations.

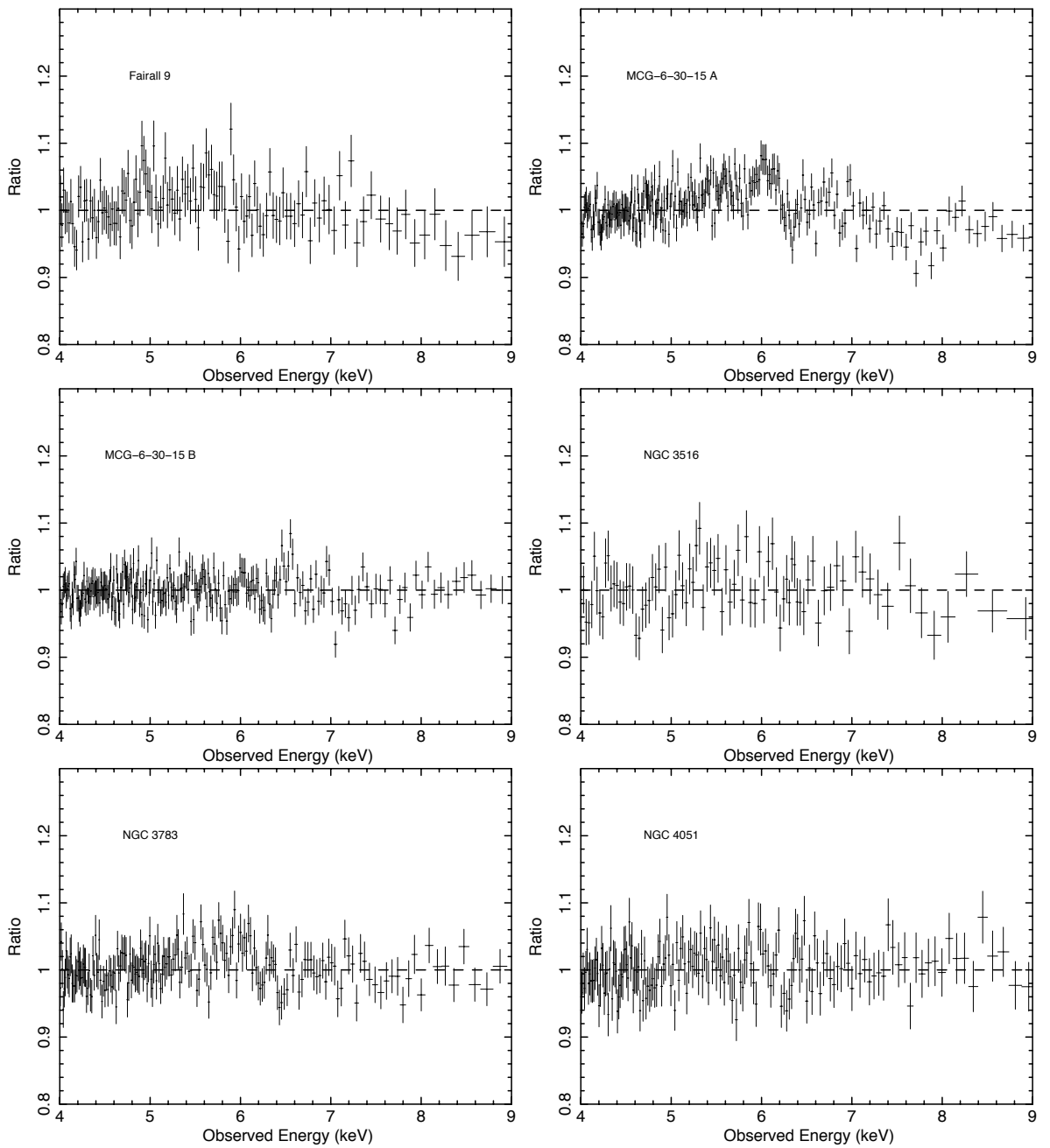


Figure 4.2: Ratio plots of the XIS-FI spectra to the baseline model (see Table C.2 on page 241, without including a broad $\text{FeK}\alpha$) revealing excesses at energies red-ward of 6.4 keV in some objects. Plot ‘MCG-6-30-15 A’ shows the residuals to the Fe K region without the use of a high column partial covering component, plot ‘MCG-6-30-15 B’ shows the residuals of the complete baseline model including the partial coverer. Note that the high column partial coverer significantly reduces the strength of the red-wing in MCG-6-30-15.

This is confirmed by the initial parameterisation of the reflection component using the PEXRAV neutral reflection model which does not include any additional atomic emission. This alternative is successful in achieving a good fit to the continuum and HXD data without the need for an additional absorption component. In an attempt to remain consistent between the baseline models for each object, the ZPHABS*REFLIONX configuration is retained. Prior to including any diskline-type models indicative of relativistic emission, ionised narrow emission lines which may result from FeXXV and FeXXVI are found at $6.68^{+0.03}_{-0.01}$ keV and $7.00^{+0.05}_{-0.05}$ keV respectively (see Table C.2 on page 241). These lines were also found in the shorter 2007 observation of Fairall 9 (Schmoll et al. 2009; Patrick et al. 2011a) with consistent energy and *EW*.

4.2.1.2 MCG–6-30-15

In this analysis the time averaged spectrum of MCG–6-30-15 is used during the January 2006 observations, a preliminary analysis reveals that the derived FeK region parameters are consistent for all three observations and as such they are co-added as per Miniutti et al. (2007). Most apparent is the presence of both a small soft and a hard excess in addition to the requirement for some degree of warm absorption. A very poor fit to the data is found without any warm absorption with the fit worsening by $\chi^2_\nu > 60$. A single low column ($N_{\text{H}} \sim 7.5 \times 10^{21} \text{ cm}^{-2}$, $\log \xi \sim 1.6$) warm absorption zone improves the overall fit to $\chi^2_\nu \sim 3.2$. A second low column ($N_{\text{H}} \sim 2.4 \times 10^{21} \text{ cm}^{-2}$) ionised absorption zone improves the fit by $\Delta\chi^2 \sim 1284$ to $\chi^2_\nu \sim 2.5$ with the absorption zones having ionisations of $\log \xi \sim 0.96$ and $\log \xi \sim 1.94$.

In order to parameterise the reflection in MCG–6-30-15, initially the PEXRAV neutral reflection model is used. This yields a reflection fraction of $R = 0.79^{+0.12}_{-0.08}$ with a good fit to the HXD and BAT data. This then allows the measurement the strength of features in the complex FeK region prior to employing a more self-consistent reflection model such as REFLIONX. There is strong neutral FeK α emission and what may be ionised FeXXV emission improving the fit by $\Delta\chi^2 \sim 331$ and ~ 51 respectively (see Table C.1 on page 239); it is, however, possible that the ionised feature may

be the blue-wing to a broadened FeK line profile. There is also ionised FeXXVI emission found which is fixed at 6.97 keV throughout the fits. In addition to this, two ionised absorption features at $6.76_{-0.02}^{+0.02}$ keV and $7.05_{-0.02}^{+0.02}$ keV (see Figure 4.1) are very clear in the FeK region and are indicative of the presence of an outflowing highly ionised absorber (as also found in a *Chandra* HETG observation of MCG–6-30-15 by Young et al. 2005). Subsequent to modelling these narrow features there is still a relatively poor fit to the data ($\chi^2_\nu \sim 1.3$), however, there are strong residuals remaining extending from ~ 5.0 – 6.4 keV. Including a broad Gaussian to model this feature results in a line centred at $5.93_{-0.14}^{+0.07}$ keV with $\sigma_{\text{width}} = 0.84_{-0.06}^{+0.06}$ keV and $EW = 149_{-9}^{+21}$ eV, improving the fit substantially by $\Delta\chi^2 \sim 302$ to $\chi^2_\nu \sim 1.15$. Previous analyses of this object restricted to energies > 3 keV found a much stronger broadened iron line, for example Miniutti et al. (2007) find consistent line energy and σ_{width} with red-wing line centroid energy of $5.38_{-0.10}^{+0.10}$ keV and $\sigma_{\text{width}} = 0.84_{-0.08}^{+0.07}$ keV although with a much higher cumulative equivalent width of $EW = 320_{-45}^{+45}$ eV in an analysis of the same time averaged data used here (note that in Miniutti et al. 2007 this feature is modelled with a ‘double Gaussian’ to account for both the red and blue-wings).

Replacing the PEXRAV model and narrow 6.4 keV Gaussian with REFLIONX (FeK β emission is retained with flux fixed as in Table C.1 on page 239) to form the baseline model provides a poor fit to the data ($\chi^2_\nu = 1.82$, note that the highly ionised absorption lines in the FeK region are no longer modelled). Despite the two absorption zones and soft emission included with REFLIONX, further soft narrow emission and absorption features are required. These can be attributed to O VIII Ly α , O VII RRC, Ne IX resonance emission and SXV/ XVI 1s-2p absorption lines at $2.37_{-0.01}^{+0.01}$ keV and $2.77_{-0.08}^{+0.04}$ keV (see Table C.3 on page 242 for a summary of narrow soft X-ray lines in each object).

After using REFLIONX to model the reflection, there is still an excess at hard X-ray energies. Since the baseline model does not assume any emission from the inner regions of the accretion disc, the additional hard excess is therefore accounted for using a high column density partial covering model to supplement the REFLIONX hard X-ray component. The resulting model provides a reasonable fit to the data at

both soft and hard X-ray energies with $\chi^2_{\nu} \sim 1.26$ (although still formally rejected, note that Fe K region features other than neutral Fe K α emission are left unmodelled) with an obscuring column density of $N_{\text{H}} \sim 3.4 \times 10^{24} \text{ cm}^{-2}$ and a covering fraction of $C_{\text{frac}} \sim 50\%$. It should be noted that due to the high column of the partial coverer, there is some effect to the residuals in the Fe K region and as such using this model to account for the hard excess may reduce the strength of any relativistic emission which may be present (see Figure 4.2). A good fit is obtained to the reflection continuum and neutral Fe K α line with purely Solar iron abundance.

The remaining residuals in the Fe K region indicate the possibility of a *moderate* red-wing below 6.4 keV extending down to ~ 5 keV in addition to narrow ionised emission from Fe XXVI and strong absorption due to Fe XXV and Fe XXVI. To model the highly ionised absorption features in the Fe K region (previously modelled using narrow Gaussians) an XSTAR generated grid is used (see Section 2.5.4 for details) and as a consequence of this some of the observed red-wing may become weaker as noted in Reeves et al. (2004). This improves the fit further by $\Delta\chi^2 \sim 298$ for an additional 3 free parameters and the residuals show no further absorption. The highly ionised absorption parameters found here ($N_{\text{H}} = 3.99^{+3.65}_{-1.28} \times 10^{22} \text{ cm}^{-2}$, $\log\xi = 3.94^{+0.08}_{-0.25} \text{ erg cm s}^{-1}$ and $v_{\text{out}} = 3200^{+400}_{-500} \text{ km s}^{-1}$, see Table C.2 on page 241) are consistent with those found in past studies of MCG–6-30-15 (Miller, Turner & Reeves 2008; 2009). The inclusion of weak Fe XXVII Ly α emission with a reduction of $\Delta\chi^2 \sim 7$ finalises the baseline model.

The baseline model (Table C.2 on page 241), therefore, provides a reasonable fit to the time averaged January 2006 without the need for any *strong* emission from the inner regions of the accretion disc with a final fit statistic of $\chi^2_{\nu} = 1.11$ (see Table C.2 on page 241). However, some previous analyses of this object have found no such feature, i.e. partial covering and absorption components alone have been claimed to give an acceptable fit. For example, Miller, Turner & Reeves (2009) model MCG–6-30-15 with ‘clumpy’ absorption zones and achieve a good fit to the data without the need for the addition of a diskline component representative of emission from the inner regions of the accretion disc. In the present analysis, however, there is still some indication of a moderate red-wing which may be due to a relativistically broadened component (see

Figure 4.2).

4.2.1.3 NGC 3516

Taking a similar approach as above, the time averaged data from the October 2009 deep observation (~ 251 ks) of NGC 3516 are used. Initially modelling the broadband spectrum with a simple power-law plus Galactic absorption and a single warm absorption zone, a poor fit is obtained with $\chi^2_\nu \sim 6.6$ and photon index of $\Gamma \sim 1.7$. The most striking residuals are at hard energies and the narrow FeK α core. There is no indication of a soft excess as found in an analysis of the 2005 observation by Markowitz et al. (2008) although it should be noted that NGC 3516 is highly variable.

Parameterising the reflection continuum with PEXRAV results in a reflection fraction of $R = 0.87^{+0.32}_{-0.22}$ and a relatively simple FeK region with a very strong narrow FeK α line with $EW = 229^{+10}_{-52}$ eV improving the fit by $\Delta\chi^2 \sim 1396$ in addition to narrow FeXXV emission (Figure 4.1). A broad Gaussian is added to the model which improves the fit by $\Delta\chi^2 \sim 17$ and $EW = 55^{+29}_{-28}$ eV giving an overall $\chi^2_\nu = 1.08$ as noted in Table C.1 on page 239.

Replacing the reflection continuum modelled by PEXRAV with that from REFLIONX (and no longer modelling the FeK region with Gaussians), however, leaves additional excesses at hard X-ray energies and requires the introduction of a high column partial covering component, consistent with the method used above for MCG-6-30-15. This makes a further significant improvement to the fit (with $\Delta\chi^2 \sim -94$) with a covering column density of $N_{\text{H}} = 1.2^{+3.0}_{-0.8} \times 10^{23} \text{ cm}^{-2}$, ionisation $\log \xi = 3.1^{+0.5}_{-0.5}$ and a covering fraction of $C_{\text{frac}} \sim 21\%$, resulting in a reasonable fit to the broadband data.

There are residuals at soft energies possibly originating from O VII recombination, Ne IX, Mg XII and what may be Mg XI 1s-3p emission (see Table C.3 on page 242), in addition to these there is a narrow emission feature observed at $7.42^{+0.05}_{-0.06}$ keV due to Ni K α with $EW = 37^{+13}_{-14}$ eV. Analysis of any remaining residuals in the FeK region do not indicate any highly ionised absorption at Fe XXV/XXVI energies. Narrow emission

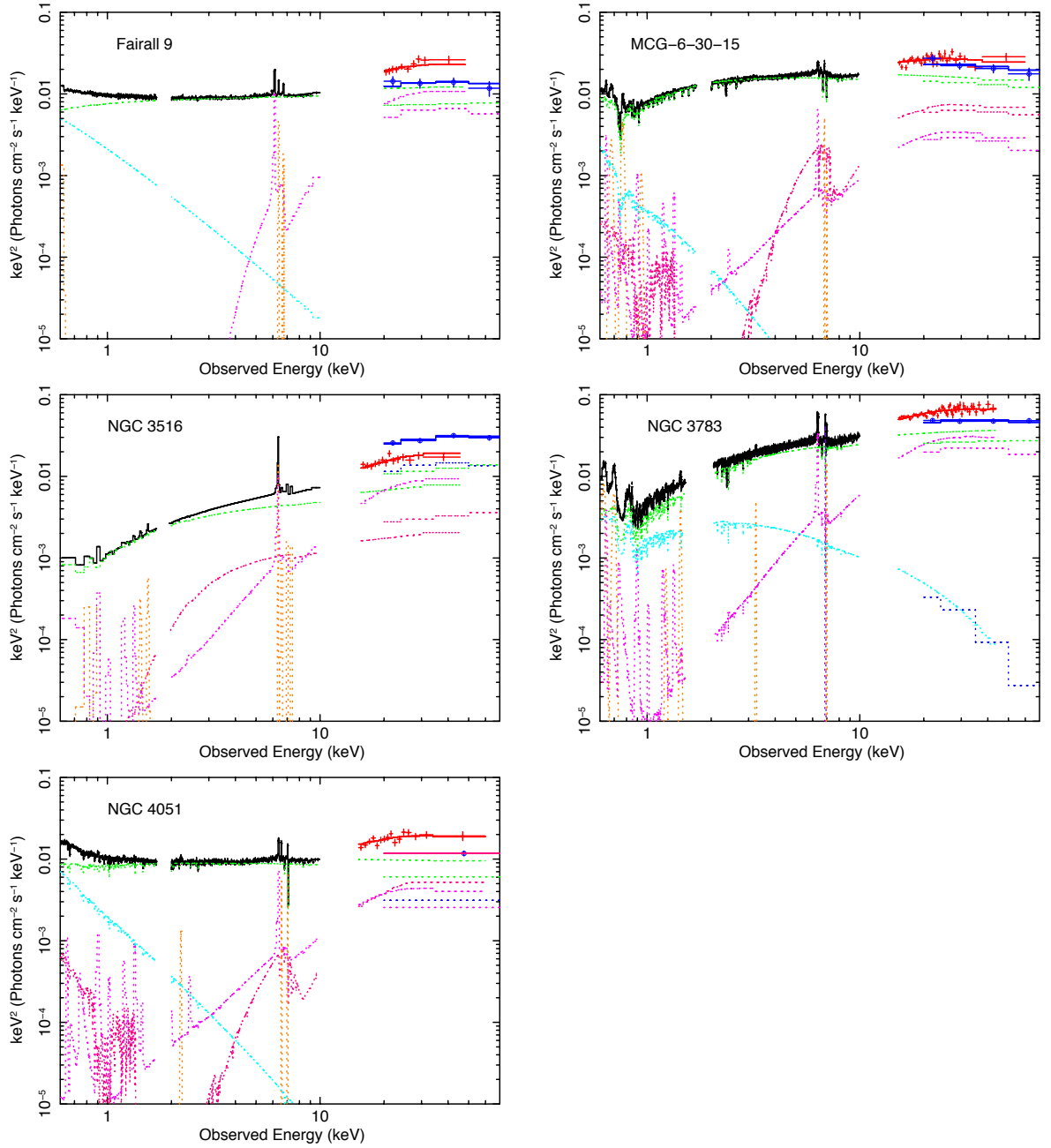


Figure 4.3: νF_ν plots of the baseline model including any absorption components: power-law (green), COMPTT (light blue), REFLIONX (purple), partial coverer (pink), narrow Gaussians to model additional FeK emission and soft emission lines (orange) where required. HXD data is in red and BAT data from *Swift* is represented by blue circles.

at $6.61_{-0.07}^{+0.08}$ keV is observed and modelled with a narrow Gaussian, improving the fit by $\Delta\chi^2 \sim 8$ for an additional two free parameters. This baseline model is a very good fit to the data with $\chi^2_\nu = 1.053$ without any relativistic line profile. There is little indication of any strong red-wing below 6.4 keV after full modelling of the broadband continuum (Figure 4.2 & Figure 4.3). However, it is possible that the partial covering component may be reducing observed spectral curvature which may in fact result from relativistic emission, the broad line is relatively weak with $EW = 55_{-28}^{+29}$ eV even without a partial coverer during 2009. In a previous analysis a 2005 *Suzaku* observation of NGC 3516, a relativistically broadened line was required (Markowitz et al. 2008), however, the 2-10 keV flux is higher by a factor ~ 1.8 in the 2005 observation. A comparison between the 2005 and 2009 epochs is made in Chapter 5 and Section 5.4.4 on page 182.

4.2.1.4 NGC 3783

In NGC 3783 there is a clear soft and hard X-ray excess along with some degree of intrinsic absorption, these are initially modelled as above using the COMPTT, PEXRAV and warm absorber components in addition to the intrinsic power-law and Galactic absorption (using WABS). Two absorption zones are required, including a low column, low ionisation zone ($N_{\text{H}} = 2.0_{-1.0}^{+0.4} \times 10^{21} \text{ cm}^{-2}$, $\log \xi = 0.7_{-0.1}^{+0.1} \text{ erg cm s}^{-1}$ and $N_{\text{H}} = 4.68_{-0.03}^{+0.03} \times 10^{23} \text{ cm}^{-2}$, $\log \xi = 2.1_{-0.1}^{+0.1} \text{ erg cm s}^{-1}$; see Table C.2 on page 241) which is consistent with Reeves et al. (2004). This still yields a poor fit to the data with $\chi^2_\nu \sim 2.4$, however, there are clear residuals at soft energies due to narrow emission lines.

The observed soft X-ray emission lines are included using narrow Gaussians due to O VIII Ly α , O VII recombination, Ne IX recombination and Mg XII Ly α (see Table C.3 on page 242). In addition to these there is a narrow emission feature at $3.28_{-0.02}^{+0.03}$ keV which may be due to Ar XVIII, improving the fit by $\Delta\chi^2 \sim 26$ and a significant narrow absorption feature at $2.39_{-0.01}^{+0.01}$ keV due to 1s-2p SXV with an improvement of $\Delta\chi^2 \sim 163$ (despite the inclusion of two warm absorption zones, however, parameters associated with the SXV absorption may be influenced by Au M-edge calibration

uncertainties).

Following on from the Reeves et al. (2004) analysis of a long *XMM-Newton* observation of NGC 3783 in 2001, the presence of strong Fe XXV absorption in the Fe K region in addition to weaker absorption due to less ionised Fe at ~ 6.5 keV (Figure 4.1) is confirmed. Modelling this absorption with two simple Gaussians results in an improvement by $\Delta\chi^2 \sim 38$ and $\Delta\chi^2 \sim 7$ respectively. However, to form a physical model to account for the observed complexity in the Fe K region a high ionisation XSTAR grid is used (as in MCG-6-30-15), whilst not as good a fit as the two simple Gaussians, the fit is improved by $\Delta\chi^2 \sim 18$. The high ionisation zone successfully models the Fe XXV absorption with the parameters given in Table C.2 on page 241, although the less ionised Fe absorption at ~ 6.5 keV is left relatively unmodelled. Attempting to model this feature with a second highly ionised absorption zone is unsuccessful due to its relatively low statistical weight and as such the absorption feature at ~ 6.5 keV is left unmodelled.

An additional narrow Fe XXVI emission line is included ($\Delta\chi^2 \sim -45$) to give the baseline model for NGC 3783 which provides a good fit to the data ($\chi^2_\nu = 1.083$). However, the inclusion of a highly ionised absorption zone still leaves a moderate redwing below 6.4 keV extending down to ~ 5 keV (Figure 4.2). This indicates the possible presence of statistically significant relativistic emission from the inner regions of the accretion disc (later fit with a KERRDISK line profile with an improvement of $\Delta\chi^2 \sim 32$, see Section 4.2.2).

4.2.1.5 NGC 4051

The X-ray spectrum of NGC 4051 is very complex as well as variable, differing between all three observations to date with *Suzaku*. An in-depth study of these observations with the aid of HETG data from *Chandra* is conducted in Lobban et al. (2011) and taking note of their findings in the analysis here of the 2008 deep observation (Obs ID: 703023010) during a period of relatively high flux for this source ($F_{2-10\text{keV}} = 2.45 \times 10^{-11} \text{erg cm}^{-2} \text{s}^{-1}$), a comparison between each of the *Suzaku* observations is conducted

in Chapter 5. There are clear soft and hard excesses which are modelled with COMPTT and PEXRAV respectively, along with two low column ($N_{\text{H}} = 0.18_{-0.11}^{+2.09} \times 10^{22} \text{ cm}^{-2}$ and $N_{\text{H}} = 0.18_{-0.11}^{+0.07} \times 10^{22} \text{ cm}^{-2}$) warm absorber zones of the XSTAR grid with ionisation parameters $\log \xi = 3.0_{-0.4}^{+0.4} \text{ erg cm s}^{-1}$ and $\log \xi = 1.9_{-0.1}^{+0.1} \text{ erg cm s}^{-1}$ respectively, providing a still poor fit to the data ($\chi_{\nu}^2 \sim 1.5$).

Given the above model of the broadband data, the remaining residuals lie in the FeK region as can be seen in Figure 4.1. As documented in Pounds et al. (2004) and Lobban et al. (2011) there is evidence of a highly ionised outflow resulting in blue-shifted Fe XXV and Fe XXVI absorption lines at $6.79_{-0.05}^{+0.07} \text{ keV}$ and $7.12_{-0.03}^{+0.03} \text{ keV}$. A parameterisation of these features with narrow Gaussians yields a good fit to the data with $\chi_{\nu}^2 \sim 1.1$, see Table C.1 on page 239.

Replacing the PEXRAV with the physically motivated REFLIONX reflection model results in a poor fit to the reflection spectrum, predominantly in the HXD and BAT data. In order to supplement the reflection continuum, adding a high column partial coverer (Table C.2 on page 241) improves the fit by $\Delta\chi^2 \sim 62$ (as above in MCG-6-30-15 and NGC 3516, no such excesses remain when using PEXRAV, with a high reflection fraction of $R = 1.52_{-0.29}^{+0.26}$), resulting in a good fit to both the high energy data and the reflection continuum. A sub-solar iron abundance of $Z_{\text{Fe}} = 0.5_{-0.4}^{+0.4}$ is also found, consistent with Lobban et al. (2011) as well as an emission feature at $2.22_{-0.03}^{+0.03} \text{ keV}$ with an improvement of $\Delta\chi^2 \sim 16$ which may be due to 1s-3p Si XIII.

Lobban et al. (2011) find that the high ionisation absorption lines in the FeK region are best fit by a highly ionised XSTAR grid with a turbulent velocity of 3000 km s^{-1} , however, in this analysis a turbulent velocity of only 1000 km s^{-1} is used to remain consistent with the procedure used above. This still models the absorption features well, improving the fit by a further $\Delta\chi^2 \sim 77$ with parameters $N_{\text{H}} = 9.55_{-5.68}^{+18.95} \times 10^{22} \text{ cm}^{-2}$, $\log \xi = 4.1_{-0.2}^{+0.3} \text{ erg cm s}^{-1}$ and $v_{\text{out}} = 5600_{-700}^{+800} \text{ km s}^{-1}$, consistent with Lobban et al. (2011). Subsequent to modelling the highly ionised zone and narrow Fe XXV emission, there are very few residuals remaining below 6.4 keV which indicates that relativistic emission from the inner regions of the accretion disc may not be required in NGC 4051 (see Figure 4.2), leaving a final $\chi_{\nu}^2 = 1.01$ for the baseline model.

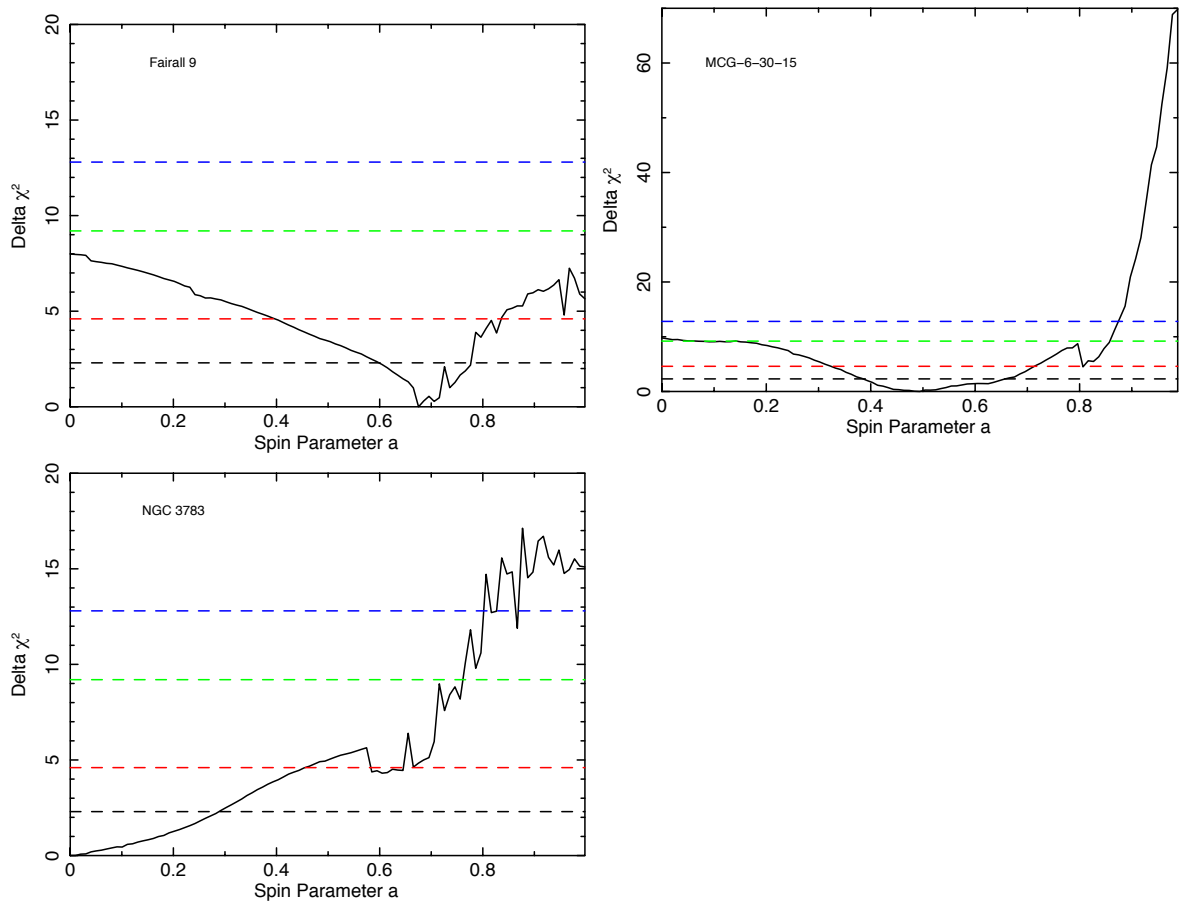


Figure 4.4: Change in fit statistic ($\Delta\chi^2$) as a function of black hole spin a for spin constraints made with the baseline+KERRDISK models. Dashed lines representing 68% (black), 90% (red), 99% (green) and 99.9% (blue) confidence levels for two interesting parameters. Note that the emissivity index q is a free parameter.

4.2.2 The Fe K region and disc parameters

Given the above baseline model in Table C.2 on page 241 for each object without broad iron line emission, residuals in the Fe K region can now be examined. As a step towards assessing the strength of any contribution from relativistically blurred emission from the inner regions of the accretion disc, the KERRDISK line profile model is used with BH spin as a variable parameter (Brenneman & Reynolds 2006). Of course, this is under the assumption that the broad residuals remaining in the Fe K region are due to

emission from the inner regions of the accretion disc.

This allows the measurement of the strength of the relativistic emission, the inner radius of the disc, the inclination and the emissivity of the disc. The emissivity index scales as R^{-q} where $q \sim 3$ would be expected from the inner regions of an accretion disc and $q > 5$ indicates that emission from the accretion disc is very centrally concentrated with a significant amount of light bending. The accretion disc is assumed to extend down to the inner-most stable circular orbit (R_{ISCO}), which itself varies according to the value of the BH spin parameter. The outer edge of the accretion disc is fixed at $R_{\text{out}} = 400 R_{\text{ms}}$ and the line centroid energy is assumed with a rest frame energy of 6.4 keV resulting from neutral Fe K α . The KERRDISK model only considers the possibility of prograde BH spin with $0 < a < 0.998$ where $a = cJ/GM^2$ (where J is angular momentum).

It should be noted that the results obtained here can only be judged as estimates due to the possible model degeneracies. In the event that residuals in the Fe K region result from the observation of relativistically blurred diskline emission, an attempt is made to consider these degeneracies and present the best estimates of the line parameters. When employing a diskline-type model (e.g. KERRDISK), care should be taken due to the interplay between the emissivity index q and the spin parameter a . As such the spin versus $\Delta\chi^2$ plots in Figure 4.4 indicate the confidence levels for two interesting parameters where both q and a are allowed to vary. The presence of narrow ionised emission lines in the Fe K region can also affect the measured emissivity index q and hence the value of the BH spin obtained with a diskline-type model. However, in these deep observations the number of counts is generally sufficient to distinguish between the presence of a narrow Gaussian or the blue-wing of a relativistically blurred line profile.

The analysis of the long 2010 *Suzaku* Fairall 9 observation here yields, similar results to those of the shorter 2007 observation in Patrick et al. (2011a). The disc emissivity is consistent here is estimated to be $q = 3.3_{-0.4}^{+2.6}$ (Table 4.2), although despite the higher signal to noise data, it is not as well constrained compared to $q = 2.7_{-0.4}^{+0.7}$ in Chapter 3 and Table B.4. In an analysis by Schmoll et al. of the same 2007 data they

Table 4.2: KERRDISK model parameters in addition to the baseline model. Absorption and COMPTT components are consistent with those quoted in Table C.2 on page 241 and are not stated again here to avoid repetition. * Denotes a frozen parameter. ^a Flux given in units (10^{-5} ph cm⁻² s⁻¹). * Denotes a frozen parameter. A positive $\Delta\chi^2$ represents a worsening in the fit upon the removal of the component. Spin cannot be constrained in NGC 3516 at the 90% confidence level.

	Fairall 9	MCG-6-30-15	NGC 3516	NGC 3783	NGC 4051
	Kerrdisk Profile				
LineE (keV)	6.4*	6.4*	6.4*	6.4*	6.4*
EW (eV)	89^{+12}_{-17}	161^{+46}_{-44}	46^{+16}_{-36}	45^{+17}_{-26}	156^{+15}_{-54}
q	$3.3^{+2.6}_{-0.4}$	$2.7^{+0.2}_{-0.1}$	$2.5^{+1.5}_{-1.0}$	$2.6^{+0.2}_{-0.1}$	3.0*
a	$0.67^{+0.10}_{-0.11}$	$0.49^{+0.20}_{-0.12}$	–	< 0.32	< 0.94
i°	33^{+3}_{-3}	44^{+6}_{-2}	51^{+11}_{-5}	< 17	46^{+3}_{-16}
Flux ^a	$3.12^{+0.41}_{-0.60}$	$5.73^{+1.63}_{-1.57}$	$1.00^{+0.35}_{-0.36}$	$3.83^{+1.12}_{-0.72}$	$3.45^{+0.33}_{-1.20}$
$\Delta\chi^2$ ($a = 0.988$)	+6	+70	+1	+15	+6
$\Delta\chi^2$ ($a = 0$)	+8	+10	+1	0	+3
$\Delta\chi^2$ (without KERRDISK)	+35	+59	+10	+32	+3
Fe XXV emis- sion	✓	–	–	–	–
Fe XXVI emis- sion	✓	✓	–	✓	–
χ^2_ν	924.4/881	1967.8/1819	519.9/497	1463.0/1374	1088.2/1083

place only a lower limit of $q > 4.9$. A significant difference which is responsible for the poorly constrained emissivity index is the clearly detected narrow FeXXV emission which is now included in the fit to the FeK region. The interplay between the narrow Gaussian used to model the feature at ~ 6.7 keV and the blue-wing of the KERRDISK line profile causes a degree of degeneracy between the emissivity index and FeXXV flux. The inclusion of narrow FeXXV emission also results in a change to the inferred value of the spin parameter a , here it is estimated to be $a = 0.67_{-0.11}^{+0.10}$, whereas a lower value of $a = 0.44_{-0.11}^{+0.04}$ is obtained in the previous analysis in Chapter 3 when the narrow emission is not included (Figure 4.4). The findings made here are, however, consistent with an analysis of a 130 ks *XMM-Newton* observation of Fairall 9 in 2009 by Emmanoulopoulos et al. (2011) who find $a = 0.39_{-0.30}^{+0.48}$.

Maximal spin is ruled out in all objects, including MCG–6-30-15 in contrast to claims to the contrary by Reynolds et al. (2005) and Miniutti et al. (2007) of $a > 0.93$ and $a > 0.92$ respectively. One possible difference is that a full broadband model has been compiled to fit the 0.6-100.0 keV spectrum, whereas the Miniutti et al. (2007) spin measurement is only valid over the 3-45 keV range and without including warm absorbers or highly ionised absorption at FeK energies. In this analysis a fairly typical emissivity index of $q = 2.7_{-0.1}^{+0.2}$ is found, firstly suggesting that emission in MCG–6-30-15 is not particularly centrally concentrated and the effects of light bending may be minimal. The spin of the central black hole in MCG–6-30-15 is estimated to a much lower spin $a = 0.49_{-0.12}^{+0.20}$ (Table 4.2), maximal spin is ruled out at $> 99.5\%$ confidence in this model where the fit is made worse by $\Delta\chi^2 \sim 70$ for the case when the spin parameter is fixed at $a = 0.998$ (see Figure 4.4).

Spin cannot be constrained in NGC 3516 and only loose constraints can be made on the emissivity index of the disc $q = 2.5_{-1.0}^{+1.5}$, this is expected due to the relatively weak line modelled using a broad Gaussian in Table C.1 on page 239. The fit is only improved by $\Delta\chi^2 \sim 10$ after adding KERRDISK emission with $EW = 46_{-36}^{+16}$ eV (Table 4.2) and no further narrow ionised emission is required in the FeK region with the KERRDISK profile taking the place of the narrow FeXXV emission (see Figure 4.5). However, the FeK region is well described by the baseline model (Table C.2 on page 241) which

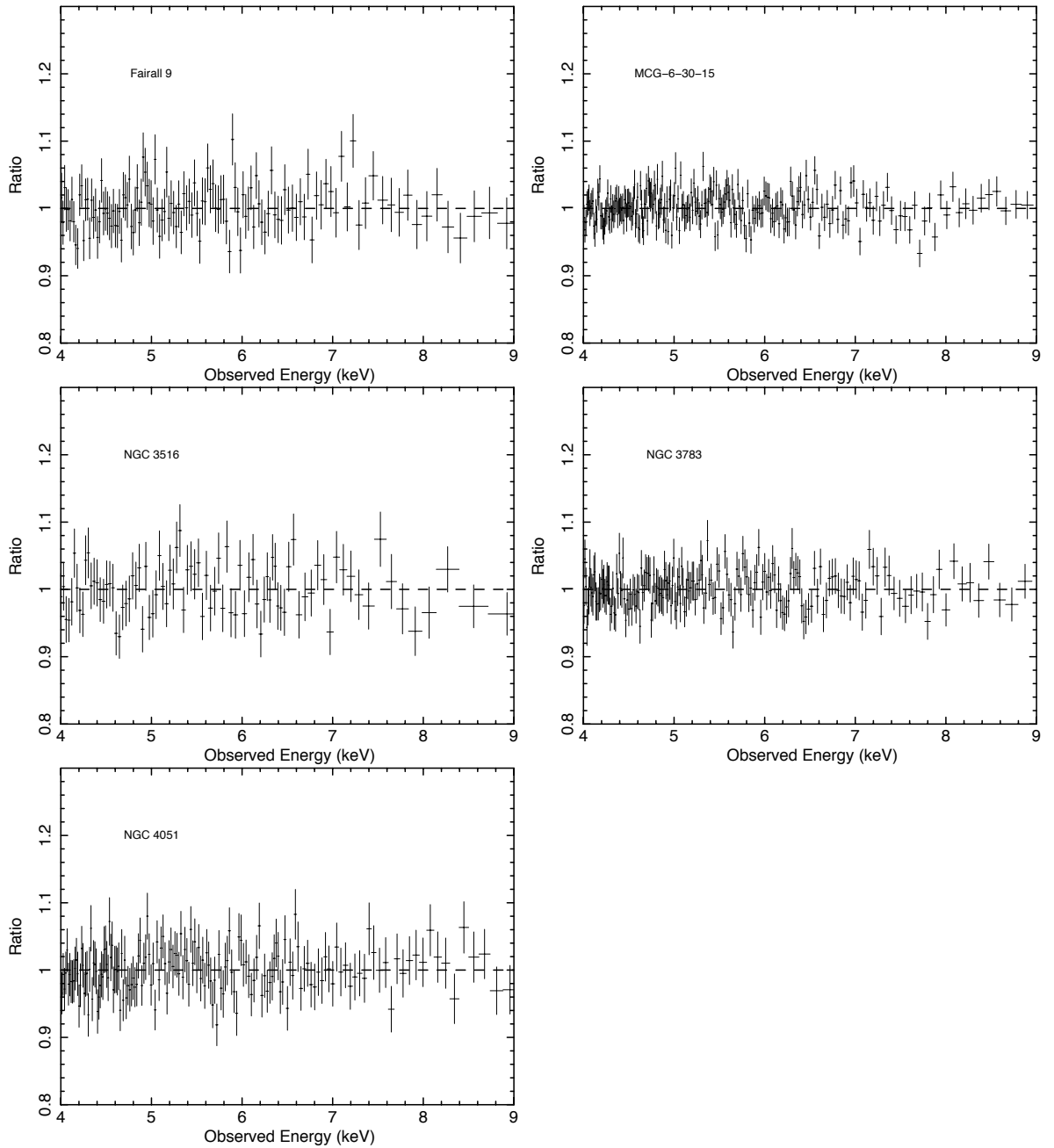


Figure 4.5: Ratio plots of the baseline+KERRDISK model between 4-9 keV. After the application of the KERRDISK relativistic line emission model there are few remaining residuals below 6.4 keV, giving a very good fit to the FeK region and the broad-band data as a whole.

includes narrow FeXXV emission and partial covering, adding a KERRDISK line profile only improves the fit in this case by $\Delta\chi^2 \sim 2$ over the baseline model in this scenario.

Only an upper limit of $a < 0.32$ at the 90% confidence level can be placed upon the spin in NGC 3783 using the KERRDISK model. A maximally rotating BH is again ruled out with a worsening to the fit by $\Delta\chi^2 \sim 15$. Similarly only an upper limit can be placed upon the inclination of the accretion disc with $i < 17^\circ$, however, the emissivity can be tightly constrained to $q = 2.6_{-0.1}^{+0.2}$. The strength of the broad line component is consistent with Reeves et al. (2004) ($EW = 46_{-36}^{+16}$ eV here compared to $EW = 58_{-12}^{+12}$ eV), being reduced significantly after including a physical model for the highly ionised absorption.

The broad line feature in NGC 4051 makes a statistically insignificant improvement to the quality of the fit with a reduction of $\Delta\chi^2 \sim 3$. Hence, none of the accretion disc parameters can be particularly well constrained, the emissivity index is fixed at $q = 3$ and only an upper limit can be made upon the spin parameter of $a < 0.94$. The FeXXV emission listed in Table C.2 on page 241 is no longer required with the introduction of the KERRDISK component and is alternatively explained as a blue-wing to the line profile (Figure 4.6). The broad line results obtained here when using a highly ionised XSTAR grid with a turbulent velocity of 1000 km s^{-1} are consistent with those when a turbulent velocity of 3000 km s^{-1} is used (e.g. by Lobban et al. 2011), i.e. the line strength, EW and R_{in} .

4.2.2.1 The effect of partial covering

As stated in Section 2.5.5, the high column density partial covering component has an effect predominantly on the hard X-ray data in the HXD and BAT detectors, however, the effect of this partial covering component on any curvature in the FeK region is tested. The partial covering component and distant reflection from REFLIONX are removed and replaced with the PEXRAV neutral reflection model (plus a narrow neutral 6.4 keV Gaussian) which achieved a good fit to the data in the initial parameterisation. This allows for an effectively free amount of reflection with a varying reflection fraction

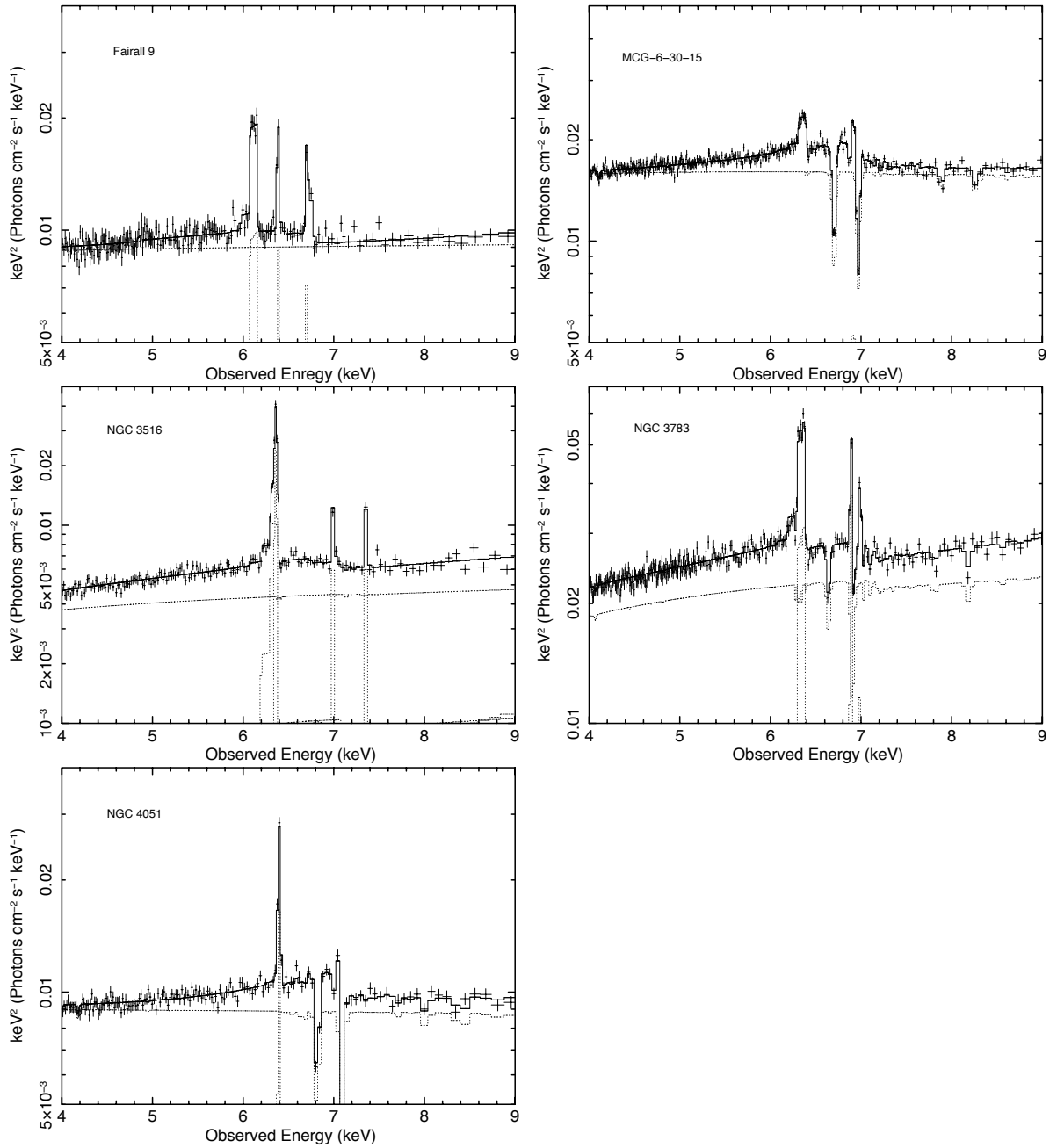


Figure 4.6: νF_ν plots of the baseline+KERRDISK model in the 4-9 keV region. Note the strong Fe K band absorption in MCG-6-30-15, NGC 3783 and NGC 4051.

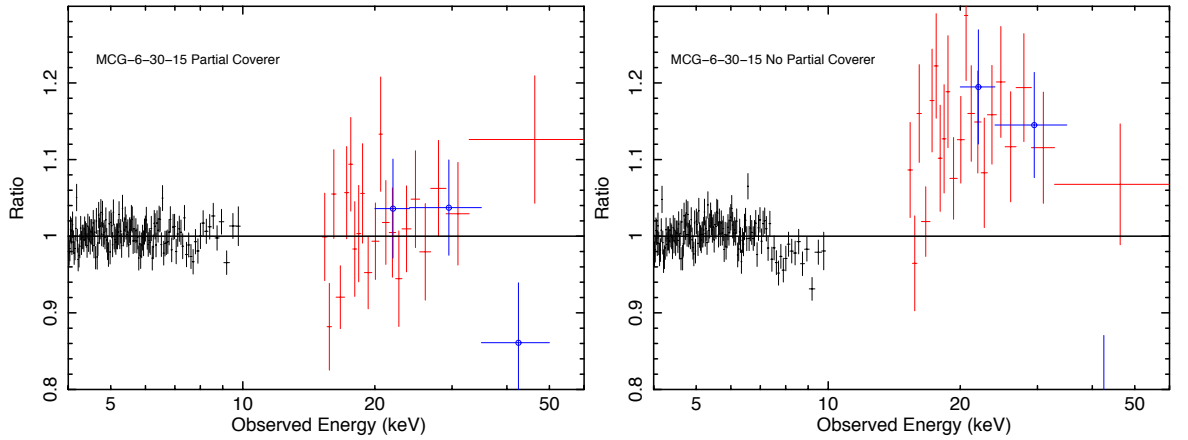


Figure 4.7: Comparison between the fit to the 4-60 keV data for MCG-6-30-15 with and without a partial covering component. The first plot shows the baseline model, in the second plot the partial coverer has been removed and the data refit, i.e. still using REFLIONX and not PEXRAV. Note that the (high column) partial covering component therefore affects predominantly the hard X-ray data, with little affect upon the Fe K region. HXD data is in red and BAT data from *Swift* is represented by blue circles.

(the R parameter), whereas the reflected flux in REFLIONX is tied to the narrow Fe K α flux. This interpretation, i.e., without partial covering, yields a slightly higher spin constraint of $a = 0.82^{+0.01}_{-0.09}$ for MCG-6-30-15, however, a maximally rotating BH is still discounted at an increase of $\Delta\chi^2 > 17$ ($> 99.5\%$ confidence) despite a fairly low reflection fraction of $R = 0.77^{+0.10}_{-0.11}$. Figure 4.7 shows the residuals to the data with the partial covering component of $N_{\text{H}} = 1.63^{+0.16}_{-0.33} \times 10^{23} \text{ cm}^{-2}$ removed (still including REFLIONX), showing that the high column partial covering component in MCG-6-30-15 predominantly affects the fit to the hard X-ray data. Only subtle curvature is introduced to the 7-10 keV spectrum in the XIS detectors.

Both NGC 3516 and NGC 4051 (which display no strong broadened emission) also feature a partial covering component in the baseline model, removing the partial coverer and instead modelling the hard excess using PEXRAV gives accretion disc parameters which are entirely consistent with those in Table 4.2 (see Table 4.3). This again suggests that significant relativistically broadened emission is probably not strongly present in these objects and the high column partial coverer does not have a significant affect upon

Table 4.3: KERRDISK model parameters when the reflection continuum is modelled with PEXRAV in place of the REFLIONX plus partial coverer configuration, i.e. no partial covering component is used here. ^a Flux given in units (10^{-5} ph cm⁻² s⁻¹). * Denotes a frozen parameter. A positive $\Delta\chi^2$ represents a worsening in the fit. Spin cannot be constrained in NGC 3516 at the 90% confidence level.

	MCG-6-30-15	NGC 3516	NGC 4051
	Kerrdisk Profile		
LineE (keV)	6.4*	6.4*	6.4*
<i>EW</i> (eV)	264 ⁺²² ₋₂₇	88 ⁺¹³ ₋₂₆	88 ⁺²³ ₋₂₅
<i>q</i>	2.7 ^{+0.2} _{-0.2}	< 2.7	3.0*
<i>a</i>	0.82 ^{+0.01} _{-0.09}	–	< 0.81
<i>i</i> ^o	45 ⁺¹ ₋₁	31 ⁺³ ₋₂	34 ⁺⁴ ₋₄
Flux ^a	9.01 ^{+0.73} _{-0.93}	1.87 ^{+0.28} _{-0.56}	1.95 ^{+0.51} _{-0.55}
$\Delta\chi^2$ (<i>a</i> = 0.998)	+17	+12	+10
$\Delta\chi^2$ (<i>a</i> = 0)	+39	+2	+2
$\Delta\chi^2$ (without Kerrdisk)	+354	+35	+28
Fe XXV emission	–	–	–
Fe XXVI emission	✓	–	–
χ^2_ν	2008.8/1821	536.9/498	1131.2/1086

the Fe K modelling. The partial covering component as used in the baseline model does have some affect upon the derived accretion disc and BH parameters, although only in MCG-6-30-15, for example the measured strength (i.e. flux and *EW*) is slightly higher without the presence of a partial coverer as is the measured BH spin (see Table 4.3). Properties of the accretion disc such as the emissivity index and the inclination remain relatively unchanged. Despite the removal of the partial covering component in all objects (where present), a maximally spinning central BH is ruled out in these objects. Note that this is not to say that the residuals in the Fe K region cannot be accounted for by a partial coverer, simply that the high column partial coverer used here does not significantly affect the measured accretion disc parameters.

Table 4.4: RELLINE model parameters in NGC 3783 (2009 observation only) allowing for retrograde SMBH spin. ^a Flux given in units (10^{-5} ph cm $^{-2}$ s $^{-1}$). * Denotes a frozen parameter. A positive $\Delta\chi^2$ represents a worsening in the fit.

NGC 3783	
	Relline Profile
LineE (keV)	6.4*
EW (eV)	43_{-16}^{+8}
q	$3.2_{-0.4}^{+0.4}$
a	< -0.04
i°	< 17
Flux ^a	$3.94_{-1.46}^{+0.73}$
$\Delta\chi^2$ ($a = 0.998$)	+13
$\Delta\chi^2$ ($a = 0$)	+3
$\Delta\chi^2$ (without RELLINE)	+44
Fe XXV emission	–
Fe XXVI emission	✓
χ^2_ν	1452.5/1374

4.2.2.2 Testing for retrograde SMBH spin

Recent work has suggested the possibility of retrograde SMBH spin in AGN, whereby the rotation of the central BH and the surrounding accretion disc are anti-parallel whilst maintaining a stable configuration (King et al. 2005). The RELLINE model (Dauser et al. 2010) is a relativistic line emission model accommodating both negatively and positively spinning central BHs, which produces line profiles consistent with established prograde spin line emission models, e.g. KERRDISK (Brenneman & Reynolds 2006) and KYRLINE (Dovčiak et al. 2004).

The spin versus $\Delta\chi^2$ plot for NGC 3783 in Figure 4.4 reveals a best-fitting spin parameter of $a = 0$ according to the KERRDISK model, assuming a strictly prograde BH spin, indeed NGC 3783 is the only object showing this trend in this sample. The RELLINE model is used in addition to the baseline model to assess the suitability of a retrograde BH in a fit to the FeK region in NGC 3783. In a similar procedure to

that employed using the KERRDISK model, it is assumed that the accretion disc extends down to R_{ISCO} and that emission occurs from neutral Fe $K\alpha$ and as such the line energy is fixed at 6.4 keV.

The accretion disc parameters obtained are very similar to those obtained with KERRDISK in Table 4.2 with a slightly higher emissivity of $q = 3.2_{-0.4}^{+0.4}$, inclination $i < 17^\circ$ and $EW = 43_{-16}^{+8}$ eV (see Table 4.4). Modelling the FeK region of NGC 3783 allowing for retrograde spin suggests an upper limit of $a < -0.04$, as shown in Figure 4.8. This modelling of NGC 3783, therefore, suggests a negatively spinning BH in NGC 3783 at the 90% confidence level, ruling out a maximally spinning *prograde* BH at $> 99.5\%$ confidence with an increase of $\Delta\chi^2 \sim 13$ when fixed at $a = +0.998$ and the data refit. Figure 4.8 also shows an emissivity q vs spin a contour plot for NGC 3783 using RELLINE, indicating the relation between these two parameters. It is interesting to note that the emissivity of the accretion disc is well constrained and, in this object, has little effect upon the measured BH spin. There is only a slight negative correlation in which emission is more centrally concentrated for lower (more negative) BH spin.

It should be noted that while a retrograde BH does indeed push the innermost stable circular orbit of the accretion disc outwards, thereby reducing the extent to which the line profile can become relativistically broadened, the line profile remains noticeably broadened and not simply representative of a series of narrow Gaussians which would otherwise be indicative of purely distant emission (see Figure 2.14 in Section 2.5.6).

4.2.3 Dual reflector

The previous KERRDISK relativistic line emission model is representative of reflection off the inner regions of the accretion disc. If strong emission arises from this region, the same relativistic broadening must also be applied to the reflection continuum as a whole, as opposed to purely the narrow 6.4 keV Fe $K\alpha$ emission line. To account for this the KERRDISK model component is replaced with a second REFLIONX component convolved with the KERRCONV kernel (Brenneman & Reynolds 2006) in addition to the

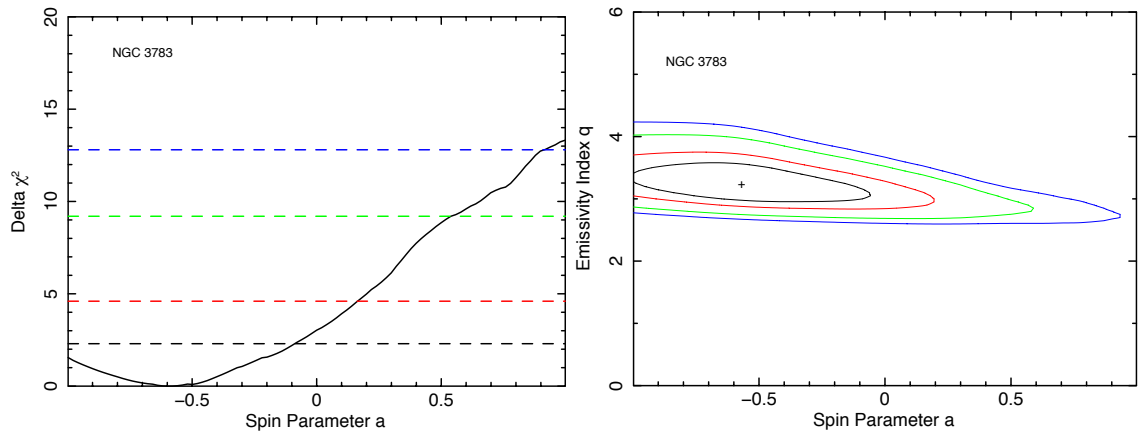


Figure 4.8: The upper plot is a fit statistic versus a plot for SMBH spin from the RELLINE model when used in conjunction with the baseline model in NGC 3783. The spin parameter a is allowed to cover the full range $-0.988 < a < +0.998$ to assess the possibility of retrograde BH spin. The lower plot shows a 2D contour plot showing the relation between emissivity index and spin, confidence levels labelled in both plots are 68% (black), 90% (red), 99% (green) and 99.9% (blue) for two interesting parameters.

unblurred reflection component from distant material. The partial covering component is also removed from the dual reflector fits to assess this alternative interpretation.

In some analyses of AGN, such a blurred reflection component has been used to model the soft excess under the assumption that the regions responsible for the smearing of discrete atomic emission features at soft energies are also responsible for broadening in the Fe K region (e.g. Schmoll et al. 2009; Nardini et al. 2010). However, in an albeit small sample of bare Seyfert AGN, Patrick et al. (2011a) (and here in Chapter 3) derived contrasting accretion disc parameters depending upon whether such blurring is allowed to model the soft excess in addition to features in the Fe K region. A significant amount of blurring is required in order to smear the soft atomic emission features into a smooth soft excess, resulting in much higher derived BH spin and highly centrally concentrated emission (i.e. high $q > 4$).

Taking this into account, in this interpretation of the data, the use of the COMPTT Comptonization origin is retained to model the soft excess, leaving the convolved reflection spectrum to account for any observed iron line broadening and hard

excess over purely distant reflection. A purely reflection origin for the hard excess is assumed and no partial covering model is used in the dual reflector fit as in MCG–6-30-15, NGC 3516 and NGC 4051. The iron abundance of both the inner and distant reflector are tied and frozen at the best fitting values from the baseline model through the fits.

A good fit can be obtained to all objects with a dual reflector model (Table C.4 on page 243), with the exception of MCG–6-30-15, the hard X-ray data from the HXD and BAT detectors are fit well without the requirement for any additional reflection or a partial covering component. Due to the increased number of free model parameters and hence complexity in the broadband model it is difficult to measure accretion disc parameters (particularly BH spin) to any reasonable accuracy, even with high quality data as used here from deep *Suzaku* observations. Consequently, no better constraints can be made using a dual reflector fit, rather the results obtained are generally consistent with the baseline+KERRDISK model (Table 4.2).

For the case of MCG–6-30-15, a reasonable quality of fit ($\chi^2_\nu = 2061.4/1823$) is obtained with a dual reflector fit. As noted above, the interpretation of the soft excess can dramatically alter the measured accretion disc parameters. In an object as complex as MCG–6-30-15 with strong reflection, broadened relativistic emission in the FeK region, complex warm absorption, highly ionised outflowing absorption at FeK energies and a soft excess, the use of a dual reflector results in a number of degeneracies when modelling the spectrum. As a result of this the COMP TT parameters are fixed at the best-fit values obtained with the baseline model and then proceed to add a blurred reflection component in place of the partial covering model. This approach ensures that the blurred reflection component does not model the soft excess in place of COMP TT and as such the accretion disc emissivity and BH spin will not be forced to extreme values in order to reproduce a smooth and featureless continuum.

The measured parameters for MCG–6-30-15 are consistent with those obtained in Table 4.2 with $q = 2.3^{+0.2}_{-0.1}$ and $a = 0.61^{+0.15}_{-0.17}$. Also requiring a FeXXV emission line which improves the fit by $\Delta\chi^2 \sim 7$, however, it is weak with a low $EW = 6^{+5}_{-3}$ eV. Solar abundances are assumed throughout and a consistent ionisation parameter ($\xi <$

11 erg cm s^{-1}) is measured in both the blurred and unblurred reflectors. The warm absorber parameters measured with the dual reflector fit are also consistent with those obtained in the baseline model.

The properties of the accretion disc are not greatly affected by the interpretation of the origin of the hard excess, i.e. whether a high column ($N_{\text{H}} \sim 10^{24} \text{ cm}^{-2}$) partial covering model or a dual blurred and unblurred reflector is used (see Table C.4 on page 243). The partial covering model used in the baseline model therefore has a limited effect upon the accretion disc parameters and BH spin measured from the Fe K region. The results obtained with the dual reflector fit in NGC 3783 are completely consistent with those measured with the previous baseline+KERRDISK model, again an upper limit on the BH spin parameter is found at $a < 0.31$ and the emissivity of the accretion disc is also similar with $q = 2.8_{-0.2}^{+0.4}$.

The complex absorption in these objects (other than Fairall 9) can mask the extent to which the smeared discrete emission features are present in the data at soft X-ray energies. More extreme blurring (a high emissivity, for example) is not required since the X-ray spectrum at soft energies in these more complex objects is far from smooth and the discrete emission features do not require smearing into a smooth continuum-like shape. As a consequence of this, the main components driving the dual reflector fits are the features in the Fe K region, rather than curvature due to the blurring of soft X-ray atomic emission.

4.3 Discussion of deep observation results

This sample of Seyfert 1 AGN includes deep *Suzaku* observations with exposures $> 200 \text{ ks}$ at high S/N, making it possible to fully model the broadband spectrum when combined with additional hard X-ray data from *Swift*/BAT. In order to robustly assess the nature of any features in the Fe K region, whether it be absorption or relativistically blurred emission, a complete modelling of the X-ray spectrum was undertaken to ensure that all features are taken into account. With complex X-ray spectra such as found in

these AGN, deep exposures are essential to help constrain a number of features prior to investigating accretion disc properties and the potential for measuring BH spin.

Some improvement is made to the fit for all objects with the addition of the KERRDISK model which represents blurred line emission from the inner regions of the accretion disc. The overall improvement to the fit for NGC 3516 and NGC 4051 is small with $\Delta\chi^2 = -10$ and -3 in each for 4 and 3 additional parameters respectively, thus even the presence of disc emission lines in these AGN is very tentative and for NGC 4051 not statistically required. Statistically much stronger broad line components are found in MCG-6-30-15 and NGC 3783 even after a complete modelling of the warm absorber components, although in some circumstances complex absorption models may in part (but not entirely) be able to account for these features.

Narrow ionised emission is found in three of the objects here after including a KERRDISK line profile, however, the blue-wing of the relativistically broadened line profile can easily become degenerate with such emission. For example, the emissivity index and the inclination of the accretion disc can be forced to values such that a narrow feature which would otherwise be attributed to FeXXV/ FeXXVI emission could be explained by the blue-wing of relativistically blurred diskline emission from neutral FeK α . Indeed, NGC 3516 and NGC 4051 require no ionised narrow emission features in the final baseline+KERRDISK model since the broad feature can successfully reproduce both the red-wing and narrow-like features in the FeK region, yet there is little requirement for broadened line profiles in either object. Emission from FeXXV is required only in Fairall 9 even after the possible degeneracies mentioned above, FeXXVI Ly α emission is more common and is found in 3/5 objects (Fairall 9, MCG-6-30-15 and NGC 3783). Future calorimeter observations with *Astro-H* (Takahashi et al. 2010) with < 6 eV FWHM resolution will be able to distinguish and resolve narrow ionised emission from the blue-wing of a diskline profile, helping to achieve more accurate FeK region statistics.

4.3.1 Average parameters of the disc

Given the measured values from the KERRDISK line profile, it is possible to calculate typical parameters of the accretion disc in this small sample. The average inclination of the disc is $i = 37^\circ \pm 8^\circ$ which is consistent with Nandra et al. (2007) who find $i = 38^\circ \pm 6^\circ$. From the baseline+KERRDISK model (Table 4.2), an average accretion disc emissivity of $q = 2.8 \pm 0.2$ is measured which (similarly to Patrick et al. 2011a and Chapter 3) is a lower value than is often assumed from light bending models (e.g. Gallo et al. 2011; Nardini et al. 2011). The initial parameterisation with a broad Gaussian measures an average strength of the broad line component of $EW = 77 \pm 23$ eV at a centroid line energy of 6.11 ± 0.10 keV (Table C.1 on page 239), also consistent with the previous findings by Nandra et al. (2007) with *XMM-Newton*. Employing the more physical KERRDISK model increases the strength to $EW = 99 \pm 28$ eV, but consistent with the above values.

The moderate emissivity indices found here are likely due to the accretion disc parameters being obtained purely from broadening in the FeK region rather than requiring the inner regions of the accretion disc to blur the reflection continuum substantially in order to model the soft excess. Here it is assumed that the soft excess originates from the Comptonisation of UV seed photons from the disc in a hot corona above the disc via the COMPTT model (Titarchuk 1994), a second soft power-law or disc blackbody would provide a quantitatively similar fit to the data. If discrete atomic features present in the reflection continuum at soft X-ray energies were allowed to model the model the soft excess through relativistic smearing due to originating from regions close to the central BH, the emissivity of the accretion disc would be forced to much higher values, i.e. $q > 4.5$ (see Patrick et al. 2011a). Such high values are not required for a good fit to the FeK region alone, therefore, *if* a blurred reflection component is responsible for the soft excess it must originate from a different part of the disc responsible for broadening in the FeK region.

The dual reflector fit in which separate REFLIONX components are used for distant and inner reflection is also consistent with the typical accretion disc measurements

made above (Table C.4 on page 243). While higher resolution spectroscopy or new hard X-ray data from *NuStar* would be required to fully distinguish between the varying scenarios, the hard excess can be explained by either a high column partial coverer or a dual reflector, although crucially still without the requirement for extreme parameters such as high q and a for very centrally concentrated emission with an average $q = 2.4 \pm 0.2$, see Section 6.4.

4.3.2 The affect of absorption in complex sources

It is known that narrow ionised emission lines from FeXXV and FeXXVI can alter properties such as the measured inclination and emissivity of the accretion disc, however, the warm absorber is often overlooked. For instance warm absorber components can introduce spectral curvature, due to the bound-free L/K-shell transitions of abundant elements (Miller & Turner 2009). In particular, the warm absorber can play a significant role in the shape of the spectrum, not only at low X-ray energies, but also higher energies closer to the FeK region (Miller, Turner & Reeves 2008; Zycki et al. 2010). Utilising the soft X-ray energies below 3 keV allows a complete modelling of the warm absorber, adding the corresponding spectral curvature due to the cumulative effect of bound-free edges, which may not otherwise be taken into account without using the available data in the 0.6-3.0 keV range. Given a broadband model, the true nature of the FeK region and any broad red-wing can be determined after appropriate spectral curvature and observed ‘broadening’ from the required warm absorbers have been taken into account. Inappropriate modelling of the warm absorber can thus alter the observed strength and dominance of the broad red-wing over the X-ray continuum, which in turn will affect the extent to which black hole spin is required and its measured value.

In addition to the warm absorber properties, modelling the highly ionised absorption lines in the FeK region with a physically consistent XSTAR grid (such as with a turbulent velocity of 1000 km s^{-1} used here) ensures the corresponding curvature is removed from the spectrum. Highly ionised zones of gas are required in three of the

objects here: MCG–6-30-15, NGC 3783 and NGC 4051, also consistent with past studies (Reeves et al. 2004; Miller, Turner & Reeves 2008; Tombesi et al. 2010b; Lobban et al. 2011). Absorption lines in the Fe K region due to highly ionised species of iron (Fe XXV and/ or Fe XXVI) are found at the appropriate energy (or blue-shifted such as in NGC 4051 and to a lesser extent in MCG–6-30-15, with outflow velocities of 5600^{+800}_{-700} km s⁻¹ and 3200^{+400}_{-500} km s⁻¹ respectively). NGC 3783 shows both broadened line emission and absorption lines in the Fe K region, however, when a 1000 km s⁻¹ high ionisation XSTAR grid is included, the observed strength and shape of the broad line is slightly reduced with a KERRDISK $EW = 67^{+15}_{-29}$ eV reducing to $EW = 45^{+17}_{-26}$ eV (although still consistent within errors). The same can be said for the highly ionised absorption present in MCG–6-30-15 with diskline-type models proving marginally weaker after the introduction of the high ionisation XSTAR grid (i.e. $EW = 180^{+29}_{-54}$ eV reduced to 161^{+46}_{-44} eV).

Complex partial covering models can provide an alternative explanation of the broadband spectrum and therefore the residuals in the Fe K region. For example, Miller, Turner & Reeves (2009) construct a model which can explain all the features in the broadband spectrum of MCG–6-30-15 with no requirement for a diskline component (although no broad component was tested for), rather the apparent ‘broad’ residuals in the Fe K region are accounted for with ‘complex clumpy’ absorbers. Here, however, even when partial covering absorption models are applied to the X-ray spectra, the addition of a broad iron line component still appears to be required in the case of MCG–6-30-15, but only marginally in NGC 3516 and NGC 4051.

4.3.3 Is MCG–6-30-15 not maximal?

Previous analyses of MCG–6-30-15 have claimed a very strong, broad iron line whilst requiring that the central black hole is spinning very rapidly in order to account for the extreme width of the broad line. Miniutti et al. (2007) measure $a > 0.92$ in a fit to the same *Suzaku* data which does not consider data below 3 keV in order to avoid the need to fit for the warm absorber. Here the full broad-band data available is used, fitting

in the 0.6-100.0 keV range, using a combination of the XIS, HXD and BAT detectors in order to properly account for any absorption components which may be present in addition to the reflection hump above 10 keV. Taking the warm absorber components into account prior to considering emission from central regions close to the BH reveals that while the majority of the effects due to the warm absorption occur at low energies (< 3 keV), significant spectral curvature is added in MCG-6-30-15 at higher energies (Zycki et al. 2010). Much of the very broad red-wing observed by Miniutti et al. (2007) is reduced, resulting in a much weaker broad line component than has previously been suggested. This results in a broad line feature which may originate from emission close to a BH with spin $a = 0.49_{-0.12}^{+0.20}$ and lower emissivity of $q = 2.7_{-0.1}^{+0.2}$ while the near maximal spin required by Reynolds et al. (2005) and Miniutti et al. (2007) is excluded at high confidence levels in the model here ($\Delta\chi^2 = +70$; see Table 4.2 and Figure 4.4).

In this analysis, hard X-ray emission in excess over those which can be reproduced by a single REFLIONX are accounted for using a high column partial coverer. Indeed in MCG-6-30-15 Miller, Turner & Reeves (2008) successfully model the entire 0.5-45.0 keV spectrum through the use of absorbers and partial covering. The full model formed here also includes such a component, although its effect upon the broadening in the FeK region is subtle. However, even if no partial covering model is included, a maximally rotating BH is still ruled out at a high confidence level ($\Delta\chi^2 = +17$) as can be seen in Table 4.3 and Figure 4.7.

4.3.4 A retrograde SMBH spin in NGC 3783?

Retrograde SMBH spin has been thought of as a mechanism through which the central BH can power radio jets in AGN. Garofalo (2009) notes that accretion onto retrograde black holes can provide a powerful mechanism resulting in higher Blandford-Znajek luminosities than those in the prograde spin case due to R_{ISCO} being located further away from the SMBH, indeed some radio-loud AGN have tentatively been found to have inner disc truncations at $\sim 8 - 9 R_g$, e.g. (3C 120, Kataoka et al. 2007) with $R_{\text{ISCO}} \sim 9 R_g$ for a maximally spinning *retrograde* BH.

The line profile produced from emission surrounding a negatively spinning BH is narrower than that obtained from a positively spinning BH, however, measuring a retrograde spin is not necessarily representative of emission occurring from simply distant regions. The inner radius of emission of the accretion disc varies according to the spin of the central BH with a maximally rotating prograde BH producing $R_{\text{ISCO}} = 1.23 R_g$, a Schwarzschild BH producing $R_{\text{ISCO}} = 6 R_g$ and maximally rotating retrograde BH producing $R_{\text{ISCO}} \sim 9 R_g$, i.e., R_{ISCO} increases with decreasing positive spin. Even assuming a maximally rotating retrograde BH (the largest and furthest out value of R_{ISCO}), emission still occurs close enough to the central black hole for substantial relativistic effects and Doppler broadening. The resultant line profile is therefore not equivalent to purely distant emission. Figure 2.14 in Section 2.5.6 shows a comparison between the line profiles produced with the RELLINE model with spin varying from $a = -0.998$ to $a = +0.998$. However, it could also be that the BH is not retrograde, rather that the inner radius of the accretion disc is truncated short of the ISCO.

In this analysis the BH spin in NGC 3783 is estimated to be $a < -0.04$ at the 90% confidence level (for one interesting parameter), with Figure 4.8 suggesting a best-fitting intermediate retrograde BH spin. Accretion disc parameters obtained with the RELLINE model are consistent with those obtained with the KERRDISK model, measuring an emissivity $q = 3.2_{-0.4}^{+0.4}$ and a low inclination of $i < 17^\circ$.

A recent analysis of NGC 3783 by Brenneman et al. (2011) of the same *Suzaku* data has suggested a BH spin of $a > 0.98$ with an accretion disc emissivity of $q = 5.2_{-0.8}^{+0.7}$ using a dual reflector model, i.e. PEXMON+(REFLIONX*RELCONV). This contrasts significantly with the estimates made here, despite Brenneman et al. (2011) including warm absorber components in their fit to the 0.7-45.0 keV data (while ignoring 1.5-2.5 keV due to calibration uncertainties). Brenneman et al. (2011) also allow for partial covering which is not required in the baseline model formed here (Table C.2 on page 241). The highly ionised absorber in the Fe K region detected here (e.g. Fe XXV absorption, $\Delta\chi^2 = -33$) and by Reeves et al. (2004) in *XMM-Newton* data is not included in their fit, instead a warm absorber with $\log \xi \sim 2.53$ is claimed to model this feature sufficiently. There are also variations in the modelling of the accretion

disc itself, for example Brenneman et al. (2011) require a super-solar iron abundance of $Z_{\text{Fe}} = 3.7_{-0.9}^{+0.9}$ and a broken emissivity law with $q_{\text{in}} = 5.2_{-0.8}^{+0.7}$, $R_{\text{br}} = 5.4_{-0.9}^{+1.9} R_{\text{g}}$ and $q_{\text{out}} = 2.9_{-0.2}^{+0.2}$, whereas the analysis here provides a good fit to the broad-band data with purely Solar iron abundance and a single (unbroken) emissivity index of $q = 3.2_{-0.4}^{+0.4}$ (Table 4.4, using RELLINE, $\chi_{\nu}^2 = 1.057$).

In order to test the conclusions here, a model is formed using essentially the same reflection components, i.e. PEXRAV+K α +K β +(REFLIONX*RELCONV) modified by warm absorption, but maintaining Solar abundances and the single emissivity law. This brief test confirms the results found here and changes the estimated spin to $a = -0.2_{-0.65}^{+0.05}$ ($\chi_{\nu}^2 = 1.072$). Further to this, allowing for a broken emissivity index and allowing the iron abundance to vary does not reproduce the Brenneman et al. (2011) results and relaxes the estimates upon the spin parameter a , while the abundance remains approximately Solar and there is no indication for the requirement of a broken emissivity, i.e., no significant improvement in the quality of the fit. It is possible that the treatment of the absorbing components, soft excess and assumptions regarding the super-Solar iron abundance and broken emissivity law may lead to the higher spin estimated by Brenneman et al. (2011). The overall fit to the 0.7-45.0 keV data in Brenneman et al. (2011) is poor, mostly influenced by the soft X-ray energies ($\chi_{\nu}^2 = 1.381$, in contrast to the best-fit model here of $\chi_{\nu}^2 = 1.057$). However, it is not clear whether the narrow soft X-ray emission lines present in the *Suzaku* data are included within the Brenneman et al. (2011) analysis. Indeed a complete modelling of the broad-band data (including any soft emission lines) may alter the BH spin estimate. A more in-depth comparison of these two differing interpretations for the SMBH in NGC 3783 is made in Section 5.4.5.

5 Analysis of the full *Suzaku* sample

The analysis of the X-ray spectra of AGN can reveal information regarding the inner regions of the accretion disc, the AGN environment as a whole and subsequently the super massive black hole (SMBH) at its heart. It was suggested by Fabian et al. (1989) that emission occurring from the very inner regions of the accretion disc may be visible and subsequently broadened by Doppler motions and relativistic effects. The majority of AGN spectra show narrow line emission from neutral iron at 6.4 keV ($\text{Fe K}\alpha$) likely originating from distant material, e.g. the torus or the outer regions of the accretion disc (Krolik & Kallman 1987; Nandra 2006), particularly strong due to the high abundance and fluorescent yield of iron. If $\text{Fe K}\alpha$ emission additionally arises from material close to the central SMBH it will become relativistically broadened (Fabian et al. 1989; Laor 1991), producing a both blue and red-wings to the traditionally narrow line profile.

In some AGN spectra this relativistic $\text{Fe K}\alpha$ emission may be strong enough to be observed allowing its shape and strength measured using disk-line emission models such as LAOR, KYRLINE, KERRDISK and RELLINE (Laor 1991; Dovčiak et al. 2004; Brenneman & Reynolds 2006; Dauser et al. 2010). The application of these models allows properties such as the inclination and emissivity index of the disc to be measured in addition to the typical inner radius of emission and in some cases the spin of the central SMBH (Nandra et al. 2007; Patrick et al. 2011a). Gaining information regarding the distribution of SMBH spins is an essential tool in aiding our understanding of galaxy evolution and distinguishing between models such as prolonged or chaotic accretion and also the effect of mergers upon the SMBH spin (Hughes & Blandford 2003; Volonteri et al. 2005; King & Pringle 2007; Rezzolla et al. 2008). A spin distribution skewed towards higher values ($a \sim 0.998$) would suggest prolonged accretion, whereas low SMBH spin ($a \sim 0$) would indicate chaotic accretion models are more appropriate. In addition to this, the magnetic extraction of BH rotational energy through the Blandford-Znajek effect (Blandford & Znajek 1977) could cause a reduction in the spin

(i.e. towards zero) of the SMBH in some AGN (Berti & Volonteri 2008).

Recent publications have made steps towards making spin estimates of SMBHs in a variety of AGN, including those which feature low levels of intrinsic absorption thereby offering the simplest spectrum to analyse, avoiding complications regarding the degree of spectral curvature introduced with warm absorbing zones (Miniutti et al. 2009; Schmoll et al. 2009; Patrick et al. 2011a; Emmanoulopoulos et al. 2011). More complex AGN spectra have also been analysed and revealed further spin estimates, e.g. MCG-06-30-15 (Miniutti et al. 2007; Patrick et al. 2011b), Mrk 79 (Gallo et al. 2011) and NGC 3783 (Brenneman et al. 2011; Patrick et al. 2011b). However, as discussed in Patrick et al. (2011a), the estimated SMBH spin is highly model dependent and strongly related to the treatment of features such as the soft excess or any intrinsic absorbing zones. Assuming a Comptonisation origin of the soft excess results in a range of low to intermediate spins, whereas using a high degree of relativistic blurring to smooth the discrete soft emission lines into a continuum typically forces the spin to near maximal values and requires very high disc emissivities.

Chapters 3 and 4 included an analysis of the ‘bare’ Seyferts and deep observations of Seyfert 1 AGN which give the best opportunity for placing estimates upon the spin of SMBHs in Seyfert 1 AGN which have been observed with *Suzaku*. This chapter completes this work by conducting an analysis of all the Seyfert 1 AGN which have been observed by *Suzaku* but which still have observations with a sufficient number of 2-10 keV counts for an analysis of the Fe K region to be statistically worthwhile. If a relativistically broadened iron line is present in the Fe K region then this analysis is able to make estimates of the properties of the line profile with the aim of calculating the average properties and frequency of occurrence of broad iron lines in Seyfert 1 AGN. Such as, for example, the typical inclination, emissivity and inner radius of emission of the accretion disc. As a consequence of a study based upon an analysis of the Fe K region, robust models of the broadband spectrum must be formed including warm absorption zones, partial covering geometries, the soft and hard excesses, high velocity outflows and the prevalence of distant narrow emission lines from H- and He-like iron.

The contents of this chapter are based upon the work in all three first-author

papers published during the course of this PhD: Patrick et al. (2011a, 2011b and 2012). This discussion of the results in this chapter are included in the subsequent Chapter 6 in order to place the results in the broader context of iron line emission from near to black holes in AGN.

5.1 The *Suzaku* sample

The objects included within this sample are listed in Table 5.1 and are all the Seyfert 1-1.9 AGN with exposures > 50 ks and 30 000 0.6-10.0 keV counts per XIS which have been observed with *Suzaku* with data publicly available in the *Suzaku* data archive¹ as of 09/2011 (see Table A.1 on page 224 for number of counts per object). This is to ensure that if a broad line of $EW \sim 100$ eV is present in the FeK region of an AGN (taken from the estimated average equivalent widths of previous analyses, e.g. Nandra et al. 2007, Patrick et al. 2011a, 2011b) it can be detected and modelled with broad Gaussian at the 90% confidence level in an X-ray spectrum with ~ 60 000 total XIS-FI 2-10 keV counts. Assuming that in each observation a minimum of two XIS-FI detectors are operational, 30 000 counts per XIS resulting in 60 000 2-10 keV counts once the front-illuminated XIS data have been co-added, resulting in a sufficient number of counts to detect a typical broad line if it is present.

Data is also included from some type 1 Seyfert like radio-loud (BLRGs – non-Blazar due to the dominance of the relativistic jet) AGN provided they fit the above exposure and count selection criteria. High energy X-ray data from *Swift*/BAT is also used in addition to that obtained from the HXD detector onboard *Suzaku* (but allowing the relative cross-normalisation to vary between *Suzaku* and *Swift*); therefore the total energy range covered is 0.6-100.0 keV. Full details of the observations included are listed in Table A.1 on page 224.

In some instances, objects may have been observed on numerous occasions, provided that there is little variation in the spectra between the data sets they are com-

¹<http://heasarc.gsfc.nasa.gov/>

Table 5.1: The full *Suzaku* Seyfert sample.

Object	RA (J2000)	Dec (J2000)	Redshift	N_H (Gal) (10^{22}cm^{-2})
1H 0419–577	04 26 00.8	–57 12 00.4	0.1040	0.0126
3C 111	04 18 21.3	+38 01 35.8	0.0485	0.2910
3C 120	04 33 11.1	+05 21 15.6	0.0330	0.1060
3C 382	18 35 03.4	+32 41 46.8	0.0579	0.0714
3C 390.3	18 42 09.0	+79 46 17.1	0.0561	0.0347
3C 445	22 23 49.5	–02 06 12.9	0.0559	0.0559
4C 74.26	20 42 37.3	+75 08 02.4	0.1040	0.1160
Ark 120	05 16 11.4	–00 08 59.4	0.0327	0.0978
Ark 564	22 42 39.3	+29 43 31.3	0.0247	0.0534
Fairall 9	01 23 45.8	–58 48 20.5	0.0470	0.0316
IC 4329A	13 49 19.3	–30 18 34.0	0.0161	0.0461
IRAS 13224–3809	13 25 19.4	–38 24 52.7	0.0658	0.0534
MCG–02-14-009	05 16 21.2	–10 33 41.4	0.0285	0.0924
MCG–02-58-22	23 04 43.65	–08 41 08.6	0.0649	0.0291
MCG–05-23-16	09 47 40.2	–30 56 55.9	0.0085	0.0870
MCG–06-30-15	13 35 53.8	–34 17 44.1	0.0077	0.0392
MCG+8-11-11	05 54 53.6	+46 26 21.6	0.0205	0.1840
MR 2251–178	22 54 05.8	–17 34 55.0	0.0640	0.0640
Mrk 79	07 42 32.8	+49 48 34.8	0.0222	0.0527
Mrk 110	09 25 12.9	+52 17 10.5	0.0353	0.0130
Mrk 205	12 21 44.0	+75 18 38.5	0.0708	0.0280
Mrk 279	13 53 03.5	+69 18 29.6	0.0305	0.0152
Mrk 335	00 06 19.5	+20 12 10.5	0.0258	0.0356
Mrk 359	01 27 32.5	+19 10 43.8	0.0174	0.0426
Mrk 509	20 44 09.7	–10 43 24.5	0.0344	0.0344
Mrk 766	12 18 26.5	+29 48 46.3	0.0129	0.0178
Mrk 841	15 04 01.2	+10 26 16.2	0.0364	0.0222
NGC 1365	03 33 36.4	–36 08 25.5	0.0055	0.0134
NGC 2992	09 45 42.1	–14 19 35.0	0.0077	0.0487
NGC 3147	10 16 53.7	+73 24 02.7	0.0093	0.0285
NGC 3227	10 23 30.6	+19 51 54.2	0.0039	0.0199
NGC 3516	11 06 47.5	+72 34 06.9	0.0088	0.0345
NGC 3783	11 39 01.7	–37 44 18.9	0.0097	0.0991

Table 5.1: *continued* - The full *Suzaku* Seyfert sample

Object	RA (J2000)	Dec (J2000)	Redshift	N_H (Gal) (10^{22}cm^{-2})
NGC 4051	12 03 09.6	+44 31 52.8	0.0023	0.0115
NGC 4151	12 10 32.6	+39 24 20.6	0.0033	0.0230
NGC 4593	12 39 39.4	-05 20 39.3	0.0090	0.0189
NGC 5506	14 13 14.9	-03 12 27.3	0.0062	0.0408
NGC 5548	14 17 59.5	+25 08 12.4	0.0172	0.0155
NGC 7213	22 09 16.3	-47 09 59.8	0.0058	0.0106
NGC 7314	22 35 46.2	-26 03 01.7	0.0048	0.0150
NGC 7469	23 03 15.6	+08 52 26.4	0.0163	0.0445
PDS 456	17 28 19.8	-14 15 55.9	0.1840	0.1960
PG 1211+143	12 14 17.7	+14 03 12.6	0.0809	0.0274
RBS 1124	12 31 36.4	+70 44 14.1	0.2080	0.0152
SWIFT J2127.4+5654	21 27 45.0	+56 56 39.7	0.0144	0.7650
TON S180	00 57 19.9	-22 22 59.1	0.0620	0.0136

bined and a single analysis is performed. If the observations do indeed show significant spectral variability, a separate analysis is performed on each data set, although with similar model components and inferred geometries where possible, e.g. the inclination angle of the accretion disc would be linked between observations. This is with the aim of creating a model which is appropriate for multiple epochs of the same object.

Objects which have been observed on multiple occasions but where the X-ray spectra (or spectral shape) does not appear have varied by a significant amount (e.g. other than simple changes in power-law normalisation) are combined into a single data file using the MATHPHA, ADDRMF and ADDARF ftools² and then a suitable model is fit to the data. This is the case for IC 4329A, MCG-06-30-15, Mrk 509, Mrk 841, NGC 2992 and NGC 5548. However, if there are discernible differences between multiple observations of the same object (e.g. differing spectra shapes or changes in absorption), these data sets are analysed separately as noted above. Such an analysis is performed for Fairall 9, NGC 1365, NGC 3227, NGC 3516, NGC 3783 and NGC 4051. Both of the 2006 observations of NGC 5506 are combined into a single spectrum

²<http://heasarc.gsfc.nasa.gov/ftools/>

while the 2007 observation is kept separate. Similarly, the later three observations of 3C 120 are combined whereas the first observation (OBSID: 700001010, see Table A.1 on page 224) is analysed separately. MCG–06-30-15 was observed on three occasions in January 2006, this analysis makes use of all three observations and the time averaged spectrum is used in the main analysis as per Chapter 4. Analysis of the individual observations yields FeK line profiles which were consistent within errors and as such all three of the January 2006 observations have been co-added with the above tools.

5.2 Model construction and the implied geometries

Spectral analysis and model fitting is performed from within XSPEC v 12.6.0q (Arnaud 1996), all models are modified by Galactic absorption which is accounted for by the WABS multiplicative model (Morrison & McCammon 1983). The respective Galactic column densities were obtained using the *NH ftool* for each source giving the weighted average N_{H} value of the LAB Survey of Galactic HI (Kalberla et al. 2005), using abundances from Anders & Grevesse (1989). Data are fit over the full 0.6-100.0 keV range available, excluding those regions affected by the uncertainties in the XIS calibration (i.e. 1.7-1.95 keV). The χ^2 minimisation technique is used throughout, all errors are quoted at the 90% confidence level ($\Delta\chi^2 = 2.71$ for one interesting parameter). Where the significance of components is quoted in terms of $\Delta\chi^2$, the component in question has been removed from the model and the data refit to ensure that the order in which components are added to the model does not affect the quoted statistical significance.

The data used in this analysis are selected such that there are a sufficient number of counts for detailed spectral analysis to be conducted. The inclusion of hard X-ray data from the HXD onboard *Suzaku* and BAT onboard *Swift* from the 58 month BAT catalogue (Baumgartner et al. 2010) means that the strength of reflection continuum and its contribution to the FeK region can be analysed in more detail than in previous studies of Seyfert 1 spectra, e.g. Nandra et al. (2007) and de la Calle Pérez et al. (2010), which only consider the 2.5-10.0 keV and 2.0-10.0 keV energy ranges respectively. The

wider 0.6-100.0 keV energy bandpass as used in this sample means that a full treatment must be given to all the main components of the X-ray spectrum of these Seyfert 1 AGN, namely the soft excess, Compton reflection, Galactic absorption, warm absorbers and any highly ionised outflows or relativistic broadening which may be present. In order to model the X-ray spectra in this sample as consistently and uniformly as possible models are constructed according to the criteria in the following sections.

5.2.1 Modelling of the soft excess

A number of AGN spectra show an excess over a simple POWERLAW at lower X-ray energies, typically < 2.0 keV, this relatively common feature has been termed the ‘soft excess’. The origin of the soft excess is as yet unknown, however, there are a number of different interpretations and methods with which to model it (see Chapter 2, Section 2.5.1). One interpretation is that the soft excess is produced by the Compton up-scattering of EUV seed photons from the disc in a hot plasma or corona lying above the disc. For example, the COMPTT model (Titarchuk 1994) allows for a large variation in photon seed temperature while still producing a relatively constant output photon temperature as is required by many of the observed soft excesses in AGN (Gierliński & Done 2004). This interpretation of the soft excess is also used throughout this analysis, consistent with the method in Patrick et al. (2011a, b); similar results can also be obtained with a second step POWERLAW component, i.e., it is essentially a steep, soft, featureless continuum.

The above methods assume a smooth shape to account for the soft excess, however, alternatives have been suggested, e.g., an atomic origin (Brenneman & Reynolds 2006). Soft X-ray emission lines emitted from regions close to the central SMBH are relativistically blurred and broadened, much in the same way as the often observed broad 6.4 keV Fe $K\alpha$ emission line and its red-wing. A series of discrete emission line features are then relativistically blurred to such an extent that they merge to form a smooth continuum (Ross, Fabian & Ballantyne 2002). A number of AGN have been modelled in this fashion, e.g., Ark 120, Fairall 9 & Mrk 335 (Schmoll et al. 2009; Nardini et

al. 2010; Patrick et al. 2011a; Walton et al. 2013), although the significant amount of relativistic blurring required to smooth the characteristically narrow features into a broad continuum forces the accretion disc emissivity index to high values ($q > 4.5$) and SMBH spin towards near maximal ($a \sim 0.998$). Indeed, Schmoll et al. (2009) note that ignoring the XIS data below 2 keV (to avoid fitting the soft excess) relaxes the spin constraint to low values. These parameters are often at odds with those similarly derived from the asymmetric line profile from the FeK region (Patrick et al. 2011a and Chapter 3), however, given the assumption that the material responsible for both the soft emission lines and FeK α emission is located in the same region, it is logical to assume that estimated accretion disc and SMBH parameters should be consistent (Patrick et al. 2011a).

Note that relativistic blurring of the reflection component at soft X-ray energies can still contribute towards the soft excess, however, the soft X-ray flux from relativistically blurred emission of the inner regions does not dominate in comparison to the flux from the Comptonisation component. Using this Comptonised disc emission approach ensures the residuals in the FeK region drive the fit with the majority of the soft X-ray flux already accounted for with the COMPTT model, leaving a diskline model or convolution thereof to model the relativistic broadening in the FeK region.

5.2.2 Compton reflection

Given that the data used within this sample includes contributions from high energy X-ray detectors such as *Suzaku*'s HXD and *Swift*'s BAT, a picture can be formed of the hard X-ray component of AGN spectra extending up to ~ 100 keV. As noted in Section 1.6.2, the Compton reflection hump at ~ 30 keV can be used to measure the strength of the reflection component and hence its contribution to the spectrum at lower energies, including the FeK region. Employing an ionised reflection model such as REFLIONX (Ross & Fabian 2005) allows properties such as the ionisation state, the iron abundance (Z_{Fe}) and strength of the reflection component to be measured while self-consistently including the Compton shoulder. The REFLIONX model includes narrow emission lines

at soft X-ray energies in addition to a narrow Fe K α line, these line features remain narrow in nature under the assumption that these originate from reflection off material sufficiently distant from the SMBH that relativistic effects are negligible.

An *unblurred* REFLIONX component representative of reflection off distant material (e.g. the torus or outer regions of the accretion disc) is included in all AGN spectra showing evidence for a hard excess. As stated above and in Section 2.5.2, in this full analysis the REFLIONX model is used to account for the distant near neutral reflection continuum with the input photon index Γ tied to that of the intrinsic POWERLAW. Neutral narrow Fe K α and the accompanying Fe K β emission at 6.4 keV and 7.056 keV respectively are ubiquitous in AGN spectra (Nandra et al. 2007). Fe K β emission at 7.056 keV with flux $F_{K\beta} = 0.13 \times F_{K\alpha}$ is not included self-consistently in REFLIONX which is therefore modelled using a narrow Gaussian of fixed width $\sigma = 0.01$ keV and with flux fixed at the value obtained during an initial parameterisation of the Fe K region and the narrow Fe K α flux when modelled with a Gaussian.

5.2.3 Emission lines from distant material

Previous studies of the iron line regions in Seyfert AGN by Bianchi et al. (2004), Nandra et al. (2007) and Patrick et al. (2011a, b) also suggest that ionised species of iron are relatively common at energies of 6.7 keV and 6.97 keV for Fe XXV and Fe XXVI respectively. Ionised lines in the Fe K region (such as Fe XXV at $\sim 6.63 - 6.7$ keV and Fe XXVI at 6.97 keV) are accounted for with narrow Gaussians ($\sigma = 0.01$ keV) if and when required, although in some circumstances these can be indistinguishable from the blue-wing of a relativistically broadened Fe K α line profile. Although soft emission lines are included in REFLIONX, these are also added on an ad-hoc basis (as in Chapter 4) when required and as such are modelled using narrow Gaussians of fixed width $\sigma = 0.01$ keV, e.g., O VIII or Ne IX emission from distant photoionised gas, e.g., the BLR or NLR.

5.2.4 Warm absorption

The X-ray spectra of many AGN feature one or more zones of warm absorbing gas, while primarily affecting the spectrum at soft X-ray energies, with higher column densities (e.g. $> 10^{22} \text{ cm}^{-2}$) it can add subtle curvature above 2.5 keV, see Section 2.5.3 and Figure 2.7. Previous studies (e.g. Miniutti et al. 2007; Nandra et al. 2007) restrict their analysis to 2.5-10.0 keV to avoid complications with the warm absorber, instead choosing to focus in upon the Fe K region. However, as found in Reeves et al. (2004), Turner et al. (2005), Miller, Turner & Reeves (2009) and Patrick et al. (2011b) the effects of the warm absorber extend even to the Fe K region, contributing significantly to the strength of the observed red-wing below 6.4 keV. For example, in MCG-06-30-15 Miniutti et al. (2007) model the time averaged January 2006 spectra without absorption, resulting in an apparent strong broad Fe K α line and near maximal SMBH spin; while a full treatment of the warm absorber extensively reduces the strength of the broad component and subsequently BH spin to more intermediate values and ruling out maximal spin at high confidence levels (Zycki et al. 2010; Patrick et al. 2011b).

To model the soft X-ray warm absorber components in this analysis, an XSTAR generated grid is used (Kallman et al. 2004) which is illuminated by a photon index of $\Gamma = 2$, abundances fixed at solar values (except Ni, which was set to zero) and with a turbulent velocity of 100 km s^{-1} . The grid is well suited to accounting for typical absorption zones due to its wide range in column density ($5 \times 10^{18} \text{ cm}^{-2} < N_{\text{H}} < 5 \times 10^{24} \text{ cm}^{-2}$) and ionisation parameter ($0 < \log \xi < 5$). During the fitting process absorption zones are added as required, in some objects more than one zone may be statistically required and in exceptional circumstances a grid with a higher turbulent velocity may be required to model highly ionised absorption in the Fe K region. This method is the same as described in Sections 2.5.3 and 4.2.1 although reiterated here.

5.2.5 Highly ionised absorption

Further to typical warm absorption, highly ionised absorbing zones of gas (where present) also play an important role in the FeK region and in the determination of the measured line parameters and strength of the observed red-wing (Reeves et al. 2004; Turner et al. 2005). Absorption lines indicative of such zones are fairly common in X-ray spectra of AGN, e.g., 1s-2p resonance lines from FeXXV and/or FeXXVI at their rest-frame energies, i.e., 6.7 keV and 6.97 keV respectively. There is also strong evidence for *blue-shifted* absorption lines in many AGN (Braitto et al. 2007; Tombesi et al. 2010a; Lobban et al. 2011; Gofford et al. 2013).

Here an XSTAR generated grid is used with a turbulent velocity of 1000 km s^{-1} (to better model the observed higher equivalent widths of the lines), an input continuum of $\Gamma = 2.0$ and a range in column density and ionisation parameter of $1 \times 10^{20} \text{ cm}^{-2} < N_{\text{H}} < 1 \times 10^{24} \text{ cm}^{-2}$ and $0 < \log \xi < 6$ respectively (as in Chapter 4).

5.2.6 Partial covering

Some AGN in this sample may show evidence for or require a partial covering geometry, i.e., where a percentage of the X-ray continuum is obscured by a surrounding zone of absorbing gas as described in Chapter 4 (e.g. Miller, Turner & Reeves 2009; Maiolino et al. 2010). In this analysis, such geometries are used to account for hard X-ray excesses over and above the reflection continuum, this can be taken into account by a high column density absorber with $N_{\text{H}} \sim 10^{24} \text{ cm}^{-2}$ taking the form (powerlaw + WA*powerlaw), see Section 2.5.5.

5.2.7 Relativistic line emission

The majority of X-ray lines originate from material sufficiently distant to the SMBH (e.g. the ubiquitous narrow 6.4 keV line) such that effects such as relativistic Doppler motions and gravitational redshift have a negligible effect upon the observed spectrum.

If, however, emission comes from the very inner regions of the accretion disc it will of course be subject to these effects. As discussed above, this is one interpretation for the commonly observed red-wing in the Fe K regions of some AGN which may remain after modelling the broad-band spectrum, taking into account warm absorbers which may be present. If an excess remains at $\sim 5 - 6.4$ keV, this is initially modelled using the relativistic line emission model RELLINE (Dauser et al. 2010). This allows properties such as the emissivity index and inclination of the disc to be measured in addition to placing estimates upon the spin of the central SMBH (or the inner radius of emission). A more comprehensive modelling of the inner regions of the accretion disc would include the accompanying blurred reflection spectrum. For example, a convolution of the RELLINE kernel (i.e. RELCONV, Dauser et al. 2010) with a table of reflection models (i.e. REFLIONX; Ross & Fabian 2005) allows relativistic effects to be applied to both the hard and soft X-ray reflection spectrum as well as to the Fe K α emission line at 6.4 keV, such an approach is investigated in Section 5.3.4. As stated in Section 5.2.1 blurring the reflected emission at soft X-ray energies can provide some explanation of the soft excess, however, it is noted that the main contributor to this emission can be via Comptonisation of soft photons, producing a soft powerlaw-like continuum below 2 keV.

5.3 Full *Suzaku* sample results

5.3.1 Baseline model

The baseline model is intended to model the entire 0.6-100.0 keV spectrum, accounting for features such as the underlying continuum, soft excess, *distant* reflection and both warm and neutral absorption. The baseline model acts as the null hypothesis whereby the X-ray spectrum of these AGN can be described by emission or absorption from purely distant material.

While the iron abundance, Z_{Fe} , of the REFLIONX component is left free to vary,

in some AGN the strength of the narrow FeK α core may force Z_{Fe} to unfeasibly high values (e.g. $Z_{\text{Fe}} > 3$) while improperly modelling the hard X-ray reflection spectrum due to the greater number of counts in the 5-6 keV region. To avoid this scenario, Z_{Fe} is fixed at Solar abundance and an additional narrow Gaussian of fixed width ($\sigma = 0.01$ keV) is added, to prevent interference with any broad component from the disc) at 6.4 keV to model the FeK α core while maintaining a good fit to the HXD and BAT data. Rather than simply being an ad-hoc solution, this could be representative of FeK α emission with no associated Compton reflection arising from Compton-thin matter such as the BLR or NLR as well as, for example scattering off a distant Compton-thick torus.

The warm absorber is treated as stated in Section 5.2.4 with successive zones of an XSTAR grid as statistically required. These zones are fixed at the redshift of the object, however, an outflowing component is allowed if no good fit can be found otherwise. If additional neutral absorption by an excess neutral N_{H} column in the AGN rest frame, this is modelled using ZPHABS. Meanwhile, some AGN such as Ark 120 and Fairall 9 may show no indication for a warm absorber component and as such are modified simply by Galactic absorption. A summary of the principal components found in these Seyfert 1 spectra can be found in Table 5.2.

5.3.2 Prevalence of typical features in X-ray spectra

As noted in Patrick et al. (2011b) the warm absorber below 2.5 keV has a significant affect upon the X-ray spectrum at higher energies, particularly important when attempting to test for the strength or indeed presence of a relativistically broadened red-wing in the FeK region. Subsequently the broadband 0.6-100.0 keV analysis conducted here suggests that the majority of Seyfert 1 AGN in this sample show evidence for at least one warm absorber zone or additional neutral absorption over the simple Galactic absorbing column.

Only 12/46 objects in this sample can be considered ‘bare’ in that no additional warm or neutral absorption whatsoever is required, these are 3C 390.3, Ark

120, Fairall 9, MCG–02-14-009, Mrk 110, Mrk 205, Mrk 335, Mrk 359, NGC 3147, NGC 7213, NGC 7469 and RBS 1124. These AGN are therefore straight forward to model, without any complications due to curvature from warm absorbing components, representing the most fiducial of AGN X-ray spectra simply consisting of ((POWERLAW+COMPTT+REFLIONX)*WABS), i.e., intrinsic power-law plus soft excess plus reflection, all of which are absorbed by a neutral Galactic line-of-sight column. Slightly more complex are those objects which are free from warm absorption, however, requiring an additional neutral absorbing column over and above that from the standard Galactic absorption. This represents 6/46 of AGN in the sample: 3C 111, 3C 120, MCG–05-23-16, NGC 2992, NGC 7314 and SWIFT J2127.4+5654. Note that the higher neutral absorption in 3C 111 is likely due to the presence of a giant molecular cloud in the line of sight, see Bania et al. (1991) and Rivers, Markowitz & Rothschild (2011b). Hence, a total of 19/46 objects in this sample do not indicate the presence of a *warm* absorbing component.

5.3.2.1 Absorbed Seyfert spectra – fully covering

The majority of the AGN in this sample do feature some degree of complex warm absorption (27/46), which is modelled with successive zones of a multiplicative XSTAR grid (see Table 5.2). The majority of these AGN are well modelled using one or more fully covering XSTAR grids with turbulent velocity $v_{\text{turb}} = 100 \text{ km s}^{-1}$ fixed at the redshift of the object (i.e. from Table 5.1).

Rather using the typical $v_{\text{turb}} = 100 \text{ km s}^{-1}$ XSTAR grid, some AGN in this sample require the use of an XSTAR generated grid with $v_{\text{turb}} = 1000 \text{ km s}^{-1}$, i.e., the turbulent velocity strongly exceeds the local thermal velocity of the absorbing ion, proving to be the dominant factor for absorption line broadening. This scenario is required when modelling the soft X-ray absorber in only 3/28 of objects featuring complex absorption: 3C 445, Ark 564 and IC 4329A. IC 4329A requires two low v_{turb} XSTAR grids in addition to the single high v_{turb} XSTAR grid. The warm absorber properties are parameterised in Table D.1 on page 245.

Table 5.2: Model applicability to each AGN. Comparison of components and features use to model each AGN; COMPTT is used to model the soft excess, an unblurred REFLIONX is used to model the reflection component if statistically required. ¹ Only an increase in the neutral Galactic column is required. ² No XSTAR grid is required in MCG-05-23-16, however, additional neutral absorption is used to absorb only the intrinsic POWERLAW. Residuals in the Fe K region are considered to be present if there is an improvement of $\Delta\chi^2 > 6.3$ with the addition of a broad Gaussian (see Table 5.3). ³ Only required in the 2006 observation of Mrk 766.

Object	Soft excess	Reflection	Partial covering	Warm abs.	High ξ abs.	Residuals at FeK
1H 0419-577	✓	✓	✓	✓	X	X
3C 111	X	X	X	X ¹	✓	✓
3C 120	✓	✓	X	X ¹	X	✓
3C 382	✓	✓	X	✓	X	✓
3C 390.3	✓	✓	X	X	X	✓
3C 445	X	✓	✓	✓	✓	✓
4C 74.26	X	✓	X	✓	X	✓
Ark 120	✓	✓	X	X	X	✓
Ark 564	✓	✓	✓	✓	X	X
Fairall 9	✓	✓	X	X	X	✓
IC 4329A	X	✓	X	✓	X	✓
IRAS 13224-3809	✓	X	✓	✓	X	✓
MCG-02-14-009	X	✓	X	X	X	X
MCG-02-58-22	✓	✓	X	✓	X	X
MCG-05-23-16	✓	✓	X	X ²	X	✓
MCG-06-30-15	✓	✓	✓	✓	✓	✓
MCG+8-11-11	X	✓	X	✓	X	✓
MR 2251-178	✓	X	X	✓	✓	✓
Mrk 79	X	X	X	✓	X	✓

Table 5.2: *continued* - Model applicability to each AGN. Comparison of components and features use to model each AGN; COMPTT is used to model the soft excess, an unblurred REFLIONX is used to model the reflection component if statistically required. ¹ Only an increase in the neutral Galactic column is required. ² No XSTAR grid is required in MCG-05-23-16, however, additional neutral absorption is used to absorb only the intrinsic POWERLAW. Residuals in the Fe K region are considered to be present if there is an improvement of $\Delta\chi^2 > 6.3$ with the addition of a broad Gaussian (see Table 5.3). ³ Only required in the 2006 observation of Mrk 766.

Object	Soft excess	Reflection	Partial covering	Warm abs.	High ξ abs.	Residuals at FeK
Mrk 110	✓	✓	X	X	X	X
Mrk 205	✓	✓	✓	X	X	X
Mrk 279	X	✓	✓	✓	X	X
Mrk 335	✓	✓	X	X	X	✓
Mrk 359	✓	✓	X	X	X	✓
Mrk 509	✓	✓	X	✓	X	✓
Mrk 766	✓	✓	✓	✓	✓	✓ ³
Mrk 841	✓	✓	X	✓	X	✓
NGC 1365	X	✓	✓	✓	✓	✓
NGC 2992	✓	✓	X	X ¹	X	✓
NGC 3147	X	✓	X	X	X	✓
NGC 3227	✓	✓	✓	✓	✓	✓
NGC 3516	X	✓	✓	✓	✓	✓
NGC 3783	✓	✓	X	✓	✓	✓
NGC 4051	✓	✓	✓	✓	✓	✓
NGC 4151	✓	✓	✓	✓	✓	X
NGC 4593	X	✓	X	✓	X	✓
NGC 5506	X	✓	✓	✓	X	✓
NGC 5548	X	✓	X	✓	✓	X

Table 5.2: *continued* - Model applicability to each AGN. Comparison of components and features use to model each AGN; COMPTT is used to model the soft excess, an unblurred REFLIONX is used to model the reflection component if statistically required. ¹ Only an increase in the neutral Galactic column is required. ² No XSTAR grid is required in MCG-05-23-16, however, additional neutral absorption is used to absorb only the intrinsic POWERLAW. Residuals in the Fe K region are considered to be present if there is an improvement of $\Delta\chi^2 > 6.3$ with the addition of a broad Gaussian (see Table 5.3). ³ Only required in the 2006 observation of Mrk 766.

Object	Soft excess	Reflection	Partial covering	Warm abs.	High ξ abs.	Residuals at Fe K
NGC 7213	✓	✓	X	X	X	X
NGC 7314	✓	X	X	X ¹	X	✓
NGC 7469	✓	✓	X	X	X	✓
PDS 456	✓	X	✓	X	✓	X
PG 1211+143	✓	X	X	✓	✓	X
RBS 1124	✓	✓	X	X	X	X
SWIFT J2127.4+5654	X	✓	X	X ¹	X	✓
TON S180	✓	✓	✓	✓	X	X
Fraction	31/46	39/46	16/46	27/46	14/46	32/46

5.3.2.2 Absorbed Seyfert spectra – partially covering

A reasonable fraction of the AGN in this sample (16/46) also require the application of a partial covering geometry whereby some fraction of the underlying power-law is subject to an extra zone of absorbing gas (the parameters are tabulated in Table C.2). The majority of the partial covering scenarios here involve high column density warm absorbing zones which have their largest effect at harder X-ray energies. For example, some AGN still exhibit a hard X-ray excess at high energies > 10 keV after the use of a single REFLIONX unblurred distant reflection component and require a partial coverer with $N_{\text{H}} \gtrsim 10^{24} \text{ cm}^{-2}$ to fully model the HXD and BAT data, see Figure 5.1. Due to the nature of a partial coverer with such a high column, there is not expected to be much interference with residuals in the Fe K region except at the Fe K edge (see Section 4.2.2.1). In some objects, residuals remain above 10 keV even after applying a reflection component such as an unblurred REFLIONX can be significant, see Figure 5.1, also see Turner et al. (2009) as example of the presence of a strong Compton-thick partial coverer. Tatum et al. 2013 apply this method of high column density partial coverers to explain the hard X-ray excesses in AGN.

Five AGN (NGC 1365, NGC 3227, NGC 3516 and NGC 4151) are best fit with a lower column density partial coverer with $N_{\text{H}} \sim 10^{23} \text{ cm}^{-2}$ which adds curvature towards lower energies at > 2 keV. In this region of the X-ray spectrum, there is likely to be some degree of interplay between the partial covering parameters (e.g. covering fraction, column density and ionisation) and the strength of ‘broad’ residuals in the Fe K region. Note that the partial coverer properties in NGC 1365 vary between each of the three *Suzaku* observations, in particular the second observation (OBSID: 705031010) requires an additional neutral absorber as well as a partially covering warm absorption zone, i.e. `POWERLAW + XSTAR*ZPHABS*POWERLAW`. Only IRAS 13224–3809 features a partial coverer with a lower column density of $N_{\text{H}} \sim 10^{22} \text{ cm}^{-2}$ which models small residuals remaining in the 2-4 keV spectrum. The 2-10 keV *Suzaku* spectrum of IRAS 13224–3809 only has a small number of counts and subsequently no great deal of information can be gathered regarding any partial covering scenario. It should be

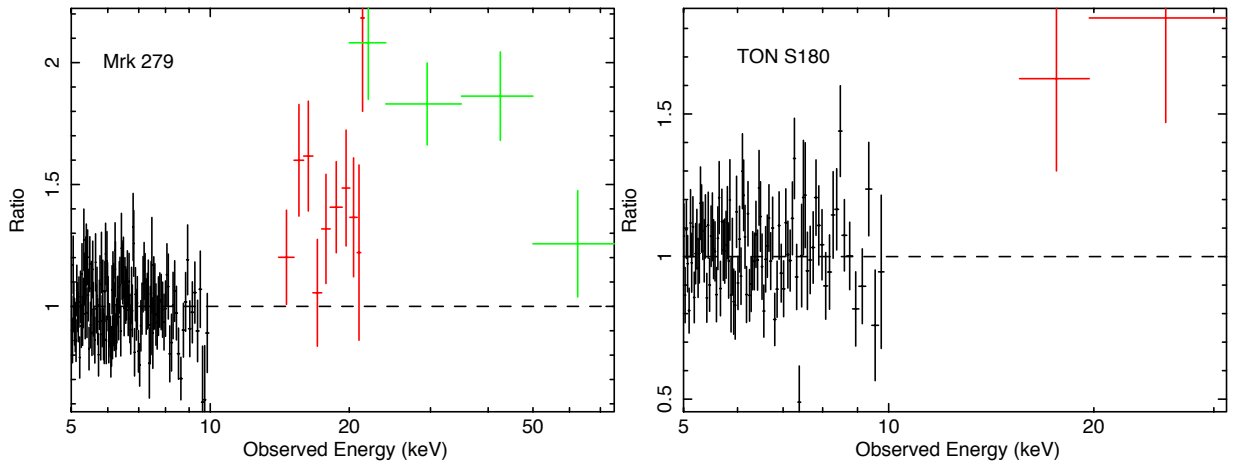


Figure 5.1: Examples of the hard excesses which sometimes remain after modelling the full broad-band spectrum with a reflection component. In the baseline model these have been accounted for using high column density partial covering geometries. The black data points are XIS, the red are HXD data and the green are BAT data from *Swift*.

noted that the majority of the partially covering zones in this sample are of low to neutral ionisation, e.g. $\log \xi < 2 \text{ erg cm s}^{-1}$.

5.3.2.3 Soft excess and reflector properties

The majority of the AGN in this sample show both soft and hard X-ray excesses above the basic intrinsic powerlaw. A substantial 31/46 AGN indicate an observed soft excess below $\sim 2 \text{ keV}$ (modelled as described in Section 5.2.1), however, this is lower than the fraction obtained in Porquet et al. (2004) in a selection of PG quasars who found that 19/21 objects exhibited a significant soft excess. It should be noted, however, that nearly all of the objects without a soft excess feature complex warm or neutral absorption. This can lead to any weak soft excess which may be present being ‘hidden’ or simply absorbed, thereby leave little trace or indication of its presence. Only MCG–02-14-009 and NGC 3147 are without additional absorption (either neutral or ionised) and still show no indications of a soft excess, whereas SWIFT J2127.4+5654

has sufficiently strong neutral absorption (no warm absorption) to mask the presence of a soft excess.

A large number of AGN in this sample also exhibit strong excesses at hard X-ray energies, indicative of reflection off distant material, e.g., the putative torus or outer accretion disc. 39/46 of objects in the sample are modelled using the REFLIONX reflection model, with properties such as ionisation and iron abundance Z_{Fe} left free to vary. The vast majority of AGN modelled using REFLIONX here are well fit with a neutral or close to neutral reflector ($\xi < 60 \text{ erg cm s}^{-1}$) with only Ton S180 featuring a moderately ionised reflector ($\xi \sim 270 \text{ erg cm s}^{-1}$). The remainder of the objects without a strong reflection component still feature neutral FeK α emission, however, IRAS 13224–3809 features neither a reflection component nor 6.4 keV FeK α emission.

In the majority of these AGN, the reflection component is well modelled with Solar iron abundance and in 23/39 of objects with evidence for strong reflection it is fixed at $Z_{\text{Fe}} = 1.0$. This fraction includes the scenario in which some proportion of the observed narrow FeK α flux additionally arises from material which may be in the broad line region (BLR), i.e., the FeK α core also originates from both reflection off distant matter and the BLR. This geometry is most evident when the strength of the narrow K α core is disproportionately stronger than the strength other reflector features such as the Compton hump, often indicated by what may be an unfeasibly high iron abundance, e.g., $Z_{\text{Fe}} > 3.0$ being forced into the fits. This is accounted for by fixing $Z_{\text{Fe}} = 1.0$ and including an additional narrow Gaussian at 6.4 keV (such as in MCG–05-23-16, Mrk 110, Mrk 509, NGC 2992, NGC 3147, NGC 3516, NGC 4151, NGC 4593 and NGC 7213). It is noted, however, that if this additional FeK α component originates from the BLR, it might be expected that the σ_{width} be higher, e.g., up to $\sigma \sim 0.10 \text{ keV}$ corresponding to a FWHM of $\sim 11000 \text{ km s}^{-1}$, typical of BLR clouds. While the exact origin of the line may be unknown (or indeed what proportion of the line flux originates where), the line width is kept at $\sigma = 0.01 \text{ keV}$ for consistency with the other additional narrow lines used in the models, noting that some moderate broadening consistent with BLR widths cannot be ruled out.

Only 4/39 of the remaining objects still require a super-Solar iron abundance;

namely 3C 120, Fairall 9, Mrk 335 and Ton S180. Sub-Solar iron abundance reflectors are found in 12/46 of objects and a good fit is found to both the Compton hump in the HXD and the flux of the narrow FeK α core with few residuals remaining. NGC 3227 and NGC 4051 (Lobban et al. 2011) are best fit with a sub-Solar iron abundance in conjunction with a narrow 6.4 keV Gaussian. This is in a similar fashion to above whereby the narrow FeK α flux exceeds that expected from a simple Solar abundance reflector, however, both of these objects appear to still have weaker relative reflection components, i.e. a sub-Solar reflector plus narrow Gaussian is preferred. The baseline model parameters for each object and observation are summarised in Table D.1 on page 245 and Table D.2 on page 252.

5.3.3 The Fe K region

5.3.3.1 Additional distant ionised emission

Similarly, the Fe K regions of these AGN are examined to determine whether emission lines due to ionised H and He-like species of iron are present, making up the final piece in the baseline models for each object. Lines at 6.63-6.70 keV and 6.97 keV (likely due to FeXXV and FeXXVI respectively) are emitted from highly ionised gas existing at large distances from the central SMBH. The presence of such lines has been well documented in many Seyfert 1 spectra and it should come as no surprise that they appear relatively common in this sample (Bianchi et al. 2004; Nandra et al. 2007; Bianchi et al. 2009; Patrick et al. 2011a). Approximately half (24/46) of the objects in this sample show evidence for FeXXV emission at ~ 6.7 keV, while fewer (18/46) show evidence for FeXXVI at 6.97 keV (Table D.2 on page 252). However, the lower fraction of H-like Fe detections may be due to its proximity to FeK β at 7.056 keV which is included self consistently in all objects in addition to the narrow 6.4 keV FeK α core.

5.3.3.2 Highly ionised absorption and outflows

Highly ionised absorption in the FeK regions of AGN can play a significant role in adding bound-free spectral curvature in the 6-7 keV band when modelled using a physically self-consistent XSTAR absorption grid. Accounting for such features in a self-consistent manner, i.e., using absorption tables rather than Gaussians, is therefore essential in order to successfully assess the strength of any observed broad redwing below 6.4 keV. A substantial proportion (14/46) of AGN in this sample are found to possess highly ionised zones which are somewhat blue-shifted with respect to absorption lines from FeXXV and FeXXVI at rest-frame energies of 6.7 keV and 6.97 keV, these are: 3C 111, 3C 445, MCG-06-30-15, MR 2251-178, Mrk 766, NGC 1365, NGC 3227, NGC 3516, NGC 3783, NGC 4051, NGC 4151, NGC 5548, PDS 456 and PG 1211+143, see Table D.2 on page 252. All of these zones (bar those in NGC 3783 and NGC 5548) are outflowing, i.e., the absorption lines are blue-shifted to higher energies with typical velocities of a few thousand km s^{-1} and column densities $1 \times 10^{21} \text{ cm}^{-2} < N_{\text{H}} < 1 \times 10^{24} \text{ cm}^{-2}$, see Table D.2 on page 252.

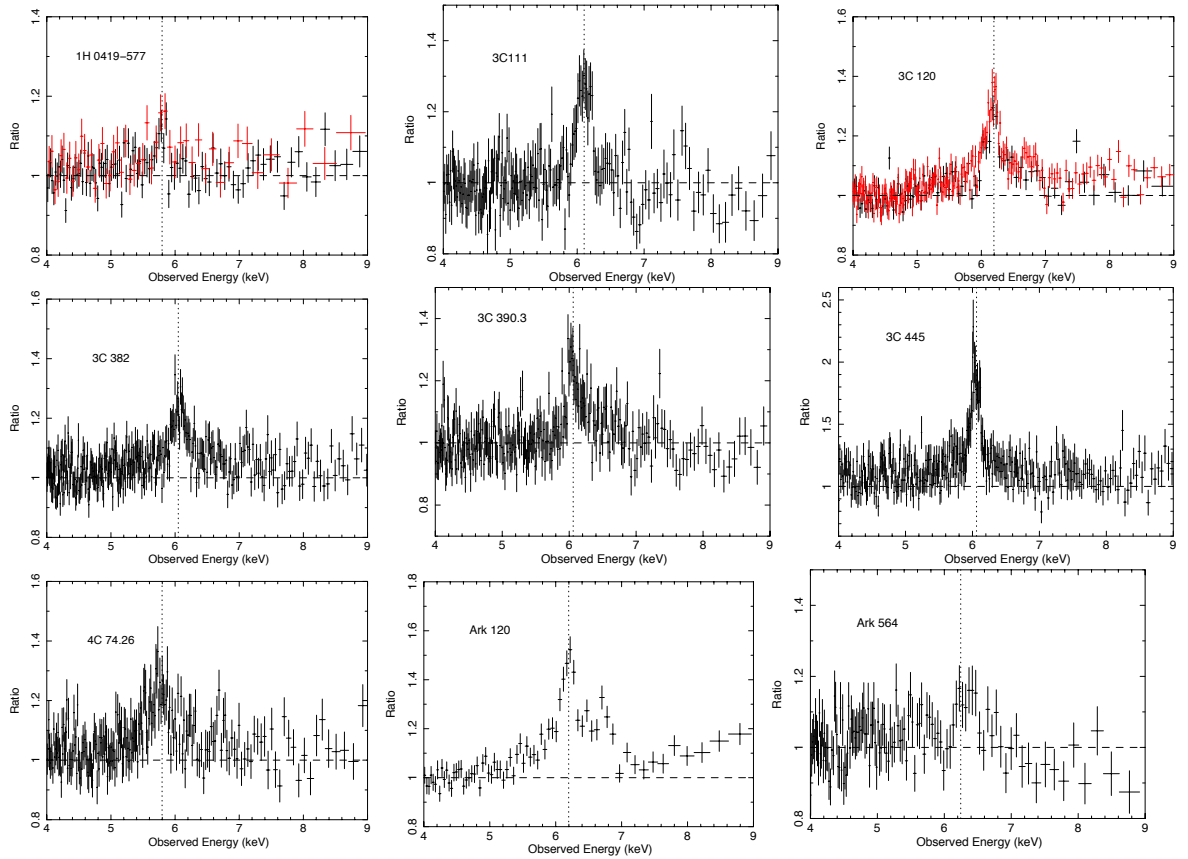


Figure 5.2: Ratio plots of the 4-9 keV residuals modelled with the baseline model minus REFLIONX, narrow lines and Fe K absorbers, i.e. the Fe K region is left totally unmodelled with only warm absorption at soft X-ray energies being taken into account in addition to the intrinsic power-law and COMP^TT (where required). The data has been refit after the removal of components. The vertical dashed lines represent 6.4 keV in the observed frames. Red data points indicate those from further observations.

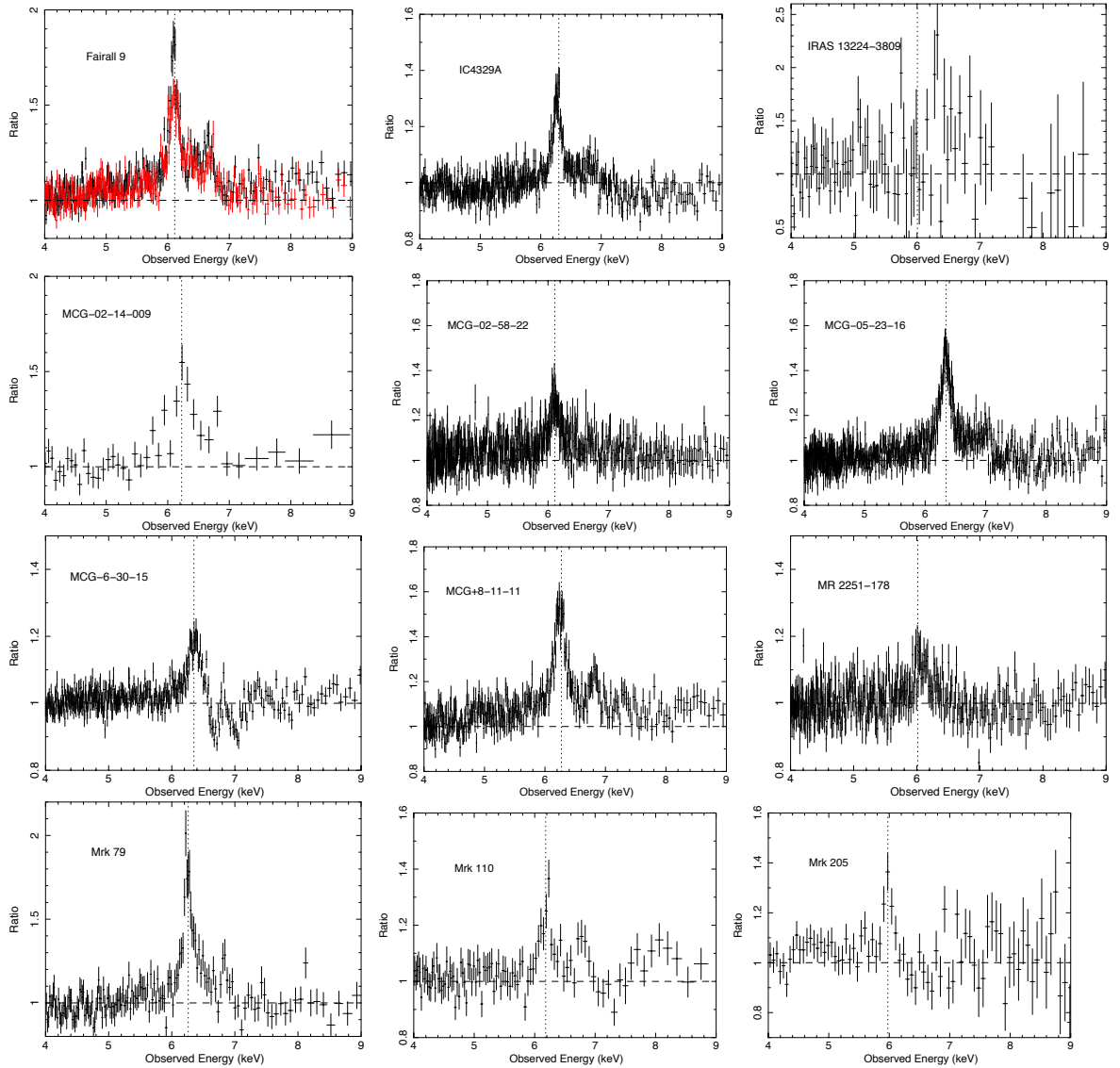


Figure 5.2: *continued* - Ratio plots of the 4-9 keV residuals without any modelling of the reflection component, i.e. the Fe K region is left totally unmodelled with only warm absorption at soft X-ray energies being taken into account in addition to the intrinsic power-law and COMPTT (where required). The data has been refit after the removal of components. The vertical dashed lines represent 6.4 keV in the observed frames. Red data points indicate those from further observations.

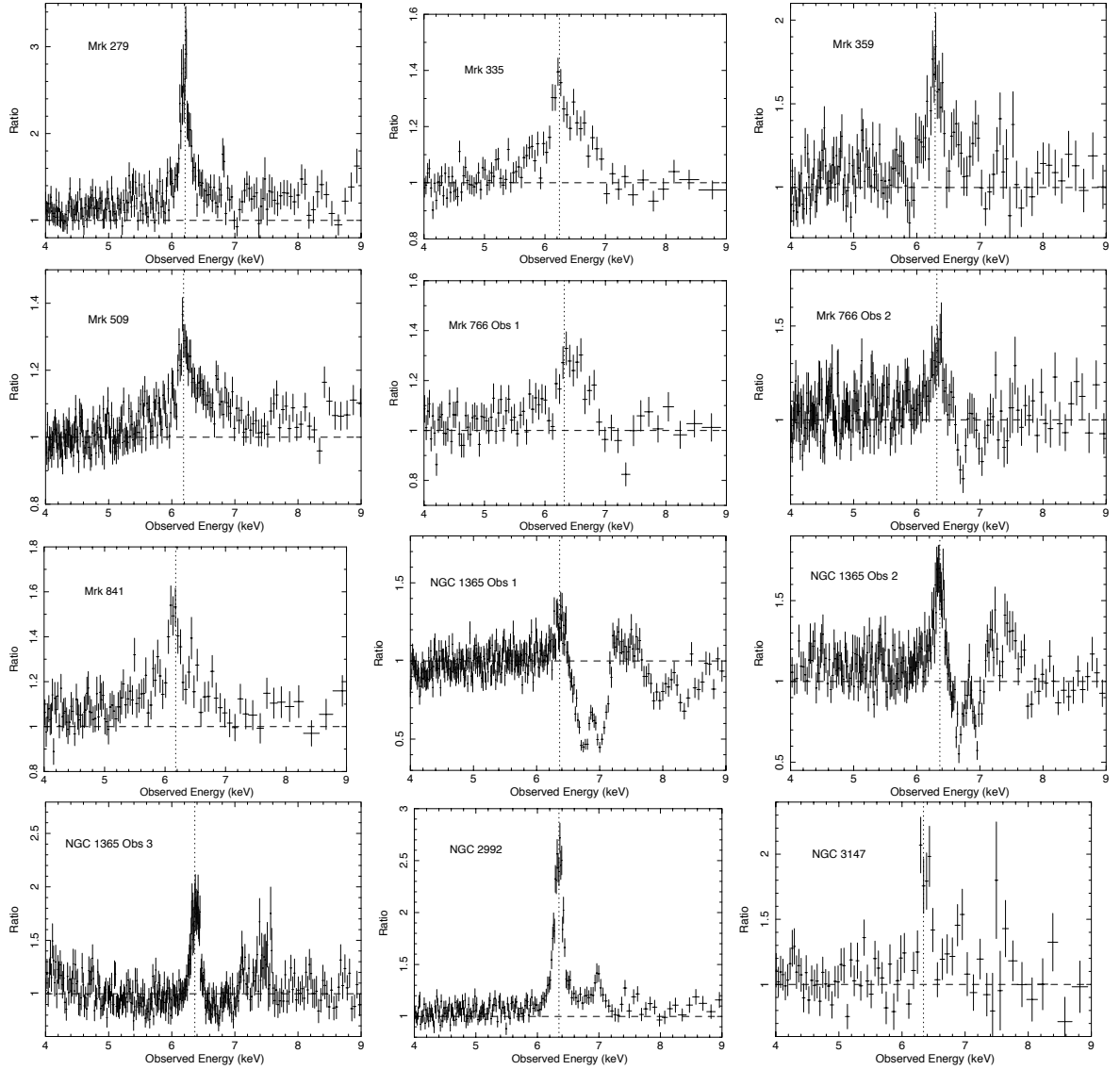


Figure 5.2: *continued* - Ratio plots of the 4-9 keV residuals without any modelling of the reflection component, i.e. the Fe K region is left totally unmodelled with only warm absorption at soft X-ray energies being taken into account in addition to the intrinsic power-law and COMPTT (where required). The data has been refit after the removal of components. The vertical dashed lines represent 6.4 keV in the observed frames. Red data points indicate those from further observations.

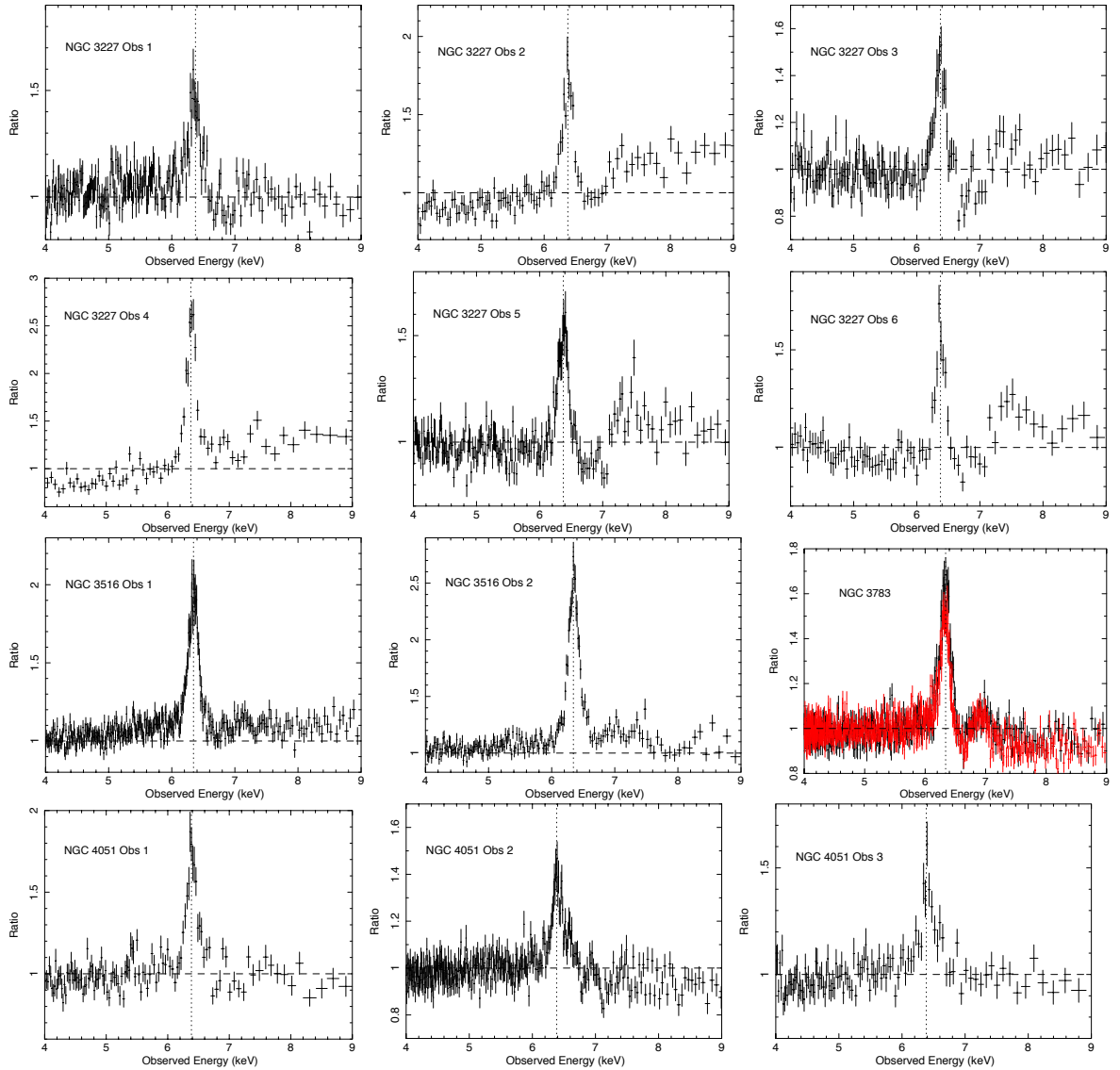


Figure 5.2: *continued* - Ratio plots of the 4-9 keV residuals without any modelling of the reflection component, i.e. the Fe K region is left totally unmodelled with only warm absorption at soft X-ray energies being taken into account in addition to the intrinsic power-law and COMPTT (where required). The data has been refit after the removal of components. The vertical dashed lines represent 6.4 keV in the observed frames. Red data points indicate those from further observations.

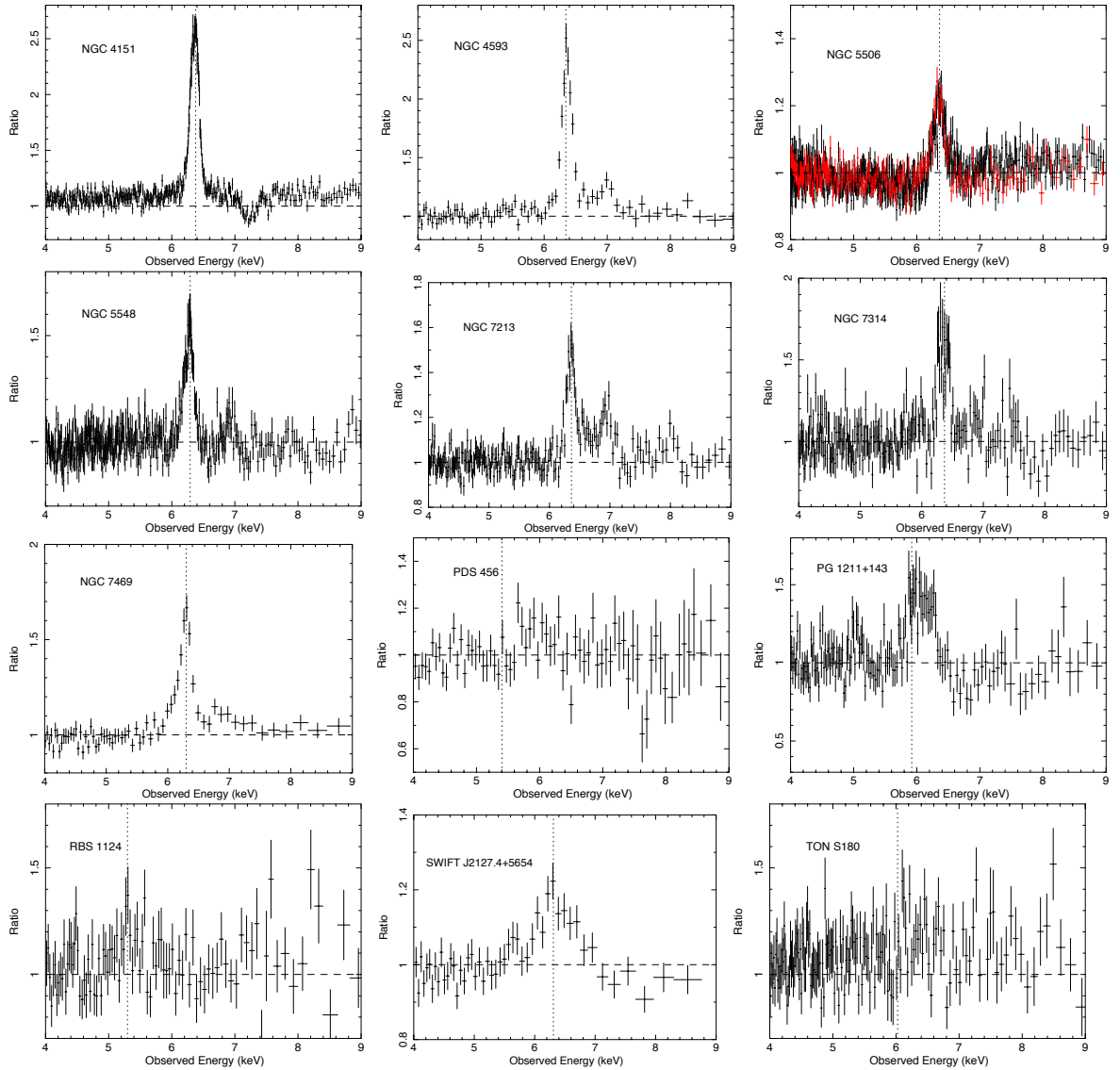


Figure 5.2: *continued* - Ratio plots of the 4-9 keV residuals without any modelling of the reflection component, i.e. the Fe K region is left totally unmodelled with only warm absorption at soft X-ray energies being taken into account in addition to the intrinsic power-law and COMPTT (where required). The data has been refit after the removal of components. The vertical dashed lines represent 6.4 keV in the observed frames. Red data points indicate those from further observations.

Table 5.3: Broad Gaussian parameterisation of Fe K region in addition to the baseline model. ^a Flux given in units (10^{-5} ph cm $^{-2}$ s $^{-1}$). ^b Parameters other than normalisation tied between multiple observations, all are tied in NGC 5506. – Indicates that no broad Gaussian can be fit, i.e. no discernible reduction in χ^2 whatsoever. A negative value in the $\Delta\chi^2$ column denotes an improvement in the fit.

Object	LineE (keV)		Broad line		Flux ^a	$\Delta\chi^2$	Fe XXV emission	Fe XXVI emission
	LineE	σ_{Broad} (keV)	σ_{Broad} (keV)	EW_{Broad} (eV)				
1H 0419-577	–	–	–	–	–	–	X	X
3C 111	6.28 ^{+0.09} _{-0.05}	< 0.136	19 ⁺²³ ₋₉	0.55 ^{+0.67} _{-0.27}	-11	✓	✓	✓
3C 120	6.38 ^{+0.01} _{-0.01}	0.124 ^{+0.025} _{-0.022}	76 ⁺⁶ ₋₉ 84 ⁺⁷ ₋₁₀	4.04 ^{+0.35} _{-0.49}	-75	✓	✓	X
3C 382	6.45 ^{+0.09} _{-0.12}	0.198 ^{+0.210} _{-0.090}	42 ⁺¹⁸ ₋₁₇	2.45 ^{+1.07} _{-1.01}	-20	X	X	X
3C 390.3	6.49 ^{+0.09} _{-0.10}	0.320 ^{+0.256} _{-0.106}	86 ⁺³¹ ₋₂₀	3.29 ^{+1.17} _{-0.78}	-40	X	X	X
3C 445	6.04 ^{+0.12} _{-0.11}	< 0.436	23 ⁺³⁰ ₋₁₃	1.07 ^{+0.58} _{-0.46}	-7	✓	✓	X
4C 74.26	6.12 ^{+0.06} _{-0.07}	< 0.186	22 ⁺¹² ₋₉	1.07 ^{+0.58} _{-0.46}	-20	✓	✓	X
Ark 120	6.36 ^{+0.08} _{-0.09}	0.320 ^{+0.110} _{-0.090}	105 ⁺²⁶ ₋₂₄	0.70 ^{+0.32} _{-0.32}	-12	X	✓	✓
Ark 564	6.42 ^{+0.09} _{-0.08}	< 0.161	20 ⁺¹⁴ ₋₁₃	0.34 ^{+0.25} _{-0.22}	-3	✓	X	X
Fairall 9	5.91 ^{+0.24} _{-0.21}	0.505 ^{+0.187} _{-0.173}	49 ⁺²⁰ ₋₁₈	1.45 ^{+0.58} _{-0.55}	-36	✓	✓	✓
IC 4329A	6.34 ^{+0.15} _{-0.15}	0.551 ^{+0.119} _{-0.100}	61 ⁺¹⁵ ₋₁₅	7.94 ^{+1.96} _{-1.91}	-53	X	✓	✓
IRAS 13224-3809	6.19 ^{+0.58} _{-0.65}	1.014 ^{+0.613} _{-0.346}	632 ⁺³⁰³ ₋₂₆₀	0.37 ^{+0.18} _{-0.15}	-9	✓	✓	X
MCG-02-14-009	6.33 ^{+0.21} _{-0.24}	0.280 ^{+0.280} _{-0.130}	92 ⁺⁵⁹ ₋₅₆	0.49 ^{+0.31} _{-0.30}	-3	X	✓	✓
MCG-02-58-22	–	–	–	–	–	X	X	X
MCG-05-23-16	6.34 ^{+0.08} _{-0.10}	0.512 ^{+0.085} _{-0.078}	108 ⁺¹⁶ ₋₁₇	12.25 ^{+1.80} _{-1.87}	-15	✓	✓	X
MCG-06-30-15	5.93 ^{+0.07} _{-0.14}	0.840 ^{+0.06} _{-0.06}	149 ⁺²¹ ₋₉	1.31 ^{+0.68} _{-0.66}	-302	X	✓	✓
MCG+8-11-11	6.35 ^{+0.03} _{-0.04}	0.170 ^{+0.056} _{-0.042}	67 ⁺¹³ ₋₁₂	5.30 ^{+1.02} _{-0.97}	-73	X	✓	✓
MR 2251-178	6.46 ^{+0.10} _{-0.17}	0.307 ^{+0.199} _{-0.100}	49 ⁺¹⁴ ₋₁₄	2.65 ^{+0.76} _{-0.75}	-26	X	X	X
Mrk 79	6.17 ^{+0.22} _{-0.27}	0.529 ^{+0.208} _{-0.159}	136 ⁺⁴⁴ ₋₄₅	2.83 ^{+0.91} _{-0.93}	-51	✓	✓	✓
Mrk 110	–	–	–	–	–	✓	✓	X

Table 5.3: *continued* - Broad Gaussian parameterisation of FeK region in addition to the baseline model. ^a Flux given in units (10^{-5} ph cm $^{-2}$ s $^{-1}$). ^b Parameters other than normalisation tied between multiple observations, all are tied in NGC 5506. - Indicates that no broad Gaussian can be fit, i.e. no discernible reduction in χ^2 whatsoever. A negative value in the $\Delta\chi^2$ column denotes an improvement in the fit.

Object	Broad line			Broad line			$\Delta\chi^2$	Fe XXV emission	Fe XXVI emission
	LineE (keV)	σ_{Broad} (keV)	EW_{Broad} (eV)	Flux ^a	$\Delta\chi^2$	Fe XXV emission			
Mrk 205	-	-	-	-	-	-	-	X	X
Mrk 279	$6.59^{+0.26}_{-0.19}$	< 0.333	20^{+25}_{-19}	$0.15^{+0.19}_{-0.14}$	-6	X	X	X	X
Mrk 355	$6.27^{+0.13}_{-0.17}$	$0.500^{+0.130}_{-0.110}$	134^{+42}_{-38}	$2.28^{+0.72}_{-0.65}$	-53	✓	✓	✓	✓
Mrk 359	$6.40^{+0.06}_{-0.06}$	< 0.177	88^{+39}_{-41}	$0.52^{+0.23}_{-0.25}$	-10	✓	✓	✓	X
Mrk 509	$6.60^{+1.28}_{-0.14}$	$0.690^{+1.363}_{-0.151}$	120^{+28}_{-27}	$6.32^{+1.50}_{-1.42}$	-57	✓	✓	✓	X
Mrk 766	$6.66^{+0.11}_{-0.07}$	$0.144^{+0.109}_{-0.115}$	73^{+27}_{-25}	$0.81^{+0.30}_{-0.28}$	-14	✓	✓	✓	X
Mrk 841	$5.89^{+0.22}_{-0.24}$	$0.402^{+0.288}_{-0.173}$	80^{+50}_{-37}	$1.47^{+0.92}_{-0.68}$	-20	✓	✓	✓	X
NGC 1365	$6.48^{+0.02}_{-0.01}$	< 0.028	< 13	< 0.29	-63	✓	✓	✓	✓
NGC 2992	$6.51^{+0.14}_{-0.11}$	$0.323^{+0.153}_{-0.100}$	73^{+28}_{-25}	$1.39^{+0.53}_{-0.47}$	-17	X	X	X	X
NGC 3147	$6.45^{+0.04}_{-0.03}$	< 0.066	110^{+51}_{-41}	$0.21^{+0.10}_{-0.08}$	-15	X	X	✓	✓
NGC 3227 ^b	$6.34^{+0.09}_{-0.09}$	$0.707^{+0.100}_{-0.087}$	80^{+24}_{-23}	$4.50^{+1.33}_{-1.28}$	-124	X	X	✓	✓
			176^{+32}_{-31}	$5.38^{+0.97}_{-0.94}$					
			26^{+25}_{-25}	$1.17^{+1.13}_{-1.13}$					
			281^{+39}_{-38}	$5.71^{+0.79}_{-0.77}$					
			55^{+23}_{-22}	$2.22^{+0.92}_{-0.90}$					
			43^{+32}_{-31}	$1.35^{+1.00}_{-0.98}$					
NGC 3516 ^b	$6.32^{+0.12}_{-0.12}$	$0.874^{+0.118}_{-0.101}$	151^{+22}_{-21}	$6.95^{+1.01}_{-0.97}$	-84	✓	✓	✓	X
			81^{+29}_{-29}	$1.89^{+0.69}_{-0.68}$					
NGC 3783 ^b	$6.07^{+0.20}_{-0.18}$	$0.761^{+0.221}_{-0.104}$	97^{+38}_{-32}	$6.38^{+2.51}_{-2.10}$	-68	X	X	✓	✓
			57^{+15}_{-15}	$4.89^{+1.25}_{-1.25}$					
NGC 4051 ^b	$6.23^{+0.17}_{-0.19}$	$0.742^{+0.151}_{-0.124}$	139^{+39}_{-36}	$1.80^{+0.50}_{-0.47}$	-70	✓	✓	✓	X
			74^{+24}_{-23}	$2.12^{+0.68}_{-0.66}$					
			112^{+37}_{-37}	$2.48^{+0.83}_{-0.81}$					

Table 5.3: *continued* - Broad Gaussian parameterisation of FeK region in addition to the baseline model. ^a Flux given in units (10^{-5} ph cm $^{-2}$ s $^{-1}$). ^b Parameters other than normalisation tied between multiple observations, all are tied in NGC 5506. – Indicates that no broad Gaussian can be fit, i.e. no discernible reduction in χ^2 whatsoever. A negative value in the $\Delta\chi^2$ column denotes an improvement in the fit.

Object	Broad line				$\Delta\chi^2$	FeXXV emission	FeXXVI emission
	LineE (keV)	σ_{Broad} (keV)	EW_{Broad} (eV)	Flux ^a			
NGC 4151	–	–	–	–	–	X	X
NGC 4593	$6.65^{+0.18}_{-0.14}$	$0.368^{+0.289}_{-0.136}$	87^{+40}_{-35}	$1.26^{+0.58}_{-0.51}$	-12	✓	X
NGC 5506 ^b	$6.50^{+0.07}_{-0.09}$	$0.317^{+0.074}_{-0.060}$	19^{+5}_{-4}	$7.83^{+1.91}_{-1.51}$	-32	✓	✓
NGC 5548	$6.36^{+0.03}_{-0.10}$	< 0.098	26^{+31}_{-22}	$0.60^{+0.72}_{-0.52}$	-5	X	X
NGC 7213	$6.74^{+0.16}_{-0.16}$	< 1.294	12^{+30}_{-9}	$0.30^{+0.74}_{-0.22}$	-4	✓	✓
NGC 7314	$6.36^{+0.35}_{-0.19}$	< 0.057	58^{+37}_{-34}	$0.66^{+0.43}_{-0.39}$	-7	X	✓
NGC 7469	$6.32^{+0.06}_{-0.11}$	$0.150^{+0.07}_{-0.03}$	62^{+928}_{-44}	$1.55^{+0.70}_{-1.10}$	-24	X	X
PDS 456	–	–	–	–	–	✓	✓
PG 1211+143	$6.49^{+0.07}_{-0.06}$	$0.142^{+0.068}_{-0.061}$	146^{+28}_{-44}	$0.87^{+0.17}_{-0.26}$	-5	✓	X
RBS 1124	–	–	–	–	–	X	X
SWIFT J2127.4+5654	$6.32^{+0.24}_{-0.25}$	$0.390^{+0.450}_{-0.260}$	71^{+53}_{-48}	$3.43^{+2.56}_{-2.32}$	-12	✓	✓
Ton S180	–	–	–	–	–	X	X

5.3.3.3 Broad residuals in the Fe K region

The baseline model provides a reasonable fit to the broadband spectra of all objects in the sample, ensuring that any absorption zones which may be present are taken into account. After modelling all of the above features where formally required, the residuals remaining in the Fe K region can be examined regarding the possible presence of broadened line emission from the inner regions of the accretion disc. Firstly the strength of any broad residuals which may remain in the Fe K regions of these objects are parameterised by including a broad Gaussian with line energy, σ_{width} and normalisation left free to vary. If this broad Gaussian component proves to be statistically significant at the 90% level (three additional parameters, i.e., an improvement to the fit of $\Delta\chi^2 > 6.3$), the next step is to add more physical models of the line emission from the inner regions of the accretion disc. Figure 5.2 shows ratio plots of the 4-9 keV region prior to any modelling of reflection or disc emission components, i.e., the Fe K band is left unmodelled to highlight the residuals.

Indeed, not all of the objects in the sample require any further modelling or broad line emission and an excellent fit is found to the data. For example, no reasonable statistical improvement is made when adding a broad Gaussian component to the following AGN in this sample: 1H 0419-577, Ark 564, MCG-02-14-009, MCG-02-58-22, Mrk 110, Mrk 205, Mrk 279, NGC 4151, NGC 5548, NGC 7213, PDS 456, PG 1211+143, RBS 1124 and Ton S180 (see Table 5.3). The remaining AGN in the sample show at least some indications of a broad red-wing in the Fe K region and therefore perhaps emission from the inner regions of the accretion disc (32/46 objects), however, it should be noted that this is only a simple parameterisation and the true fraction of AGN may differ from this when a more physical model is used. From Table 5.3 the mean parameters of the simple broad Gaussian can be estimated at $\text{LineE} = 6.32 \pm 0.04$ keV, $\sigma_{\text{width}} = 0.470 \pm 0.051$ keV and equivalent width $EW = 97 \pm 19$ eV. Of course, attempting to model an asymmetric line emission profile with a simple Gaussian can lead to a mis-modelling of the Fe K region, for example, broader Gaussians (such as some of those found here) are heavily influenced by the way in which the narrow

FeK α core and Compton shoulder are modelled. Since the use of a broad Gaussian is essentially simply a means of adding curvature to the 5-7 keV region, in a sample of complex AGN featuring warm absorption/ highly ionised outflows there is likely to be a reasonable amount of interplay between the width and strength of the broad line with the absorber properties.

After applying the RELLINE model to those AGN in which a broad Gaussian appears to be required a good fit is found in all the remaining objects, some of which are significantly improved with the introduction of a relativistic diskline type line emission model. Emission from the inner regions of the disc is not formally statistically required at the 90% confidence level in 20/46 objects (see Table 5.4 for a summary of RELLINE fits). Of the remaining 26/46 objects which do require emission from the inner regions of the accretion disc (23/46 of the objects in this sample require the RELLINE model at > 99.5% confidence), also finding a moderate average strength of $EW = 96 \pm 10$ eV and a low accretion disc emissivity index of $q = 2.4 \pm 0.1$ at an inclination of $i = 33 \pm 2^\circ$ (see Figure 5.3). Alternatively fixing $a = 0.998$ and allowing R_{in} to vary yields an average $R_{\text{in}} = 21 \pm 6 R_g$.

With the advent of high quality broadband X-ray data, tentative steps can be made towards placing estimates upon black hole spin. In particular, objects with multiple or deep observations may possess spectra with a sufficient number of counts and temporal information with which to form models allowing for consistent spin estimates and the variation in spectral shapes between observations. Here a total of 11 tentative constraints upon the spin parameter a are made (with upper and lower bounds in 5 AGN), see Table 5.4. In addition to the spin estimates placed in Chapters 3 and 4, three further measurements are made here; MCG-05-23-16 ($a < 0.50$), Mrk 79 ($a < 0.80$) and NGC 3516 ($a < 0.30$). The typical parameters obtained here using the RELLINE line emission model and SMBH spin estimates are discussed later in Section 6.2.6.

Table 5.4: Summary of relline fits to objects in which some statistical improvement is made. Line energy fixed at 6.4 keV. * Denotes a frozen parameter. ^a Flux given in units (10^{-5} ph cm $^{-2}$ s $^{-1}$). ^b Inner radius of emission is quoted as an alternative to the spin parameter a , i.e. spin is frozen at maximal ($a = 0.998$) and the inner radius is allowed to vary away from R_{ISCO} . ^c Relline component is only employed in the 2006 of Mrk 766 observation. ^d Emissivity frozen at best-fit value from Patrick et al. (2011b). A negative value in the $\Delta\chi^2$ column denotes an improvement in the fit.

Object	EW (eV)	q	a	i°	Flux ^a	R_{in}^b	Fe XXV	Fe XXVI	$\Delta\chi^2$	χ^2_c
3C 111	37 ⁺³⁰ ₋₁₇	< 2.7	–	22 ⁺¹² ₋₅	0.98 ^{+0.79} _{-0.44}	< 59	✓	✓	-10	1091.2/1094
3C 120	78 ⁺¹⁴ ₋₁₆ 93 ⁺¹⁷ ₋₁₉	1.5 ^{+0.2} _{-0.3}	–	17 ⁺¹ ₋₁	4.17 ^{+0.76} _{-0.85}	< 17	✓	X	-45	3586.4/3449
3C 382	57 ⁺²⁰ ₋₁₈	2.7 ^{+1.2} _{-0.8}	–	30 ⁺² ₋₄	2.65 ^{+0.93} _{-0.85}	15 ⁺¹⁴ ₋₆	X	X	-27	959.9/934
3C 390.3	142 ⁺²⁴ ₋₃₀	2.3 ^{+0.6} _{-0.3}	–	49 ⁺³ ₋₃	4.96 ^{+0.84} _{-1.06}	< 15	X	X	-42	1457.2/1482
3C 445	71 ⁺⁴⁸ ₋₃₃	< 1.6	–	> 45	1.05 ^{+0.71} _{-0.49}	< 332	X	X	-6	452.2/421
4C 74.26	48 ⁺²⁵ ₋₂₆	< 1.7	–	72 ⁺¹⁷ ₋₃₅	1.82 ^{+0.94} _{-0.99}	< 89	X	X	-5	1339.7/1301
Ark 120	95 ⁺³² ₋₂₆	2.3 ^{+0.4} _{-0.4}	< 0.94	33 ⁺² ₋₁₇	3.62 ^{+1.22} _{-0.99}	25 ⁺¹⁹ ₋₇	X	✓	-22	724.4/648
Fairall 9	54 ⁺²⁶ ₋₂₅ 69 ⁺¹⁸ ₋₁₇	2.9 ^{+0.5} _{-0.4}	0.60 ^{+0.19} _{-0.62}	31 ⁺⁴ ₋₅	1.49 ^{+0.72} _{-0.70}	4 ⁺² ₋₁	✓	✓	-46	3558.7/3271
IC 4329A	69 ⁺¹³ ₋₁₄	2.3 ^{+0.3} _{-0.4}	–	51 ⁺⁴ ₋₃	8.25 ^{+1.54} _{-1.72}	37 ⁺⁸ ₋₉	X	✓	-46	2374.8/2198
MCG-02-14-009	142 ⁺⁴⁷ ₋₄₆	2.0 ^{+0.4} _{-0.4}	< 0.88	24 ⁺¹⁰ ₋₉	6.64 ^{+2.20} _{-2.15}	> 13	X	✓	-12	611.6/538
MCG-05-23-16	94 ⁺¹¹ ₋₁₅	2.5 ^{+0.4} _{-0.5}	< 0.50	24 ⁺³ ₋₃	10.16 ^{+1.19} _{-1.65}	9 ⁺⁵ ₋₂	X	X	-112	1471.2/1462
MCG-06-30-15	161 ⁺⁴⁶ ₋₄₄	2.7 ^{+0.2} _{-0.1}	0.49 ^{+0.20} _{-0.12}	44 ⁺⁶ ₋₂	5.73 ^{+1.63} _{-1.57}	5 ⁺¹ ₋₁	X	✓	-59	1967.8/1819
MCG+8-11-11	72 ⁺¹⁴ ₋₁₄	2.1 ^{+0.3} _{-0.4}	–	18 ⁺² ₋₂	5.50 ^{+1.07} _{-1.07}	< 18	X	✓	-79	970.7/932
MR 2251-178	55 ⁺²² ₋₁₂	2.4 ^{+1.4} _{-1.0}	–	36 ⁺¹⁰ ₋₄	2.74 ^{+1.08} _{-0.61}	< 35	X	X	-30	947.3/898
Mrk 79	199 ⁺⁴⁰ ₋₃₇	2.7 ^{+0.8} _{-0.6}	< 0.80	34 ⁺³ ₋₃	3.08 ^{+0.62} _{-0.57}	19 ⁺⁷ ₋₉	X	✓	-51	551.1/539

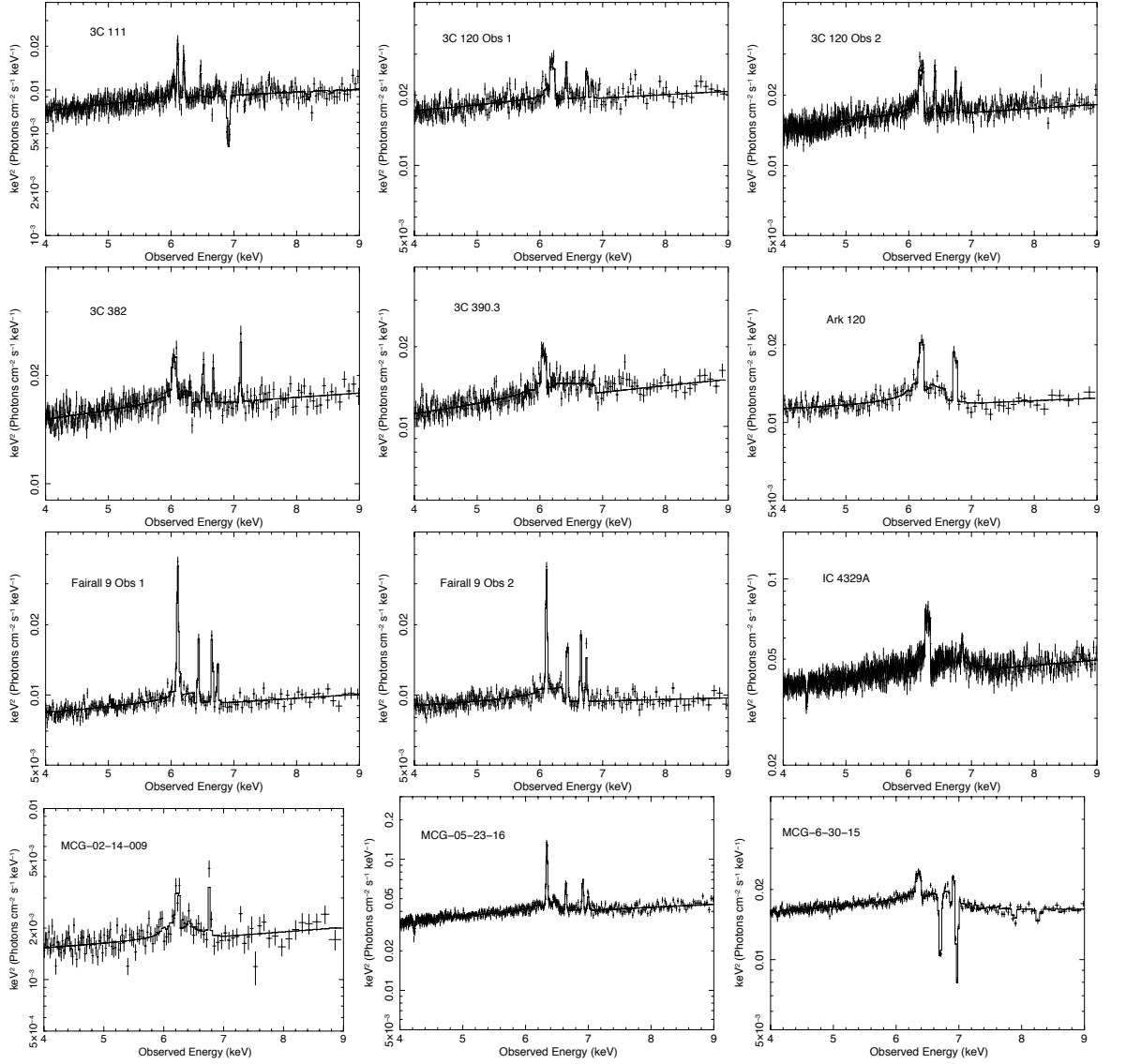


Figure 5.3: $\nu F\nu$ plots of the baseline+RELLINE model in the 4-9 keV region. Note the strong absorption in the FeK region in many objects and relatively weak red-wing. The solid black line shows the total model.

5.3.4 Dual reflector fits

If strong emission arises from reflection off the inner regions of the accretion disc producing a relativistically broadened FeK α line profile, the same degree of broadening

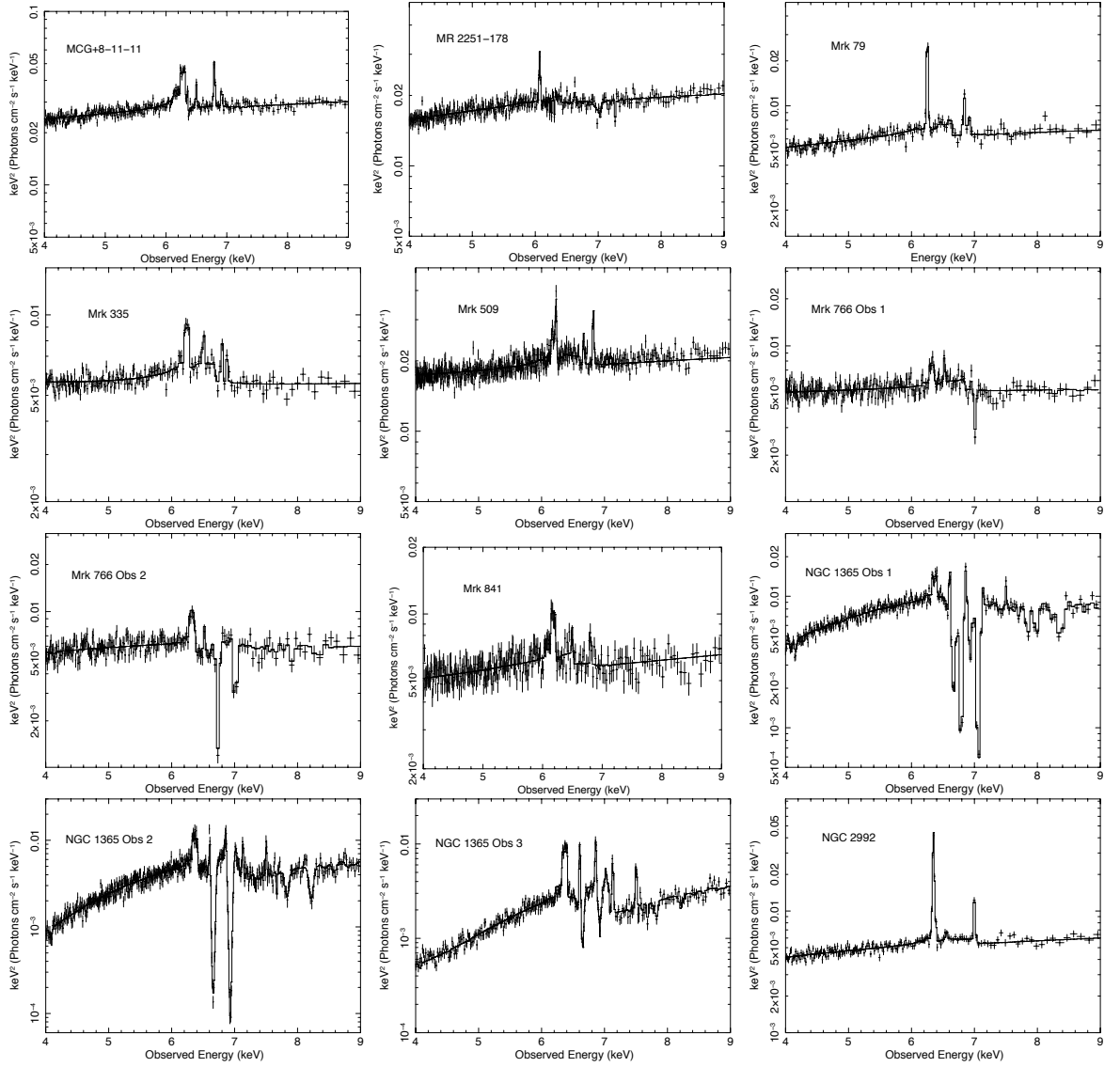


Figure 5.3: *continued* - $\nu F\nu$ plots of the baseline+RELLINE model in the 4-9 keV region. Note the strong absorption in the FeK region in many objects and relatively weak red-wing. The solid black line shows the total model.

and relativistic effects can also be applied to the entire reflection continuum. In this scenario dual reflector fits are formed (for those objects which do formally require a RELLINE component, see Table 5.4) consisting of a distant unblurred REFLIONX and a second inner REFLIONX convolved with the RELCONV kernel (Dauser et al. 2010).

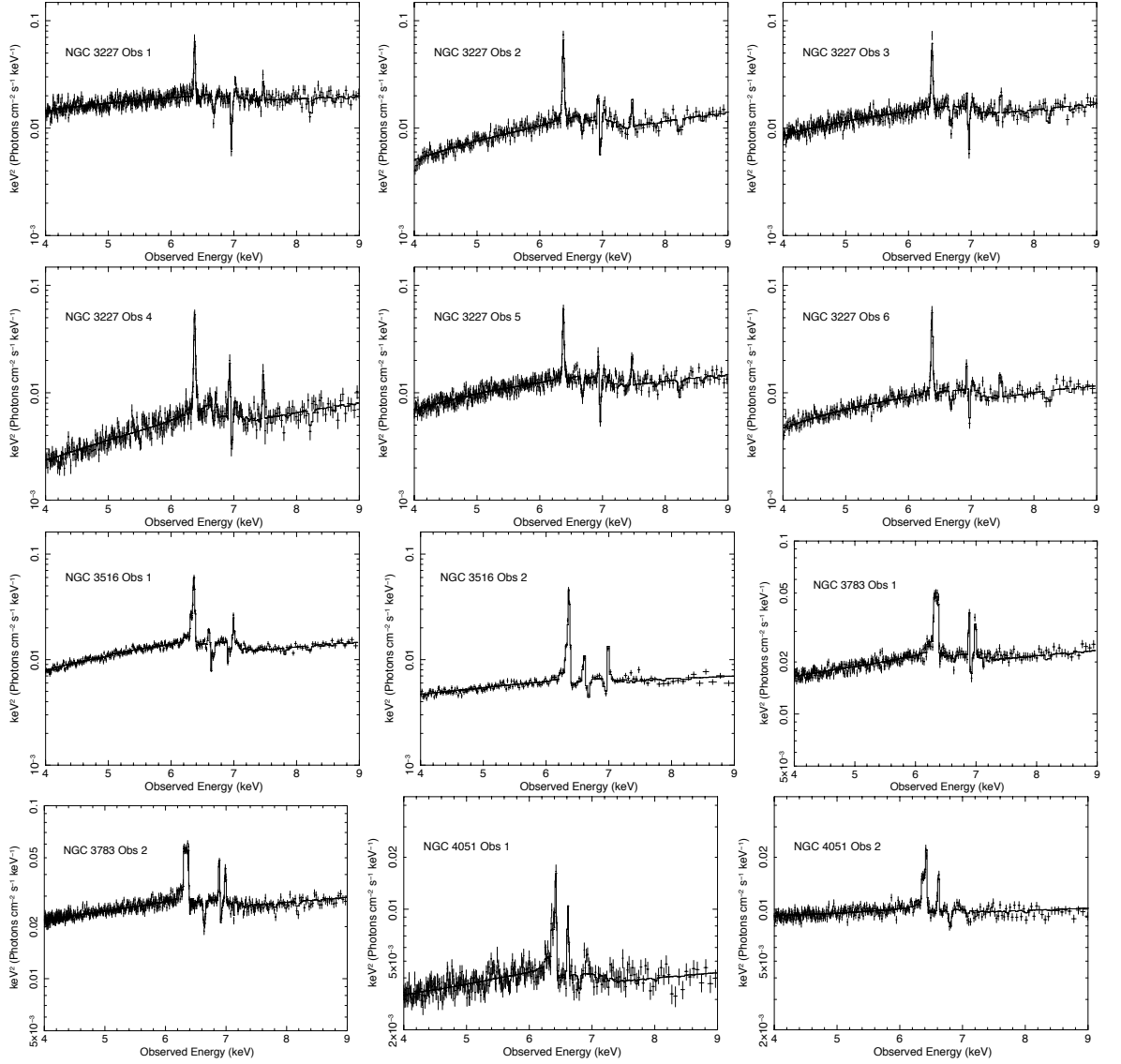


Figure 5.3: *continued* - νF_{ν} plots of the baseline+RELLINE model in the 4-9 keV region. Note the strong absorption in the FeK region in many objects and relatively weak red-wing. The solid black line shows the total model.

However, a COMPTT component is still included to model the soft excess continuum. For example, the analysis of a small sample of ‘bare’ Seyferts in Patrick et al. (2011a) suggests that in order to produce the significant amount of blurring required to smooth the discrete soft emission lines into a continuum, both the spin parameter a and emis-

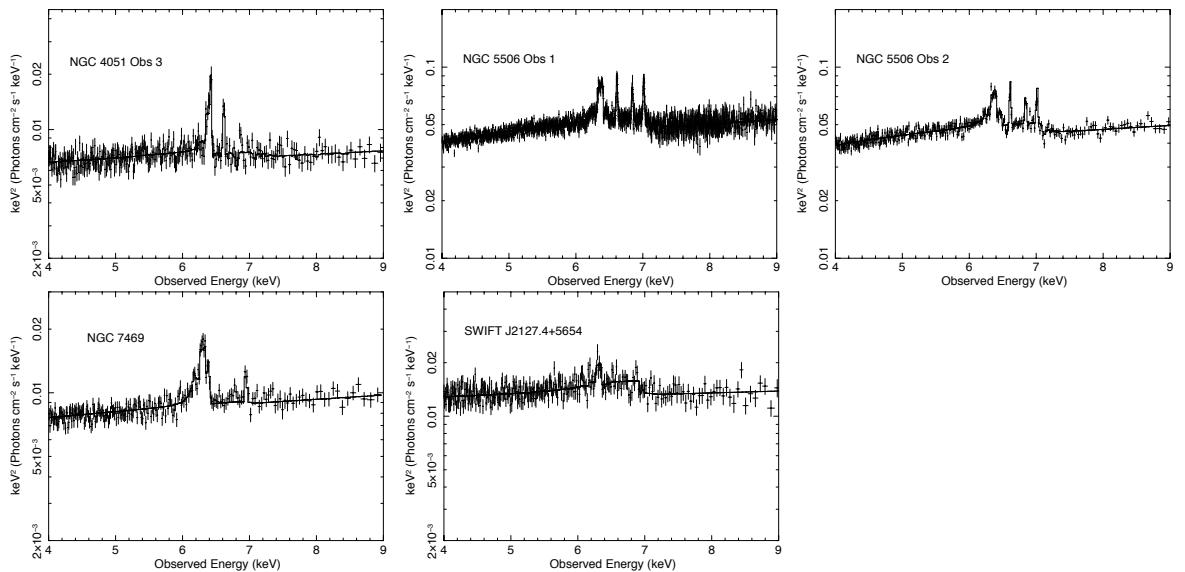


Figure 5.3: *continued* - $\nu F\nu$ plots of the baseline+RELLINE model in the 4-9 keV region. Note the strong absorption in the FeK region in many objects and relatively weak red-wing. The solid black line shows the total model.

sivity of the disc are forced to high and extreme values ($a = 0.998$ and $q > 4$). Retaining the use of the COMPTT to model the soft excess ensures that the main feature driving the fit of the blurred reflector are the broad residuals in the FeK region regardless of the interpretation of the soft excess.

Due to the additional hard X-ray flux produced by a dual reflector model, this is tested as an alternative to high column partial covering scenarios, i.e., partial covering geometries are avoided during fitting unless no good fit can be found without a partially covering model. The iron abundance is tied between the inner and distant reflectors for consistency. The ionisation of the two reflectors are initially allowed to vary but are tied if both are approximately equal within errors.

Simply replacing the RELLINE component in each model with the RELCONV*REFLIONX convolution produces a good fit to the data in objects without partial covering, with estimated accretion disc parameters consistent with those obtained in the previous model (Table D.3 on page 256). This should come as no surprise since the FeK region

remains the main driver behind the fit. The dual reflector approach as an alternative to partial covering provides a reasonable fit to Mrk 766 ($\Delta\chi^2 = 1109.6/1002$), however, this is notably worse than when the use of a partial covering geometry is retained ($\Delta\chi^2 = 1055.1/995$). A poor fit is obtained to all three observations of NGC 4051 while keeping the iron abundance of both reflectors tied ($Z_{\text{Fe}} = 1.0$), however, disc parameters are forced to extreme values, i.e. $q > 7$ and $a = 0.998$). In addition to this the 2-100 keV blurred reflector flux of the 2005 observation is approximately 2-3 times that of the 2008 observations despite being in a far more absorbed state, therefore the use of a partial coverer is retained due to both physical and statistical arguments (see Section 5.4.6 for more details on NGC 4051).

A poor and statistically inferior fit to the broadband data is found in some objects when a high column partial coverer is replaced with a dual reflector as an alternate mechanism for accounting for additional hard X-ray flux above 10 keV. A partial covering geometry is still statistically required in Mrk 766, NGC 1365, NGC 3227, NGC 3516 and NGC 4051 (Table D.3 on page 256). Treating these AGN as above and replacing RELLINE with RELCONV*RELFIONX while still including a partial coverer again produces a good fit to the data with consistent accretion disc parameters to those in Table 5.4 (see Table D.3 on page 256). Removing the partial coverer and accounting for the hard excess with the inner reflector yields an improved fit to MCG-06-30-15 and NGC 5506 (i.e. 2/16), however, the parameters obtained are consistent with those estimated with a partial covering geometry.

5.4 Selected individual objects

Notes are included below on the fitting of individual AGN, many of which have long or multi-epoch observations.

5.4.1 Fairall 9

The Fe K region of the ‘bare’ Seyfert Fairall 9 has been well studied (Schmoll et al. 2009; Emmanoulopoulos et al. 2011; Patrick et al. 2011a, 2011b), here a simultaneous analysis of both the 2007 and 2010 observations provides a good fit to the data simply allowing the normalisation of the components to vary. In line with each of the previous analyses, here an emissivity of $q = 2.9_{-0.4}^{+0.5}$ is found although a somewhat more poorly constrained spin parameter $a = 0.60_{-0.62}^{+0.19}$, i.e. consistent with zero spin in this analysis of both Fairall 9 *Suzaku* observations

5.4.2 Mrk 205

The best-fit model for Mrk 205 presented here features partial covering to account for additional flux at X-ray energies > 10 keV. The subsequent addition of a broad Gaussian or RELLINE component has little affect upon the overall fit (an improvement of $\Delta\chi^2 \sim 4$) due to the spectral curvature introduced as a result of a partial coverer with column density $N_{\text{H}} = (5.1_{-2.5}^{+5.5}) \times 10^{23} \text{ cm}^{-2}$, ionisation $\log(\xi) = 2.8_{-0.5}^{+0.7} \text{ erg cm s}^{-1}$ and covering fraction $C_{\text{frac}} = 13\%$. However, this AGN can be equally well described with a very broad iron line with equivalent width $EW = 254_{-59}^{+72} \text{ eV}$ and an increase of $\Delta\chi^2 \sim 23$ when the RELLINE component is removed and the model refit without a partial coverer in place. This yields a relatively high emissivity index of $q = 3.4_{-0.5}^{+1.4}$, an inclination of $i^\circ = 30_{-9}^{+10}$ and a lower limit placed upon the spin parameter $a > 0.1$.

5.4.3 NGC 3227

The six observations of NGC 3227 amount to nearly 500 000 2-10 keV counts and a relatively simple model is formed to describe each component and the variations between observations. The best-fit model for NGC 3227 consists of a high-column partial covering component of column $N_{\text{H}} = (2.9_{-0.1}^{+0.1}) \times 10^{23} \text{ cm}^{-2}$ with a covering fraction of $C_{\text{frac}} \sim 32 - 89\%$ in addition to a complex warm absorber and both hard

and soft excesses fitted with REFLIONX and COMPTT respectively. Examining the Fe K region there are clear blue-shifted absorption lines due to Fe XXV and Fe XXVI and small residuals indicative of weak to moderate emission from the inner regions of the accretion disc (with EW generally higher in a lower continuum flux spectrum). A good fit to each of the six observations is found simply by letting the strength of the REFLIONX and COMPTT to vary as well as the covering fraction of the partial coverer. All absorber properties such as ionisation and column density are tied between observations other than the covering fraction and ionisation of the partial coverer which is required to vary between $\log\xi \sim 0.50-1.53$ with each observation. Using the RELLINE model to account for the broad residuals with parameters tied (but again allowing normalisation to vary) yields an improved fit to the data with $\chi^2_\nu = 4465.6/4189$. The RELLINE model yields a relatively typical emissivity of $q = 2.7^{+0.5}_{-0.4}$ and an inclination of $i = 33^{+2}_{-2}^\circ$ and $R_{\text{in}} = 11^{+3}_{-6} R_g$ (Table 5.4 and Figure 5.4).

5.4.4 NGC 3516

The two observations of NGC 3516 differ in their shape significantly (e.g. Markowitz et al. 2008), the 2005 *Suzaku* observation 2-10 keV flux is a factor of 1.8 higher than in the 2009 observation (see Figure 5.4). Here a model is formed which is a good fit to both observations, allowing for changes in the absorber/ partial coverer properties and strength of reflection between data sets, although the basic geometry is maintained and a good overall fit is found. As noted in Patrick et al. (2011b) and Turner et al. (2011), the 2009 observation showed no strong indication of a broad red-wing, however, the Markowitz et al. (2008) analysis of the earlier 2005 data does suggest the presence of such a feature. The 2005 observation is more absorbed than the 2009 observation (i.e. $C_{\text{frac}} = 83\%$ compared to 18% in the 2009 observation), yet it has a much higher continuum flux level throughout the spectrum above ~ 2 keV (Figure 5.4). This simultaneous analysis yields consistent results with previous work, retrieving the broad feature found by Markowitz et al. (2008) in the 2005 data. Fitting a RELLINE component to both data sets with all parameters (other than normalisation)

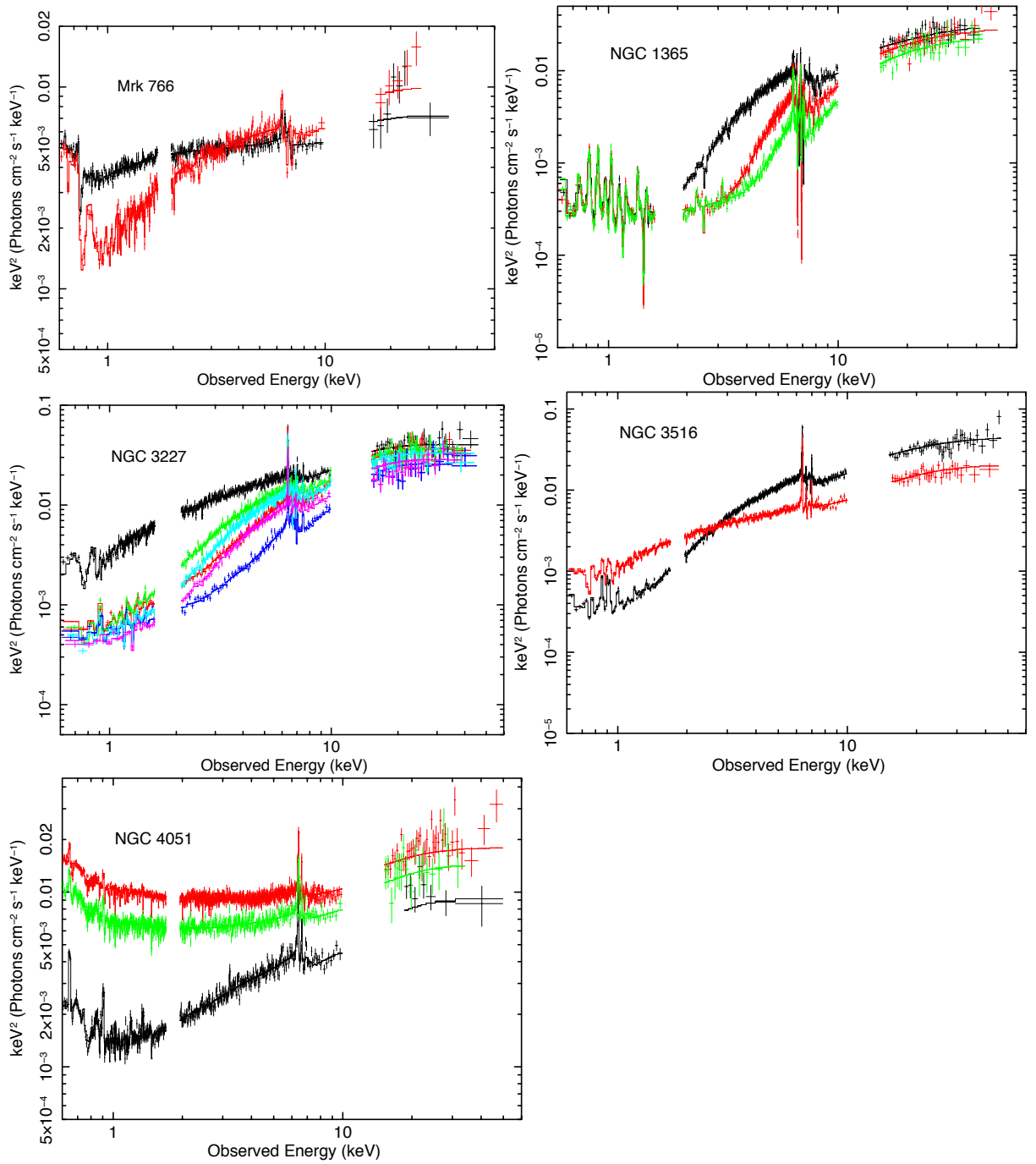


Figure 5.4: $\nu F\nu$ plots of the full broad-band models of some objects displaying significant variability. Note that the 2005 (black) observation of NGC 3516 is higher flux, yet appears to be more absorbed whereas in the majority of these examples it intuitively appears that simply the covering fraction has varied between observations.

tied suggest a fairly typical and relatively weak broad line with $EW = 58_{-9}^{+9}$ eV and significantly weaker $EW = 14_{-2}^{+2}$ eV in the 2005 and 2009 observations respectively. An upper limit to the spin parameter is found $a < 0.30$ and inclination $i < 41^\circ$ at a disc emissivity of $q = 3.1_{-0.2}^{+0.4}$.

5.4.5 NGC 3783 - High or low spin?

Note that the discussion in this subsection is taken from Section 4.3.4 in Patrick et al. (2012) which was written with the guidance of Dr. James Reeves and Dr. Delphine Porquet due to the controversial debates regarding the *Suzaku* observations of NGC 3783 at around the time of writing.

In an analysis of the long 210 ks 2009 *Suzaku* observation of NGC 3783, Patrick et al. (2011b) concluded that the data appeared to rule out a maximal black hole in NGC 3783 (constraining spin to $a < 0.31$ in a dual reflector model), while the fit could be achieved with approximate Solar abundances for the reflector. However, Brenneman et al. (2011) came to the opposite conclusion, appearing to require near maximal black hole spin from fits to the iron line data in NGC 3783 (with $a > 0.98$ at $> 90\%$ confidence) and obtaining a high iron abundance of $Z_{\text{Fe}} = 3.7_{-0.9}^{+0.9}$ and a steep inner emissivity law for the innermost disc. Subsequently Reynolds et al. (2012b) also appeared to confirm the high spin, high abundance scenario in a re-analysis of the 2009 dataset, suggesting that the iron abundance of the reflector and the black hole spin may be degenerate upon each other and that a statistically preferred fit can be obtained with higher abundances and higher spin.

In this section an attempt is made to discuss the differences between these works, by considering the long 2009 *Suzaku* observation of NGC 3783. Firstly the model of Brenneman et al. (2011) was reconstructed, in order to understand the difference in the spectral modelling. The main difference between the Brenneman et al. (2011) and Patrick et al. (2011b) models is the construction of the warm absorber; in Brenneman et al. (2011) all 3 zones of the warm absorber only partially cover the AGN, where

a fraction of $\sim 17\%$ of the direct continuum is unabsorbed by the warm absorber, or alternatively is scattered back into the line of sight. On the other hand in Patrick et al. (2011b) and in Patrick et al. (2012), the warm absorber fully covers the X-ray continuum emission. Indeed, it should be noted that previous analyses have not needed to invoke partial covering in order to model the warm absorber in NGC 3783 (Reeves et al. 2004; Yaqoob et al. 2005), including high resolution X-ray spectroscopy from *XMM-Newton* RGS (Blustin et al. 2002) and during a 900 ks *Chandra* HETG observation (Kaspi et al. 2002).

The other main difference in the model construction is that the PEXMON³ neutral reflection model (Nandra et al. 2007) is used for the distant (narrow) reflector in Brenneman et al. (2011). In Patrick et al. (2011b) and in Patrick et al. (2012), the REFLIONX ionised reflection model (Ross & Fabian 2005) is adopted, allowing the ionisation state to reach a low value of $\xi = 1 \text{ erg cm s}^{-1}$ appropriate for low ionisation iron. For the disc (i.e. blurred) reflection, both analyses use the REFLIONX table, convolved with a relativistic blurring function such as KERRCONV (Brenneman & Reynolds 2006) or RELCONV (Dauser et al. 2010). For simplicity and comparison with Brenneman et al. (2011), in this section the KERRCONV model is used, with spin allowed to vary between $a = 0 - 0.998$ for a prograde black hole. The emissivity index is modelled as a broken power-law function (where q_1 is the inner emissivity and q_2 the outer emissivity and usually $q_1 > q_2$), breaking at a disk radius of R_b in units of R_G . The inner disk radius is set equal to the ISCO, while the outer radius is set to $400R_G$. Adopted here are the Solar abundances of Anders & Grevesse (1989) for the Galactic column, noting that there is little difference to the blurred reflector model parameters if the Wilms et al. (2000) ISM abundances are used instead.

In order to test the Brenneman et al. (2011) model, the identical energy ranges for the XISFI spectrum and HXD/PIN are used as adopted by Brenneman et al. (2011), from 0.7–45 keV, ignoring the 1.5–2.5 keV band in the XIS. The same warm

³PEXMON is a modification of the PEXRAV model, but which includes FeK α , FeK β and NiK α emission lines with EW as predicted via reflection off a Compton-thick slab.

absorber model and tables are used as per the Brenneman et al. (2011) and Reynolds et al. (2012b) papers. The Brenneman et al. (2011) model has a steep index for the inner emissivity law, a high black hole spin consistent with maximal and a high iron abundance of the inner reflector of $Z_{\text{Fe,inner}} \sim 3$, while the iron abundance of the distant reflector is initially fixed equal to Solar, i.e. $Z_{\text{Fe,outer}} = 1$. This model as detailed in Brenneman et al. (2011) initially gives a poor fit ($\chi^2_{\nu} = 1501/1234$), however, subsequently refitting the model parameters then gives an excellent fit to the data, with $\chi^2_{\nu} = 1329/1234$. Nonetheless the model parameters are in good agreement with those obtained in Brenneman et al. (2011), where a formal 90% lower limit of $a > 0.82$ to the black hole spin is obtained for 1 interesting parameter, a disc inclination of $i = 22 \pm 4$, while the emissivity indices have values of $q_1 = 4.4 \pm 1.2$ and $q_2 = 2.8 \pm 0.2$, with a break radius of $\sim 6R_G$.

However, upon taking the same model and fixing the spin to $a = 0$, then the fit statistic obtained is only slightly worse, where $\chi^2_{\nu} = 1340/1237$. In this case only a single emissivity is required, where $q_1 = q_2 = 3.0 \pm 0.5$, while the disc abundance is consistent with Solar. Given that the high black hole spin model only shows a marginal improvement in fit statistic (by $\Delta\chi^2 \sim 11$ for 3 fewer degrees of freedom), then the claim of high black hole spin cannot be confirmed at a high confidence level, compared to the case where $a \sim 0$. Furthermore if the Brenneman et al. (2011) model is altered such that all 3 soft X-ray warm absorber zones fully cover the AGN, then this leads to a lower (and less constrained) value for the black hole spin, of $a = 0.35^{+0.59}_{-0.10}$ and is then formally consistent with the upper-limit of $a < 0.31$ from the dual reflector model in Patrick et al. (2011b).

The lower spin value may be due to the fact that the fully covering absorber adds greater spectral curvature to the model due to bound-free absorption, compared to the partial coverer. In the latter case, the absorption is diluted by an unabsorbed powerlaw, reducing the amount of spectral curvature, while the breadth of the iron line profile can increase to compensate. Finally it is noted that replacing the PEXMON model with a REFLIONX table for the distant reflector made little difference to any of the blurred reflection parameters and this appears unaffected by the parameterisation

of the distant reflection component.

The maximal spin scenario subsequently presented by Reynolds et al. (2012b) is recreated, but applied to the model as constructed in Patrick et al. (2011b) and in Patrick et al. (2012). Thus, in this case it is assumed that all 3 zones of the warm absorber in NGC 3783 fully cover the AGN as per Patrick et al. (2011b) and use the same warm absorber grids as in Patrick et al. (2012) and this chapter, although the choice of a particular absorption model grid appears to not effect the reflection models. For ease of comparison the same energy ranges as used by Brenneman et al. (2011) are adopted as above. Focussing in particular on the iron abundances, which Reynolds et al. (2012b) suggest is critical for determining the blurred reflection parameters, the values for the disc reflector parameters from Table 1 in Reynolds et al. (2012b) are used, namely the iron abundances, spin, emissivities and break radii, all with the inner and outer radii set to the ISCO and $400R_g$ respectively. In summary three scenarios are tested for the 2009 data: (i) $Z_{\text{Fe,inner}} = Z_{\text{Fe,outer}} = 3.3$ with near maximal spin; (ii) $Z_{\text{Fe,inner}} = Z_{\text{Fe,outer}} = 1$ with $a = 0$; (iii) $Z_{\text{Fe,inner}} = 4.2$, $Z_{\text{Fe,outer}} = 1$ with near maximal spin. These correspond closely to the models A, B and C respectively, as presented in Table 1 of Reynolds et al. (2012). The KERRCONV model is used to blur the disc reflection spectra, while an unblurred low ionisation REFLIONX grid is maintained to model the distant reflector. Aside from the blurred reflection parameters as per Reynolds et al. (2012b), the fit parameters are allowed to vary.

All three scenarios give a good fit to the data, with reduced chi-squared values of $\chi^2_\nu = 1300/1227, 1280/1227, 1284/1227$ for models (i), (ii) and (iii) respectively. Thus all the spin and abundance scenarios are statistically acceptable, while the $a = 0$ and Solar abundance case formally gives the better fit. Allowing the disc parameters to vary for the Solar abundance case then gives a constraint on the spin of $a < 0.45$ at 90% confidence, while the disk emissivity is $q_1 = q_2 = 3.0 \pm 0.5$ and no break radius is required. Indeed the same Solar abundance model when fitted over the energy ranges used in this analysis also gives identical results and an equally good fit, with $\chi^2_\nu = 1414/1374$, see Table D.3 on page 256.

Comparing the fit focusing in on the iron K band in Figure 5.5, where the top

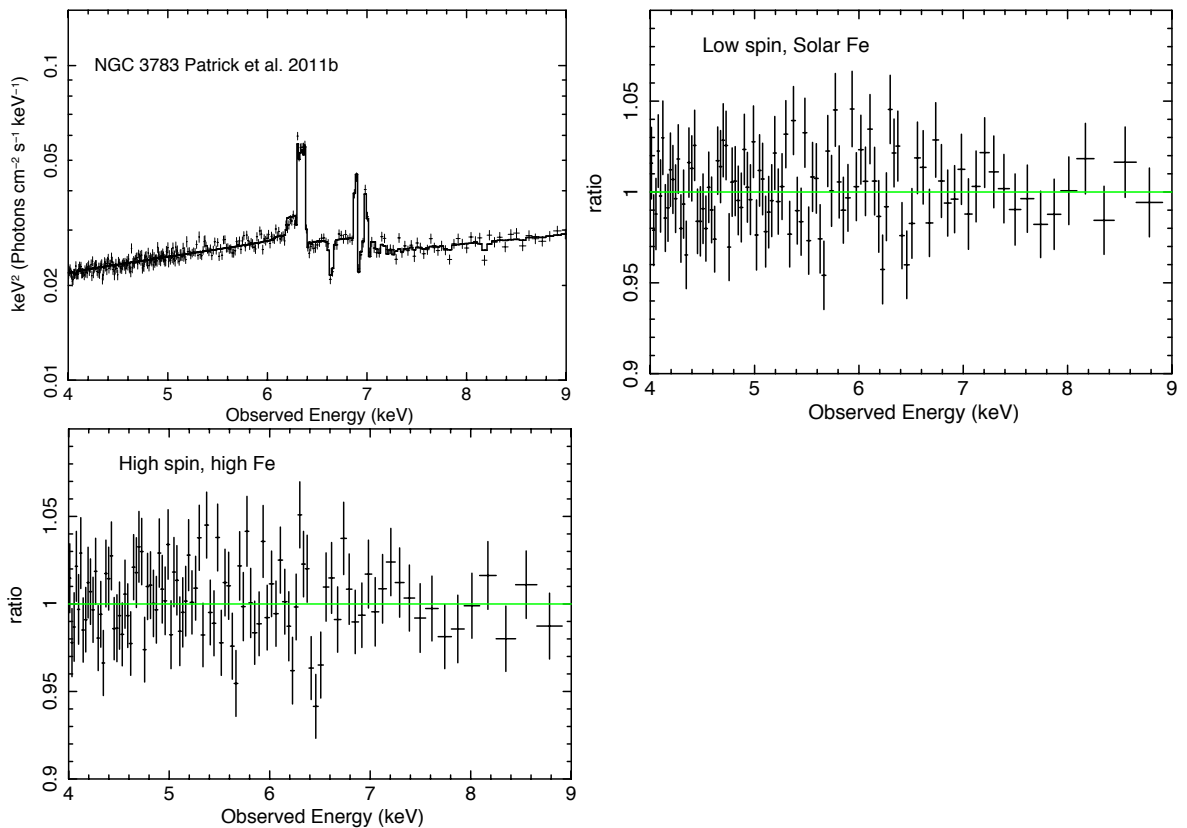


Figure 5.5: *Top left panel* νF_ν 4–9 keV plot of the Patrick et al. (2011b) best-fit model (with $a = 0$) to the 2009 NGC 3783 *Suzaku* data, note that the FeK region is well modelled in the fit as is the broad red-wing below 6.4 keV. *Top right panel* Residuals to the best fit dual reflector model, as shown in the upper panel with $a = 0$. *Lower panel* Residuals from the model with inner disc parameters as obtained by Reynolds et al. (2012b), i.e. with maximal spin, high emissivity and $Z_{\text{Fe}} > 3$. Both of the residual plots in the lower two panels show no noticeable difference in the iron K region, thus it appears difficult to discriminate between the two scenarios.

left panel shows the best fit dual reflector model presented here (with $a = 0$) and the top right and lower panels show the data/model ratios for the scenarios (i) and (ii) above, with high spin and low spin respectively, clearly there is little difference in the residuals between either the high spin scenario with super Solar abundances and the low spin scenario with Solar abundance. The only marginal difference is the narrow core of the Fe $K\alpha$ line at 6.4 keV is slightly over-predicted in the high spin, high Fe

abundance scenario. This is in contrast to the plots shown in Figure 5 of Reynolds et al. (2012b), where the $a = 0$ scenario strongly over-predicts the red-wing of the line between 5-6 keV. This could be due to the fact that the blurred reflector has a higher normalisation in the high spin scenario, which when applied directly to the $a = 0$ case could appear to over-predict the red-wing, unless the normalisation of the reflector is refitted accordingly.

Finally it is noted that if the RELLINE model is used instead of a blurred reflection component, then a lower spin value is usually preferred. For example, the upper-limit on spin to NGC 3783 with this model is $a < 0.24$ (also see Table 5.4). Indeed, Patrick et al. (2011b) also noticed some tendency (although not statistically significant) for the line to favour a retrograde black hole spin. The lower spin value may be due to the fact that the model only fits the broad iron line and not the reflected continuum, where the latter can often be blurred to such an extent that it is hard to distinguish from the direct continuum.

Thus, the overall conclusion would appear to be that it is very difficult to definitively determine the black hole spin in NGC 3783 with the present data, given the complexities of the models involved and the deep warm absorber present in this AGN. For instance as discussed above, the construction of overall the model and the warm absorber in particular can have an effect. In addition, the spin value is indeed degenerate upon the iron abundance, as discussed in Reynolds et al. (2012b) and thus the high spin cases always require high centrally concentrated iron abundances. Nonetheless, a statistically good fit is obtained with a simple Solar abundance reflector and no black hole spin. The evidence for a more complex picture with high abundances, complex emissivity profiles and high spin, would appear not to formally be required at high confidence, although neither can the high spin case be ruled out at present.

5.4.6 NGC 4051

The three *Suzaku* observations of NGC 4051 (as used in Lobban et al. 2011) included in this analysis vary significantly (see Figure 5.4). In particular, in the 2005 observation

(OBSID: 700004010) the source dips into an extended period of low flux versus the two 2008 observations which show the object in a period of high flux ($F_{2-10\text{ keV}2008} \sim 3.8 \times F_{2-10\text{ keV}2005}$, see Figure 5.4, Table D.4 on page 259). Similarly to Lobban et al. (2011), each observation and the long term spectral variability are successfully described with a partial covering scenario whereby parameters such as the column density and ionisation of the absorbing zones of gas remain approximately constant ($N_{\text{H}} \sim 9 \times 10^{22} \text{ cm}^{-2}$, over these time scales at least). The differences in the broad-band spectrum of each observation can be accounted for simply by allowing the normalisation of the intrinsic powerlaw, soft excess and distant reflection component to vary, in addition to the covering fraction of the partially covering absorption zone. Here covering fractions of 67%, 11% and 27% for observations 1, 2 and 3 respectively are found albeit with a much flatter intrinsic power-law ($\Gamma \sim 1.88$ here versus $\Gamma \sim 2.49$ in Lobban et al. 2011), however, this is likely due to the treatment of the soft excess and reflection components. Here (for consistency with the analysis of other objects in the sample) the soft excess is accounted for with a COMPTT component which is akin to a second soft POWERLAW, this could in part explain the discrepancies between the two different intrinsic power-law components.

Similarly to Lobban et al. (2011), there is strong evidence for blue-shifted absorption in the Fe K region indicative of an outflowing highly ionised zone of gas. When described as such, an outflow velocity of $5800_{-1300}^{+1400} \text{ km s}^{-1}$ in each observation is measured, consistent with Lobban et al. (2011). Both the Lobban et al. (2011) and the baseline models in this analysis describe the spectral variability with absorption dominated models. Replacing the partial coverer with a reflection component representing emission from the inner regions of the accretion disc as an alternate means of accounting for the hard excess and spectral curvature (i.e. a dual reflector) yields a fit worse by $\Delta\chi^2 \sim 145$ for 4 fewer degrees of freedom. Parameters such as SMBH spin and the emissivity index of the disc are forced to high values, i.e. $a \sim 0.996$ and $q = 6.1_{-0.1}^{+0.3}$. This is in order to smooth the reflection continuum to the extent to which it can successfully account for the long term spectral variability between observations, i.e. accounting for both the hard excess and subtle continuum curvature changes. The

partial covering scenario is therefore preferred both statistically and in terms of physical implications, i.e. extreme parameters and relativistic blurring are not required which would otherwise significantly deviate from the sample norm. Note that there is still a evidence for an highly ionised outflow in the FeK region, regardless of the application of a dual reflector or partial covering based model.

Based upon this, it is clear that the long term spectral variability of NGC 4051 cannot be produced purely by varying the reflected flux in a reflection dominated model; instead a partial covering scenario *must* be invoked to some extent in order to accurately reproduce the differences between each of the three *Suzaku* observations. Reintroducing a partial covering geometry (in addition to a dual reflector, Section 5.3.4) restores a fit similar to the baseline model. It is, therefore, perhaps more feasible that the broad-band spectrum and variability of NGC 4051 (in addition to other AGN) is primarily a result of variations in covering fraction in an absorption and not reflection dominated spectrum.

5.5 Conclusions

Based upon an analysis of all the publicly available *Suzaku* observations of Seyfert 1 AGN with observations longer than 50 ks and greater than 30000 XIS counts, the following conclusions can be made:

1. The majority (59%) of AGN in this sample feature complex warm absorption which has a significant affect upon the FeK region and any accretion disc parameters derived from it. The use of the full 0.6-100.0 keV broad-band data is therefore essential prior to any attempt to use relativistic line profile models as a diagnostic for the inner regions of the accretion disc. The mean photon index of the 46 objects on the sample is $\Gamma = 1.82 \pm 0.03$.
2. Absorption in the FeK region due to highly ionised gas producing absorption features from Fe XXV and Fe XXVI are relatively common in AGN (30%), most

of which (86%) are outflowing at high velocities. While a large fraction of the detected highly ionised winds are outflowing, there may be a larger number of low velocity winds which are not detected due to the possible presence of ionised Fe XXV and Fe XXVI emission lines. The additional curvature added to the region through modelling with an appropriate XSTAR grid, while subtle, has a notable effect upon the strength of any broad residuals which may remain below 6.4 keV and be interpreted as strong relativistic emission.

3. A partial covering geometry is required in 35% of all objects in the sample. These high column density zones primarily affect the hard X-ray spectrum above 7 keV although reducing the strength of broad residuals in the Fe K region rather than removing them entirely.
4. Narrow ionised emission in the Fe K region from Fe XXV and Fe XXVI are relatively common in these AGN, featuring in 24/46 and 18/46 of objects respectively. Of these AGN, 10/46 feature both Fe XXV and Fe XXVI emission. These lines are found to be much more common compared to an *XMM-Newton* survey by Nandra et al. (2007) despite possible interplay with the blue-wing of more sophisticated relativistic line emission models which could reduce the number of narrow line detections.
5. Examining the Fe K region after a complete modelling of the broad-band 0.6-100.0 keV spectrum and all required absorption zones yields a range of weak to moderate strength broad residuals below 6.4 keV. 26/46 (56%) of the objects in this sample require some degree of relativistic line emission in the Fe K region at 90% confidence and 23/46 (50%) at > 99.5% confidence.
6. These broad residuals are well fit with the RELLINE model and yield an average broad line strength of $EW = 96 \pm 10$ eV for the total of 26 objects. The line energy and σ_{width} of the broad residuals when modelled with a Gaussian are consistent with Nandra et al. (2007).

7. An average emissivity index of the accretion disc of $q = 2.4 \pm 0.1$ is estimated from this sample, suggesting that emission from the accretion disc responsible for relativistic lines is not extremely centrally concentrated when purely the line profile in the Fe K region is used as a diagnostic. The majority of the line flux therefore occurs from the blue-wing of the line profile with emission being insufficiently close to R_{ISCO} as to redshift a significant proportion of the X-ray flux into a strong red-wing. An average disc inclination of $i = 33^\circ \pm 2^\circ$ and inner radius of emission $R_{\text{in}} = (21 \pm 6) R_g$ is also found.
8. With the assumption that the inner radius of the accretion disc (R_{in}) extends down to the innermost stable circular orbit (R_{ISCO}), loose constraints upon the SMBH spin parameter a can be made. The relativistic line emission profiles are sufficiently distinguished in 11/46 objects to place upper or lower bounds on the spin. After a broadband analysis the following estimates can be made: Ark 120, $a < 0.94$; Fairall 9, $a = 0.60_{-0.63}^{+0.19}$; MCG-02-14-009, $a < 0.88$; MCG-05-23-16, $a < 0.50$; MCG-06-30-15, $a = 0.49_{-0.12}^{+0.20}$; Mrk 79, $a < 0.80$; Mrk 335, $a = 0.70_{-0.01}^{+0.12}$; NGC 3516, $a < 0.30$; NGC 3783, $a < 0.24$; NGC 7469, $a = 0.69_{-0.09}^{+0.09}$ and SWIFT J2127.4+5654 with $a = 0.70_{-0.14}^{+0.10}$. Under the assumption that $R_{\text{in}} = R_{\text{ISCO}}$, a maximally rotating SMBH is ruled out in each of these 11 objects.

6 Discussion

This sample of 46 objects includes all the Seyfert 1 AGN matching the selection criteria outlined in Section 5.1 with observations which are publicly available in the *Suzaku* archive. The aim of this work was to form detailed broad-band models for each object, fully modelling and accounting for any absorption where required which then allows for the parameterisation of the FeK regions and ultimately an assessment of in how many objects can SMBH spin be constrained or estimated. The main motivation for conducting this analysis is to produce an in-depth study of the FeK regions of these AGN and to assess the strength and prevalence of broad emission from the inner regions of the accretion disc. In order to accurately examine both emission and absorption properties in the FeK region, it is essential that high energy data is used to measure the strength of the Compton hump and hard X-ray excess as part of the formation of a broad-band model; the *Suzaku* X-ray observatory is unique its ability to provide such data simultaneously with soft X-ray data. The data included in this sample have been selected with sufficient S/N such that, if broadened line emission from the inner regions of the accretion disc exists, it should be possible to detect it.

It should be noted that the broad-band X-ray spectra of these AGN are complex with many of them featuring multiple absorption zones which have a significant role in adding spectral curvature and hence have a significant affect upon and ‘broad’ residuals in the FeK region. Nandra et al. (2007) also note that the continua are complex in a study of the 2.5-10.0 keV energy band with data obtained with *XMM-Newton*, however, here this study is taken a step further by also considering a detailed modelling of the 0.6-10.0 keV soft X-ray data, allowing the formation of more complete models of the entire X-ray spectrum up to 100 keV. Low energy X-ray data below 2.5 keV is essential to perform a detailed analysis of the FeK region of any object since first forming an appropriate baseline model is an important prerequisite to account for continuum curvature due to the warm absorber (e.g. Reeves et al. 2004; Turner & Miller 2009; Miller, Turner & Reeves 2009).

6.1 Typical broadband Seyfert 1 spectra

6.1.1 Soft and hard excesses

The use of the HXD instrument on *Suzaku* and BAT onboard *Swift* allows us to examine the hard X-ray spectra of the objects in this sample and to appropriately parameterise the distant reflection component. This may arise, for example, from the reflection of continuum X-rays off the cold ($T < 10^6$ K) outer regions of the accretion disc or via a parsec scale torus.

The majority of AGN in this sample show evidence for a reflection component, only 7/46 (see Table 6.1) do not require the addition of the unblurred REFLIONX model (3C 111, IRAS 13224–3809, MR 2251–178, Mrk 79, NGC 7314 and PG 1211+143). Neither are these objects best described with a high column density partially covering absorbing zone with $N_{\text{H}} \sim 10^{24} \text{ cm}^{-2}$ which can replicate a hard X-ray excess to some extent, i.e. there is no apparent hard excess in these objects. Table D.4 on page 259 also indicates that the large majority of AGN in this sample do feature excess emission in the 15–50 keV region over the extrapolated 2–10 keV intrinsic powerlaw. A number of the objects in the sample feature particularly strong reflection with 15–50 keV reflector flux $F_{\text{reflector}} > 3 \times 10^{-11} \text{ erg cm}^{-2} \text{ s}^{-1}$, namely IC 4329A, MCG+8-11-11, NGC 3227, NGC 3783, NGC 4151 and NGC 5506. In addition to this, a large number of the AGN in this sample feature particularly hard X-ray spectra, i.e. those with a high hardness ratio $F_{15-50 \text{ keV}}/F_{2-10 \text{ keV}} > 3$: 3C 445, Mrk 279, NGC 1365, NGC 3227 (Obs 2, 4 & 6), NGC 3516 (Obs 1) and NGC 4151 (see Table D.4 on page 259). For comparison, the hardness ratio for a typical $\Gamma = 1.8$ power-law continuum and $R = 1$ reflection would be $F_{15-50 \text{ keV}}/F_{2-10 \text{ keV}} = 1.5$ (see Section 6.1.2), this implies either very strong reflection as per the light bending model (Miniutti & Fabian 2004) or high column partial covering (Turner & Miller 2009; Tatum et al. 2013).

A significant number of AGN in this sample are fit very well assuming a simple Solar iron abundance, i.e. $Z_{\text{Fe}} = 1.0$ when allowed to vary as a free parameter within REFLIONX. Although the narrow FeK α core is sufficiently strong in at least

9 objects that further neutral iron emission is required from material distant to the central SMBH, e.g., the broad line region in addition to reflection off the torus. Four objects strongly require sub-Solar iron abundance (IC 4329A, NGC 3227, NGC 5506 and SWIFT J2127.4+5654) while 4/39 statistically prefer a slight super-Solar iron abundance (typically $Z_{\text{Fe}} < 3$). This suggests that the hypothesis of Solar abundances throughout the disc and central engines of these AGN is a reasonable assumption in contrast to some analyses which appear to require strongly super-Solar Z_{Fe} based upon inner disc reflection (e.g. Brenneman et al. 2011; Fabian et al. 2012). The analysis of the 46 objects in this sample indicates that the reflection in an overwhelming majority of the Seyfert 1 type AGN in the *Suzaku* archive is well described by reflection of a cold, distant, neutral material with Solar abundances throughout, also see Nandra & Pounds (1994) and Rivers, Markowitz & Rothschild (2011a) for similar findings regarding the recurrent presence of the Compton hump.

6.1.2 Soft X-ray absorption and partial covering

The way in which absorbing zones are modelled in X-ray spectra can have a significant affect upon the FeK region and the estimation of properties relating to the central SMBH and the surrounding accretion disc. Within this *Suzaku* sample, a large proportion of AGN feature complex absorbers, requiring one or more zones of an XSTAR grid. Only 12/46 (26%) of objects in this sample can be considered ‘bare’ for the purposes of this work - featuring no statistically significant additional absorption zones in addition to the neutral Galactic column, these are 3C 390.3, Ark 120, Fairall 9, MCG–02-14-009, Mrk 110, Mrk 205, Mrk 335, Mrk 359, NGC 3147, NGC 7213, NGC 7469 and RBS 1124. A few objects in the sample (5/46, 11%) feature an additional neutral zone of absorbing gas at the redshift of the object, while the remaining 27/46 (59%) all require the application of complex warm (i.e. ionised) zones of gas to model the broadband spectrum.

Of these 27 AGN, 16 also statistically require a partially covering geometry (i.e. 35% of the total sample, Table 6.1). In this scenario one of the absorbing zones of gas

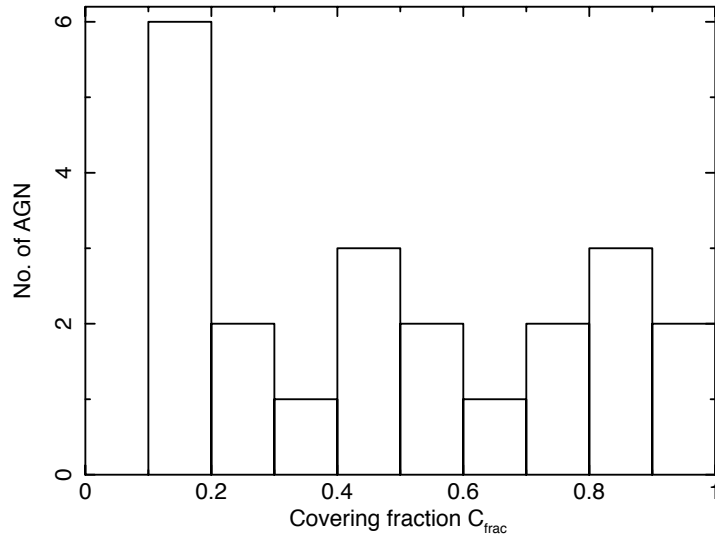


Figure 6.1: The distribution of partial covering covering fractions. Note that the full range is covered with a relatively even distribution.

(typically high column $N_{\text{H}} > 5 \times 10^{23} \text{ cm}^{-2}$) partially obscures the nucleus in addition to one or more lower column density fully-covering absorbing zone. The majority of the partial covering models in this sample have a sufficiently high column density such that their predominant effect is to supplement and increase the hard X-ray flux. The distribution of covering fractions for the partial covering fits here cover the full range from low to high covering fractions (Figure 6.1).

It is noted that only single layer partial covering geometries are used here (where formally required) in this analysis since multiple layers can be somewhat ambiguous and care must be taken to ensure that layers are not added on an ad-hoc basis until all features are removed from the spectrum. None of the objects in this sample require more than a single layer of partial covering in order to obtain an acceptable fit to the broad-band data.

Partial covering scenarios in some previous analyses have been used to model spectral curvature in the Fe K region which may otherwise be attributed to relativistic line emission e.g. MCG-6-30-15 by Miller, Turner & Reeves (2009). However, careful examination of the effects of high column partial coverers such as those used here sug-

gests that the measured strength of broad line emission in the FeK region is simply reduced (i.e. lower EW ; see Section 4.2.2.1) while the estimated accretion disc parameters and BH spin estimates remain relatively unchanged (for example, MCG–06-30-15 in Patrick et al. 2011b).

Tatum et al. (2013) conducted an analysis of the hard X-ray excesses in a sample of 43 type 1-1.9 AGN which feature both *Suzaku* and *Swift* observations in order to examine the extent to which partial covering of the continuum source by Compton-thick gas is present in a large sample of objects. In the Tatum et al. (2013) analysis 90% of objects have a hardness ratio ≥ 1.1 which is the estimated hardness ratio for an illuminating continuum of photon index $\Gamma = 2.0$ plus reflection from an optically thin, Compton-thick disc subtending 2π sr. From this they suggest that 90% of objects show evidence for hard X-ray emission above a simple power-law plus 2π sr reflection geometry, finding that 80% of the sources in their sample show evidence for a 15-50 keV/2-10 keV hardness ratio consistent with a partial coverer with $N_{\text{H}} \sim 10^{24} \text{ cm}^{-2}$, a low ionisation and a covering fraction of $> 50\%$. Tatum et al. (2013) also find that if the hard X-ray excess is produced purely by reflection the FeK α flux is over predicted, i.e. there is an excess of hard X-rays in addition to what is expected from reflection alone.

Taking the average properties of the full *Suzaku* sample in the analysis made in Chapter 5, the average power-law photon index is a flatter $\Gamma \sim 1.8$ (Table 6.2). Therefore, the typical hardness ratio expected from an intrinsic power-law continuum plus $R = 1$ reflection (as above) is ~ 1.5 , this reduces the percentage of objects with evidence for partial coverers in the Tatum et al. (2013) sample to a lower 60% which is comparable to the 50% of objects found in Chapter 5 with a hardness ratio > 1.5 (see ratios in Table D.4 on page 259). While the number of objects which may require partial covering (or indeed additional reflection from the inner regions of the accretion disc) is lower than suggested by Tatum et al. (2013), a significant number of objects do arguably require some additional hard X-ray flux above a simple power-law plus distant reflection scenario.

Indeed, fitting the broadband spectra of these objects with the reflected flux

Table 6.1: Table of main model components and the percentage of objects in the sample of 46 objects which feature those components based upon $> 90\%$ confidence levels.

Component	Percentage
Soft excess	$67 \pm 6\%$
Reflection	$85 \pm 6\%$
Warm absorber	$59 \pm 5\%$
Partial covering	$35 \pm 4\%$
Fe K outflow	$30 \pm 4\%$
Fe XXV emission	$52 \pm 5\%$
Fe XXVI emission	$39 \pm 4\%$
Broad Fe K α line	$57 \pm 5\%$

dependent upon the narrow Fe K α core flux suggests that 35% (Table 6.1) of objects in this sample require a partial covering geometry. However, this fraction may be in fact be closer to the $\sim 60\%$ suggested by Tatum et al. (2013); since the hard X-ray flux produced by the REFLIONX reflection model throughout this analysis is related to the narrow Fe K α core flux, if a portion of this flux arises from distant Compton-thin matter (i.e. without associated reflection), the distant reflector contribution will be reduced thereby leaving an excess of hard X-rays which may indicate the presence of a partial covering geometry. The results presented within this work generally agree with those presented by Tatum et al. (2013) in that a significant fraction of Seyfert 1 AGN feature hard X-ray excesses over and above the X-ray flux predicted by distant reflection and the illuminating power-law alone. This suggests a patchy distribution of Compton-thick matter along sight lines to type 1 AGN which partially cover the nucleus and not just in Seyfert 2s as predicted by unified models.

6.2 Relativistic emission and black hole spin in Seyfert 1 AGN

6.2.1 Broad Fe K line statistics

When the broad Fe K α lines are parameterised with a Gaussian, there is an average line centroid energy of $\text{LineE} = 6.32 \pm 0.04 \text{ keV}$ (see Figure 6.2), $\sigma_{\text{width}} = 0.47 \pm 0.05 \text{ keV}$ and equivalent width $EW = 97 \pm 19 \text{ eV}$ (Table 6.2), both of which are also generally consistent with a similar parameterisation with a broad Gaussian by Nandra et al. (2007) who find an average $\text{LineE} = 6.27 \pm 0.07 \text{ keV}$, $\sigma_{\text{width}} = 0.34 \pm 0.05 \text{ keV}$ and $EW = 91 \pm 13 \text{ eV}$. In an analysis of the 2-10 keV spectrum of 149 radio-quiet Type 1 Seyfert AGN with *XMM-Newton*, de la Calle Pérez (2010) estimate a mean broad line equivalent width of $EW = 143 \pm 27 \text{ eV}$, which is higher than that obtained here, however, the authors note that this may be an overestimate due to an inability to detect weak lines and a bias towards higher values.

After the formation of a complete baseline model, the physically motivated relativistic line emission model `RELLINE` was introduced to account for any remaining broad residuals in the Fe K region. The criteria for the presence of a broad component is $\Delta\chi^2 > 7.8$ with the introduction of four additional free parameters (q , a , i and normalisation), this is equivalent to the 90% confidence level. Based upon this requirement 26/46 (i.e. 57%, Table 6.1) of the AGN (by object, not observation) in this sample formally statistically require relativistic emission from the inner regions of the accretions disc. Furthermore, 23/46 (50%, Table 5.4 on page 175) require broadened line emission at $> 99.5\%$ confidence ($\Delta\chi^2 > 15$). This fraction is somewhat lower (although not substantially so) than that obtained by Nandra et al. (2007) who find that 18/26 (69%) of objects in their sample show evidence for broad line emission at $> 99\%$ confidence. The disparity between the two surveys may be due to the energy range over which the analysis has been conducted: 0.6-100.0 keV here, versus 2.5-10.0 keV. This study also takes into account partial covering where required.

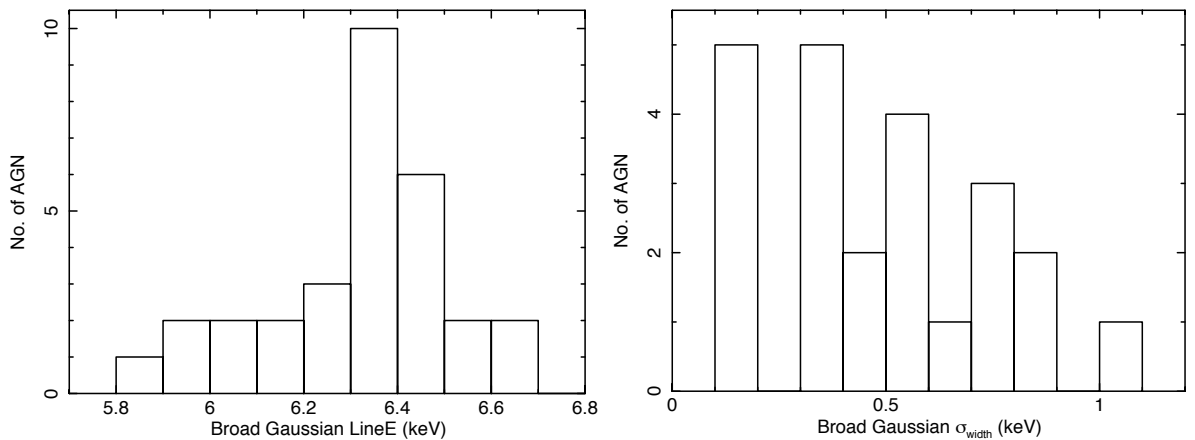


Figure 6.2: Histograms showing the distribution of line centroid energy and σ_{width} when broadened emission in the Fe K region is modelled with a Gaussian.

6.2.2 Ionised emission in the Fe K region

Narrow ionised emission from distant material is found to be relatively common (in the baseline model) amongst these Seyfert 1 AGN with 24/46 of objects featuring Fe XXV emission at 6.63-6.7 keV and 18/46 featuring Fe XXVI emission at ~ 6.97 keV. Meanwhile 10/46 objects feature both Fe XXV and Fe XXVI emission (Table D.2 on page 252). These fractions are much higher than those obtained by Nandra et al. (2007) who only find significant emission at 6.7 keV in NGC 5506 and significant 6.97 keV emission in both NGC 3783 and NGC 4593. The findings here, however, concur with those found by Bianchi et al. (2009) and Patrick et al. (2011a) who similarly find that narrow ionised emission lines are a common feature in a number of Seyfert 1 spectra.

After the inclusion of a component such as RELLINE to account for any broad iron line residuals, these fractions can be somewhat reduced due to interplay with the blue-wing of a relativistically broadened line profile falling in the 6.6-7.0 keV region in some AGN. For example, a feature at ~ 6.7 keV can often be modelled as either narrow ionised emission or as part of a broad line profile with fairly typical emissivity and inclination parameters. It is likely, therefore, that the true fraction of Seyfert 1 spectra with narrow ionised emission (Fe XXV in particular) is lower after the inclusion of a

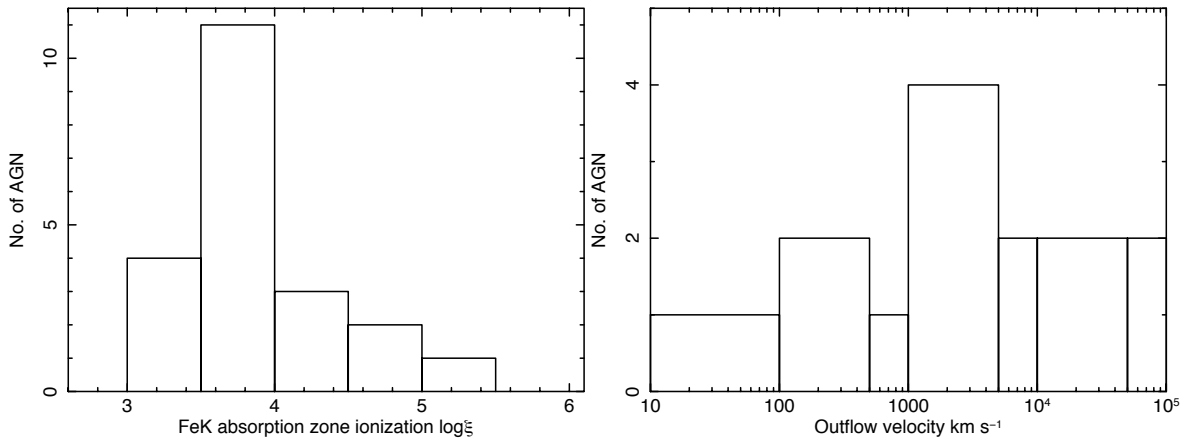


Figure 6.3: The distribution of ionisation and outflow velocity of absorption zones at FeK energies. Note that the outflow velocity covers a wide range of velocities with no significant peak within the parameter space. For outflow velocities for which only an upper limit can be placed, the best-fit value is used to create the distribution.

broad line component. In 4 objects the feature at ~ 6.7 keV is preferentially described by a relativistic line profile for the above reasons, leaving the final number of AGN in this sample with distant FeXXV emission as 18/46 objects. Calorimeter resolution spectra from *Astro-H* will help to solve these issues by resolving any narrow discrete ionised emission lines from any blue-wing of a relativistic line profile which may be present.

6.2.3 Highly ionised absorption and outflows

In addition to absorption at soft X-ray energies, absorption in the FeK region due to 1s-2p resonance lines from FeXXV and FeXXVI are found to be relatively common amongst the AGN in this sample. Evidence for highly ionised absorption is found 14/46 (30%) of objects: 3C 111, 3C 445, MCG-6-30-15, MR 2251-178, Mrk 766, NGC 1365, NGC 3227, NGC 3516, NGC 3783, NGC 4051, NGC 4151, NGC 5548, PDS 456 and PG 1211+143; consistent with the 36% detected by Tombesi et al. (2010b) in a sample of 101 *XMM-Newton* observations (of 42 AGN) searching for ultra-fast outflows. The

majority (12/14) of these lines are blue-shifted, suggesting that they originate from an outflowing zone of absorbing gas. When modelled with a high turbulent velocity XSTAR grid ($v_{\text{turb}} = 1000 \text{ km s}^{-1}$) there is a mean column density $N_{\text{H}} = (1.74 \pm 0.85) \times 10^{23} \text{ cm}^{-2}$, mean ionisation $\log(\xi) = 3.97 \pm 0.13$ and a wide range in outflow velocity ranging between $400 \text{ km s}^{-1} < v_{\text{out}} < 84600 \text{ km s}^{-1}$ with no significant peak in the distribution of v_{out} values (as shown in Figure 6.3).

It is important to note that highly ionised absorption zones also influence the strength of any broad residuals in the Fe K region, for example, Reeves et al. (2004) found that no broad residuals remained in an *XMM-Newton* observation of NGC 3783 after the implication of the required XSTAR grid to model the highly ionised absorption. The measured strength of any ‘broad’ residuals is therefore reduced given an appropriate high ξ absorption zone and hence the detection and modelling of such zones is essential if robust statistics regarding the Fe K region are to be formed. Based upon the work by Tombesi et al. (2010a & 2010b) the actual fraction of AGN with statistically significant outflows may indeed be higher than the 30% found here (see Table D.2 on page 252) due to the presence of ultra fast outflows with absorption lines blue-shifted to $> 7 \text{ keV}$ since these have not been systematically searched for here from 7-10 keV (see Gofford et al. 2013 for a systematic analysis of outflows in a sample of *Suzaku* observations). The fraction of AGN with highly ionised zones presented here may also in fact be larger. It is possible that the presence of narrow emission lines from ionised species of iron may reduce our ability to detect absorption lines in CCD resolution spectra from the same species of iron with current instruments, therefore, it is plausible that 30% is likely the minimum fraction of AGN with highly ionised absorption zones.

6.2.4 Typical parameters of the disc

Taking the parameters obtained with RELLINE for the 26 objects featuring broadened line emission (Table 5.4 on page 175) the typical parameters of the accretion disc can be estimated (Table 6.2). The average inclination of the disc is $i = 33^\circ \pm 2^\circ$ for 21 objects,

Table 6.2: Table of average parameters of the sample, values quoted for a broad Gaussian and RELLINE are for the objects in which such components were statistically significant at $> 90\%$ confidence level.

Parameter	Average value
POWERLAW	
Γ	1.82 ± 0.03
Broad Gaussian	
Energy (keV)	6.32 ± 0.04
EW (eV)	97 ± 19
σ_{width} (keV)	0.47 ± 0.05
RELLINE	
EW (eV)	96 ± 10
q	2.4 ± 0.1
$R_{\text{in}} (R_{\text{g}})$	21 ± 6
Inclination ($^{\circ}$)	33 ± 2

consistent with Nandra et al. (2007) who find $i = 38^{\circ} \pm 6^{\circ}$. The average emissivity index of the disc is measured at a low to moderate $q = 2.4 \pm 0.1$ (for the 20 objects in which it can be constrained) and is consistent with an analysis of 6 ‘bare’ Seyferts by Patrick et al. (2011a) and an *XMM-Newton* survey by de la Calle Pérez (2010) who find $q = 2.4 \pm 0.4$ and $i = 28^{\circ} \pm 5^{\circ}$. This value is much lower compared to an often high emissivity ($q > 5$) assumed by many light bending models and interpretations (Miniutti & Fabian 2004; Miniutti et al. 2009; Brenneman et al. 2011; Gallo et al. 2011; Nardini et al. 2011), suggesting that strong GR effects may not be present in the X-ray spectra of these Seyfert AGN.

Figure 6.4 shows the distribution of the emissivity indices for the sample, note that there is a relatively small dispersion in q with the majority of values centred around $q \sim 2.4$. The average strength of the RELLINE component is measured at $EW = 96 \pm 10$ eV for the total of 26 objects, consistent within errors with Patrick et al. (2011a) and Nandra et al. (2007). This is also similar to that predicted by George & Fabian (1991) for reflection off a cold disc subtending 2π sr for a typical Γ and inclination, see Figure 6.5. As can be seen from Figure 6.4, there is also a wide range

in the measured equivalent widths of the RELLINE component, revealing a possible bi-modal nature with a group centering around $EW \sim 70$ eV and a second stronger though less populated group at $EW \sim 150$ eV. However, there are insufficient statistics in this sample to draw any conclusions from this, indeed the distribution may be more continuous when taking error bars and different confidence levels into account. It is also interesting to note that in the cases where BH spin can be constrained, maximal spin is ruled out in all objects with the spin parameter a preferring to take low to intermediate values, similarly the typical inner radius of emission is at tens of R_g with many clustered around $R_{in} \sim 20 - 30 R_g$ (see Figure 6.4).

6.2.5 Shape of the line profile

The emissivity index obtained here is based primarily upon any remaining residuals in the Fe K region, i.e., RELLINE is modelling a relativistic line profile which takes into account both red and blue-wings of a line profile rather than simply adding a broad ‘hump’ to the data below 6.4 keV (as, for example, a Gaussian might). Despite the narrow nature of the blue-wing at low a and q , its strength relative to the red-wing (and continuum) is typically insufficient to provide an alternative explanation for narrow emission lines commonly attributed to distant Fe XXV (at $\sim 30^\circ$) or Fe XXVI emission (at $\sim 40^\circ$). However, there should be some caution to account for the presence of narrow ionised emission lines prior to applying a relativistic line model to ensure that the correct inclination of the disc is measured.

The driving factor behind the estimated emissivity and spin values is therefore primarily the strength and width of the red-wing. Figure 6.2 indicates that when modelled with a broad Gaussian, the typical line centroid energy of the broad line peaks at 6.3–6.4 keV which also suggests that any broad emission in the Fe K region is not strongly gravitationally redshifted. The low average emissivity index ($q = 2.4 \pm 0.1$) of the disc found in this sample of 46 objects is as a result of including XSTAR grids for the required absorption zones which dominate the spectrum in many objects below 2.5 keV, it is also noted that the associated spectral curvature these zones add at

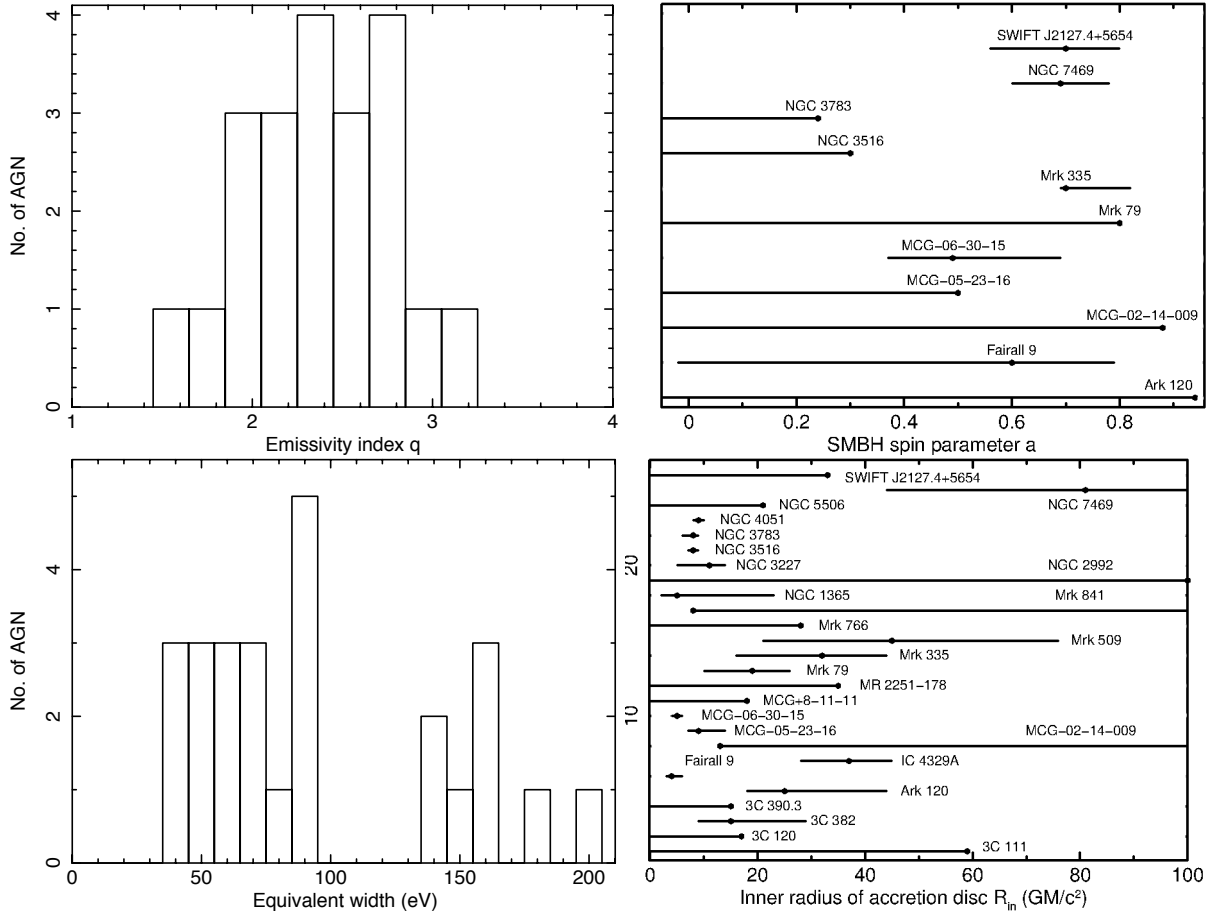


Figure 6.4: Figures of the distribution of emissivity index, RELLINE equivalent width, SMBH spin and inner radius of emission. Note that the typical inner radius of the disc for the sample centres around tens of R_g . Data taken from Table 5.4 on page 175.

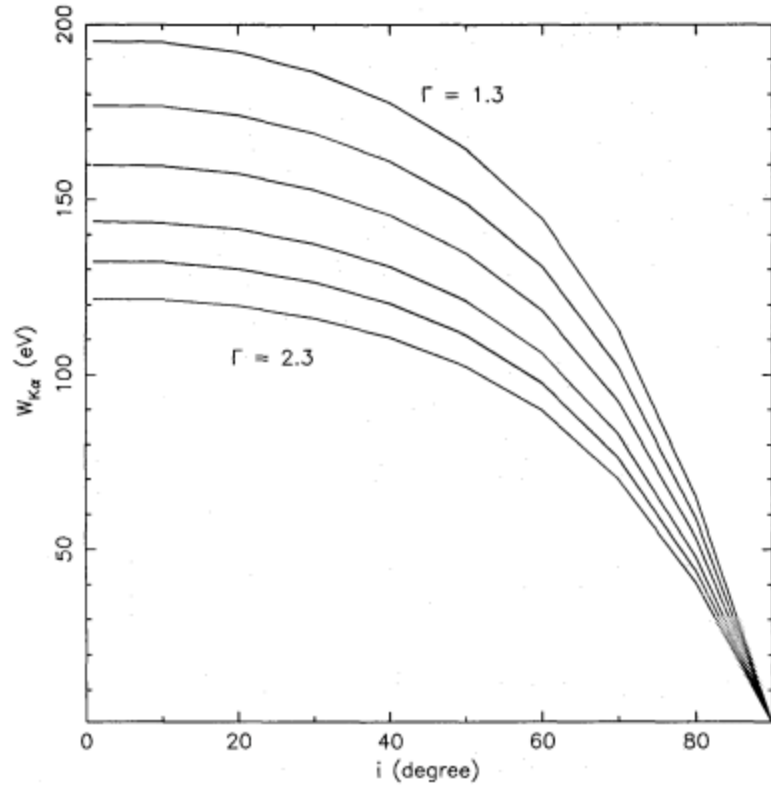


Figure 6.5: Predicted equivalent width of an FeK α line versus disc inclination for reflection off a cold slab subtending 2π sr plotted for ranging photon indices for the illuminating continuum. Figure taken from George & Fabian (1991).

higher energies (Miller, Turner & Reeves 2008; Zycki et al. 2010) leave little room for a significantly broadened relativistic line profile with high q and maximal spin. As a consistency check, the average emissivity index for those objects without any intrinsic warm absorption is $q = 2.3 \pm 0.1$, this is consistent with the emissivity index for the sample as a whole and for those AGN with warm absorbers ($q = 2.5 \pm 0.1$).

The extremely centrally concentrated emission that emissivities of $q > 4$ suggest are simply no longer required and relativistic emission from the disc (if present) originates from regions more distant to the BH (typically tens of R_g , see Table 5.4 and

Figure 6.4), not the very inner regions which would invoke strong GR effects such as significant light bending. This is, however, under the assumption that a relativistically blurred reflection continuum is not responsible for the soft excess, see Section 6.3.4.

6.2.6 Distribution of SMBH spin, disc parameters and the implications

With the use of broadband data from observatories such as *Suzaku* tentative steps can be made towards estimating the spin of the central supermassive black hole. The primary effect of the spin parameter a upon the line profile is to set the degree to which the red-wing extends to the soft X-ray energies, i.e., a maximal Kerr black hole would have the smallest inner radius of the accretion disc, thereby subjecting emitted photons to a stronger red-shift and sharply extending the red-wing into the soft X-ray regime. A Schwarzschild black hole ($a = 0$), however, truncates the red-wing of the line profile at $\sim 4 - 5$ keV due to a minimum inner radius of $6 R_g$ (indeed a maximally retrograde BH pushes the inner radius further out to $R_{\text{in}} \sim 9 R_g$). It is clear to see, therefore, that if the spectral curvature associated with various warm absorbing zones is not taken into account, a relativistic line emission model such as RELLINE or KERRDISK may be forced to higher near maximal spin values to ‘take up the slack’ of an improperly modelled continuum.

Many of the prime candidates for measuring BH spin with *Suzaku* have already been presented in previous papers and chapters, firstly the ‘bare’ Seyferts (Patrick et al. 2011a; i.e. Chapter 3) and a collection of deep *Suzaku* observations (Patrick et al. 2011b; i.e. Chapter 4), hence few new BH spin estimates are presented here. In Fairall 9, NGC 3516 and NGC 3783, however, an analysis is made of each of the multiple *Suzaku* observations of each object, finding a baseline+RELLINE model which can accurately describe the objects in different flux states with only subtle variations to the model over time e.g. changes in continuum flux. Finding a model which can adapt over time to fit each observation while retaining the same basic properties (e.g. emissivity, inclination, spin) arguably increases the robustness of the results.

The work within this thesis suggests a range of low-to-moderate SMBH spin values in a small number of AGN. Out of the total of 46 objects, spin constraints can be placed on 11/46, while 5 of these allow us to place upper and lower bounds upon a and hence constrain the spin to some degree. Albeit with this relatively small number of SMBH spin estimates, tentative steps can be made towards starting to develop a basic picture of the spin distribution of these Seyfert 1 AGN. A maximal prograde SMBH is ruled out in all of the objects where it can be constrained in the full sample at a minimum of 90% confidence and $> 99.5\%$ confidence in 5/11 (MCG–6-30-15, NGC 3516, NGC 3783, NGC 7469 and SWIFT J2127.4+5654, Figure 6.4). However, this does not rule out the possibility of a maximally rotating BH with an accretion disc truncated short of the ISCO.

From the work within this thesis, it is found that in general a maximally spinning SMBH can be ruled out with $> 90\%$ confidence. This is in contrast to many existing estimates in the literature which suggest maximally spinning BHs, see Section 1.7.2 for a summary. While this sample of AGN and number of spin estimates is far too small from which to draw any robust overall conclusions, there are nevertheless tentative suggestions. The fact that in this, albeit small, sample of AGN no evidence is found for the presence of maximally spinning Kerr black holes could suggest that periods of prolonged accretion are not the common method of SMBH accretion, at least in the context of this sample of relatively local galaxies. An extended period of constant accretion would intuitively ‘spin-up’ or increase the spin of the central SMBH therefore resulting in a population of spin parameters with $a = 0.998$ (Volonteri et al. 2005). If, however, there are instead periods of chaotic accretion or accretion in which the AGN ‘switches’ on and off this may result in a range of low to intermediate spins (King & Pringle 2007; King et al. 2008). The results here, although tentative, suggest that this may be the appropriate scenario for this local population.

A recent publication by Walton et al. (2013) conducted an analysis of 26 ‘bare’ Seyferts which have been observed with *Suzaku*, although they note that six of these objects do show evidence for ionised absorption at soft X-ray energies which is modelled with an appropriate XSTAR grid, therefore they are not *strictly* ‘bare’. The authors

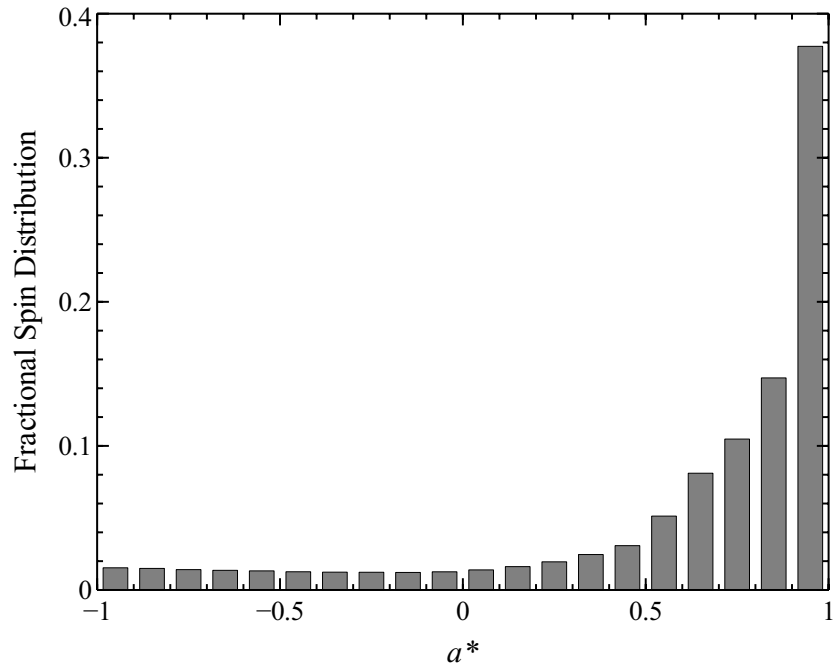


Figure 6.6: Skewed distribution of SMBH spin taken from Walton et al. (2013) based upon reflection dominated models, i.e. the reflection continuum is used to model the smooth soft excess which forces the disc parameters and SMBH spin to extreme values. The work presented with this thesis, however, suggests a range of low to intermediate SMBH spin.

note that a purely reflection origin for the soft excess is assumed throughout while also requiring that the emissivity is $q > 3$ which is justified by the assumption that emission is centrally concentrated, noting that if emission arises from the very inner regions of the accretion disc it will be subjected to general relativistic light bending and time dilation (Miniutti & Fabian 2004; Wilkins & Fabian 2011).

Walton et al. (2013) find that in the vast majority of these AGN rapidly spinning SMBHs are found resulting in a highly skewed spin distribution towards $a \sim 0.998$ (see Figure 6.6). However, based upon the results in Chapter 3, this is to be expected when assuming a blurred atomic origin of the soft excess, see Section 1.5.4. The high disc ionisations, steep emissivity profiles, maximal spin and high inclinations all point towards a blurred reflector geometry which is being forced into a smooth soft X-ray

continuum to model the strength of the soft excess. It should be noted that of the objects in the Walton et al. (2013) sample, the objects which do not feature a soft excess typically do not have spin estimates placed upon them, i.e., the Fe K region is not being fitted such that a relativistically broadened line profile does not facilitate the estimation of accretion disc and SMBH spin parameters.

The SMBH spin estimates made by Walton et al. (2013) are therefore only valid if blurred reflection alone is responsible for the soft excess, i.e. Model E from Chapter 3 (Section 3.3.5). If there is any contribution from a reprocessed thermal component in a corona above the disc, as is popularly believed (see Porquet et al. 2004; Dewangan et al. 2007; Lohfink et al. 2013; Noda et al. 2013 etc), then the high spin estimates and accretion disc properties presented in Walton et al. (2013) will be significantly altered, leading to results which may then be consistent with the work presented in Chapter 3 and Patrick et al. (2011a).

6.2.6.1 Comparison with stellar mass BHs

A number of stellar mass black holes have also had their spin estimated through two competing methods. The first is to measure the temperature of the accretion disc in combination with its luminosity in order to determine the rate at which material is swept through the disc and the inner radius of emission. A higher temperature for a given luminosity suggests a spinning BH, i.e., $R_{\text{in}} < 5 R_g$ (Done et al. 2007). Fitting the X-ray spectra of black hole binaries (BHB) with this approach in the disc dominated high/ soft state suggests a range of low to intermediate BH spins (e.g. Davis et al. 2006; Middleton et al. 2006; Kolehmainen et al. 2011). An alternate method for measuring the spin of stellar mass black holes, however, is similar to that used in the X-ray spectra of AGN whereby the broadening applied to the Fe K α line is assessed in order to determine the strength of relativistic effects and hence the inner radius of emission required to produce those effects. This method of using a reflection dominated model again results in high to maximal spin estimates as per the AGN case (e.g. Miller et al. 2008; Reis et al. 2008; Miller et al. 2009)

Similarly to the problems encountered when estimating the black hole spin of SMBHs, the spin of stellar mass BHs is highly model dependent. For example, the modelling of the continuum prior to employing a relativistic line profile model affects the derived accretion disc parameters and BH spin, therefore when reflection dominated models and diskline-type models are applied it is difficult to determine the true extent of the broadening to the FeK α line profile. Hence, the reflection dominated models for both stellar mass and SMBHs often lead to highly if not maximally spinning BHs, for example, see Walton et al. (2013) for reflection dominated models applied to a sample of ‘bare’ AGN which perhaps bear the most similarity to the X-ray spectra of high state Galactic BH binaries i.e. either lacking or with low intrinsic absorption (see also Chapter 3 and Section 3.3.5). Measuring the spin of stellar mass BHs through estimating the temperature of the disc and modelling the soft X-ray continuum with a Comptonised disc spectrum (e.g. COMPTT, see Kolehmainen et al. 2011) gives a wide range of spins (although excluding maximal) as in the results found within this work. This is likely due to the requirement in both methodologies to have a robust and physical interpretation for the broadband X-ray continuum.

While in both mass regimes there is still a great deal of discussion to be made of the differing interpretations, it is clear that reflection dominated models alone, whether in BHBs or in AGN, drive the estimated BH spin to extreme values and require highly concentrated emission. An absorption or disc corona dominated model, however, tends to rule out this scenario and instead suggests a distribution of intermediate spin BHs with emission occurring at typically tens of R_g (e.g. see Kolehmainen et al. 2011). Figure 6.7 shows a comparison of two interpretations of BHB X-ray spectra and how the observed strength of a relativistically broadened FeK line can differ according to the continuum model. This bears similarity to AGN, for example, the case of MCG–06-30-15 in the SMBH mass regime in which Miniutti et al. 2007 find a strong iron line and maximal spin due to a continuum modelled with a simple unabsorbed power-law whereas here a much weaker broad iron line and an intermediate black hole spin is found (see Figure 1.9 and Figure 4.2). Similarly for the case of ‘bare’ Seyfert AGN and the discrepancies between a Comptonised disc approach and strongly blurred inner

reflection.

While the mechanism for the production of SMBHs is currently unknown, the progenitors for stellar mass BHs is widely accepted, i.e., resulting from supernovae. Theoretical predictions suggest that the slowly rotating core of supernovae will impart this low spin onto the subsequent stellar mass BH and spin-up is reduced due to angular momentum loss (King & Kolb 1999; Gammie, Shapiro & McKinney 2004). While comparisons between the mass regimes may be limited, the study of black hole spin evolution can lend evidence towards a suggested spin distribution for SMBHs. If, for example, a range of low spin stellar mass black holes are found, this may suggest that mergers and episodes of chaotic rather than prolonged accretion may be preferable and this scenario may be replicated at the SMBH scale although at longer timescales (Volonteri et al. 2005; King & Pringle 2007; King et al. 2008).

6.3 Alternative mechanisms and scenarios

6.3.1 An atomic origin of the soft excess?

As noted in Chapter 2, Section 2.5.1 the observed soft excess in the X-ray spectra of AGN can be modelled in a number of ways. The two most favoured scenarios being the Comptonisation of EUV photons from the disc in a corona above the disc (e.g. Porquet et al. 2004; Dewangan et al. 2007; Lohfink et al. 2013; Noda et al. 2013) and an atomic origin whereby discrete soft emission lines are relativistically blurred into a smooth continuum (e.g. Nardini et al. 2011, 2012; Walton et al. 2013).

The findings in Chapter 3 suggest that the two differing interpretations give concurring spin constraints only when the blurred reflector is not required to model the soft excess, leading to the conclusion that the component responsible for the soft excess must be independently fitted before conclusive spin constraints can be made. If a series of emission lines are blurred to form a smooth soft excess, this by its very nature forces the accretion disc parameters and black hole spin to extreme values, i.e.

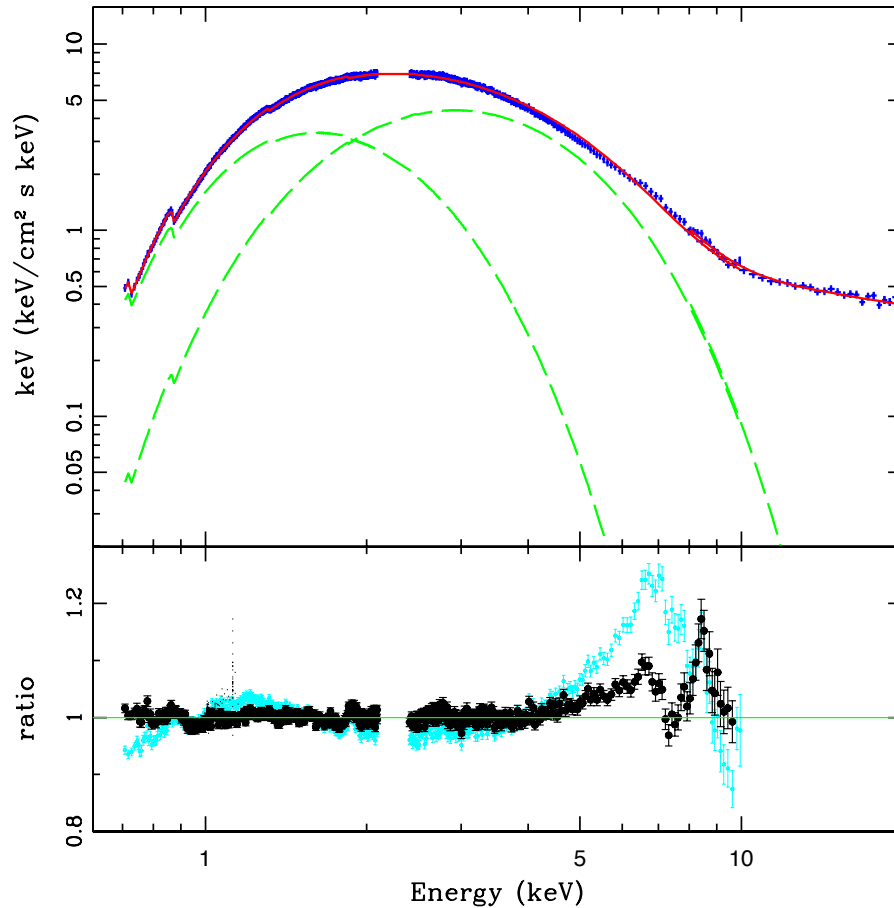


Figure 6.7: An *XMM-Newton* observation of the low mass X-ray binary GX 339–4 in an analysis made by Kolehmainen et al. (2011). The black residuals represent the data/ model ratio of a model consisting of thermal emission from the disc and Comptonised disc emission from *COMPTT*, i.e. a model similar to the baseline model used throughout this thesis. The light blue points show the residuals to a model consisting of thermal disc emission and a power-law component (e.g. Reis et al. 2008 where a stronger broad line is predicted). Note how the residuals in the FeK region are very different depending upon the interpretation of the soft X-rays and continuum.

high emissivity, high iron abundance, maximal spin. These estimates are not, however, in-line with those which are obtained purely from the FeK region which suggest more a more moderate q , low to intermediate a and simple Solar abundances, see Chapter

3.

When obtaining measurements for the emissivity index of the disc and subsequently the spin of the SMBH, the way in which the soft excess is modelled can have a significant effect. For example, as per Chapter 3, if the soft excess is not modelled according to a soft Comptonisation origin (e.g. `COMP`TT, or to a lesser extent `DISKBB`) and instead an atomic origin is preferred, the disc parameters are drastically altered. The `RELCONV*REFLIONX` convolution is forced to blur soft X-ray energy emission lines into a smooth continuum in an attempt to model the shape of the soft excess, resulting in particularly high emissivities and typically high BH spin. These parameters are at odds with those which are obtained purely from the FeK region, for example, Miniutti et al. (2010) find $q = 4.1_{-0.9}^{+5.3}$ and $a > 0.6$ in RBS 1124 although the authors note that there is no evidence for a strong broad line in the FeK region, indeed none is found here. Therefore, if the FeK line is to be used as a diagnostic for determining accretion disc parameters and constraining SMBH spin, the treatment of the soft excess has a significant role to play in ensuring that it is not driving the fit if blurred reflection models are used in the fitting process.

6.3.2 Disc winds

Recent work by Tatum et al. (2012) suggests an alternative mechanism to fully model the FeK region is emission from a Compton thick disc wind based upon a disc wind model by Sim et al. (2008, 2010), rather than reflection from the inner regions of the accretion disc. Compton-thick outflows are expected in AGN featuring a high Eddington ratio (King & Pounds 2003) and these are thought to arise from relatively close to the central SMBH (Proga et al. 2000), given a high wind density, strong features are imprinted upon the spectrum, e.g., absorption lines and a broadened FeK α line profile. Sim et al. (2008, 2010) found that Compton-thick wind spectra showed broadened line profiles with FWHM ~ 1 keV despite being launched at $\sim 30 R_g$ to negate relativistic blurring, instead the broadening is due to Compton scattering and the rotational velocity of the wind (see Figure 6.8).

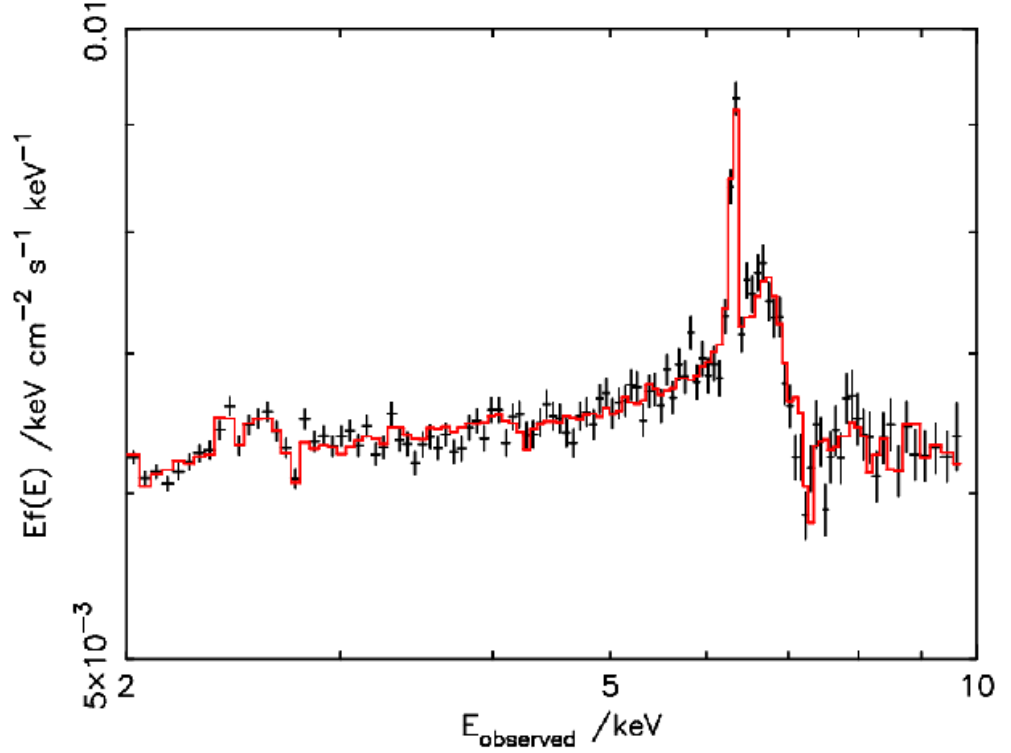


Figure 6.8: Compton-thick disc wind model from Sim et al. (2008) fitted to the 2-10 keV spectrum of Mrk 766. Broadened Fe $K\alpha$ line profiles can be produced without the need for emission from the inner regions of the disc, e.g. the disc wind modelled here responsible for the line profile broadening has an inner radius of $\sim 400 R_g$.

The authors take the cleanest sources possible free of absorption, i.e. the ‘bare’ Seyfert sample from Patrick et al. (2011a) and assuming a relatively face-on viewing angle whereby only the scattered light from the wind is observed rather than any absorption features with a more edge-on viewing angle through the wind. The line profiles are therefore subject to velocity broadening due to Doppler velocity shear across the wind and Compton down-scattering of the Fe $K\alpha$ flux, these can combine to imitate a broad line profile from reflection off the inner regions of the accretion disc. Tatum et al. (2012) find good fits to the broadband spectra for this model without the requirement for any further broadened emission from reflection off the inner regions of the disc. In this scenario, the full Fe K line profile is reproduced with

Solar iron abundances at typically tens to hundreds of R_g , however, in some objects an additional cold neutral reflector and neutral Fe K α line component is still required in order to model the Fe K edge and hard X-ray excess.

While the disc wind model alone can start replicate many of the features in the broad-band spectrum, it is likely that the true scenario is a combination of absorption, reflection and scattered components from disc winds, an argument which may not be resolved with current X-ray observatories without calorimeter resolution spectra in the Fe K band. It is, however, interesting to note that the tentative bi-modality of the broad line equivalent widths in this sample (Figure 6.4) may represent such a scenario whereby a fraction of the weaker observed broad lines are as a result of disc wind geometries. Meanwhile objects which display stronger broad lines ($EW > 150$ eV) could plausibly result from the inner regions of the disc. It must be stressed, however, that the apparent (albeit weak) bi-modal nature of the equivalent widths in this sample may simply be due to insufficient statistics.

6.3.3 A truncated disc

As can be seen from Table 5.4 on page 175 and Figure 6.4, the majority of AGN in this sample do not feature strong emission from the very inner regions of the accretion disc, both the emissivity index and spin of the central BH take typically low values. This suggests that the dominant regions producing the typical broad iron line profile are regions close to but more distant from the central BH than has been estimated in many analyses (Reynolds et al. 2005; Brenneman et al. 2006, 2011; Miniutti et al. 2007; Reynolds et al. 2012a), originating at typically tens of R_g and hence with a significant amount of flux present in the blue-wing of the line profile as opposed to the red-wing. The RELLINE fits in Table 5.4 on page 175 are under the assumption that the inner radius of the accretion disc extends down the inner-most stable circular orbit (i.e. R_{ISCO}). If the majority of the line profile originates from the outer regions of the disc, it is plausible that in some cases the accretion disc may be truncated at a few to tens of R_g . For example, Lobban et al. (2010) suggest a truncated accretion

disc in NGC 7213, stating a lack of a significant broad component in the Fe K region and weak reflection (see also Lu & Wang 2000; Done et al. 2000; Markowitz & Reeves 2009; Svoboda et al. 2010).

6.3.4 Inner reflection versus partial covering

The baseline model constructed in the main models of this work makes use of a high column partial coverer to account for any additional hard X-ray flux which may be present in the X-ray spectra of these AGN. An alternate scenario is to use a blurred reflection component from the inner regions of the disc in addition to an unblurred reflector from the outer regions of the disc can provide a means of supplementing the total hard X-ray flux at > 10 keV. As noted in Section 5.3.4, this scenario can provide a good description of the broad-band spectrum for MCG–06-30-15 and NGC 5506 whilst retaining relatively typical accretion disc parameters, i.e. low to moderate emissivity index and inclination, similar to those obtained from an analysis of the broad Fe K α line profile (see Section 5.3.3.3 and Table 5.4 on page 175).

The fit to the remaining objects (Mrk 766, NGC 1365, NGC 3516, NGC 3783 and NGC 4051) is worse without a partial covering geometry. This may be due to the inability of the inner reflector geometry to successfully describe the long term variability (e.g. variability in spectral curvature) of these AGN, all of which are noted to have varied between each of the observations analysed here (see Section 5.3.4 and Figure 5.4). In each of these AGN the disc parameters are either poorly constrained or are forced to extreme values, for example, in order to describe the broad-band spectrum and long term variability of NGC 4051 the emissivity of the disc is increased to $q = 6.1_{-0.1}^{+0.3}$ and spin to near maximal $a > 0.99$, while producing an overall worse fit. This suggests that emission is required to be very centrally concentrated with the inner reflector proving the dominant component in the broad-band model. For example, the inner reflector for 2005 observation of NGC 4051 has 15-50 keV flux $\sim 8.8\times$ higher than the outer reflector ($F_{2005\text{ inner}} = (1.49_{-0.03}^{+0.02}) \times 10^{-11} \text{erg cm}^{-2} \text{s}^{-1}$ versus $F_{2005\text{ outer}} = (0.17_{-0.02}^{+0.01}) \times 10^{-11} \text{erg cm}^{-2} \text{s}^{-1}$). Comparing this to the alternative

(i.e. with partial covering explaining the long term spectral variability, Table D.3 on page 256), the inner reflector 15-50 keV flux is significantly reduced when partial covering is invoked: $F_{2005 \text{ inner}} = (0.29_{-0.03}^{+0.03}) \times 10^{-11} \text{ erg cm}^{-2} \text{ s}^{-1}$ compared to $F_{2005 \text{ outer}} = (0.37_{-0.05}^{+0.08}) \times 10^{-11} \text{ erg cm}^{-2} \text{ s}^{-1}$ i.e. no longer reflection dominated.

In the majority of cases here, the dual reflector scenario does not provide a reasonable alternative to a partial covering geometry particularly in objects which feature significant long term spectral variability (see Table D.3 on page 256). NGC 1365 is very poorly fit with $\chi_{\nu}^2 \sim 2.2$ above 2 keV and $\chi_{\nu}^2 \sim 5.1$ over the 0.6-100 keV range; NGC 3227 and NGC 3516 also featuring poor fits with $\chi_{\nu}^2 \sim 1.2$ and $\chi_{\nu}^2 \sim 1.8$ respectively when fitted without partial covering (e.g. Turner & Miller 2009). It should be noted that many of the iron line parameters in Tables D.3 on page 256 are poorly constrained, this is due to the interplay between the inner reflector and outer reflector (and/ or partial covering) at hard X-ray energies and the COMPTT component at soft X-ray energies. Indeed, Tatum et al. (2013) find in a study of the brightest AGN at hard X-ray energies that sharp FeK absorption edges cannot be explained without a Compton-thick layer of absorbing gas which partially covers the continuum source.

A recent analysis of the first *NuStar* observation by Risaliti et al. (2013) of NGC 1365 claims that the broadband spectrum is reflection dominated and that emission arises from within $2.5 R_g$ ($a > 0.84$), ruling out absorption models suggesting that partial covering models fail to reproduce the hard X-ray spectrum and spectral variability below 10 keV. The authors reject a Compton-thick partially covering absorption model to fit the hard excess, instead requiring significant reflection from the inner regions of the disc. It should be noted, however, that both interpretations give a statistically good fit to the data and that both still require a slightly lower column density partial coverer below 10 keV ($N_H \sim 10^{23} \text{ cm}^{-2}$). An absorption dominated model (i.e. with a high column density partial coverer) is claimed to be implausible due to an unfeasibly high X-ray luminosity with an X-ray to [O III] flux ratio of $\sim 70 - 200$ whereas this is typically ~ 10 for unobscured AGN (Alonso-Herrero et al. 2012).

Miller & Turner (2013), however, note that the models formed by Risaliti et al. (2013) make use of non-scattering slab absorbers, hence no reasonable statistical com-

parison can be drawn between the reflection and absorption dominated geometries. The lack of a scattered component also greatly effects the estimation of the continuum suppression, i.e. the X-ray to [O III] flux ratio calculated by Risaliti et al. (2013) is incorrect, instead suggesting that the continuum suppression is similar to that suggested by light bending models (i.e. up to 75%; Miniutti & Fabian 2004) subsequently lowering the X-ray to [O III] ratio. There is still much debate regarding the origin of the hard excess in Seyfert 1 AGN, although it is clear that with new X-ray observatories such as *NuStar* new hard X-ray data will allow much greater insight into the inner workings of AGN.

6.4 Future prospects

Following on from the work in this thesis the next generation of X-ray telescopes will be able to provide new data at sensitivities over an order of magnitude greater than ever before. Since the reflection continuum peaks at hard X-ray energies it essential that high quality high energy X-ray data is available if accurate measurements of black hole spin are to be made. While *Suzaku*'s HXD can give a some hard X-ray data, the new NASA lead mission *NuStar* (Harrison et al. 2010) launched in 2012 (and now making observations in 2013) will be able a factor of $\sim 100\times$ more sensitive to hard X-ray fluxes. With bandpass covering 3-79 keV there will be overlap with existing CCD instruments onboard *XMM-Newton* and *Suzaku* which will allow for easy cross-normalisation between observations from multiple epochs and the true strength of the hard X-ray continuum relative to the soft X-rays can be determined.

One of the currently unanswered questions in the field of AGN X-ray spectroscopy is the origin of the hard excess. For example, it is currently debated whether a strong hard X-ray excess is due to highly blurred reflection from the very inner regions of the accretion disc, or if it arises from absorption whereby a particularly high column density absorber either totally or partially covers the central source. In this scenario the central X-ray source is intrinsically brighter and relatively low energy X-rays are al-

most totally absorbed, thereby accentuating the hard X-ray continuum. An absorption based geometry typically has no requirement for a spinning black hole, rather broad emission from the Fe K region is thought to originate from tens of R_g . In contrast to this, for reflection dominated spectra there must be strong emission from regions very close to the black hole itself and hence a population of maximally spinning Kerr black holes is suggested. With the most sensitive data from *NuStar* these issues could potentially be resolved, removing one of the significant degeneracies when modelling the X-ray spectrum and particularly when assessing the strength of emission in the Fe K region and estimating SMBH spin. The very first analyses of observations made with *NuStar* are being made, with suggestions that the SMBH in NGC 1365 is maximally spinning according to Risaliti et al. (2013; see Section 6.3.4), however, the data are not currently public and have not therefore been subjected to alternative explanations or interpretations. Figure 6.9 nonetheless shows an example of the hard X-ray spectra which can be expected from *NuStar* in a fairly typical ~ 80 ks observation, revealing the now well defined shape of the hard X-ray excess.

Aside from *NuStar*, a collaborative effort between NASA and the Japanese space agency JAXA will see the launch of *Astro-H* in 2015 which is considered to be the successor to *Suzaku* (Takahashi et al. 2010). *Astro-H* will provide very high resolution data with up to a factor of $20\times$ higher energy resolution at Fe K energies than *Suzaku* being able to resolve down to a FWHM resolution of ~ 7 eV courtesy of a calorimeter detector sensitive from 0.5-10.0 keV. With this much improved energy resolution, many of the current ambiguities when modelling X-ray spectra can be resolved. For example, the interplay between the peak of the blue-wing of a relativistically blurred line profile can be much more easily distinguished from the possible presence of narrow emission lines from material which is relatively distant from the central SMBH. High resolution data will also be able to resolve the contribution of the warm absorber at Fe K energies, as well as the contribution of partial covering gas from the Fe K edge structure, e.g. Kallman et al. (2004).

Further to this, if the soft excess in AGN features the blurring of discrete emission lines at soft X-ray energies the calorimeter onboard *Astro-H* will be able to detect the

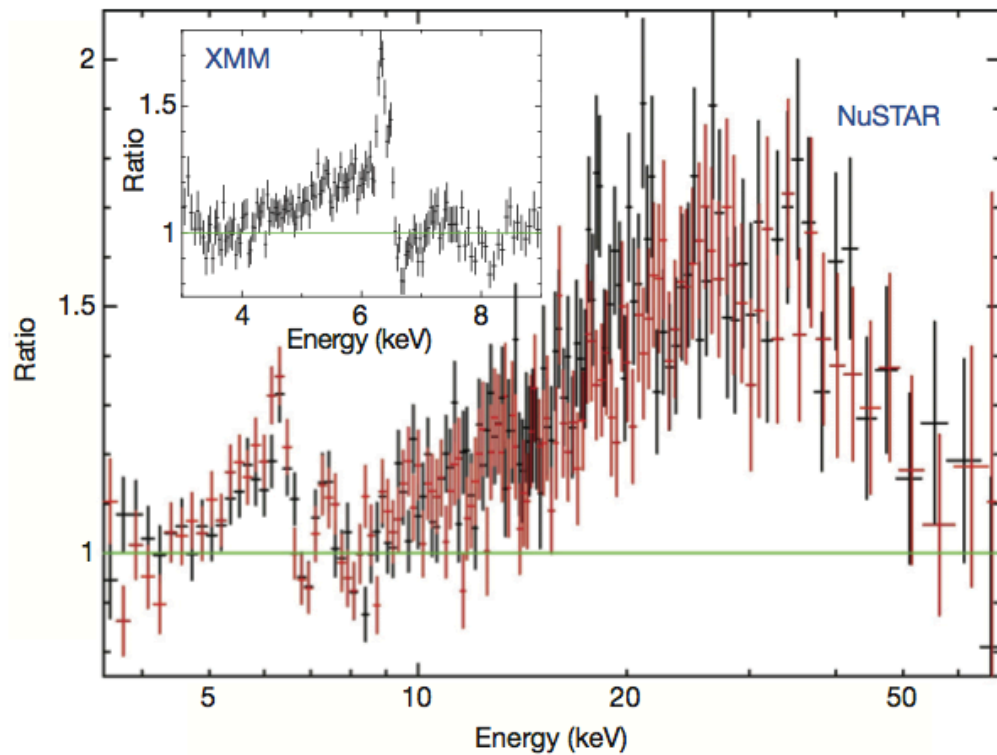


Figure 6.9: Broadband hard X-ray data from the new observatory *NuStar* which will allow for much improved constraints upon the hard excess. Plot taken from a recent analysis of NGC 1365 by Risaliti et al. (2013) in which an absorbed power-law is fitted to 3-4 keV, 7-10 keV and 50-80 keV to reveal a strong hard excess.

relativistic blurring of the individual lines, revealing the presence of emission from the very inner regions of the accretion disc. If, however, the soft excess originates from the Comptonisation of EUV disc photons in a corona, *Astro-H* will instead see a smooth continuum instead of discrete blurred emission lines.

Combining data from both *NuStar* and *Astro-H* the first truly robust measurements of SMBH black hole spin can be made once the origin of the key components of the broadband X-ray spectrum have been determined, i.e. the soft and hard X-ray excesses as well as the warm absorber and information regarding outflowing gas in AGN. Progress can then be made towards developing the local SMBH spin distribution of nearby Seyfert 1AGN. Of course, once a large enough number of AGN have had robust measurements of their spin made, conclusions can be drawn regarding the evolution of these galaxies.

A Observation details

Table A.1: Summary of observations for the objects in the sample. ¹ The observed 2–10 keV flux for XIS, 15–50 keV flux for HXD and 20–100 keV flux for BAT, in units $10^{-11} \text{ erg cm}^{-2} \text{ s}^{-1}$ from the baseline model. The XIS count rates listed are per XIS. BAT data is from the 58 month BAT catalogue (Baumgartner et al. 2010).

Object	Mission	Instrument	Date	Exposure (s)	Count rate	Flux ¹	Obs. ID	No. Counts
1H 0419–577	XIS			205863	1.251 ± 0.002	1.75		519055
	Suzaku	HXD	2007-07-25	142600	0.052 ± 0.002	2.93	702041010	45303
	XIS			122835	0.866 ± 0.02	1.40		217440
3C 111	Suzaku	HXD	2010-01-16	104900	0.028 ± 0.001	2.18	704064010	22240
	Swift	BAT	–	–	$(2.4 \pm 0.3) \times 10^{-4}$	1.71		940
3C 382	XIS			122378	0.610 ± 0.002	1.95		152164
	Suzaku	HXD	2008-08-22	101900	0.068 ± 0.002	3.29	703034010	36150
	Swift	BAT	–	–	$(10.2 \pm 0.3) \times 10^{-4}$	7.43		
3C 120	XIS			41932	3.082 ± 0.005	4.63		389949
	Suzaku	HXD	2006-02-09	31870	0.099 ± 0.004	6.24	700001010	13996
	XIS			42555	2.464 ± 0.004	4.01		309300
	Suzaku	HXD	2006-02-16	34540	0.144 ± 0.005	5.72	700001020	21832
	XIS			40907	2.53 ± 0.004	4.04		312550
	Suzaku	HXD	2006-02-23	36200	0.110 ± 0.004	6.07	700001030	15360
3C 390.3	XIS			40905	2.351 ± 0.004	3.96		290680
	Suzaku	HXD	2006-03-02	37870	0.093 ± 0.003	5.59	700001040	14533
	Swift	BAT	–	–	$(8.5 \pm 0.2) \times 10^{-4}$	5.82		
3C 382	XIS			130580	2.596 ± 0.003	4.05		683288
	Suzaku	HXD	2007-04-27	114300	0.097 ± 0.002	5.11	702125010	47714
	Swift	BAT	–	–	$(7.6 \pm 0.2) \times 10^{-4}$	5.11		
3C 390.3	XIS			179800	1.831 ± 0.003	3.10		333573
	Suzaku	HXD	2006-12-14	92060	0.096 ± 0.003	5.81	701060010	37078
	Swift	BAT	–	–	$(9.09 \pm 0.18) \times 10^{-4}$	6.82		

Table A.1: *continued* - Summary of observations for the objects in the sample. ¹ The observed 2–10 keV flux for XIS, 15–50 keV flux for HXD and 20–100 keV flux for BAT, in units $10^{-11} \text{ erg cm}^{-2} \text{ s}^{-1}$ from the baseline model. The XIS count rates listed are per XIS. BAT data is from the 58 month BAT catalogue (Baumgartner et al. 2010).

Object	Mission	Instrument	Date	Exposure (s)	Count rate	Flux ¹	Obs. ID	No. Counts
3C 445	Suzaku	XIS	2007-05-25	139769	0.159 ± 0.001	0.70	702056010	48098
		HXD		109500	0.049 ± 0.002	2.69		37749
	Swift	BAT	–	–	$(3.7 \pm 0.2) \times 10^{-4}$	2.35		
4C 74.26	Suzaku	XIS	2007-10-28	91583	1.493 ± 0.003	3.13	702057010	276179
		HXD		87340	0.084 ± 0.002	4.00		34810
	Swift	BAT	–	–	$(4.6 \pm 0.2) \times 10^{-4}$	3.37		
Ark 120	Suzaku	XIS	2007/04/01	100864	1.896 ± 0.003	3.05	702014010	384821
		HXD		89470	0.114 ± 0.003	3.46		51795
	Swift	BAT	–	2453000	$(6.9 \pm 0.4) \times 10^{-4}$	4.89		1690
Ark 564	Suzaku	XIS	2007-06-26	99978	2.277 ± 0.003	1.84	702117010	458819
		HXD		81330	0.021 ± 0.002	1.54		15343
Fairall 9	Suzaku	XIS	2007/06/07	167814	1.718 ± 0.002	2.32	702043010	581331
		HXD		127310	0.089 ± 0.002	2.97		46809
	Suzaku	XIS	2010/08/26	229296	1.780 ± 0.002	2.17	705063010	742007
		HXD		162200	0.039 ± 0.002	3.51		65230
	Swift	BAT	–	–	$(4.7 \pm 0.2) \times 10^{-4}$	3.34		1619
		XIS	2007-08-01	25453	5.212 ± 0.010	10.64	702113010	266796
IC 4329A	Suzaku	HXD		20050	0.289 ± 0.006	15.96		11647
	Suzaku	XIS	2007-08-06	30623	6.138 ± 0.010	12.58	702113020	377880
		HXD		24080	0.340 ± 0.005	17.97		15349
	Suzaku	XIS	2007-08-11	26896	5.554 ± 0.010	11.89	702113030	300624
		HXD		22110	0.345 ± 0.006	18.77		15541
	Suzaku	XIS	2007-08-16	24219	5.261 ± 0.010	10.88	702113040	256495
IRAS 13224–3809	Suzaku	HXD		18750	0.300 ± 0.006	16.47		11923
	Suzaku	XIS	2007-08-20	24026	3.221 ± 0.008	7.03	702113050	156141
		HXD		17520	0.242 ± 0.006	13.69		9755
	Swift	BAT	–	–	$(26.8 \pm 0.3) \times 10^{-4}$	19.02		
IRAS 13224–3809	Suzaku	XIS	2007-01-26	197938	0.085 ± 0.001	0.06	701003010	39148
		HXD		158500	0.004 ± 0.002	0.015		86214

Table A.1: *continued* - Summary of observations for the objects in the sample. ¹ The observed 2–10 keV flux for XIS, 15–50 keV flux for HXD and 20–100 keV flux for BAT, in units $10^{-11} \text{erg cm}^{-2} \text{s}^{-1}$ from the baseline model. The XIS count rates listed are per XIS. BAT data is from the 58 month BAT catalogue (Baumgartner et al. 2010).

Object	Mission	Instrument	Date	Exposure (s)	Count rate	Flux ¹	Obs. ID	No. Counts
MCG-02-14-009	Suzaku	XIS	2008/08/28	142152	0.216 ± 0.001	0.43	703060010	63436
		HXD		120028	0.017 ± 0.002	0.61		40150
MCG-02-58-22	Suzaku	XIS	2009-12-02	138969	2.921 ± 0.003	4.87	704032010	817420
		HXD		97980	0.163 ± 0.002	8.73		44009
	Swift	BAT		–	$(9.8 \pm 0.2) \times 10^{-4}$	7.48		
MCG-05-23-16	Suzaku	XIS	2005-12-07	95677	2.822 ± 0.003	8.93	700002010	815975
		HXD		79690	0.313 ± 0.003	14.52		55913
	Swift	BAT		–	$(19.8 \pm 0.2) \times 10^{-4}$	14.27		4526
MCG-06-30-15	Suzaku	XIS	2006/01/09	143196	2.862 ± 0.003	4.38	700007010	1240090
		HXD		118900	0.094 ± 0.002	4.70		53689
	Suzaku	XIS	2006/01/23	98483	2.461 ± 0.003	3.81	700007020	734189
				HXD	76800	0.103 ± 0.003		5.06
	Suzaku	XIS	2006/01/27	96691	2.708 ± 0.003	4.16	700007030	792389
				HXD	83660	0.104 ± 0.002		4.98
Swift	BAT	–	–	$(6.8 \pm 0.3) \times 10^{-4}$	3.86			
MCG+8-11-11	Suzaku	XIS	2007-09-17	98748	2.863 ± 0.004	6.48	702112010	568883
		HXD		82900	0.196 ± 0.003	10.44		43023
	Swift	BAT		–	$(8.8 \pm 0.2) \times 10^{-4}$	6.27		2082
MR 2251-178	Suzaku	XIS	2009-05-07	136924	2.089 ± 0.003	4.23	704055010	576608
		HXD		103800	0.101 ± 0.002	5.47		40562
	Swift	BAT		–	$(9.1 \pm 0.2) \times 10^{-4}$	6.02		
Mrk 79	Suzaku	XIS	2007-04-03	83704	0.768 ± 0.002	1.47	702044010	130639
		HXD		76920	0.027 ± 0.002	1.79		19777
	Swift	BAT		–	$(4.1 \pm 0.2) \times 10^{-4}$	2.87		
Mrk 110	Suzaku	XIS	2007-11-02	90871	1.220 ± 0.003	2.13	702124010	224098
		HXD		80370	0.053 ± 0.002	2.99		26958
	Swift	BAT		–	$(5.4 \pm 0.3) \times 10^{-4}$	3.95		2128

Table A.1: *continued* - Summary of observations for the objects in the sample. ¹ The observed 2–10 keV flux for XIS, 15–50 keV flux for HXD and 20–100 keV flux for BAT, in units $10^{-11} \text{ erg cm}^{-2} \text{ s}^{-1}$ from the baseline model. The XIS count rates listed are per XIS. BAT data is from the 58 month BAT catalogue (Baumgartner et al. 2010).

Object	Mission	Instrument	Date	Exposure (s)	Count rate	Flux ¹	Obs. ID	No. Counts
Mrk 205	Suzaku	XIS	2010-05-22	100961	0.501 ± 0.002	0.93	705062010	103464
		HXD		85280	0.019 ± 0.001	1.94		13647
	Swift	BAT	–	–	$(1.4 \pm 0.2) \times 10^{-4}$	1.05		
Mrk 279	Suzaku	XIS	2009-05-14	160351	0.263 ± 0.001	0.49	704031010	88122
		HXD		139800	0.024 ± 0.001	2.42		29520
	Swift	BAT	–	–	$(5.2 \pm 0.3) \times 10^{-4}$	3.93		2617
Mrk 335	Suzaku	XIS	2006/08/21	151296	1.324 ± 0.002	1.49	701031010	606927
		HXD		131744	0.012 ± 0.001	1.31	701031010	22385
	Swift	BAT	–	–	$(2.5 \pm 0.3) \times 10^{-4}$	1.81		830
Mrk 359	Suzaku	XIS	2007-02-06	107507	0.329 ± 0.001	0.52	701082010	73004
		HXD		96130	0.007 ± 0.001	0.98		13136
	Swift	BAT	–	–	$(1.2 \pm 0.1) \times 10^{-4}$	0.92		
Suzaku	XIS		2006-04-25	24576	2.984 ± 0.006	4.68	701093010	221506
		HXD		14510	0.143 ± 0.006	7.50		6647
	XIS		2006-10-14	25930	3.802 ± 0.007	4.98	701093020	297900
Suzaku	HXD			21880	0.128 ± 0.005	7.89		9680
	XIS		2006-11-15	24447	3.792 ± 0.009	4.74	701093030	186702
	HXD			17340	0.118 ± 0.005	7.57		7260
Suzaku	XIS		2006-11-27	33094	3.278 ± 0.007	4.73	701093040	218248
	HXD			27560	0.110 ± 0.004	7.19		11925
	Swift	BAT	–	–	$(8.4 \pm 0.2) \times 10^{-4}$	6.53		
Suzaku	XIS		2006-11-16	97869	0.927 ± 0.002	1.32	701035010	183736
	HXD			90500	0.025 ± 0.002	1.48		26879
	XIS		2007-11-17	59364	0.685 ± 0.002	1.36	701035020	82749
Swift	HXD			47660	0.024 ± 0.002	1.67		8974
	BAT		–	–	$(2.5 \pm 0.2) \times 10^{-4}$	1.66		
	XIS		2007-01-22	51753	0.819 ± 0.003	1.40	701084010	86781
Mrk 841	HXD			40710	0.039 ± 0.003	2.42		11274
	XIS		2007-07-23	50925	0.830 ± 0.003	1.44	701084020	86626
	HXD			44370	0.054 ± 0.003	2.82		13282
Swift	BAT	–	–	$(3.2 \pm 0.2) \times 10^{-4}$	2.29			

Table A.1: *continued* - Summary of observations for the objects in the sample. ¹ The observed 2–10 keV flux for XIS, 15–50 keV flux for HXD and 20–100 keV flux for BAT, in units $10^{-11} \text{ erg cm}^{-2} \text{ s}^{-1}$ from the baseline model. The XIS count rates listed are per XIS. BAT data is from the 58 month BAT catalogue (Baumgartner et al. 2010).

Object	Mission	Instrument	Date	Exposure (s)	Count rate	Flux ¹	Obs. ID	No. Counts
NGC 1365	Suzaku	XIS	2008-01-21	160506	0.326 ± 0.001	1.28	702047010	107383
		HXD		136600	0.084 ± 0.002	4.72		55436
NGC 1365	Suzaku	XIS	2010-06-27	151613	0.159 ± 0.001	0.61	705031010	51909
		HXD		114300	0.070 ± 0.002	4.33		38083
NGC 1365	Suzaku	XIS	2010-07-15	302175	0.116 ± 0.001	0.39	705031020	77717
		HXD		231500	0.060 ± 0.001	3.49		84887
Swift	BAT		–	–	$(5.2 \pm 0.1) \times 10^{-4}$	5.11		
NGC 2992	Suzaku	XIS	2005-11-06	37503	0.372 ± 0.002	1.04	700005010	43167
		HXD		29900	0.020 ± 0.003	1.71		7137
NGC 2992	Suzaku	XIS	2005-11-19	37494	0.486 ± 0.002	1.37	700005020	56041
		HXD		31890	0.042 ± 0.003	2.23		10370
NGC 2992	Suzaku	XIS	2005-12-13	46836	0.408 ± 0.002	1.15	700005030	59084
		HXD		41470	0.047 ± 0.003	2.44		15070
Swift	BAT		–	–	$(2.6 \pm 0.2) \times 10^{-4}$	1.84		
NGC 3147	Suzaku	XIS	2010-06-03	150048	0.093 ± 0.001	0.17	705054010	31054
		HXD		122800	0.009 ± 0.001	0.29		21785
NGC 3147	Suzaku	XIS	2008-10-28	58917	1.475 ± 0.004	3.91	703022010	175651
		HXD		48070	0.145 ± 0.003	5.58		21550
NGC 3147	Suzaku	XIS	2008-11-04	53700	0.496 ± 0.002	1.85	703022020	54717
		HXD		46740	0.123 ± 0.003	7.26		18735
NGC 3147	Suzaku	XIS	2008-11-12	56572	0.707 ± 0.003	2.58	703022030	81449
		HXD		46680	0.117 ± 0.003	6.78		18919
NGC 3227	Suzaku	XIS	2008-11-20	64568	0.278 ± 0.002	1.01	703022040	37518
		HXD		43430	0.083 ± 0.003	4.82		17263
NGC 3227	Suzaku	XIS	2008-11-27	79430	0.568 ± 0.002	2.16	703022050	92162
		HXD		37420	0.104 ± 0.003	6.26		14795
NGC 3227	Suzaku	XIS	2008-12-02	51411	0.413 ± 0.002	1.61	703022060	43570
		HXD		36910	0.082 ± 0.003	5.70		13177
Swift	BAT		–	–	$(10.3 \pm 0.2) \times 10^{-4}$	7.68		

Table A.1: *continued* - Summary of observations for the objects in the sample. ¹ The observed 2–10 keV flux for XIS, 15–50 keV flux for HXD and 20–100 keV flux for BAT, in units $10^{-11} \text{erg cm}^{-2} \text{s}^{-1}$ from the baseline model. The XIS count rates listed are per XIS. BAT data is from the 58 month BAT catalogue (Baumgartner et al. 2010).

Object	Mission	Instrument	Date	Exposure (s)	Count rate	Flux ¹	Obs. ID	No. Counts
NGC 3516	Suzaku	XIS	2005/10/12	134469	0.681 ± 0.001	2.37	100031010	289936
		HXD		115400	0.125 ± 0.002	6.68		49782
NGC 3783	Suzaku	XIS	2009/10/28	251356	0.456 ± 0.001	1.35	704062010	235894
		HXD		178200	0.059 ± 0.001	3.32		58222
	Swift	BAT	–	–	$(10.5 \pm 0.2) \times 10^{-4}$	7.76		
NGC 4051	Suzaku	XIS	2006/06/24	75719	2.066 ± 0.003	4.59	701033010	416485
		HXD		63930	0.167 ± 0.003	9.26		33592
NGC 4151	Suzaku	XIS	2009/07/10	209503	1.942 ± 0.002	5.92	704063010	805999
		HXD		162000	0.235 ± 0.002	12.04		87319
	Swift	BAT	–	–	$(16.6 \pm 0.2) \times 10^{-4}$	11.54		
NGC 4593	Suzaku	XIS	2005/11/10	119578	0.406 ± 0.001	0.87	700004010	149284
		HXD		112600	0.037 ± 0.002	1.63		29700
NGC 4151	Suzaku	XIS	2008/11/06	274350	1.858 ± 0.002	2.46	703023020	1036060
		HXD		204500	0.062 ± 0.001	3.05		75619
NGC 4593	Suzaku	XIS	2008/11/23	78385	1.276 ± 0.003	1.79	703023010	202942
		HXD		58530	0.048 ± 0.002	2.54		21296
	Swift	BAT	–	–	$(4.0 \pm 0.2) \times 10^{-4}$	2.80		
NGC 506	Suzaku	XIS	2006-12-18	124980	1.036 ± 0.002	4.35	701034010	262831
		HXD		123500	0.293 ± 0.002	15.90		78564
	Swift	BAT	–	–	$(43.6 \pm 0.2) \times 10^{-4}$	32.50		
NGC 4151	Suzaku	XIS	2007-12-15	118842	0.524 ± 0.002	1.04	702040010	127503
		HXD		101600	0.033 ± 0.002	2.15		30049
	Swift	BAT	–	–	$(7.3 \pm 0.2) \times 10^{-4}$	5.74		
NGC 5506	Suzaku	XIS	2006-08-08	47753	3.064 ± 0.005	10.05	701030010	441844
		HXD		38550	0.324 ± 0.004	17.30		25416
NGC 4151	Suzaku	XIS	2006-08-11	53296	3.230 ± 0.005	10.58	701030020	519889
		HXD		44830	0.343 ± 0.004	18.40		30625
NGC 4151	Suzaku	XIS	2007-01-31	57406	2.854 ± 0.005	9.90	701030030	330141
		HXD		44670	0.321 ± 0.004	17.11		29399
	Swift	BAT	–	–	$(23.2 \pm 0.2) \times 10^{-4}$	15.95		

Table A.1: *continued* - Summary of observations for the objects in the sample. ¹ The observed 2–10 keV flux for XIS, 15–50 keV flux for HXD and 20–100 keV flux for BAT, in units $10^{-11} \text{erg cm}^{-2} \text{s}^{-1}$ from the baseline model. The XIS count rates listed are per XIS. BAT data is from the 58 month BAT catalogue (Baumgartner et al. 2010).

Object	Mission	Instrument	Date	Exposure (s)	Count rate	Flux ¹	Obs. ID	No. Counts
NGC 7213	Suzaku	XIS	2007-06-18	31119	0.369 ± 0.003	0.81	702042010	23857
		HXD		25590	0.046 ± 0.004	2.70		9397
NGC 7314	Suzaku	XIS	2007-06-24	35915	0.650 ± 0.003	1.34	702042020	47786
		HXD		31210	0.050 ± 0.003	3.12		9880
NGC 7469	Suzaku	XIS	2007-07-08	30700	1.349 ± 0.005	2.54	702042040	83863
		HXD		26960	0.064 ± 0.004	4.34		9824
PDS 456	Suzaku	XIS	2007-07-15	30020	0.834 ± 0.004	1.74	702042050	51085
		HXD		24470	0.062 ± 0.004	4.16		7612
NGC 5548	Suzaku	XIS	2007-07-22	28918	1.656 ± 0.005	3.28	702042060	96936
		HXD		23060	0.095 ± 0.004	0.22		8336
NGC 7213	Suzaku	XIS	2007-07-29	31810	1.075 ± 0.004	2.19	702042070	69507
		HXD		27610	0.075 ± 0.004	4.71		9377
PDS 456	Suzaku	XIS	2007-08-05	38776	0.558 ± 0.003	1.19	702042080	44486
		HXD		30380	0.054 ± 0.003	3.41		9958
	Swift	BAT	–	–	$(6.1 \pm 0.2) \times 10^{-4}$	4.56		
NGC 7213	Suzaku	XIS	2006-10-22	90736	1.528 ± 0.002	2.41	701029010	419604
		HXD		84290	0.064 ± 0.002	3.48		33910
NGC 7314	Swift	BAT	–	–	$(3.6 \pm 0.2) \times 10^{-4}$	5.13		
	Suzaku	XIS	2007-04-25	109020	0.296 ± 0.001	0.88	702015010	67434
	Swift	BAT	–	–	$(4.6 \pm 0.2) \times 10^{-4}$	1.43		25675
NGC 7469	Suzaku	XIS	2008/06/24	112113	1.091 ± 0.002	2.10	703028010	248180
		HXD		85315	0.068 ± 0.002	3.22		29831
PDS 456	Swift	BAT	–	3286000	$(6.6 \pm 0.3) \times 10^{-4}$	4.87		2179
	Suzaku	XIS	2007-02-24	190600	0.237 ± 0.001	0.35	701056010	92499
		HXD		64150	0.012 ± 0.003	0.25		20372

Table A.1: *continued* - Summary of observations for the objects in the sample. ¹ The observed 2–10 keV flux for XIS, 15–50 keV flux for HXD and 20–100 keV flux for BAT, in units $10^{-11} \text{erg cm}^{-2} \text{s}^{-1}$ from the baseline model. The XIS count rates listed are per XIS. BAT data is from the 58 month BAT catalogue (Baumgartner et al. 2010).

Object	Mission	Instrument	Date	Exposure (s)	Count rate	Flux ¹	Obs. ID	No. Counts
PG 1211+143	Suzaku	XIS	2005-11-24	96324	0.268 ± 0.001	0.39	700009010	81584
		HXD		78800	0.004 ± 0.002	0.50		29181
RBS 1124	Suzaku	XIS	2007-04-14	86228	0.260 ± 0.001	0.49	702114010	46699
		HXD		82970	0.016 ± 0.001	0.91		14206
SWIFT J2127.4+5654	Suzaku	XIS	2007/12/09	91730	1.373 ± 0.004	3.35	702122010	127435
		HXD		83321	0.074 ± 0.002	3.33		27970
	Swift	BAT	–	–	$(4.3 \pm 0.3) \times 10^{-4}$	3.62		1689
TON S180	Suzaku	XIS	2006-12-09	120661	0.701 ± 0.002	0.56	701021010	172889
		HXD		102400	0.012 ± 0.002	0.77		27241

B Bare Seyfert sample tables

Table B.1: Model A components for the ‘bare’ *Suzaku* XIS, HXD and BAT data from *Swift*. ^a POWERLAW normalisation given in units (10^{-2} ph keV $^{-1}$ cm $^{-2}$ s $^{-1}$). ^b Flux for COMPTT quoted over the 0.5-10.0 keV range in units 10^{-11} erg cm $^{-2}$ s $^{-1}$. Note that a negative $\Delta\chi^2$ denotes an improvement in the fit.

	Ark 120	Fairall 9	MCG-02-14-009	Mrk 335	NGC 7469	SWIFT J2127.4+5654
Soft Excess	\checkmark	\checkmark	X	\checkmark	\checkmark	X
Γ	$1.99^{+0.04}_{-0.04}$	$1.87^{+0.04}_{-0.04}$	$1.89^{+0.04}_{-0.04}$	$2.00^{+0.04}_{-0.02}$	$1.80^{+0.01}_{-0.01}$	$2.19^{+0.05}_{-0.05}$
Norm ^a	$1.04^{+0.05}_{-0.06}$	$0.68^{+0.04}_{-0.05}$	$0.13^{+0.04}_{-0.04}$	$0.56^{+0.16}_{-0.02}$	$0.57^{+0.06}_{-0.07}$	$1.60^{+0.07}_{-0.06}$
Plasma Temperature (keV)	< 8.5	< 18.6	–	< 8.3	< 8.4	–
Plasma Optical Depth τ	< 2.4	< 2.1	–	< 2.2	$0.8^{+0.2}_{-0.5}$	–
Flux ^b	$1.05^{+0.05}_{-0.05}$	$0.59^{+0.03}_{-0.03}$	–	$0.98^{+0.02}_{-0.02}$	$0.22^{+0.03}_{-0.03}$	–
$\Delta\chi^2$	-250	-240	–	-955	-194	–
Neutral FeK α Line (keV)	$6.40^{+0.02}_{-0.02}$	$6.39^{+0.01}_{-0.01}$	$6.43^{+0.06}_{-0.08}$	$6.39^{+0.03}_{-0.02}$	$6.40^{+0.02}_{-0.02}$	$6.37^{+0.05}_{-0.05}$
σ_{Narrow} (eV)	< 84	< 45	< 110	< 72	< 43	< 190
EW_{Narrow} (eV)	40^{+11}_{-12}	90^{+9}_{-10}	55^{+28}_{-51}	60^{+38}_{-23}	71^{+38}_{-25}	< 35
Flux (10^{-5} ph cm $^{-2}$ s $^{-1}$)	$1.49^{+0.41}_{-0.46}$	$2.50^{+0.26}_{-0.27}$	$0.29^{+0.15}_{-0.27}$	$1.00^{+0.63}_{-0.38}$	$1.92^{+1.02}_{-0.69}$	< 1.49
FeXXV Line (keV)	–	$6.74^{+0.04}_{-0.04}$	–	$6.69^{+0.06}_{-0.05}$	–	–
EW (eV)	–	17^{+8}_{-9}	–	33^{+13}_{-7}	–	–
Flux (10^{-5} ph cm $^{-2}$ s $^{-1}$)	–	$0.46^{+0.22}_{-0.24}$	–	$0.47^{+0.18}_{-0.10}$	–	–
$\Delta\chi^2$	–	-7	–	-14	–	–

Table B.1: *continued* - Model A components for the 'bare' Suzaku XIS, HXD and BAT data from Swift. ^a POWERLAW normalisation given in units (10^{-2} ph keV $^{-1}$ cm $^{-2}$ s $^{-1}$). ^b Flux for COMPTT quoted over the 0.5-10.0 keV range in units 10^{-11} erg cm $^{-2}$ s $^{-1}$. Note that a negative $\Delta\chi^2$ denotes an improvement in the fit.

	Ark 120	Fairall 9	MCG-02-14-009	Mrk 335	NGC 7469	SWIFT J2127.4+5654
FeXXVI Line (keV)	$6.96^{+0.04}_{-0.04}$	$6.98^{+0.02}_{-0.02}$	$6.94^{+0.06}_{-0.09}$	$6.98^{+0.06}_{-0.14}$	—	—
EW (eV)	24^{+11}_{-11}	30^{+8}_{-10}	< 51	21^{+13}_{-13}	—	—
Flux (10^{-5} ph cm $^{-2}$ s $^{-1}$)	$0.70^{+0.32}_{-0.32}$	$0.70^{+0.19}_{-0.23}$	< 0.22	$0.24^{+0.07}_{-0.06}$	—	—
$\Delta\chi^2$	-12	-24	-3	-8	—	—
Broad Line (keV)	$6.36^{+0.08}_{-0.09}$	$6.16^{+0.20}_{-0.20}$	$6.33^{+0.21}_{-0.24}$	$6.27^{+0.13}_{-0.17}$	$6.32^{+0.06}_{-0.11}$	$6.32^{+0.24}_{-0.25}$
σ_{Broad} (keV)	$0.32^{+0.11}_{-0.09}$	$0.37^{+0.21}_{-0.13}$	$0.28^{+0.28}_{-0.13}$	$0.50^{+0.13}_{-0.11}$	$0.15^{+0.07}_{-0.03}$	$0.39^{+0.45}_{-0.26}$
EW_{Broad} (eV)	105^{+26}_{-24}	53^{+27}_{-38}	92^{+59}_{-56}	134^{+42}_{-38}	62^{+28}_{-44}	71^{+53}_{-48}
Flux (10^{-5} ph cm $^{-2}$ s $^{-1}$)	$3.74^{+0.93}_{-0.86}$	$1.64^{+0.83}_{-1.17}$	$0.49^{+0.31}_{-0.30}$	$2.28^{+0.72}_{-0.65}$	$1.55^{+0.70}_{-1.10}$	$3.43^{+2.56}_{-2.32}$
$\Delta\chi^2$	-57	-28	-3	-53	-24	-12
R_{frac}	$0.88^{+0.23}_{-0.21}$	$0.52^{+0.20}_{-0.18}$	$1.30^{+0.63}_{-0.53}$	< 0.36	$1.46^{+0.37}_{-0.32}$	$2.5^{+1.1}_{-0.8}$
BAT const	$1.04^{+0.12}_{-0.11}$	$0.83^{+0.11}_{-0.10}$	—	$1.25^{+0.28}_{-0.28}$	$1.24^{+0.16}_{-0.14}$	$0.78^{+0.13}_{-0.12}$
χ^2_{ν}	713.4/648	873.4/831	606.1/540	830.4/720	765.7/809	839.9/867

Table B.2: Model B components for the ‘bare’ *Suzaku* XIS, HXD and BAT data from *Swift*. The ionisation parameter ξ is given in units erg cm s^{-1} . ^a POWERLAW normalisation given in units ($10^{-2} \text{ ph keV}^{-1} \text{ cm}^{-2} \text{ s}^{-1}$). ^b REFLECTION normalisation given in units 10^{-5} . Note that a negative $\Delta\chi^2$ denotes an improvement in the fit.

	Ark 120	Fairall 9	MCG-02-14-009	Mrk 335	NGC 7469	SWIFT J2127.4+5654
Γ	$1.90^{+0.01}_{-0.04}$	$1.83^{+0.01}_{-0.04}$	$1.86^{+0.01}_{-0.04}$	$2.00^{+0.02}_{-0.02}$	$1.78^{+0.07}_{-0.10}$	$2.11^{+0.03}_{-0.02}$
Norm ^a	$0.95^{+0.06}_{-0.06}$	$0.64^{+0.02}_{-0.04}$	$0.12^{+0.04}_{-0.03}$	$0.51^{+0.01}_{-0.02}$	$0.54^{+0.04}_{-0.06}$	$1.52^{+0.04}_{-0.05}$
ξ	< 22	< 20	< 21	27^{+9}_{-4}	< 11	< 13
Fe/Solar	$1.4^{+0.5}_{-0.3}$	$1.9^{+0.9}_{-0.3}$	$0.9^{+0.7}_{-0.3}$	$2.2^{+1.1}_{-0.4}$	$1.6^{+0.3}_{-0.3}$	$0.5^{+0.1}_{-0.1}$
Norm ^b	$0.89^{+0.42}_{-0.51}$	$1.11^{+0.12}_{-0.62}$	$0.27^{+0.06}_{-0.11}$	$0.16^{+0.05}_{-0.05}$	$1.18^{+0.10}_{-0.20}$	$2.05^{+0.33}_{-1.00}$
FeXXV Line (keV)	$6.66^{+0.04}_{-0.05}$	$6.73^{+0.03}_{-0.03}$	–	$6.68^{+0.03}_{-0.05}$	–	$6.66^{+0.07}_{-0.05}$
<i>EW</i> (eV)	20^{+7}_{-7}	19^{+6}_{-6}	–	40^{+8}_{-8}	–	25^{+11}_{-11}
Flux ($10^{-5} \text{ ph cm}^{-2} \text{ s}^{-1}$)	$0.72^{+0.25}_{-0.25}$	$0.52^{+0.16}_{-0.16}$	–	$0.64^{+0.13}_{-0.13}$	–	$0.94^{+0.41}_{-0.41}$
$\Delta\chi^2$	-20	-27	–	-67	–	-16
FeXXVI Line (keV)	$6.95^{+0.03}_{-0.03}$	$6.98^{+0.02}_{-0.02}$	$6.94^{+0.05}_{-0.11}$	$6.96^{+0.06}_{-0.16}$	–	$6.98^{+0.09}_{-0.26}$
<i>EW</i> (eV)	31^{+9}_{-9}	31^{+7}_{-7}	39^{+24}_{-23}	21^{+9}_{-9}	–	16^{+13}_{-13}
Flux ($10^{-5} \text{ ph cm}^{-2} \text{ s}^{-1}$)	$0.92^{+0.27}_{-0.27}$	$0.71^{+0.16}_{-0.16}$	$0.16^{+0.10}_{-0.10}$	$0.28^{+0.12}_{-0.12}$	–	$0.49^{+0.40}_{-0.40}$
$\Delta\chi^2$	-31	-38	-7	-14	–	-4
BAT const	$1.07^{+0.12}_{-0.12}$	$0.83^{+0.10}_{-0.10}$	–	$1.03^{+0.23}_{-0.23}$	$1.03^{+0.10}_{-0.09}$	$0.70^{+0.10}_{-0.10}$
χ^2_ν	741.8/649	864.7/834	623.6/543	842.9/723	840.2/812	871.6/867

Table B.3: Fit parameters from Model C to Suzaku XIS, HXD and BAT data from Swift. Line energies are quoted in the rest frame. * denotes a frozen parameter, for cases where the emissivity index is fixed at $q = 3$ it is unconstrained. The improvement $\Delta\chi^2$ in the fit with the introduction of a LAOR profile is noted in comparison with the purely distant reflection as present in this model. Note that the FeXXV emission line is no longer required in Ark 120, Fairall 9 and SWIFT J2127.4+5654. ^a POWERLAW normalisation given in units $(10^{-2} \text{ ph keV}^{-1} \text{ cm}^{-2} \text{ s}^{-1})$. ^b REFLECTION normalisation given in units 10^{-5} . Note that a negative $\Delta\chi^2$ denotes an improvement in the fit.

	Ark 120	Fairall 9	MCG-02-14-009	Mrk 335	NGC 7469	SWIFT J2127.4+5654
Γ	$1.91^{+0.03}_{-0.03}$	$1.84^{+0.03}_{-0.03}$	$1.86^{+0.03}_{-0.03}$	$2.01^{+0.02}_{-0.02}$	$1.78^{+0.01}_{-0.01}$	$2.13^{+0.03}_{-0.03}$
Norm ^a	$0.97^{+0.03}_{-0.05}$	$0.64^{+0.03}_{-0.02}$	$0.12^{+0.04}_{-0.03}$	$0.56^{+0.02}_{-0.02}$	$0.55^{+0.04}_{-0.06}$	$1.54^{+0.04}_{-0.05}$
	Laor Profile					
Line E (keV)	6.4*	< 6.56	6.4*	6.4*	< 6.44	6.4*
Eqw (eV)	85^{+21}_{-17}	79^{+21}_{-22}	119^{+58}_{-52}	126^{+33}_{-35}	60^{+26}_{-22}	140^{+41}_{-41}
q	$3.0^{+1.6}_{-1.0}$	$3.5^{+2.9}_{-0.9}$	3.0*	$3.9^{+1.9}_{-1.0}$	3.0*	$2.5^{+0.7}_{-0.6}$
R_{in} (GM/c^2)	$25^{+1.9}_{-7}$	16^{+17}_{-6}	> 13	32^{+12}_{-16}	81^{+82}_{-37}	< 33
i°	34^{+7}_{-5}	34^{+5}_{-3}	30^{+17}_{-9}	38^{+10}_{-8}	24^{+12}_{-8}	46^{+9}_{-9}
Flux ($10^{-5} \text{ ph cm}^{-2} \text{ s}^{-1}$)	$3.85^{+0.95}_{-0.77}$	$1.79^{+0.50}_{-0.50}$	$0.59^{+0.30}_{-0.26}$	$2.28^{+0.62}_{-0.64}$	$2.56^{+1.02}_{-0.84}$	$5.39^{+1.58}_{-1.58}$
$\Delta\chi^2$	-24	-33	-14	-37	-20	-34
ξ	< 19	< 21	< 15	33^{+18}_{-9}	< 13	< 15
Fe/Solar	1.0*	$1.7^{+0.3}_{-0.3}$	$0.6^{+0.6}_{-0.4}$	$2.0^{+0.9}_{-0.8}$	< 1.4	$0.4^{+0.1}_{-0.1}$
Norm ^b	$1.06^{+0.15}_{-0.57}$	$0.97^{+0.23}_{-0.32}$	$0.23^{+0.07}_{-0.11}$	$0.11^{+0.06}_{-0.05}$	$1.07^{+0.08}_{-0.48}$	$1.96^{+0.24}_{-0.92}$
FeXXV Line (keV)	-	-	-	$6.65^{+0.09}_{-0.07}$	-	-
EW (eV)	-	-	-	10^{+8}_{-8}	-	-
Flux ($10^{-5} \text{ ph cm}^{-2} \text{ s}^{-1}$)	-	-	-	$0.17^{+0.13}_{-0.13}$	-	-
$\Delta\chi^2$	-	-	-	-2	-	-
FeXXVI Line (keV)	$6.96^{+0.04}_{-0.04}$	$6.99^{+0.03}_{-0.03}$	$6.94^{+0.04}_{-0.06}$	$7.02^{+0.05}_{-0.06}$	-	-
EW (eV)	33^{+12}_{-19}	27^{+9}_{-15}	42^{+23}_{-24}	19^{+9}_{-9}	-	-
Flux ($10^{-5} \text{ ph cm}^{-2} \text{ s}^{-1}$)	$0.98^{+0.34}_{-0.57}$	$0.63^{+0.21}_{-0.35}$	$0.18^{+0.10}_{-0.10}$	$0.25^{+0.12}_{-0.12}$	-	-
$\Delta\chi^2$	-10	-13	-5	-11	-	-
BAT const	$1.10^{+0.12}_{-0.12}$	$0.86^{+0.10}_{-0.10}$	-	$1.11^{+0.25}_{-0.25}$	$1.08^{+0.11}_{-0.09}$	$0.73^{+0.10}_{-0.10}$
χ^2_ν	721.6/648	857.7/831	609.6/540	806.3/719	820.3/808	855.8/867

Table B.4: Fit parameters from Model D to *Suzaku* XIS, HXD and BAT data from *Swift*. Line energies are quoted in the rest frame. * denotes a frozen parameter. ^a POWERLAW normalisation given in units (10^{-2} ph keV $^{-1}$ cm $^{-2}$ s $^{-1}$). ^b REFLECTION normalisation given in units 10^{-5} . Note that a negative $\Delta\chi^2$ denotes an improvement in the fit.

	Ark 120	Fairall 9	MCG-02-14-009	Mrk 335	NGC 7469	SWIFT J2127.4+5654
Γ	$1.90^{+0.03}_{-0.03}$	$1.84^{+0.02}_{-0.03}$	$1.86^{+0.01}_{-0.01}$	$2.02^{+0.03}_{-0.02}$	$1.78^{+0.01}_{-0.01}$	$2.13^{+0.04}_{-0.03}$
Norm ^a	$0.97^{+0.04}_{-0.05}$	$0.64^{+0.01}_{-0.04}$	$0.13^{+0.04}_{-0.04}$	$0.56^{+0.01}_{-0.01}$	$0.55^{+0.04}_{-0.06}$	$1.55^{+0.05}_{-0.05}$
Line E (keV)	6.4*	6.4*	6.47 $^{+0.03}_{-0.03}$	6.4*	6.4*	6.4*
Eqw (eV)	95^{+32}_{-26}	63^{+36}_{-19}	142^{+47}_{-46}	146^{+39}_{-39}	91^{+9}_{-8}	178^{+82}_{-69}
q	$2.3^{+0.4}_{-0.3}$	$2.7^{+0.7}_{-0.4}$	$2.0^{+0.4}_{-0.4}$	$2.6^{+0.5}_{-0.3}$	$1.7^{+0.4}_{-0.6}$	$2.6^{+1.0}_{-0.4}$
a	< 0.94	$0.44^{+0.04}_{-0.11}$	< 0.88	$0.70^{+0.12}_{-0.01}$	$0.69^{+0.09}_{-0.09}$	$0.70^{+0.10}_{-0.14}$
i°	33^{+2}_{-17}	38^{+8}_{-5}	24^{+10}_{-9}	38^{+2}_{-2}	23^{+15}_{-7}	43^{+5}_{-10}
Flux (10^{-5} ph cm $^{-2}$ s $^{-1}$)	$3.62^{+1.22}_{-0.99}$	$1.78^{+1.02}_{-0.54}$	$6.64^{+2.20}_{-2.15}$	$2.52^{+0.67}_{-0.67}$	$2.23^{+0.22}_{-0.20}$	$6.35^{+2.91}_{-2.46}$
$\Delta\chi^2$ (kerddisk)	-23	-30	-12	-40	-25	-37
$\Delta\chi^2$ (zero spin)	+1	+4	0	+4	+10	+7
ξ	< 16	< 17	< 16	41^{+7}_{-16}	< 11	< 13
Fe/Solar	1.0*	$1.6^{+0.3}_{-0.4}$	$0.8^{+0.6}_{-0.4}$	$1.9^{+0.9}_{-0.6}$	$0.8^{+0.4}_{-0.2}$	$0.3^{+0.2}_{-0.2}$
Norm ^b	$0.97^{+0.50}_{-0.64}$	$1.09^{+0.09}_{-0.29}$	$0.25^{+0.07}_{-0.16}$	$0.07^{+0.07}_{-0.01}$	$0.69^{+0.22}_{-0.15}$	$2.12^{+0.63}_{-0.83}$
Fe XXV Line (keV)	-	-	-	$6.67^{+0.06}_{-0.05}$	-	-
EW (eV)	-	-	-	16 $^{+8}_{-8}$	-	-
Flux (10^{-5} ph cm $^{-2}$ s $^{-1}$)	-	-	-	$0.26^{+0.13}_{-0.13}$	-	-
$\Delta\chi^2$	-	-	-	-4	-	-
Fe XXVI Line (keV)	$6.99^{+0.04}_{-0.06}$	$6.98^{+0.04}_{-0.03}$	$6.94^{+0.08}_{-0.09}$	$7.02^{+0.04}_{-0.05}$	-	-
EW (eV)	22^{+23}_{-15}	30^{+8}_{-10}	44^{+26}_{-38}	22^{+10}_{-10}	-	-
Flux (10^{-5} ph cm $^{-2}$ s $^{-1}$)	$0.65^{+0.68}_{-0.44}$	$0.70^{+0.19}_{-0.24}$	$0.18^{+0.11}_{-0.16}$	$0.28^{+0.12}_{-0.12}$	-	-
$\Delta\chi^2$	-7	-12	-9	-14	-	-
BAT const	$1.05^{+0.12}_{-0.12}$	$0.85^{+0.10}_{-0.10}$	-	$1.05^{+0.23}_{-0.23}$	$1.06^{+0.11}_{-0.09}$	$0.67^{+0.09}_{-0.09}$
χ^2_ν	724.4/648	861.2/832	611.6/538	803.0/719	815.5/808	852.3/867

Table B.5: Fit parameters from Model E to *Suzaku* XIS, HXD and BAT data from *Swift*. (A) represents the unblurred REFLIONX and (B) represents the blurred REFLIONX. The ionisation parameter ξ is given in units erg cm s^{-1} , a POWERLAW normalisation given in units $(10^{-2} \text{ ph keV}^{-1} \text{ cm}^{-2} \text{ s}^{-1})$, b REFLIONX normalisation in units 10^{-5} . * denotes a parameter frozen at the best-fitting value from Model D. In some cases the spin parameter a could not be constrained, denoted by $-$. Note that a negative $\Delta\chi^2$ denotes an improvement in the fit.

	Ark 120	Fairall 9	MCG-02-14-009	Mrk 335	NGC 7469	SWIFT J2127.4+5654
Soft Excess	\checkmark	\checkmark	X	\checkmark	\checkmark	X
Γ	$2.12^{+0.01}_{-0.02}$	$2.01^{+0.01}_{-0.01}$	$1.90^{+0.03}_{-0.03}$	$2.15^{+0.01}_{-0.02}$	$1.80^{+0.01}_{-0.01}$	$2.20^{+0.05}_{-0.05}$
Norm a	$1.13^{+0.02}_{-0.02}$	$0.78^{+0.02}_{-0.02}$	$0.12^{+0.05}_{-0.03}$	$0.57^{+0.02}_{-0.02}$	$0.55^{+0.05}_{-0.07}$	$1.65^{+0.05}_{-0.08}$
q	$4.1^{+0.8}_{-0.8}$	> 6.15	Kerrconv < 3.5	$6.6^{+2.0}_{-1.0}$	> 3.0	$2.2^{+0.6}_{-0.4}$
a	> 0.97	$0.98^{+0.01}_{-0.01}$	< 0.96	$0.87^{+0.05}_{-0.06}$	< 0.97	$-$
i°	48^{+3}_{-6}	70^{+5}_{-2}	40^{+11}_{-14}	53^{+6}_{-6}	70^{+4}_{-3}	43^{+18}_{-7}
Fe/Solar (A)	1.4^*	1.9^*	0.4^*	$2.0^{+0.8}_{-0.4}$	1.6^*	> 0.2
ξ (A)	< 13	< 11	< 543	< 11	< 11	< 26
Norm (A) b	$1.31^{+0.14}_{-0.15}$	$1.13^{+0.08}_{-0.19}$	$0.10^{+0.17}_{-0.10}$	$0.47^{+0.05}_{-0.10}$	$1.13^{+0.11}_{-0.21}$	$0.67^{+0.60}_{-0.60}$
Fe/Solar (B)	$1.5^{+0.3}_{-0.3}$	$0.8^{+0.2}_{-0.3}$	> 1.1	$1.0^{+0.1}_{-0.1}$	< 0.4	$1.0^{+0.8}_{-0.3}$
ξ (B)	56^{+12}_{-3}	24^{+17}_{-9}	< 14	207^{+5}_{-5}	< 24	< 14
Norm (B) b	$0.38^{+0.21}_{-0.13}$	$0.24^{+0.04}_{-0.03}$	$0.27^{+0.19}_{-0.20}$	$0.06^{+0.01}_{-0.01}$	$0.30^{+0.36}_{-0.12}$	$3.68^{+1.50}_{-1.99}$
Fe XXV Line (keV)	$6.65^{+0.05}_{-0.07}$	$6.74^{+0.04}_{-0.04}$	$-$	$6.67^{+0.03}_{-0.03}$	$-$	$-$
EW (eV)	17^{+7}_{-7}	16^{+6}_{-6}	$-$	34^{+8}_{-8}	$-$	$-$
Flux ($10^{-5} \text{ ph cm}^{-2} \text{ s}^{-1}$)	$0.62^{+0.26}_{-0.27}$	$0.44^{+0.17}_{-0.17}$	$-$	$0.55^{+0.13}_{-0.13}$	$-$	$-$
$\Delta\chi^2$	-8	-10	$-$	-10	$-$	$-$
Fe XXVI Line (keV)	$6.95^{+0.03}_{-0.03}$	$6.88^{+0.02}_{-0.03}$	$6.95^{+0.06}_{-0.07}$	$6.97^{+0.07}_{-0.12}$	$-$	$-$
EW (eV)	29^{+9}_{-9}	27^{+7}_{-7}	34^{+23}_{-23}	16^{+9}_{-8}	$-$	$-$
Flux ($10^{-5} \text{ ph cm}^{-2} \text{ s}^{-1}$)	$0.85^{+0.27}_{-0.27}$	$0.63^{+0.17}_{-0.17}$	$0.14^{+0.10}_{-0.10}$	$0.23^{+0.13}_{-0.12}$	$-$	$-$
$\Delta\chi^2$	-16	-25	-4	-10	$-$	$-$
BAT const	$1.11^{+0.11}_{-0.11}$	$0.87^{+0.10}_{-0.10}$	$-$	$1.06^{+0.23}_{-0.23}$	$0.93^{+0.08}_{-0.08}$	$0.68^{+0.10}_{-0.09}$
χ^2_ν	$770.2/647$	$879.6/832$	$612.0/538$	$811.6/722$	$835.4/808$	$830.4/865$

Table B.6: Fit parameters from Model F to Suzaku XIS, HXD and BAT data from *Swift*. * denotes a parameter frozen at the best-fit value from Model D. ^a POWERLAW normalisation given in units (10^{-2} ph keV $^{-1}$ cm $^{-2}$ s $^{-1}$). ^b Flux for COMPTT quoted over the 0.5-10.0 keV range in units 10^{-11} erg cm $^{-2}$ s $^{-1}$. ^c REFLECTIONX normalisation given in units 10^{-5} . In some cases the spin parameter a could not be constrained, denoted by $-$. ¹ with 75% confidence. Note that a negative $\Delta\chi^2$ denotes an improvement in the fit.

	Ark 120	Fairall 9	MCG-02-14-009	MRK 335	NGC 7469	SWIFT J2127.4+5654
Γ	$1.98^{+0.04}_{-0.04}$	$1.95^{+0.02}_{-0.04}$	$1.90^{+0.02}_{-0.02}$	$2.04^{+0.02}_{-0.03}$	$1.80^{+0.01}_{-0.01}$	$2.19^{+0.05}_{-0.03}$
Norm ^a	$1.02^{+0.01}_{-0.01}$	$0.76^{+0.01}_{-0.01}$	$0.12^{+0.01}_{-0.01}$	$0.57^{+0.01}_{-0.01}$	$0.56^{+0.01}_{-0.01}$	$1.64^{+0.06}_{-0.08}$
Plasma Temperature (keV)	< 55.5	< 76.2	$-$	< 4.2	< 19.9	$-$
Plasma Optical Depth τ	< 2.4	$0.4^{+19.9}_{-0.1}$	$-$	< 0.8	< 0.8	$-$
Flux ^b	$0.67^{+0.06}_{-0.09}$	$0.25^{+0.04}_{-0.02}$	$-$	$0.70^{+0.03}_{-0.02}$	$0.10^{+0.06}_{-0.02}$	$-$
$\Delta\chi^2$	-261	-111	$-$	-246	-42	$-$
Neutral Fe K α Line (keV)	$6.39^{+0.02}_{-0.02}$	$6.39^{+0.01}_{-0.01}$	$6.42^{+0.04}_{-0.04}$	$6.38^{+0.03}_{-0.03}$	$6.39^{+0.01}_{-0.01}$	$6.37^{+0.06}_{-0.07}$
E_{Narrow} (eV)	33^{+10}_{-10}	80^{+8}_{-8}	59^{+23}_{-24}	27^{+17}_{-12}	98^{+13}_{-13}	17^{+12}_{-12}
Flux (10^{-5} ph cm $^{-2}$ s $^{-1}$)	$1.24^{+0.38}_{-0.38}$	$2.28^{+0.22}_{-0.22}$	$0.31^{+0.12}_{-0.13}$	$0.46^{+0.30}_{-0.21}$	$2.34^{+0.32}_{-0.30}$	$0.70^{+0.48}_{-0.49}$
Kerrconv						
q	$2.2^{+0.1}_{-0.6}$	$2.4^{+0.2}_{-0.2}$	< 2.0	$2.0^{+0.2}_{-0.3}$	$1.7^{+0.1}_{-0.8}$	$2.2^{+0.4}_{-0.9}$
a	$-$	$< 0.77^1$	$-$	$-$	$0.72^{+0.18}_{-0.17}$	$> 0.40^1$
i°	45^{+6}_{-5}	37^{+5}_{-3}	> 29	38^*	80^{+8}_{-5}	42^{+16}_{-7}
ξ	< 21	< 12	< 13	25^{+7}_{-3}	< 13	< 18
Fe/Solar	$2.2^{+1.2}_{-1.0}$	$0.8^{+0.1}_{-0.2}$	$0.7^{+0.5}_{-0.3}$	$2.5^{+1.1}_{-0.6}$	$0.9^{+0.5}_{-0.2}$	$0.9^{+0.3}_{-0.3}$
Norm ^c	$1.66^{+0.20}_{-0.81}$	$1.68^{+0.10}_{-0.34}$	$0.38^{+0.06}_{-0.14}$	$0.27^{+0.06}_{-0.09}$	$1.26^{+0.13}_{-0.36}$	$4.30^{+0.33}_{-2.33}$
Fe XXV Line (keV)	$-$	$-$	$-$	$6.71^{+0.07}_{-0.05}$	$-$	$-$
E_{W} (eV)	$-$	$-$	$-$	21^{+10}_{-9}	$-$	$-$
Flux (10^{-5} ph cm $^{-2}$ s $^{-1}$)	$-$	$-$	$-$	$0.34^{+0.15}_{-0.15}$	$-$	$-$
$\Delta\chi^2$	$-$	$-$	$-$	-11	$-$	$-$
Fe XXVI Line (keV)	$6.96^{+0.03}_{-0.03}$	$6.97^{+0.02}_{-0.02}$	$6.94^{+0.05}_{-0.07}$	$7.00^{+0.05}_{-0.06}$	$-$	$-$
E_{W} (eV)	35^{+9}_{-9}	35^{+7}_{-7}	36^{+23}_{-23}	21^{+9}_{-9}	$-$	$-$
Flux (10^{-5} ph cm $^{-2}$ s $^{-1}$)	$1.01^{+0.27}_{-0.27}$	$0.80^{+0.17}_{-0.17}$	$0.15^{+0.10}_{-0.10}$	$0.28^{+0.12}_{-0.13}$	$-$	$-$
$\Delta\chi^2$	-6	-32	-5	-13	$-$	$-$
BAT const	$1.09^{+0.12}_{-0.11}$	$0.93^{+0.11}_{-0.11}$	$-$	$1.01^{+0.23}_{-0.23}$	$1.03^{+0.09}_{-0.09}$	$0.67^{+0.10}_{-0.10}$
χ^2_ν	715.5/644	847.5/831	601.5/539	820.0/721	780.9/805	830.8/866

C Deep observation sample tables

Table C.1: Initial parameterisation of the 0.6-100.0 keV spectrum, modelled using powerlaw, warm absorption components, COMPTT, PEXRAV and Gaussians (all where appropriate). ^a POWERLAW normalisation given in units (10^{-2} ph keV $^{-1}$ cm $^{-2}$ s $^{-1}$). ^b Flux for COMPTT quoted over the 0.6-10.0 keV range in units 10^{-11} erg cm $^{-2}$ s $^{-1}$. ^c Flux given in units (10^{-5} ph cm $^{-2}$ s $^{-1}$). ^d Column density measured in units 10^{22} cm $^{-2}$. ^e Ionisation parameter given in units erg cm s $^{-1}$. * Denotes a frozen parameter. † Emission line has been confined to the range 6.63-6.70 keV. Note that a negative $\Delta\chi^2$ denotes an improvement in the fit.

Feature	Parameter	Fairall 9	MCG-6-30-15	NGC 3516	NGC 3783	NGC 4051
Powerlaw	Γ	$2.06^{+0.03}_{-0.03}$	$2.04^{+0.02}_{-0.02}$	$1.73^{+0.03}_{-0.06}$	$1.87^{+0.05}_{-0.01}$	$2.09^{+0.03}_{-0.03}$
	Norm ^a	$0.92^{+0.02}_{-0.03}$	$1.73^{+0.04}_{-0.04}$	$0.34^{+0.02}_{-0.02}$	$0.81^{+0.01}_{-0.02}$	$1.05^{+0.03}_{-0.02}$
COMPTT	kT (keV)	$8.9^{+2.3}_{-6.2}$	< 15.9	–	$8.3^{+0.2}_{-0.1}$	$3.7^{+1.9}_{-0.8}$
	τ	$0.4^{+0.2}_{-0.2}$	< 0.2	–	$1.2^{+0.1}_{-0.1}$	$0.3^{+0.7}_{-0.2}$
	Flux ^b	$0.29^{+0.01}_{-0.01}$	$0.27^{+0.03}_{-0.03}$	–	$1.86^{+0.15}_{-0.28}$	$0.40^{+0.02}_{-0.02}$
	$\Delta\chi^2$	-295	-30	–	-33	-707
Reflection	R	$1.55^{+0.26}_{-0.24}$	$0.79^{+0.12}_{-0.08}$	$0.87^{+0.32}_{-0.22}$	$1.04^{+0.04}_{-0.04}$	$1.52^{+0.26}_{-0.29}$
Fe K α core	LineE (keV)	$6.39^{+0.01}_{-0.01}$	$6.39^{+0.01}_{-0.01}$	$6.40^{+0.01}_{-0.01}$	$6.39^{+0.01}_{-0.01}$	$6.40^{+0.01}_{-0.01}$
	EW (eV)	75^{+8}_{-8}	30^{+3}_{-3}	229^{+10}_{-52}	101^{+34}_{-10}	67^{+7}_{-7}
	Flux ^c	$2.21^{+0.23}_{-0.24}$	$1.39^{+0.16}_{-0.13}$	$4.16^{+0.19}_{-0.94}$	$7.93^{+0.27}_{-0.78}$	$1.71^{+0.18}_{-0.18}$
	$\Delta\chi^2$	-337	-331	-1396	-1366	-320
Fe K β	Norm ^c	0.29*	0.18*	0.53*	1.03*	0.22*
Fe XXV emission	LineE (keV)	$6.66^{+0.04}_{-0.05}$	$6.63^{+0.04}_{-0.04}$ †	$6.60^{+0.05}_{-0.05}$	–	$6.65^{+0.08}_{-0.04}$
	EW (eV)	15^{+7}_{-7}	12^{+4}_{-3}	19^{+8}_{-8}	–	33^{+9}_{-8}
	Flux ^c	$0.44^{+0.21}_{-0.22}$	$0.52^{+0.19}_{-0.12}$	$0.42^{+0.18}_{-0.17}$	–	$0.93^{+0.27}_{-0.22}$
	$\Delta\chi^2$	-10	-51	-16	–	-57
Fe XXVI emission	LineE (keV)	–	6.97^*	–	6.97^*	–
	EW (eV)	–	15^{+5}_{-3}	–	13^{+1}_{-1}	–
	Flux ^c	–	$0.56^{+0.018}_{-0.11}$	–	$8.50^{+0.31}_{-0.31}$	–
	$\Delta\chi^2$	–	-6	–	-17	–

Table C.1: *continued* - Initial parameterisation of the 0.6-100.0 keV spectrum, modelled using powerlaw, warm absorption components, COMPTT, PEXRAV and Gaussians (all where appropriate). ^a POWERLAW normalisation given in units (10^{-2} ph keV $^{-1}$ cm $^{-2}$ s $^{-1}$). ^b Flux for COMPTT quoted over the 0.6-10.0 keV range in units 10^{-11} erg cm $^{-2}$ s $^{-1}$. ^c Flux given in units (10^{-5} ph cm $^{-2}$ s $^{-1}$). ^d Column density measured in units 10^{22} cm $^{-2}$. ^e Ionisation parameter given in units erg cm s $^{-1}$. * Denotes a frozen parameter. † Emission line has been confined to the range 6.63-6.70 keV. Note that a negative $\Delta\chi^2$ denotes an improvement in the fit.

Feature	Parameter	Fairall 9	MCG-6-30-15	NGC 3516	NGC 3783	NGC 4051
Broad line	LineE (keV)	$6.36^{+0.33}_{-0.40}$	$5.93^{+0.07}_{-0.14}$	$6.10^{+0.26}_{-0.33}$	$6.04^{+0.13}_{-0.05}$	6.4*
	σ_{Broad} (keV)	$0.81^{+0.43}_{-0.18}$	$0.84^{+0.06}_{-0.06}$	< 0.88	$0.21^{+0.12}_{-0.05}$	$0.96^{+0.76}_{-0.38}$
	EW_{Broad} (eV)	62^{+35}_{-30}	149^{+21}_{-9}	55^{+29}_{-28}	30^{+9}_{-6}	87^{+67}_{-46}
	Flux ^c	$2.00^{+1.12}_{-0.96}$	$1.31^{+0.68}_{-0.66}$	$2.42^{+0.74}_{-0.46}$	$2.43^{+1.87}_{-1.29}$	$2.43^{+1.87}_{-1.29}$
	$\Delta\chi^2$	-13	-302	-17	-55	-10
Fe XXV abs.	LineE (keV)	-	$6.76^{+0.02}_{-0.02}$	-	$6.72^{+0.03}_{-0.03}$	$6.79^{+0.07}_{-0.05}$
	EW (eV)	-	$-(27^{+3}_{-3})$	-	$-(14^{+5}_{-4})$	$-(15^{+5}_{-5})$
	Flux ^c	-	$-(1.12^{+0.12}_{-0.11})$	-	$-(1.02^{+0.28}_{-0.39})$	$-(0.47^{+0.17}_{-0.17})$
	$\Delta\chi^2$	-	-62	-	-33	-11
Fe XXVI abs.	LineE (keV)	-	$7.05^{+0.02}_{-0.02}$	-	-	$7.12^{+0.03}_{-0.03}$
	EW (eV)	-	$-(21^{+3}_{-4})$	-	-	$-(27^{+7}_{-7})$
	Flux ^c	-	$-(0.75^{+0.13}_{-0.11})$	-	-	$-(0.55^{+0.14}_{-0.14})$
	$\Delta\chi^2$	-	-81	-	-	-47
Warm abs. 1	N_{H} ^d	-	$0.23^{+0.04}_{-0.02}$	$3.21^{+0.55}_{-1.65}$	$0.07^{+0.14}_{-0.06}$	$0.57^{+0.47}_{-0.18}$
	$\log(\xi)$ ^e	-	$0.79^{+0.06}_{-0.09}$	$2.15^{+0.03}_{-0.05}$	$2.10^{+0.04}_{-0.01}$	$3.01^{+0.22}_{-0.03}$
Warm abs. 2	N_{H} ^d	-	$0.70^{+0.09}_{-0.06}$	-	$0.32^{+0.04}_{-0.05}$	$0.09^{+0.07}_{-0.04}$
	$\log(\xi)$ ^e	-	$1.84^{+0.05}_{-0.05}$	-	$0.68^{+0.12}_{-0.57}$	$1.84^{+0.06}_{-0.09}$
WABS	N_{H} ^d	0.0316*	0.0392*	$0.158^{+0.038}_{-0.018}$	0.0991*	0.0115*
XIS/BAT	Const	$0.75^{+0.06}_{-0.05}$	$0.87^{+0.05}_{-0.04}$	$1.74^{+0.08}_{-0.07}$	$0.82^{+0.02}_{-0.02}$	$0.69^{+0.05}_{-0.05}$
	χ^2_{ν}	958.7/897	2085.3/1820	537.7/497	1528.6/1376	1136.0/1085

Table C.2: Components for the baseline model (without broad or diskline emission) to the long observations with *Suzaku* XIS, HXD and BAT data from *Swift*. ^a POWERLAW normalisation given in units (10^{-2} ph keV $^{-1}$ cm $^{-2}$ s $^{-1}$). ^b Column density for partial coverer (P/C) measured in units 10^{23} cm $^{-2}$. ^c Ionisation parameter given in units erg cm s $^{-1}$. ^d Flux for COMP TT quoted over the 0.6-10.0 keV range and REFLIONX over the 2.0-100.0 keV range in units 10^{-11} erg cm $^{-2}$ s $^{-1}$. ^e REFLIONX normalisation given in units 10^{-5} . ^f Flux given in units (10^{-5} ph cm $^{-2}$ s $^{-1}$). ^g Column density measured in units 10^{22} cm $^{-2}$. * indicates a frozen parameter. The highly ionized zone for NGC 3783 has redshift fixed at $z = 0.0097$. Note that a negative $\Delta\chi^2$ denotes an improvement in the fit.

Component	Parameter	Fairall 9	MCG-6-30-15	NGC 3516	NGC 3783	NGC 4051
Powerlaw	Γ	$1.94^{+0.02}_{-0.03}$	$1.87^{+0.04}_{-0.04}$	$1.75^{+0.04}_{-0.06}$	$1.79^{+0.02}_{-0.13}$	$2.04^{+0.04}_{-0.05}$
	Norm ^a	$0.88^{+0.03}_{-0.03}$	$1.62^{+0.05}_{-0.04}$	$0.34^{+0.02}_{-0.03}$	$1.52^{+0.02}_{-0.11}$	$0.95^{+0.04}_{-0.05}$
Absorbed powerlaw	Norm ^a	–	$1.63^{+0.16}_{-0.33}$	$0.06^{+0.04}_{-0.04}$	–	$0.55^{+0.14}_{-0.15}$
P/C	N_{H} ^b	–	$34.07^{+2.38}_{-3.77}$	$1.15^{+3.02}_{-0.75}$	–	$35.91^{+5.92}_{-6.15}$
	$\log(\xi)$ ^c	–	$2.4^{+0.1}_{-0.1}$	$3.1^{+0.5}_{-0.5}$	–	$2.6^{+0.3}_{-0.6}$
	C_{frac}	–	$\sim 50\%$	$\sim 21\%$	–	$\sim 37\%$
COMP TT	kT (keV)	< 4.1	< 8.8	–	$8.5^{+0.2}_{-0.1}$	$5.4^{+3.1}_{-1.0}$
	τ	$0.8^{+1.4}_{-0.6}$	$0.8^{+12.9}_{-0.1}$	–	$1.6^{+0.1}_{-0.1}$	$0.9^{+0.4}_{-0.2}$
	Flux ^d	$0.50^{+0.14}_{-0.14}$	$0.72^{+0.18}_{-0.10}$	–	$2.24^{+5.31}_{-0.76}$	$0.49^{+0.08}_{-0.08}$
	$\Delta\chi^2$	-413	-74	–	-461	-333
REFLIONX	ξ ^c	< 11	< 12	< 12	< 14	< 21
	Z_{Fe}	$2.0^{+1.5}_{-0.3}$	1.0*	1.0*	$0.8^{+0.1}_{-0.1}$	$0.5^{+0.4}_{-0.4}$
	Norm ^e	$2.53^{+0.34}_{-0.33}$	$1.02^{+0.09}_{-0.28}$	$1.47^{+0.23}_{-0.43}$	$5.39^{+1.44}_{-0.26}$	$0.86^{+0.62}_{-0.42}$
	Flux ^d	$2.70^{+0.36}_{-0.35}$	$1.28^{+0.11}_{-0.35}$	$2.38^{+0.37}_{-0.70}$	$8.90^{+2.38}_{-0.43}$	$1.20^{+0.86}_{-0.58}$
	LineE (keV)	$6.68^{+0.03}_{-0.03}$	–	$6.61^{+0.07}_{-0.07}$	–	$6.59^{+0.05}_{-0.07}$
Fe XXV em.	EW (eV)	23^{+6}_{-6}	–	12^{+8}_{-8}	–	16^{+7}_{-7}
	Flux ^f	$0.69^{+0.18}_{-0.18}$	–	$0.25^{+0.17}_{-0.16}$	–	$0.49^{+0.20}_{-0.19}$
	$\Delta\chi^2$	-40	–	-8	–	-21
Fe XXVI em.	LineE (keV)	$7.01^{+0.05}_{-0.05}$	6.97*	–	$6.96^{+0.01}_{-0.01}$	–
	EW (eV)	17^{+8}_{-8}	10^{+4}_{-4}	–	44^{+11}_{-10}	–
	Flux ^f	$0.40^{+0.18}_{-0.18}$	$0.41^{+0.18}_{-0.18}$	–	$4.90^{+1.19}_{-1.09}$	–
	$\Delta\chi^2$	-14	-7	–	-45	–
Warm abs. 1	N_{H} ^g	–	$0.22^{+0.06}_{-0.03}$	$1.90^{+0.66}_{-0.21}$	$4.68^{+0.03}_{-0.03}$	$0.18^{+2.09}_{-0.11}$
	$\log(\xi)$ ^c	–	$0.76^{+0.13}_{-0.09}$	$1.98^{+0.13}_{-0.06}$	$2.10^{+0.01}_{-0.01}$	$3.01^{+0.37}_{-0.37}$
Warm abs. 2	N_{H} ^g	–	$0.47^{+0.09}_{-0.03}$	–	$0.19^{+0.04}_{-0.10}$	$0.18^{+0.07}_{-0.11}$
	$\log(\xi)$ ^c	–	$1.76^{+0.05}_{-0.08}$	–	$0.69^{+0.11}_{-0.10}$	$1.88^{+0.07}_{-0.09}$
High ξ abs.	N_{H} ^g	–	$3.99^{+3.65}_{-1.28}$	–	$4.30^{+0.80}_{-0.72}$	$9.55^{+18.95}_{-5.68}$
	$\log(\xi)$ ^c	–	$3.94^{+0.08}_{-0.25}$	–	$3.99^{+0.07}_{-0.08}$	$4.11^{+0.25}_{-0.15}$
	v_{out} (km s $^{-1}$)	–	3200^{+400}_{-500}	–	–	5600^{+800}_{-700}
WABS	N_{H} ^g	0.0316*	0.0392*	$0.178^{+0.011}_{-0.017}$	0.0991*	0.0115*
XIS/BAT	Const	$0.69^{+0.06}_{-0.06}$	$0.95^{+0.06}_{-0.07}$	$1.82^{+0.11}_{-0.08}$	$0.84^{+0.03}_{-0.02}$	$0.68^{+0.06}_{-0.05}$
	χ^2_{ν}	959.1/885	2026.8/1823	521.2/495	1493.1/1379	1091.5/1086

Table C.3: List of soft X-ray emission and absorption lines included within the baseline model. ^a Flux given in units (10^{-5} ph cm $^{-2}$ s $^{-1}$), negative flux and *EW* indicate an absorption line.

LineE (keV)	<i>EW</i> (eV)	Flux ^a	$\Delta\chi^2$	Identification
Fairall 9				
$0.66^{+0.01}_{-0.02}$	10^{+4}_{-4}	$42.07^{+16.77}_{-16.81}$	-18	O VIII Ly α
MCG-6-30-15				
$0.68^{+0.01}_{-0.01}$	7^{+1}_{-2}	$31.72^{+4.44}_{-9.05}$	-31	O VIII Ly α
$0.77^{+0.01}_{-0.01}$	20^{+5}_{-4}	$71.38^{+16.62}_{-13.07}$	-892	O VII RRC
$0.95^{+0.01}_{-0.01}$	4^{+1}_{-1}	$5.58^{+1.48}_{-1.31}$	-70	Ne IX resonance
$2.37^{+0.01}_{-0.01}$	$-(9^{+1}_{-1})$	$-(2.65^{+0.33}_{-0.34})$	-196	S XV 1s-2p
$2.77^{+0.04}_{-0.08}$	$-(2^{+2}_{-2})$	$-(0.45^{+0.36}_{-0.35})$	-9	S XVI 1s-2p
NGC 3516				
$0.80^{+0.01}_{-0.01}$	17^{+10}_{-9}	$11.18^{+6.89}_{-5.84}$	-7	O VII RRC / Fe XVII 3d-2p
$0.91^{+0.02}_{-0.23}$	9^{+10}_{-8}	$3.96^{+4.35}_{-3.52}$	-13	Ne IX He α
$1.44^{+0.02}_{-0.02}$	5^{+3}_{-2}	$0.78^{+0.42}_{-0.39}$	-11	Mg XII Ly α
$1.56^{+0.02}_{-0.02}$	8^{+3}_{-3}	$1.03^{+0.37}_{-0.39}$	-21	Mg XI He β
NGC 3783				
$0.63^{+0.01}_{-0.01}$	10^{+1}_{-2}	$197.10^{+21.19}_{-39.54}$	-30	O VIII Ly α
$0.70^{+0.01}_{-0.01}$	17^{+2}_{-2}	$97.03^{+13.55}_{-8.86}$	-146	O VII RRC
$1.24^{+0.01}_{-0.01}$	2^{+1}_{-1}	$5.56^{+1.72}_{-2.28}$	-25	Ne IX RRC / Ne X 1s-3p
1.47*	13^{+1}_{-1}	$15.65^{+1.59}_{-1.29}$	-359	Mg XII Ly α
$2.39^{+0.01}_{-0.01}$	$-(13^{+2}_{-2})$	$-(5.60^{+0.71}_{-0.72})$	-163	S XV 1s-2p
$3.28^{+0.03}_{-0.02}$	6^{+2}_{-2}	$1.55^{+0.47}_{-0.52}$	-26	Ar XVIII Ly α
NGC 4051				
$2.22^{+0.03}_{-0.03}$	4^{+3}_{-2}	$0.63^{+0.41}_{-0.38}$	-16	Si XII 1s-3p

Table C.4: Components for the dual reflector fit to the long observations with *Suzaku* XIS, HXD and BAT data from *Swift*. ^a POWERLAW normalisation given in units (10^{-2} ph keV $^{-1}$ cm $^{-2}$ s $^{-1}$). ^b Flux for COMPTT quoted over the 0.6-10.0 keV range and REFLIONX over the 2.0-100.0 keV range in units 10^{-11} erg cm $^{-2}$ s $^{-1}$. ^c Ionisation parameter given in units erg cm s $^{-1}$. ^d REFLIONX normalisation given in units 10^{-5} . ^e Flux given in units (10^{-5} ph cm $^{-2}$ s $^{-1}$). ^f Column density measured in units 10^{22} cm $^{-2}$. * Denotes a frozen parameter. † Emission line has been confined to the range 6.63-6.70 keV. Spin can only be constrained in MCG-6-30-15 and NGC 3783 at the 90% confidence level. The highly ionized zone for NGC 3783 has redshift fixed at $z = 0.0097$ and v_{out} is fixed at the best fit value from the baseline model (Table C.2) for MCG-6-30-15 and NGC 4051. The COMPTT parameters for MCG-6-30-15 have been frozen at their best-fit values from the baseline model. Note that a negative $\Delta\chi^2$ denotes an improvement in the fit.

Component	Parameter	Fairall 9	MCG-6-30-15	NGC 3516	NGC 3783	NGC 4051
Powerlaw	Γ	$2.00^{+0.03}_{-0.01}$	$2.05^{+0.01}_{-0.01}$	$1.76^{+0.04}_{-0.03}$	$1.85^{+0.05}_{-0.01}$	$2.05^{+0.02}_{-0.04}$
	Norm ^a	$0.87^{+0.03}_{-0.03}$	$1.73^{+0.02}_{-0.02}$	$0.35^{+0.02}_{-0.01}$	$1.54^{+0.01}_{-0.04}$	$0.93^{+0.05}_{-0.05}$
COMPTT	kT (keV)	< 14.1	3.9*	–	> 9.5	$5.7^{+8.0}_{-2.9}$
	τ	$0.5^{+1.6}_{-0.2}$	0.8*	–	$1.9^{+0.1}_{-0.1}$	$0.2^{+0.4}_{-0.1}$
	Flux ^b	$0.36^{+0.02}_{-0.02}$	0.72*	–	$2.59^{+0.17}_{-0.12}$	$0.49^{+0.04}_{-0.04}$
	$\Delta\chi^2$	-449	–	–	-2062	-251
Unblurred REFLIONX	ξ^c	< 58	< 11	< 20	< 11	< 30
	Z_{Fe}	2.0*	1.0*	1.0*	1.0*	1.0*
	Norm ^d	$0.98^{+1.73}_{-0.54}$	$0.70^{+0.08}_{-0.10}$	$0.72^{+0.21}_{-0.43}$	$4.50^{+0.12}_{-0.33}$	$0.99^{+0.10}_{-0.44}$
	Flux ^b	$2.42^{+4.28}_{-1.34}$	$0.71^{+0.08}_{-0.10}$	$1.16^{+0.34}_{-0.69}$	$6.92^{+0.19}_{-0.51}$	$1.00^{+0.16}_{-0.65}$
KERCONV*REFLIONX	q	$2.7^{+2.3}_{-0.2}$	$2.3^{+0.2}_{-0.1}$	$2.4^{+1.0}_{-0.8}$	$2.8^{+0.4}_{-0.2}$	$1.9^{+0.5}_{-1.1}$
	a	–	$0.61^{+0.15}_{-0.17}$	–	< 0.31	–
	i°	33^{+4}_{-5}	35^{+2}_{-2}	35^{+6}_{-5}	< 13	41^{+7}_{-7}
	ξ^c	40^{+29}_{-15}	< 11	< 24	52^{+8}_{-27}	< 18
	Z_{Fe}	2.0*	1.0*	1.0*	1.0*	1.0*
	Norm ^d	$0.26^{+0.75}_{-0.16}$	$2.42^{+0.28}_{-0.27}$	$0.44^{+0.75}_{-0.18}$	$1.98^{+0.65}_{-0.77}$	$1.30^{+0.18}_{-0.72}$
Fe XXV emission	Flux ^b	$0.72^{+2.06}_{-0.44}$	$2.28^{+0.26}_{-0.25}$	$1.28^{+2.18}_{-0.52}$	$2.91^{+0.96}_{-1.13}$	$1.00^{+0.14}_{-0.76}$
	LineE (keV)	$6.69^{+0.05}_{-0.05}$	$6.63^{+0.04}_{-0.04}$ †	–	–	–
	EW (eV)	15^{+11}_{-8}	6^{+5}_{-3}	–	–	–
	Flux ^e	$0.43^{+0.30}_{-0.22}$	$0.25^{+0.20}_{-0.13}$	–	–	–
	$\Delta\chi^2$	-14	-7	–	–	–

Table C.4: *continued* - Components for the dual reflector fit to the long observations with *Suzaku* XIS, HXD and BAT data from *Swift*. ^a POWERLAW normalisation given in units (10^{-2} ph keV $^{-1}$ cm $^{-2}$ s $^{-1}$). ^b Flux for COMPTT quoted over the 0.6-10.0 keV range and REFLIONX over the 2.0-100.0 keV range in units 10^{-14} erg cm $^{-2}$ s $^{-1}$. ^c Ionisation parameter given in units erg cm s $^{-1}$. ^d REFLIONX normalisation given in units 10^{-5} . ^e Flux given in units (10^{-5} ph cm $^{-2}$ s $^{-1}$). ^f Column density measured in units 10^{22} cm $^{-2}$. * Denotes a frozen parameter. † Emission line has been confined to the range 6.63-6.70 keV. Spin can only be constrained in MCG-6-30-15 and NGC 3783 at the 90% confidence level. The highly ionized zone for NGC 3783 has redshift fixed at $z = 0.0097$ and v_{out} is fixed at the best fit value from the baseline model (Table C.2) for MCG-6-30-15 and NGC 4051. The COMPTT parameters for MCG-6-30-15 have been frozen at their best-fit values from the baseline model. Note that a negative $\Delta\chi^2$ denotes an improvement in the fit.

Component	Parameter	Fairall 9	MCG-6-30-15	NGC 3516	NGC 3783	NGC 4051
Fe XXVI emission	LineE (keV)	$7.02^{+0.05}_{-0.04}$	6.97^*	–	$6.96^{+0.01}_{-0.01}$	–
	EW (eV)	20^{+7}_{-7}	45^{+33}_{-19}	–	44^{+27}_{-9}	–
	Flux ^e	$0.47^{+0.17}_{-0.17}$	$2.81^{+2.08}_{-1.18}$	–	$3.40^{+2.06}_{-0.73}$	–
	$\Delta\chi^2$	-14	-10	–	-49	–
Warm absorption zone 1	N_{H}^f	–	$0.21^{+0.03}_{-0.03}$	$2.58^{+0.39}_{-0.24}$	$4.61^{+0.05}_{-0.02}$	$0.24^{+0.31}_{-0.15}$
	$\log(\xi)^c$	–	$0.69^{+0.10}_{-0.11}$	$2.09^{+0.05}_{-0.02}$	$2.09^{+0.01}_{-0.01}$	$2.77^{+0.23}_{-0.44}$
	N_{H}^f	–	$0.73^{+0.05}_{-0.06}$	–	$0.15^{+0.24}_{-0.08}$	$0.19^{+0.11}_{-0.14}$
Warm absorption zone 2	$\log(\xi)^c$	–	$1.77^{+0.04}_{-0.06}$	–	< 0.86	$1.89^{+0.06}_{-0.07}$
	N_{H}^f	–	$11.01^{+5.10}_{-3.95}$	–	$1.59^{+0.56}_{-0.28}$	$13.21^{+13.52}_{-6.72}$
	$\log(\xi)^c$	–	$4.08^{+0.09}_{-0.09}$	–	$3.87^{+0.08}_{-0.09}$	$4.11^{+0.21}_{-0.12}$
High ξ zone	v_{out} (km s $^{-1}$)	–	3200^*	–	–	5600^*
	N_{H}^f	0.0316^*	0.0392^*	$0.182^{+0.013}_{-0.013}$	0.0991^*	0.0115^*
WABS	Const	$0.71^{+0.06}_{-0.05}$	$0.84^{+0.06}_{-0.05}$	$1.84^{+0.10}_{-0.07}$	$0.84^{+0.02}_{-0.02}$	$0.77^{+0.05}_{-0.06}$
XIS/BAT	χ^2_{ν}	929.3/881	2061.4/1823	510.9/495	1444.8/1378	1111.2/1084

D Full sample tables

Table D.1: Components for the baseline model (without broad or diskline emission) to the observations with *Suzaku* XIS, HXD and BAT data from *Swift* in the full *Suzaku* sample. ^a Unabsorbed POWERLAW normalisation given in units (10^{-2} ph keV $^{-1}$ cm $^{-2}$ s $^{-1}$). ^b Flux for COMP TT quoted over the 0.6-10.0 keV range and REFLIONX over the 2.0-100.0 keV range in units 10^{-11} erg cm $^{-2}$ s $^{-1}$. ^c Ionisation parameter given in units erg cm s $^{-1}$. ^d Column density measured in units 10^{22} cm $^{-2}$. ^e $v_{\text{turb}} = 1000$ km s $^{-1}$. ^f only the intrinsic powerlaw is absorbed. * indicates a frozen parameter. † indicates parameters are tied during the analysis of multiple observations.

Object	Powerlaw			COMP TT			REFLIONX			Warm absorber			χ^2_{ν}
	Γ	Norm ^a	kT (keV)	τ	Flux ^b	Z_{Fe}	ξ^c	Flux ^b	N_{H}^d	$\log(\xi)^c$	C_{frac}		
1H 0419-577	1.70 $^{+0.01}_{-0.01}$	0.39 $^{+0.01}_{-0.01}$	7.5 $^{+0.4}_{-0.4}$	1.4 $^{+0.1}_{-0.1}$	0.59 $^{+0.01}_{-0.01}$	1.0*	10.1 $^{+1.9}_{-3.0}$	0.36 $^{+0.21}_{-0.14}$	15.83 $^{+51.61}_{-15.68}$	> 2.87	100%	1788.9/1750	
1H 0419-577	1.70†	0.31 $^{+0.01}_{-0.01}$	7.5†	1.4†	0.46 $^{+0.01}_{-0.01}$	1.0†	10.1†	0.45 $^{+0.28}_{-0.17}$	178.0 $^{+78.0}_{-54.0}$	2.05 $^{+0.43}_{-0.77}$	18%		
3C 111	1.58 $^{+0.01}_{-0.01}$	0.44 $^{+0.01}_{-0.01}$	—	—	—	—	—	—	178.0†	2.05†	15%		
3C 120 Obs	1.65 $^{+0.01}_{-0.01}$	0.98 $^{+0.01}_{-0.01}$	6.9 $^{+0.3}_{-0.3}$	1.8 $^{+0.1}_{-0.1}$	1.82 $^{+0.03}_{-0.03}$	1.5 $^{+0.3}_{-0.2}$	< 19.4	1.92 $^{+0.30}_{-0.28}$	0.61 $^{+0.01}_{-0.01}$	Neutral	100%	1101.1/1098	
1,2,3,4	—	—	—	—	—	—	—	—	0.09 $^{+0.01}_{-0.01}$	Neutral	100%	3630.5/3452	
3C 120 Obs	1.65†	0.86 $^{+0.01}_{-0.01}$	6.9†	1.8†	0.97 $^{+0.01}_{-0.01}$	1.5†	< 19.4†	2.34 $^{+0.35}_{-0.30}$	0.09†	Neutral	100%		
4	—	—	—	—	—	—	—	—	—	—	—		
3C 382	1.78 $^{+0.01}_{-0.01}$	1.16 $^{+0.01}_{-0.01}$	< 56.5	1.0 $^{+1.4}_{-1.0}$	0.35 $^{+0.36}_{-0.31}$	1.0*	< 2.1	1.67 $^{+0.14}_{-0.93}$	0.35 $^{+0.14}_{-0.09}$	2.74 $^{+0.09}_{-0.12}$	100%	986.6/938	
3C 390.3	1.73 $^{+0.02}_{-0.02}$	0.75 $^{+0.01}_{-0.01}$	< 55.9	< 25	< 0.429	0.5 $^{+0.1}_{-0.1}$	2 †	2.37 $^{+2.44}_{-0.65}$	—	—	—	1499.4/1486	
3C 445	1.43 $^{+0.01}_{-0.01}$	0.03 $^{+0.01}_{-0.01}$	—	—	—	1.0*	9.9 $^{+4.5}_{-7.8}$	2.79 $^{+10.65}_{-1.03}$	3.31 $^{+0.21e}_{-0.17}$	1.93 $^{+0.03}_{-0.03}$	100%	458.1/422	
4C 74.26	1.92 $^{+0.01}_{-0.01}$	1.06 $^{+0.01}_{-0.01}$	—	—	—	1.0*	< 5.2	1.23 $^{+1.36}_{-0.81}$	18.94 $^{+0.78}_{-0.75}$	Neutral	89%		
Ark 120	1.90 $^{+0.01}_{-0.04}$	0.95 $^{+0.06}_{-0.06}$	< 8.5	< 2.4	1.05 $^{+0.05}_{-0.05}$	1.4 $^{+0.5}_{-0.3}$	< 22	0.93 $^{+0.44}_{-0.53}$	0.27 $^{+0.03}_{-0.01}$	1.00 $^{+0.10}_{-0.07}$	100%	1344.8/1303	
												741.8/649	

Table D.1: *continued* - Components for the baseline model (without broad or diskline emission) to the observations with *Suzaku* XIS, XRD and BAT data from *Swift*. *a* Unabsorbed POWERLAW normalisation given in units (10^{-2} ph keV $^{-1}$ cm $^{-2}$ s $^{-1}$). *b* Flux for COMP-TT quoted over the 0.6-10.0 keV range and REFLIONX over the 2.0-100.0 keV range in units 10^{-11} erg cm $^{-2}$ s $^{-1}$. *c* Ionisation parameter given in units erg cm s $^{-1}$. *d* Column density measured in units 10^{22} cm $^{-2}$. *e* $v_{\text{turb}} = 1000$ km s $^{-1}$. *f* only the intrinsic powerlaw is absorbed. * indicates a frozen parameter. † indicates parameters are tied during the analysis of multiple observations.

Object	Powerlaw			COMP-TT			REFLIONX			Warm absorber			
	Γ	Norm ^a	kT (keV)	τ	Flux ^b	Z_{Fe}	ξ^c	Flux ^b	N_{H}^d	$\log(\xi)^c$	C_{frac}	χ^2_{ν}	
Ark 564	$2.34^{+0.01}_{-0.01}$	$1.10^{+0.01}_{-0.01}$	$4.7^{+27.3}_{-2.4}$	< 2.0	$3.29^{+3.22}_{-2.53}$	1.0*	< 7.8	$0.12^{+0.19}_{-0.09}$	$0.05^{+0.01}_{-0.01}$	Neutral	100%	1148.9/1024	
Fairall 9	$1.81^{+0.01}_{-0.01}$	$0.61^{+0.01}_{-0.01}$	$9.2^{+0.7}_{-0.6}$	$1.1^{+0.1}_{-0.1}$	$0.42^{+0.01}_{-0.01}$	$2.2^{+1.3}_{-0.4}$	$14.8^{+7.7}_{-9.0}$	$7.94^{+1.83}_{-0.61}$	—	—	—	2254.9/2078	
Obs 1													
Fairall 9	1.81†	$0.56^{+0.01}_{-0.01}$	9.2†	1.1†	$3.87^{+0.03}_{-0.03}$	2.2†	14.8†	$7.13^{+5.47}_{-3.39}$	—	—	—		
Obs 2													
IC 4329A	$1.91^{+0.01}_{-0.01}$	$3.51^{+0.01}_{-0.01}$	—	—	—	$0.6^{+0.1}_{-0.1}$	< 1.1	$9.15^{+0.18}_{-1.31}$	$< 0.02^e$	$1.53^{+0.29}_{-0.48}$	100%	2421.4/2200	
Obs 1,2,3,4,5													
IRAS 13224-3809	$2.50^{+0.20}_{-0.16}$	< 0.02	< 14.8	< 1.5	$0.33^{+0.01}_{-0.01}$	—	—	—	$0.35^{+0.03}_{-0.04}$	$1.84^{+0.05}_{-0.05}$	100%		
									$0.60^{+0.02}_{-0.02}$	< 0.01	100%		
									$< 0.04^e$	> 0.63	100%	484.86/447	
MCG-02-14-009	$1.86^{+0.01}_{-0.04}$	$0.12^{+0.04}_{-0.03}$	—	—	—	$0.9^{+0.7}_{-0.3}$	< 21.0	$0.41^{+0.09}_{-0.17}$	$0.22^{+0.01}_{-0.02}$	Neutral	100%	623.6/543	
MCG-02-58-22	$1.64^{+0.01}_{-0.01}$	$0.94^{+0.01}_{-0.01}$	$10.5^{+148.4}_{-5.9}$	$1.5^{+1.4}_{-1.5}$	$1.61^{+1.89}_{-1.41}$	1.0*	$56.6^{+8.4}_{-5.2}$	$2.74^{+0.47}_{-0.49}$	$5.00^{+2.17}_{-2.56}$	< 0.52	72%		
MCG-05-23-16	$1.84^{+0.01}_{-0.01}$	$2.87^{+0.03}_{-0.03}$	$5.3^{+0.3}_{-0.3}$	$16.7^{+1.1}_{-1.0}$	$0.45^{+0.02}_{-0.02}$	1.0*	< 1.0	$2.76^{+0.21}_{-0.27}$	$1.46^{+0.01,f}_{-0.01}$	Neutral	100%	1582.8/1466	

Table D.1: *continued* - Components for the baseline model (without broad or diskline emission) to the observations with *Suzaku* XIS, XRD and BAT data from *Swift*. ^a Unabsorbed POWERLAW normalisation given in units (10^{-2} ph keV $^{-1}$ cm $^{-2}$ s $^{-1}$). ^b Flux for COMP-TT quoted over the 0.6-10.0 keV range and REFLIONX over the 2.0-100.0 keV range in units 10^{-11} erg cm $^{-2}$ s $^{-1}$. ^c Ionisation parameter given in units erg cm s $^{-1}$. ^d Column density measured in units 10^{22} cm $^{-2}$. ^e $v_{\text{turb}} = 1000$ km s $^{-1}$. ^f only the intrinsic powerlaw is absorbed. * indicates a frozen parameter. † indicates parameters are tied during the analysis of multiple observations.

Object	Powerlaw			COMP-TT			REFLIONX			Warm absorber				
	Γ	Norm ^a	kT (keV)	τ	Flux ^b	Z _{Fe}	ξ^c	Flux ^b	N _H ^d	log(ξ) ^c	C _{frac}	χ^2_{ν}		
MCG-06-30-15	1.87 ^{+0.04} _{-0.04}	1.62 ^{+0.05} _{-0.04}	< 8.8	0.8 ^{+12.9} _{-0.1}	0.72 ^{+0.18} _{-0.10}	1.0*	< 12	1.28 ^{+0.11} _{-0.35}	0.22 ^{+0.06} _{-0.03}	0.76 ^{+0.13} _{-0.09}	100%	2026.8/1823		
Obs 1,2,3														
MCG+8-11-11	1.80 ^{+0.01} _{-0.01}	1.86 ^{+0.01} _{-0.01}	-	-	-	1.0*	8.0 ^{+3.5} _{-2.4}	4.79 ^{+2.32} _{-1.57}	0.47 ^{+0.09} _{-0.03} 341.0 ^{+24.0} _{-38.0}	1.76 ^{+0.05} _{-0.08} 2.43 ^{+0.02} _{-0.05} 2.43 ^{+0.03} _{-0.03}	100% 50% 100%	1049.9/938		
MR 2251-178	1.56 ^{+0.01} _{-0.01}	0.90 ^{+0.01} _{-0.01}	4.6 ^{+51.8} _{-2.3}	2.2 ^{+1.4} _{-1.1}	0.80 ^{+0.08} _{-0.08}	-	-	-	0.06 ^{+0.01} _{-0.01} 0.89 ^{+0.26} _{-0.20}	Neutral 2.88 ^{+0.07} _{-0.08}	100% 100%	977.5/902		
Mrk 79	1.55 ^{+0.02} _{-0.02}	0.32 ^{+0.01} _{-0.01}	-	-	-	-	-	-	0.54 ^{+0.03} _{-0.03} 0.06 ^{+0.04} _{-0.01} 0.98 ^{+0.44} _{-0.28}	1.68 ^{+0.03} _{-0.03} 1.50 ^{+0.21} _{-0.14} 2.66 ^{+0.13} _{-0.14}	100% 100% 100%	601.7/545		
Mrk 110	1.71 ^{+0.01} _{-0.01}	0.52 ^{+0.01} _{-0.01}	< 48.7	2.8 ^{+0.9} _{-0.1}	0.31 ^{+0.17} _{-0.20}	1.0*	49.4 ^{+5.7} _{-31.5}	0.42 ^{+0.88} _{-0.13}	-	-	-	483.1/471		
Mrk 205	1.97 ^{+0.02} _{-0.02}	0.31 ^{+0.01} _{-0.01}	10.3 ^{+32.4} _{-8.0}	< 2.0	0.08 ^{+0.20} _{-0.03}	1.0*	< 1.5	0.45 ^{+0.06} _{-0.17}	50.94 ^{+54.76} _{-24.99}	2.75 ^{+0.70} _{-0.52}	13%	167.7/165		
Mrk 279	1.76 ^{+0.01} _{-0.01}	0.11 ^{+0.01} _{-0.01}	-	-	-	1.0*	2.8 ^{+1.0} _{-0.5}	1.14 ^{+0.29} _{-0.30}	0.08 ^{+0.03} _{-0.03} > 452.53	1.39 ^{+0.30} _{-0.31} 1.24 ^{+0.36} _{-0.23}	100% 72%	712.4/669		
Mrk 335	2.00 ^{+0.02} _{-0.02}	0.51 ^{+0.01} _{-0.02}	< 8.3	< 2.2	0.98 ^{+0.02} _{-0.02}	2.2 ^{+1.1} _{-0.4}	27.0 ^{+9.0} _{-4.0}	0.46 ^{+0.14} _{-0.14}	-	-	-	842.9/723		
Mrk 359	1.74 ^{+0.01} _{-0.01}	0.12 ^{+0.01} _{-0.01}	< 151.5	< 4.3	0.08 ^{+0.28} _{-0.07}	1.0*	21.8 ^{+5.8} _{-9.1}	0.52 ^{+0.44} _{-0.17}	-	-	-	610.1/562		
Mrk 509	1.66 ^{+0.01} _{-0.01}	0.89 ^{+0.01} _{-0.01}	11.7 ^{+36.9} _{-5.3}	1.2 ^{+1.0} _{-1.0}	2.54 ^{+2.25} _{-1.86}	1.0*	21.4 ^{+30.9} _{-18.4}	1.51 ^{+0.94} _{-0.94}	0.24 ^{+0.03} _{-0.02}	2.20 ^{+0.06} _{-0.07}	100%	1976.2/1870		
Obs 1,2,3,4														
Mrk 766	1.99 ^{+0.01} _{-0.01}	0.50 ^{+0.01} _{-0.01}	7.1 ^{+3.0} _{-2.3}	0.4 ^{+0.4} _{-0.2}	0.13 ^{+0.02} _{-0.01}	1.0*	3.2 ^{+0.5} _{-0.4}	0.50 ^{+0.11} _{-0.09}	0.31 ^{+0.03} _{-0.02}	1.20 ^{+0.06} _{-0.07}	100%	1057.1/1000		
Obs 1														

Table D.1: *continued* - Components for the baseline model (without broad or diskline emission) to the observations with *Suzaku* XIS, XRD and BAT data from *Swift*. *a* Unabsorbed POWERLAW normalisation given in units (10^{-2} ph keV $^{-1}$ cm $^{-2}$ s $^{-1}$). *b* Flux for COMP-TT quoted over the 0.6-10.0 keV range and REF-LIONX over the 2.0-100.0 keV range in units 10^{-11} erg cm $^{-2}$ s $^{-1}$. *c* Ionisation parameter given in units erg cm s $^{-1}$. *d* Column density measured in units 10^{22} cm $^{-2}$. *e* $v_{\text{turb}} = 1000$ km s $^{-1}$. *f* only the intrinsic powerlaw is absorbed. * indicates a frozen parameter. † indicates parameters are tied during the analysis of multiple observations.

Object	Powerlaw			COMP-TT			REF-LIONX			Warm absorber			
	Γ	Norm ^a	kT (keV)	τ	Flux ^b	Z _{Fe}	ξ^c	Flux ^b	N_{H}^d	$\log(\xi)^c$	C_{frac}	χ^2_{ν}	
Mrk 766 Obs 2	1.99†	< 0.05	7.1†	0.4†	0.15 $^{+0.02}_{-0.02}$	1.0†	3.2†	0.68 $^{+0.14}_{-0.12}$	2.41 $^{+0.10}_{-0.09}$	1.81 $^{+0.03}_{-0.03}$	100%		
Mrk 841 Obs 1,2	1.79 $^{+0.01}_{-0.01}$	0.36 $^{+0.01}_{-0.01}$	< 116.9	< 3.9	0.30 $^{+1.44}_{-0.23}$	0.8 $^{+0.2}_{-0.2}$	3.9 $^{+2.0}_{-1.4}$	1.43 $^{+0.86}_{-0.51}$	5.88 $^{+1.40}_{-0.98}$ 0.46 $^{+0.09}_{-0.10}$	2.94 $^{+0.05}_{-0.05}$ 2.17 $^{+0.10}_{-0.11}$	> 92% 100%	937.6/857	
NGC 1365 Obs 1	1.69 $^{+0.01}_{-0.01}$	0.03 $^{+0.01}_{-0.01}$	–	–	–	1.0*	24.3 $^{+1.0}_{-0.9}$	1.20 $^{+0.10}_{-0.09}$	2.71 $^{+0.69}_{-0.74}$	Neutral	96%		
NGC 1365 Obs 2	1.69†	0.02 $^{+0.01}_{-0.01}$	–	–	–	1.0†	24.3†	1.36 $^{+0.11}_{-0.10}$	29.57 $^{+3.35}_{-3.00}$ 36.79 $^{+1.98}_{-1.92}$	0.80 $^{+0.17}_{-0.16}$ Neutral	96%	2172.5/1979	
NGC 1365 Obs 3	1.69†	0.02 $^{+0.01}_{-0.01}$	–	–	–	1.0†	24.3†	1.43 $^{+0.06}_{-0.08}$	16.41 $^{+7.16}_{-6.72}$ 65.38 $^{+6.18}_{-3.33}$	2.16 $^{+0.18}_{-0.39}$ Neutral	95%		
NGC 2992 Obs 1, 2,3	1.58 $^{+0.01}_{-0.01}$	0.26 $^{+0.01}_{-0.01}$	< 16.6	0.76 $^{+0.04}_{-0.10}$	1.45 $^{+0.31}_{-1.14}$	1.0*	54.8 $^{+7.8}_{-8.3}$	1.59 $^{+0.29}_{-0.29}$	17.99 $^{+6.29}_{-15.77}$ 0.84 $^{+0.01}_{-0.01}$	< 1.90 Neutral	100%	1088.2/1079	
NGC 3147 NGC 3227 Obs 1	1.72 $^{+0.02}_{-0.03}$ 1.92 $^{+0.01}_{-0.01}$	0.04 $^{+0.01}_{-0.02}$ 1.11 $^{+0.02}_{-0.04}$	– 4.8 $^{+0.4}_{-0.4}$	– 1.2 $^{+0.1}_{-0.1}$	– 4.42 $^{+0.08}_{-0.08}$	1.0* 0.2 $^{+0.1}_{-0.1}$	49.3 $^{+23.4}_{-26.9}$ 2.3 $^{+0.1}_{-0.1}$	0.11 $^{+0.15}_{-0.06}$ 15.77 $^{+0.88}_{-0.89}$	– 3.37 $^{+0.11}_{-0.07}$	– 2.05 $^{+0.02}_{-0.01}$	– 100%	280.3/266	
NGC 3227 Obs 2	1.79†	0.13 $^{+0.01}_{-0.01}$	4.8†	1.2†	0.93 $^{+0.03}_{-0.03}$	0.2†	2.3†	13.274 $^{+0.37}_{-0.37}$	0.43 $^{+0.01}_{-0.01}$ 29.24 $^{+0.46}_{-0.46}$ 3.37†	Neutral 0.50 $^{+0.18}_{-0.27}$ 2.05†	100% 32% 100%	4585.7/4198	
									0.43† 29.24†	Neutral 1.53 $^{+0.09}_{-0.10}$	100% 81%		

Table D.1: *continued* - Components for the baseline model (without broad or diskline emission) to the observations with *Suzaku* XIS, HXD and BAT data from *Swift*. ^a Unabsorbed POWERLAW normalisation given in units (10^{-2} ph keV $^{-1}$ cm $^{-2}$ s $^{-1}$). ^b Flux for COMP TT quoted over the 0.6-10.0 keV range and REFLIONX over the 2.0-100.0 keV range in units 10^{-11} erg cm $^{-2}$ s $^{-1}$. ^c Ionisation parameter given in units erg cm s $^{-1}$. ^d Column density measured in units 10^{22} cm $^{-2}$. ^e $v_{\text{turb}} = 1000$ km s $^{-1}$. ^f only the intrinsic powerlaw is absorbed. * indicates a frozen parameter. † indicates parameters are tied during the analysis of multiple observations.

Object	Powerlaw			COMP TT			REFLIONX			Warm absorber			χ^2_{ν}
	Γ	Norm ^e	kT (keV)	τ	Flux ^b	Z_{Fe}	ξ^c	Flux ^b	N_{H}^d	$\log(\xi)^c$	C_{frac}		
NGC 3227 Obs 3	1.79†	0.25 ^{+0.01} _{-0.01}	4.8†	1.2†	0.76 ^{+0.03} _{-0.03}	0.2†	2.3†	13.17 ^{+0.39} _{-0.39}	3.37†	2.05†	100%		
NGC 3227 Obs 4	1.79†	0.07 ^{+0.01} _{-0.01}	4.8†	1.2†	0.91 ^{+0.02} _{-0.02}	0.2†	2.3†	8.13 ^{+0.22} _{-0.22}	0.43† 29.24† 3.37†	Neutral 0.50 ^{+0.03} _{-0.13} 2.05†	100% 81% 100%		
NGC 3227 Obs 5	1.79†	0.13 ^{+0.01} _{-0.01}	4.8†	1.2†	0.79 ^{+0.02} _{-0.02}	0.2†	2.3†	11.79 ^{+0.48} _{-0.48}	0.43† 29.24† 3.37†	Neutral 1.50 ^{+0.12} _{-0.13} 2.05†	100% 75% 100%		
NGC 3227 Obs 6	1.79†	0.10 ^{+0.01} _{-0.01}	4.8†	1.2†	0.64 ^{+0.02} _{-0.02}	0.2†	2.3†	9.46 ^{+0.47} _{-0.46}	0.43† 29.24† 3.37†	Neutral 0.70 ^{+0.05} _{-0.05} 2.05†	100% 89% 100%		
NGC 3516 Obs 1	1.68 ^{+0.01} _{-0.01}	0.15 ^{+0.01} _{-0.01}	-	-	-	1.0*	6.3 ^{+0.3} _{-0.3}	3.50 ^{+0.22} _{-0.20}	0.43† 29.24† 13.40 ^{+9.06} _{-6.40}	Neutral 1.41 ^{+0.12} _{-0.23} 3.55 ^{+0.22} _{-0.10}	100% 89% 100%		
NGC 3516 Obs 2	1.68†	0.29 ^{+0.01} _{-0.01}	-	-	-	1.0†	6.3†	1.96 ^{+0.12} _{-0.12}	2.76 ^{+0.30} _{-0.17} 0.12 ^{+0.02} _{-0.01} 24.83 ^{+1.74} _{-1.69} 0.35 ^{+0.09} _{-0.06}	1.93 ^{+0.09} _{-0.06} Neutral 0.60 ^{+0.08} _{-0.09} 1.02 ^{+0.12} _{-0.13}	100% 100% 83% 100%	1263.2/1126	
									1.54 ^{+0.10} _{-0.26} 0.08 ^{+0.02} _{-0.02} 69.18 ^{+25.66} _{-24.57}	2.20 ^{+0.05} _{-0.06} Neutral 2.80 ^{+0.10} _{-0.10}	100% 100% 18%		

Table D.1: *continued* - Components for the baseline model (without broad or diskline emission) to the observations with *Suzaku* XIS, HXD and BAT data from *Swift*. *a* Unabsorbed POWERLAW normalisation given in units (10^{-2} ph keV $^{-1}$ cm $^{-2}$ s $^{-1}$). *b* Flux for COMP-TT quoted over the 0.6-10.0 keV range and REFLIONX over the 2.0-100.0 keV range in units 10^{-11} erg cm $^{-2}$ s $^{-1}$. *c* Ionisation parameter given in units erg cm s $^{-1}$. *d* Column density measured in units 10^{22} cm $^{-2}$. *e* $v_{\text{turb}} = 1000$ km s $^{-1}$. *f* only the intrinsic powerlaw is absorbed. * indicates a frozen parameter. † indicates parameters are tied during the analysis of multiple observations.

Object	Powerlaw			COMP-TT			REFLIONX			Warm absorber				χ^2_{ν}
	Γ	Norm ^a	kT (keV)	τ	Flux ^b	Z_{Fe}	ξ^c	Flux ^b	N_{H}^d	$\log(\xi)^c$	C_{frac}			
NGC 3783 Obs 1	$1.79^{+0.01}_{-0.01}$	$1.30^{+0.01}_{-0.01}$	$7.4^{+0.5}_{-0.4}$	$1.1^{+0.1}_{-0.1}$	$0.78^{+0.02}_{-0.02}$	$0.9^{+0.1}_{-0.1}$	$4.4^{+0.1}_{-0.1}$	$7.99^{+0.26}_{-0.26}$	$0.16^{+0.02}_{-0.02}$	$0.27^{+0.14}_{-0.09}$	100%		2554.2/2305	
NGC 3783 Obs 2	1.79†	$1.73^{+0.01}_{-0.01}$	7.4†	1.1†	$2.58^{+0.08}_{-0.08}$	0.9†	4.4†	$8.26^{+0.27}_{-0.26}$	$3.02^{+0.07}_{-0.08}$ $0.27^{+0.03}_{-0.03}$	$2.05^{+0.01}_{-0.01}$ $0.83^{+0.05}_{-0.06}$	100%			
NGC 4051 Obs 1	$1.88^{+0.01}_{-0.01}$	$0.10^{+0.01}_{-0.01}$	$6.9^{+0.2}_{-0.2}$	$1.5^{+0.1}_{-0.1}$	$0.13^{+0.01}_{-0.01}$	$0.9^{+0.1}_{-0.1}$	$9.6^{+0.4}_{-0.5}$	$1.07^{+0.07}_{-0.06}$	$3.81^{+0.08}_{-0.08}$ $0.29^{+0.06}_{-0.05}$	$2.09^{+0.01}_{-0.01}$ $2.97^{+0.05}_{-0.04}$	100%			
NGC 4051 Obs 2	1.88†	$0.61^{+0.01}_{-0.01}$	6.9†	1.5†	$1.56^{+0.02}_{-0.02}$	0.9†	9.6†	$8.96^{+0.47}_{-0.26}$ $1.54^{+0.10}_{-0.08}$	$0.31^{+0.01}_{-0.01}$ $1.95^{+0.03}_{-0.03}$ 0.29†	$1.85^{+0.01}_{-0.01}$ 67%	100%		3204.7/2944	
NGC 4051 Obs 3	1.88†	$0.39^{+0.01}_{-0.01}$	6.9†	1.5†	$1.06^{+0.01}_{-0.01}$	0.9†	9.6†	$1.40^{+0.12}_{-0.13}$	0.31† 8.96† 0.29†	1.85† 1.95† 2.97†	100% 11% 100%			
NGC 4151	$1.56^{+0.01}_{-0.01}$	$0.27^{+0.01}_{-0.01}$	$3.4^{+0.1}_{-0.1}$	$10.6^{+0.2}_{-0.2}$	$3.63^{+0.07}_{-0.07}$	1.0*	$43.6^{+7.1}_{-9.9}$	$12.63^{+3.01}_{-1.48}$	$0.09^{+0.02}_{-0.01}$ $14.45^{+0.19}_{-0.18}$ $45.82^{+3.58}_{-7.78}$	< 0.12 $2.16^{+0.01}_{-0.01}$ $0.52^{+0.26}_{-0.16}$	100% 100% 58%		647.1/583	
NGC 4593	$1.60^{+0.01}_{-0.01}$	$0.21^{+0.01}_{-0.01}$	–	–	–	1.0*	$5.4^{+14.7}_{-5.4}$	$0.61^{+3.24}_{-0.46}$	$0.53^{+0.09}_{-0.10}$	$2.19^{+0.11}_{-0.11}$	100%		293.62/289	

Table D.1: *continued* - Components for the baseline model (without broad or diskline emission) to the observations with *Suzaku* XIS, HXD and BAT data from *Swift*. ^a Unabsorbed POWERLAW normalisation given in units (10^{-2} ph keV $^{-1}$ cm $^{-2}$ s $^{-1}$). ^b Flux for COMP TT quoted over the 0.6-10.0 keV range and REFLIONX over the 2.0-100.0 keV range in units 10^{-11} erg cm $^{-2}$ s $^{-1}$. ^c Ionisation parameter given in units erg cm s $^{-1}$. ^d Column density measured in units 10^{22} cm $^{-2}$. ^e $v_{\text{turb}} = 1000$ km s $^{-1}$. ^f only the intrinsic powerlaw is absorbed. * indicates a frozen parameter. † indicates parameters are tied during the analysis of multiple observations.

Object	Powerlaw		COMP TT		REFLIONX		Warm absorber				χ^2_{ν}	
	Γ	Norm ^e	kT (keV)	τ	Flux ^b	Z_{Fe}	ξ^c	Flux ^b	N_{H}^d	$\log(\xi)^c$		C_{frac}
NGC 5506 Obs 1,2	$2.08^{+0.01}_{-0.01}$	$5.58^{+0.02}_{-0.02}$	—	—	—	$0.5^{+0.1}_{-0.1}$	$10.5^{+0.2}_{-0.2}$	$9.69^{+0.35}_{-0.34}$	$2.23^{+0.35}_{-0.45}$	< 0.05	100%	
NGC 5506 Obs 3	2.08^{\dagger}	$5.36^{+0.02}_{-0.02}$	—	—	—	0.5^{\dagger}	10.5^{\dagger}	$8.48^{+0.31}_{-0.31}$	$3.26^{+0.31}_{-0.33}$ $1.51^{+0.02e}_{-0.02}$ $449.0^{+40.0}_{-36.0}$ 2.23^{\dagger}	$0.59^{+0.10}_{-0.06}$ $1.30^{+0.02}_{-0.02}$ < 1.20 0.05^{\dagger}	100% 100% 19% 100%	3189.6/2872
NGC 5548 Obs 1,2, 3,4,5,6,7	$1.70^{+0.01}_{-0.01}$	$0.44^{+0.01}_{-0.01}$	—	—	—	$1.0^{+0.1}_{-0.1}$	< 2.2	$2.12^{+1.27}_{-0.75}$	$0.59^{+0.09}_{-0.13}$	$2.28^{+0.07}_{-0.08}$	100%	1772.0/1734
NGC 7213	$1.74^{+0.01}_{-0.01}$	$0.61^{+0.01}_{-0.01}$	< 61.8	$2.1^{+0.5}_{-1.6}$	$0.03^{+0.08}_{-0.02}$	1.0^*	$29.6^{+26.9}_{-16.9}$	$0.33^{+0.63}_{-0.20}$	$0.26^{+0.06}_{-0.03}$	$0.98^{+0.14}_{-0.08}$	100%	703.5/707
NGC 7314	$1.68^{+0.01}_{-0.01}$	$0.22^{+0.01}_{-0.01}$	< 15.8	< 0.8	$0.34^{+1.03}_{-0.26}$	—	—	—	$0.74^{+0.02}_{-0.02}$	Neutral	100%	592.3/545
NGC 7469	$1.78^{+0.07}_{-0.10}$	$0.57^{+0.04}_{-0.06}$	< 8.4	$0.8^{+0.2}_{-0.5}$	$0.22^{+0.03}_{-0.03}$	$1.6^{+0.3}_{-0.3}$	< 11.0	$1.69^{+0.14}_{-0.29}$	—	—	—	840.2/812
PDS 456	$2.41^{+0.03}_{-0.03}$	$0.23^{+0.01}_{-0.01}$	< 33.4	$1.4^{+0.6}_{-1.1}$	< 0.204	—	—	—	421.40 $3.82^{+1.90}_{-1.09}$ $3.05^{+0.35}_{-0.67}$	$3.16^{+0.19}_{-0.08}$ Neutral $2.85^{+0.06}_{-0.08}$	50% 50% 100%	146.9/132 813.62/702
PG 1211+143	$1.82^{+0.01}_{-0.01}$	$0.12^{0.01}_{-0.01}$	< 18.3	$0.8^{+0.3}_{-0.7}$	< 0.11	—	—	—	—	—	—	—
RBS 1124	$1.71^{+0.01}_{-0.01}$	$0.12^{+0.01}_{-0.01}$	< 52.9	$0.8^{+11.3}_{-0.4}$	< 0.19	$0.7^{+0.5}_{-0.3}$	< 15.1	$0.32^{+4.34}_{-0.21}$	—	—	—	386.8/364
SWIFT J2127.4+5654	$2.11^{+0.03}_{-0.02}$	$1.52^{+0.04}_{-0.05}$	—	—	—	$0.5^{+0.1}_{-0.1}$	< 13.0	$2.28^{+0.37}_{-1.11}$	$0.08^{+0.02}_{-0.02}$	Neutral	100%	871.6/867
TON S180	$2.14^{+0.02}_{-0.01}$	$0.23^{+0.01}_{-0.01}$	$6.3^{+54.9}_{-4.1}$	$1.2^{+1.8}_{-1.2}$	< 1.14	$2.4^{+0.8}_{-0.5}$	$269.6^{+65.0}_{-30.5}$	$0.10^{+0.03}_{-0.03}$	$0.02^{+0.01}_{-0.01}$	$1.44^{+0.34}_{-1.06}$ $1.99^{+0.54}_{-0.74}$	100% 60%	750.0/692

Table D.2: Fe K region properties - distant emission lines and ionized absorption zones in the baseline model. Absorption zones are typically modelled with an XSTAR grid with $v_{\text{turb}} = 1000 \text{ km s}^{-1}$. ^a $v_{\text{turb}} = 3000 \text{ km s}^{-1}$. Line flux given in units $10^{-5} \text{ erg cm}^{-2} \text{ s}^{-1}$. Column density given in units 10^{22} cm^{-2} . † indicates that parameters are tied in multiple observations. * denotes a frozen parameter. Note that a negative $\Delta\chi^2$ denotes an improvement in the fit.

Object	Emission lines			High ξ zone				
	LineE	EW (eV)	Flux	$\Delta\chi^2$	N_{H}	$\log\xi$	$v_{\text{out}} (\text{km s}^{-1})$	$\Delta\chi^2$
3C 111	$6.50^{+0.06}_{-0.05}$	19^{+23}_{-11}	$0.53^{+0.62}_{-0.30}$	-9	> 3.60	$4.40^{+1.11}_{-0.37}$	84600^{+42600}_{-42400}	-28
	$6.78^{+0.11}_{-0.08}$	11^{+8}_{-8}	$0.27^{+0.21}_{-0.21}$	-5				
3C 120	$6.76^{+0.07}_{-0.07}$	8^{+4}_{-4}	$0.42^{+0.21}_{-0.20}$	-12				
3C 445	$6.68^{+0.07}_{-0.10}$	17^{+402}_{-9}	$0.29^{+6.74}_{-0.15}$	-6	> 22.88	$4.95^{+0.05}_{-0.60}$	4000^{+600}_{-500}	-8
4C 74.26	$6.68^{+0.09}_{-0.08}$	10^{+7}_{-7}	$0.43^{+0.31}_{-0.31}$	-5				
Ark 120	$6.66^{+0.04}_{-0.05}$	20^{+7}_{-7}	$0.72^{+0.25}_{-0.25}$	-20				
	$6.95^{+0.03}_{-0.03}$	31^{+9}_{-9}	$0.92^{+0.27}_{-0.27}$	-31				
Ark 564	6.63^*	20^{+16}_{-13}	$0.31^{+0.25}_{-0.20}$	-7				
Fairall 9	$6.71^{+0.03}_{-0.02}$	20^{+5}_{-6}	$0.58^{+0.15}_{-0.17}$	-32				
	$6.96^{+0.03}_{-0.03}$	20^{+6}_{-6}	$0.48^{+0.13}_{-0.15}$	-25				
IC 4329A	$6.95^{+0.05}_{-0.06}$	9^{+5}_{-5}	$0.93^{+0.53}_{-0.51}$	-9				
IRAS 13224-3809	$6.72^{+0.06}_{-0.06}$	101^{+67}_{-67}	$0.06^{+0.04}_{-0.04}$	-6				
MCG-02-14-009	$6.94^{+0.05}_{-0.11}$	39^{+24}_{-23}	$0.16^{+0.10}_{-0.10}$	-7				
MCG-5-23-16	$6.40^{+0.01}_{-0.01}$	54^{+7}_{-6}	$6.02^{+0.73}_{-0.68}$	-82				
MCG-6-30-15	6.97^*	10^{+4}_{-4}	$0.41^{+0.18}_{-0.18}$	-7	$3.99^{+3.65}_{-1.28}$	$3.94^{+0.08}_{-0.25}$	3200^{+400}_{-500}	-298
MCG+8-11-11	$6.93^{+0.03}_{-0.03}$	21^{+6}_{-6}	$1.39^{+0.40}_{-0.40}$	-17				
MR 2251-178	$6.48^{+0.06}_{-0.06}$	12^{+9}_{-9}	$0.66^{+0.47}_{-0.50}$	-4	$0.29^{+0.31}_{-0.09}$	$3.12^{+0.23}_{-0.08}$	33600^{+7000}_{-7700}	-39
Mrk 79	$6.39^{+0.01}_{-0.01}$	110^{+15}_{-15}	$2.05^{+0.28}_{-0.28}$	-45				
	$6.60^{+0.05}_{-0.06}$	26^{+14}_{-13}	$0.51^{+0.27}_{-0.25}$	-11				
	$6.98^{+0.06}_{-0.07}$	20^{+17}_{-17}	$0.30^{+0.25}_{-0.25}$	-5				
Mrk 110	$6.66^{+0.12}_{-0.11}$	11^{+10}_{-10}	$0.26^{+0.25}_{-0.24}$	-4				

Table D.2: *continued* - Fe K region properties - distant emission lines and ionized absorption zones in the baseline model. Absorption zones are typically modelled with an XSTAR grid with $v_{\text{turb}} = 1000 \text{ km s}^{-1}$. ^a $v_{\text{turb}} = 3000 \text{ km s}^{-1}$. Line flux given in units $10^{-5} \text{ erg cm}^{-2} \text{ s}^{-1}$. Column density given in units 10^{22} cm^{-2} . † indicates that parameters are tied in multiple observations. * denotes a frozen parameter. Note that a negative $\Delta\chi^2$ denotes an improvement in the fit.

Object	Emission lines			High ξ zone				
	LineE	EW (eV)	Flux	$\Delta\chi^2$	N_{H}	$\log\xi$	v_{out} (km s^{-1})	$\Delta\chi^2$
Mrk 335	$6.68^{+0.03}_{-0.05}$	40^{+8}_{-8}	$0.64^{+0.13}_{-0.13}$	-67	-	-	-	-
	$6.96^{+0.06}_{-0.16}$	21^{+9}_{-9}	$0.28^{+0.12}_{-0.12}$	-14	-	-	-	-
Mrk 359	$6.74^{+0.05}_{-0.04}$	32^{+18}_{-19}	$0.19^{+0.11}_{-0.11}$	-6	-	-	-	-
	$6.43^{+0.03}_{-0.02}$	23^{+17}_{-11}	$1.29^{+0.98}_{-0.51}$	-9	-	-	-	-
Mrk 509	$6.67^{+0.08}_{-0.10}$	8^{+12}_{-6}	$0.45^{+0.71}_{-0.37}$	-4	-	-	-	-
	$6.64^{+0.04}_{-0.05}$	27^{+10}_{-10}	$0.37^{+0.14}_{-0.14}$	-28	> 3.90	$5.44^{+0.41}_{-1.16}$	5200^{+2900}_{-2900}	-108
Mrk 766	6.64^{\dagger}	27^{\dagger}	0.37^{\dagger}	-	$7.83^{+3.54}_{-2.61}$	$3.68^{+0.08}_{-0.11}$	5200^{\dagger}	-
Mrk 841	$6.69^{+0.06}_{-0.06}$	19^{+12}_{-13}	$0.32^{+0.20}_{-0.22}$	-5	-	-	-	-
NGC 1365	$6.64^{+0.01}_{-0.01}$	26^{+5}_{-5}	$0.71^{+0.14}_{-0.15}$	-11	$11.07^{+5.93^a}_{-2.19}$	$3.74^{+0.07}_{-0.06}$	< 300	-2052
	$6.89^{+0.01}_{-0.01}$	28^{+6}_{-5}	$0.41^{+0.09}_{-0.08}$	-32	$52.84^{+7.43^a}_{-13.95}$	$3.96^{+0.02}_{-0.04}$	4900^{+400}_{-500}	-
NGC 1365	6.64^{\dagger}	24^{+5}_{-5}	0.71^{\dagger}	-	$41.53^{+17.64^a}_{-11.58}$	$4.00^{+0.21}_{-0.03}$	$< 300^{\dagger}$	-
	6.89^{\dagger}	41^{+9}_{-8}	0.41^{\dagger}	-	$< 6.72^a$	$3.46^{+0.02}_{-0.02}$	< 500	-
NGC 1365	6.64^{\dagger}	37^{+7}_{-8}	0.71^{\dagger}	-	$< 190.40^a$	> 4.11	$< 300^{\dagger}$	-
	6.89^{\dagger}	42^{+9}_{-8}	0.41^{\dagger}	-	$5.98^{+0.49^a}_{-0.48}$	$3.41^{+0.02}_{-0.02}$	< 200	-
NGC 2992	$6.40^{+0.01}_{-0.01}$	154^{+18}_{-18}	$2.60^{+0.30}_{-0.30}$	-23	-	-	-	-
NGC 3147	$6.97^{+0.05}_{-0.06}$	84^{+43}_{-54}	$0.13^{+0.07}_{-0.08}$	-6	-	-	-	-

Table D.2: *continued* - Fe K region properties - distant emission lines and ionized absorption zones in the baseline model. Absorption zones are typically modelled with an XSTAR grid with $v_{\text{turb}} = 1000 \text{ km s}^{-1}$.^a $v_{\text{turb}} = 3000 \text{ km s}^{-1}$. Line flux given in units $10^{-5} \text{ erg cm}^{-2} \text{ s}^{-1}$. Column density given in units 10^{22} cm^{-2} . † indicates that parameters are tied in multiple observations. * denotes a frozen parameter. Note that a negative $\Delta\chi^2$ denotes an improvement in the fit.

Object	Emission lines			High ξ zone				
	LineE	EW (eV)	Flux	$\Delta\chi^2$	N_{H}	$\log\xi$	v_{out} (km s^{-1})	$\Delta\chi^2$
NGC 3227	$6.40^{+0.01}_{-0.01}$	59^{+3}_{-4}	$2.98^{+0.17}_{-0.19}$	-80	$20.88^{+2.48}_{-3.04}$	$4.35^{+0.06}_{-0.08}$	< 2100	-67
	$6.83^{+0.01}_{-0.01}$	28^{+3}_{-3}	$1.20^{+0.13}_{-0.13}$	-25				
NGC 3227	6.40^\dagger	107^{+6}_{-7}	2.98^\dagger	-	20.88^\dagger	4.35^\dagger	$< 2100^\dagger$	
NGC 3227	6.83^\dagger	56^{+6}_{-6}	1.20^\dagger	-				
	6.40^\dagger	75^{+4}_{-5}	2.98^\dagger	-	20.88^\dagger	4.35^\dagger	$< 2100^\dagger$	
NGC 3227	6.83^\dagger	37^{+4}_{-4}	1.20^\dagger	-				
	6.40^\dagger	168^{+9}_{-10}	2.98^\dagger	-	20.88^\dagger	4.35^\dagger	$< 2100^\dagger$	
NGC 3227	6.83^\dagger	95^{+11}_{-10}	1.20^\dagger	-				
	6.40^\dagger	85^{+5}_{-5}	2.98^\dagger	-	20.88^\dagger	4.35^\dagger	$< 2100^\dagger$	
NGC 3227	6.83^\dagger	42^{+5}_{-5}	1.20^\dagger	-				
	6.40^\dagger	109^{+6}_{-7}	2.98^\dagger	-	20.88^\dagger	4.35^\dagger	$< 2100^\dagger$	
NGC 3516	6.83^\dagger	56^{+6}_{-6}	1.20^\dagger	-				
	$6.42^{+0.01}_{-0.01}$	51^{+4}_{-4}	$2.19^{+0.18}_{-0.18}$	-15	$2.12^{+1.24}_{-0.95}$	$3.87^{+0.18}_{-0.14}$	< 4500	-23
NGC 3516	$6.69^{+0.03}_{-0.04}$	8^{+3}_{-3}	$0.39^{+0.14}_{-0.13}$	-8				
	6.42^\dagger	108^{+9}_{-9}	2.19^\dagger	-	$2.33^{+2.79}_{-0.82}$	$3.80^{+0.25}_{-0.12}$	< 9600	
NGC 3783	6.69^\dagger	19^{+7}_{-6}	0.9^\dagger	-				
	$6.96^{+0.01}_{-0.02}$	30^{+7}_{-8}	$2.37^{+0.58}_{-0.64}$	-21	$5.46^{+21.31}_{-2.02}$	$4.22^{+0.66}_{-0.19}$	< 400	-50
NGC 4051	6.96^\dagger	26^{+7}_{-7}	2.37^\dagger	-	$2.40^{+0.75}_{-0.58}$	$3.87^{+0.11}_{-0.11}$	$< 400^\dagger$	
	$6.43^{+0.03}_{-0.02}$	42^{+2}_{-2}	$0.53^{+0.03}_{-0.03}$	-5	$1.17^{+0.27}_{-0.26}$	$3.68^{+0.05}_{-0.05}$	5800^{+1400}_{-1300}	-51
NGC 4051	$6.62^{+0.03}_{-0.04}$	21^{+9}_{-9}	$0.26^{+0.11}_{-0.11}$	-3				
	6.43^\dagger	19^{+1}_{-1}	0.53^\dagger	-5	1.17^\dagger	3.68^\dagger	5800^\dagger	
NGC 4051	6.62^\dagger	10^{+4}_{-4}	0.26^\dagger	-3				
	6.43^\dagger	25^{+1}_{-1}	0.53^\dagger	-5	1.17^\dagger	3.68^\dagger	5800^\dagger	
NGC 4051	6.62^\dagger	12^{+5}_{-5}	0.26^\dagger	-3				

Table D.2: *continued* - Fe K region properties - distant emission lines and ionized absorption zones in the baseline model. Absorption zones are typically modelled with an XSTAR grid with $v_{\text{turb}} = 1000 \text{ km s}^{-1}$. ^a $v_{\text{turb}} = 3000 \text{ km s}^{-1}$. Line flux given in units $10^{-5} \text{ erg cm}^{-2} \text{ s}^{-1}$. Column density given in units 10^{22} cm^{-2} . † indicates that parameters are tied in multiple observations. * denotes a frozen parameter. Note that a negative $\Delta\chi^2$ denotes an improvement in the fit.

Object	Emission lines			High ξ zone				
	LineE	EW (eV)	Flux	$\Delta\chi^2$	N_{H}	$\log\xi$	$v_{\text{out}} (\text{km s}^{-1})$	$\Delta\chi^2$
NGC 4151	$6.38^{+0.01}_{-0.01}$	91^{+6}_{-6}	$8.79^{+0.56}_{-0.56}$	-193	$2.58^{+41.80}_{-2.53}$ $145.27^{+66.56}_{-107.01}$	> 3.57 > 4.41	12800^{+1800}_{-4800} 12800^\dagger	-164
NGC 4593	$6.42^{+0.01}_{-0.01}$ $6.71^{+0.13}_{-0.09}$	173^{+21}_{-21} 20^{+10}_{-10}	$2.23^{+0.27}_{-0.28}$ $0.29^{+0.14}_{-0.14}$	-24 -8	-	-	-	-
NGC 5506	6.63^*	< 25	< 1.10	-15	-	-	-	-
NGC 5506	$6.98^{+0.06}_{-0.10}$ 6.63^*	10^{+11}_{-8} $< 25^\dagger$	$0.88^{+0.97}_{-0.68}$ $< 1.10^\dagger$	-36	-	-	-	-
NGC 5548	6.98^\dagger	10^\dagger	0.88^\dagger	-	-	-	-	-
NGC 7213	- $6.39^{+0.01}_{-0.01}$ $6.61^{+0.04}_{-0.35}$ $6.96^{+0.13}_{-0.02}$ $6.38^{+0.02}_{-0.02}$	67^{+10}_{-11} < 27 31^{+15}_{-20} 116^{+16}_{-16}	$1.78^{+0.27}_{-0.28}$ < 0.75 $0.71^{+0.34}_{-0.45}$ $1.15^{+0.16}_{-0.16}$	-45 -31 -31 -131	$0.88^{+0.74}_{-0.54}$	$3.73^{+0.23}_{-0.29}$	< 1700	-12
NGC 7314	$6.98^{+0.05}_{-0.06}$ $6.75^{+0.06}_{-0.07}$	38^{+17}_{-17} 25^{+17}_{-19}	$0.33^{+0.15}_{-0.15}$ $0.12^{+0.08}_{-0.09}$	-12 -5	-	-	-	-
PDS 456	$7.00^{+0.48}_{-0.13}$	19^{+19}_{-17}	$0.09^{+0.09}_{-0.08}$	-4	> 6.31	$4.98^{+0.35}_{-0.90}$	82200^{+5500}_{-5500}	-27
PG 1211+143	$6.40^{+0.10}_{-0.09}$ $6.75^{+0.07}_{-0.07}$	22^{+16}_{-16} 44^{+34}_{-21}	$0.14^{+0.10}_{-0.10}$ $0.24^{+0.18}_{-0.11}$	-4 -3	$0.22^{+0.19}_{-0.14}$ $7.13^{+14.22}_{-3.04}$	$3.03^{+0.14}_{-0.33}$ $3.79^{+0.29}_{-0.09}$	< 163200 18800^{+4800}_{-5300}	-30
SWIFT J2127.4+5654	$6.66^{+0.07}_{-0.05}$ $6.98^{+0.09}_{-0.26}$	25^{+11}_{-11} 16^{+13}_{-13}	$0.94^{+0.41}_{-0.40}$ $0.49^{+0.40}_{-0.40}$	-16 -4	-	-	-	-

Table D.3: Components for the dual reflector fit to the observations with *Suzaku* XIS, HXD and BAT data from *Swift*. COMP TT and warm absorber parameters are consistent with those in the baseline model. The inner blurred reflector properties are quote here, some of which are tied to the out unblurred REFLECTION. Fits include partial covering geometries where required as per the baseline model. Where a reasonable fit can also be obtained without the use of a partial coverer, both scenarios are tabulated, for those without partial covering the change in χ^2 is quoted with respect to the dual reflector plus partial covering fit. Note that in some objects accretion disc parameters cannot be constrained, denoted by $-$. a Ionisation parameter given in units erg cm s^{-1} . * Denotes a frozen parameter. † $\Delta\chi^2$ in relation to the dual reflector fit without partial covering (which for these objects has not been tabulated) compared to the fit with partial covering tabulated here. b Best-fit parameters to the 2009 NGC 3783 *Suzaku* data only for the Solar abundance model presented in Section 5.4.5.

Object	Γ	Z_{Fe}	ξ^a	q	a	i°	$\Delta\chi^2$	χ^2_{ν}
3C 111	$1.60^{+0.02}_{-0.03}$	$0.8^{+2.4}_{-0.5}$	< 102	< 2.69	$-$	$-$		1087.8/1092
3C 120	$1.62^{+0.01}_{-0.01}$	1.0^*	19^{+1}_{-1}	$1.7^{+0.3}_{-0.4}$	$-$	18^{+2}_{-1}		3564.8/3448
3C 382	$1.79^{+0.03}_{-0.02}$	1.0^*	< 1.4	< 3	$-$	30^{+31}_{-6}		972.3/933
3C 390.3	$1.72^{+0.01}_{-0.01}$	1.4	< 2	$1.8^{+1.0}_{-0.5}$	$-$	39^{+20}_{-7}		1478.7/1482
Ark 120	$1.98^{+0.04}_{-0.04}$	$2.2^{+0.1}_{-0.6}$	< 21	$2.2^{+0.1}_{-0.6}$	$-$	45^{+6}_{-5}		715.5/644
Fairall 9	$1.91^{+0.01}_{-0.01}$	$1.7^{+0.1}_{-0.1}$	3^{+1}_{-1}	$2.7^{+0.6}_{-0.5}$	< 0.95	42^{+3}_{-2}		3558.3/3271
IC 4329A	$1.93^{+0.02}_{-0.01}$	$0.8^{+0.1}_{-0.1}$	7^{+2}_{-1}	2.4^*	< 0.73	36^*		2342.8/2199
MCG-02-14-009	$1.90^{+0.02}_{-0.02}$	$0.7^{+0.5}_{-0.3}$	< 13	< 2.0	$-$	> 29		601.5/539
MCG-05-23-16	$1.84^{+0.01}_{-0.02}$	1.0^*	< 1.0	$1.6^{+0.5}_{-0.7}$	$-$	24^*		1989.5/1890
MCG-06-30-15 (p/c)	$2.05^{+0.01}_{-0.01}$	1.0^*	< 11	$2.3^{+0.2}_{-0.1}$	$0.61^{+0.15}_{-0.17}$	35^{+2}_{-2}		2061.4/1823
MCG-06-30-15 (no p/c)	$2.09^{+0.01}_{-0.01}$	1.0^*	< 10	$2.9^{+0.2}_{-0.1}$	$-$	36^{+1}_{-1}	-41	2020.2/1823
MCG+8-11-11	$1.82^{+0.01}_{-0.02}$	1.0^*	7^{+3}_{-2}	1.9^*	$-$	$-$		1034.0/933
MR 2251-178	$1.54^{+0.06}_{-0.10}$	1.0^*	$-$	3.0^*	$-$	$-$		969.0/897
Mrk 79	$1.61^{+0.02}_{-0.02}$	1.0^*	984^{+319}_{-396}	3.0^*	< -0.25	< 25		573.2/542
Mrk 335	$2.04^{+0.02}_{-0.03}$	$2.5^{+1.1}_{-0.6}$	25^{+7}_{-3}	$2.0^{+0.2}_{-0.3}$	$-$	50^{+9}_{-13}		820.0/721
Mrk 509	$1.69^{+0.03}_{-0.05}$	1.0^*	23^{+2}_{-4}	$1.5^{+0.8}_{-1.3}$	$-$	35^*		1959.4/1867
Mrk 766 (p/c)	$1.99^{+0.01}_{-0.01}$	1.0^*	3^{+1}_{-1}	$-$	$-$	$-$		1055.1/995
Mrk 766 (no p/c)	$2.01^{+0.01}_{-0.01}$	1.0^*	4^{+1}_{-1}	3.0^*	$-$	80^{+2}_{-3}	+54	1109.6/1002
Mrk 841	$1.96^{+0.05}_{-0.04}$	$1.0^{+0.3}_{-0.2}$	< 2	$2.7^{+0.3}_{-0.2}$	> -0.40	$-$		910.8/853
NGC 1365	$1.69^{+0.01}_{-0.01}$	1.0^*	25^{+1}_{-1}	3.0^*	> 0.70	83^{+7}_{-4}	+7995†	2157.0/1974

Table D.3: *continued* - Components for the dual reflector fit to the observations with *Suzaku* XIS, HXD and BAT data from *Swift*. COMPTT and warm absorber parameters are consistent with those in the baseline model. The inner blurred reflector properties are quote here, some of which are tied to the out unblurred REFLLIONX. Fits include partial covering geometries where required as per the baseline model. Where a reasonable fit can also be obtained without the use of a partial coverer, both scenarios are tabulated, for those without partial covering the change in χ^2 is quoted with respect to the dual reflector plus partial covering fit. Note that in some objects accretion disc parameters cannot be constrained, denoted by -. ^a Ionisation parameter given in units erg cm s^{-1} . * Denotes a frozen parameter. † $\Delta\chi^2$ in relation to the dual reflector fit without partial covering (which for these objects has not been tabulated) compared to the fit with partial covering tabulated here. ^b Best-fit parameters to the 2009 NGC 3783 *Suzaku* data only for the Solar abundance model presented in Section 5.4.5.

Object	Γ	Z_{Fe}	ξ^a	q	a	i°	$\Delta\chi^2$	χ^2_ν
NGC 2992	$1.60^{+0.04}_{-0.05}$	1.0^*	59^{+16}_{-14}	< 1.8	-	-		1082.3/1076
NGC 3227	$1.80^{+0.01}_{-0.01}$	$0.4^{+0.1}_{-0.1}$	6^{+1}_{-1}	$2.5^{+0.3}_{-0.3}$	< -0.35	47^{+3}_{-2}	+433†	4373.9/4075
NGC 3516	$1.70^{+0.01}_{-0.01}$	1.0^*	6^{+1}_{-1}	$2.6^{+0.1}_{-0.3}$	< -0.50	-	+814†	1228.6/1121
NGC 3783	$1.79^{+0.01}_{-0.01}$	$1.1^{+0.1}_{-0.1}$	4^{+1}_{-1}	$3.9^{+1.4}_{-0.6}$	< -0.35	19^{+4}_{-7}		2502.6/2300
NGC 3783 ^b	$1.84^{+0.05}_{-0.01}$	1.0 ± 0.2	< 11	$3.0^{+0.5}_{-0.5}$	< 0.45	< 13		1413.7/1374
NGC 4051 (p/c)	$1.89^{+0.01}_{-0.01}$	$1.1^{+0.2}_{-0.1}$	18^{+2}_{-3}	3.0^*	-	-		3177.1/2939
NGC 4051 (no p/c)	$1.93^{+0.01}_{-0.01}$	$0.8^{+0.1}_{-0.1}$	12^{+1}_{-1}	$6.1^{+0.3}_{-0.1}$	> 0.99	13^{+2}_{-2}	+137	3321.9/2943
NGC 5506 (p/c)	$2.08^{+0.02}_{-0.03}$	$0.7^{+0.1}_{-0.1}$	10^{+1}_{-1}	3.0^*	-	26^{+5}_{-4}		3191.2/2868
NGC 5506 (no p/c)	$2.07^{+0.01}_{-0.01}$	$0.8^{+0.1}_{-0.1}$	9^{+1}_{-1}	$1.7^{+0.3}_{-0.8}$	-	48^{+19}_{-4}	-12	3179.5/2871
NGC 7469	$1.80^{+0.01}_{-0.01}$	$0.9^{+0.5}_{-0.2}$	< 13	$1.7^{+0.1}_{-0.8}$	$0.72^{+0.18}_{-0.17}$	80^{+8}_{-5}		780.9/805
SWIFT J2127.4+5654	$2.19^{+0.05}_{-0.03}$	$0.9^{+0.3}_{-0.3}$	< 18	$2.2^{+0.4}_{-0.9}$	-	42^{+16}_{-7}		830.8/866

Table D.4: List of 15-50 keV component fluxes for each object and the full model 2-10 keV flux. The full model flux includes all model components, reflector flux is the 15-50 keV flux of the REFLECTION component in the RXD whereas the continuum flux is the model flux minus any contribution from reflection or partial covering. The hardness ratio is the ratio of the full model 15-50 keV to 2-10 keV flux, a powerlaw with slope $\Gamma = 2.0$ gives a hardness ratio of 0.75. The reflection fraction, R_{15-50} , is the ratio of the 15-50 keV reflector flux to the 15-50 keV continuum flux i.e. to the full model minus reflector flux. Flux given in units $10^{-11} \text{ erg cm}^{-2} \text{ s}^{-1}$.

Object	Full model	Reflector	Continuum	Full model 2-10 keV flux	Hardness ratio	R_{15-50}
1H 0419-577 Obs 1	2.848 ± 0.110	$0.237^{+0.138}_{-0.092}$	2.156 ± 0.055	1.753	1.625 ± 0.063	$0.091^{+0.053}_{-0.036}$
1H 0419-577 Obs 2	2.315 ± 0.083	$0.301^{+0.187}_{-0.114}$	1.719 ± 0.055	1.374	1.685 ± 0.060	$0.149^{+0.094}_{-0.058}$
3C 111	3.292 ± 0.097	0	3.292 ± 0.097	1.947	1.691 ± 0.050	–
3C 120 Obs 1	6.236 ± 0.239	$0.889^{+0.139}_{-0.130}$	5.347 ± 0.055	4.629	1.347 ± 0.052	$0.166^{+0.027}_{-0.026}$
3C 120 Obs 2	5.788 ± 0.187	$1.082^{+0.162}_{-0.139}$	4.706 ± 0.055	3.963	1.461 ± 0.047	$0.230^{+0.036}_{-0.032}$
3C 382	5.108 ± 0.105	$1.093^{+0.092}_{-0.609}$	4.015 ± 0.035	4.045	1.263 ± 0.026	$0.272^{+0.025}_{-0.157}$
3C 390.3	5.812 ± 0.182	$1.444^{+1.487}_{-0.396}$	$4.368^{+0.058}_{-0.116}$	3.101	1.874 ± 0.059	$0.331^{+0.359}_{-0.096}$
3C 445	2.692 ± 0.110	$0.902^{+3.278}_{-0.333}$	1.790 ± 0.597	0.699	3.851 ± 0.157	$0.504^{+2.051}_{-0.211}$
4C 74.26	3.996 ± 0.095	$0.821^{+0.908}_{-0.541}$	3.175 ± 0.030	3.127	1.278 ± 0.030	$0.259^{+0.295}_{-0.176}$
Ark 120	3.858 ± 0.102	$1.188^{+0.562}_{-0.677}$	2.670 ± 0.169	3.051	1.263 ± 0.033	$0.445^{+0.231}_{-0.278}$
Ark 564	1.536 ± 0.146	$0.078^{+0.124}_{-0.059}$	0.822 ± 0.007	1.837	0.836 ± 0.079	$0.053^{+0.085}_{-0.041}$
Fairall 9 Obs 1	3.370 ± 0.076	$1.269^{+0.091}_{-0.084}$	2.101 ± 0.031	2.317	1.454 ± 0.033	$0.604^{+0.055}_{-0.052}$
Fairall 9 Obs 2	3.511 ± 0.180	$1.043^{+0.070}_{-0.070}$	2.468 ± 0.034	2.165	1.622 ± 0.083	$0.423^{+0.044}_{-0.044}$
IC 4329A	16.778 ± 0.139	$5.309^{+0.104}_{-0.760}$	11.469 ± 0.033	10.711	1.566 ± 0.013	$0.463^{+0.011}_{-0.073}$
IRAS 13224-3809	0.021 ± 0.011	0	< 0.009	0.055	0.382 ± 0.200	–
MCG-02-14-009	0.789 ± 0.093	$0.413^{+0.091}_{-0.171}$	$0.376^{+0.125}_{-0.094}$	0.430	1.835 ± 0.216	$1.098^{+0.451}_{-0.728}$
MCG-02-58-22	8.726 ± 0.107	$1.752^{+0.301}_{-0.313}$	6.974 ± 0.074	4.872	1.791 ± 0.022	$0.251^{+0.045}_{-0.046}$
MCG-05-23-16	14.518 ± 0.139	$1.797^{+0.137}_{-0.321}$	12.721 ± 0.133	8.929	1.626 ± 0.016	$0.141^{+0.011}_{-0.026}$
MCG-06-30-15	5.013 ± 0.067	$0.584^{+0.050}_{-0.160}$	$3.093^{+0.095}_{-0.076}$	4.160	1.205 ± 0.016	$0.132^{+0.012}_{-0.036}$
MCG+8-11-11	10.440 ± 0.160	$3.111^{+1.507}_{-1.020}$	7.329 ± 0.039	6.480	1.611 ± 0.025	$0.424^{+0.224}_{-0.151}$
MR 2251-178	5.465 ± 0.108	0	5.365 ± 0.108	4.230	1.292 ± 0.026	–
Mrk 79	1.875 ± 0.139	0	1.875 ± 0.139	1.466	1.279 ± 0.095	–

Table D.4: *continued* - List of 15-50 keV component fluxes for each object and the full model 2-10 keV flux. The full model flux includes all model components, reflector flux is the 15-50 keV flux of the REFLIONX component in the HXD whereas the continuum flux is the model flux minus any contribution from reflection or partial covering. The hardness ratio is the ratio of the full model 15-50 keV to 2-10 keV flux, a powerlaw with slope $\Gamma = 2.0$ gives a hardness ratio of 0.75. The reflection fraction, R_{15-50} , is the ratio of the 15-50 keV reflector flux to the 15-50 keV continuum flux i.e. to the full model minus reflector flux. Flux given in units $10^{-11} \text{ erg cm}^{-2} \text{ s}^{-1}$.

Object	Full model	Reflector	Continuum	Full model 2-10 keV flux	Hardness ratio	R_{15-50}
Mrk 110	2.990 ± 0.113	$0.267^{+0.559}_{-0.083}$	2.723 ± 0.052	2.126	1.406 ± 0.053	$0.098^{+0.206}_{-0.031}$
Mrk 205	1.184 ± 0.062	$0.299^{+0.040}_{-0.113}$	$0.711^{+0.023}_{-0.046}$	0.934	1.268 ± 0.066	$0.338^{+0.053}_{-0.137}$
Mrk 279	2.322 ± 0.101	$0.736^{+0.187}_{-0.194}$	0.554 ± 0.050	0.489	4.748 ± 0.207	$0.464^{+0.133}_{-0.138}$
Mrk 335	1.502 ± 0.125	$0.288^{+0.088}_{-0.088}$	$1.214^{+0.024}_{-0.048}$	1.490	1.008 ± 0.084	$0.237^{+0.078}_{-0.078}$
Mrk 359	0.984 ± 0.141	$0.337^{+0.285}_{-0.110}$	0.647 ± 0.054	0.515	1.912 ± 0.274	$0.521^{+0.509}_{-0.223}$
Mrk 509	7.186 ± 0.162	$0.966^{+6.077}_{-0.601}$	6.220 ± 0.070	4.723	1.521 ± 0.034	$0.161^{+0.989}_{-0.098}$
Mrk 766 Obs 1	1.476 ± 0.118	$0.329^{+0.072}_{-0.059}$	1.140 ± 0.023	1.325	1.181 ± 0.094	$0.287^{+0.072}_{-0.061}$
Mrk 766 Obs 2	1.846 ± 0.154	$0.414^{+0.091}_{-0.078}$	0	1.363	1.354 ± 0.113	$0.289^{+0.073}_{-0.065}$
Mrk 841	2.618 ± 0.105	$0.948^{+0.570}_{-0.338}$	1.670 ± 0.046	1.416	1.849 ± 0.074	$0.568^{+0.394}_{-0.235}$
NGC 1365 Obs 1	4.880 ± 0.116	$0.752^{+0.263}_{-0.056}$	0.162 ± 0.054	1.284	6.489 ± 0.154	$0.182^{+0.065}_{-0.015}$
NGC 1365 Obs 2	4.428 ± 0.127	$0.860^{+0.070}_{-0.063}$	0.143 ± 0.073	0.610	7.259 ± 0.208	$0.241^{+0.022}_{-0.020}$
NGC 1365 Obs 3	3.615 ± 0.060	$0.909^{+0.038}_{-0.051}$	0.146 ± 0.075	0.385	9.390 ± 0.116	$0.336^{+0.017}_{-0.021}$
NGC 2992	2.106 ± 0.101	$0.620^{+0.113}_{-0.113}$	1.486 ± 0.057	1.182	1.782 ± 0.085	$0.417^{+0.087}_{-0.087}$
NGC 3147	0.294 ± 0.033	$0.072^{+0.098}_{-0.098}$	0.223 ± 0.056	0.165	1.782 ± 0.200	$0.324^{+0.467}_{-0.049}$
NGC 3227 Obs 1	7.564 ± 0.156	$3.010^{+0.167}_{-0.169}$	$3.209^{+0.043}_{-0.012}$	3.956	2.357 ± 0.049	$0.661^{+0.049}_{-0.030}$
NGC 3227 Obs 2	6.705 ± 0.164	$5.218^{+0.147}_{-0.144}$	$0.365^{+0.011}_{-0.014}$	1.853	3.618 ± 0.089	$3.509^{+0.529}_{-0.524}$
NGC 3227 Obs 3	6.858 ± 0.170	$3.419^{+0.153}_{-0.152}$	0.682 ± 0.016	2.551	2.688 ± 0.067	$0.994^{+0.079}_{-0.079}$
NGC 3227 Obs 4	4.704 ± 0.170	$4.127^{+0.113}_{-0.111}$	0.228 ± 0.013	0.996	4.723 ± 0.171	$7.153^{+2.538}_{-2.524}$
NGC 3227 Obs 5	6.194 ± 0.179	$3.128^{+0.129}_{-0.127}$	0.360 ± 0.014	2.138	2.897 ± 0.084	$1.020^{+0.085}_{-0.084}$
NGC 3227 Obs 6	5.283 ± 0.193	$3.250^{+0.160}_{-0.158}$	$0.221^{+0.011}_{-0.009}$	1.571	3.363 ± 0.123	$1.599^{+0.212}_{-0.211}$

Table D.4: *continued* - List of 15-50 keV component fluxes for each object and the full model 2-10 keV flux. The full model flux includes all model components, reflector flux is the 15-50 keV flux of the REFLECTION component in the HXD whereas the continuum flux is the model flux minus any contribution from reflection or partial covering. The hardness ratio is the ratio of the full model 15-50 keV to 2-10 keV flux, a powerlaw with slope $\Gamma = 2.0$ gives a hardness ratio of 0.75. The reflection fraction, R_{15-50} , is the ratio of the 15-50 keV reflector flux to the 15-50 keV continuum flux i.e. to the full model minus reflector flux. Flux given in units $10^{-11} \text{ erg cm}^{-2} \text{ s}^{-1}$.

Object	Full model	Reflector	Continuum	Full model 2-10 keV flux	Hardness ratio	R_{15-50}
NGC 3516 Obs 1	7.321 ± 0.117	$2.093^{+0.132}_{-0.120}$	0.920 ± 0.061	2.370	3.089 ± 0.049	$0.400^{+0.029}_{-0.026}$
NGC 3516 Obs 2	3.340 ± 0.057	$1.198^{+0.073}_{-0.073}$	0.920 ± 0.061	2.370	1.409 ± 0.024	$0.559^{+0.042}_{-0.042}$
NGC 3783 Obs 1	9.917 ± 0.178	$4.465^{+0.145}_{-0.145}$	5.452 ± 0.042	4.586	2.162 ± 0.039	$0.819^{+0.044}_{-0.026}$
NGC 3783 Obs 2	12.003 ± 0.100	$4.650^{+0.152}_{-0.146}$	7.353 ± 0.043	5.921	2.027 ± 0.017	$0.632^{+0.026}_{-0.025}$
NGC 4051 Obs 1	1.648 ± 0.089	$0.592^{+0.039}_{-0.033}$	0.339 ± 0.034	0.873	1.888 ± 0.102	$0.561^{+0.063}_{-0.059}$
NGC 4051 Obs 2	3.223 ± 0.052	$0.887^{+0.058}_{-0.046}$	2.116 ± 0.035	2.464	1.308 ± 0.021	$0.380^{+0.028}_{-0.023}$
NGC 4051 Obs 3	2.591 ± 0.110	$0.823^{+0.071}_{-0.076}$	1.322 ± 0.034	1.794	1.444 ± 0.061	$0.465^{+0.033}_{-0.036}$
NGC 4151	15.901 ± 0.109	$7.825^{+1.865}_{-0.917}$	4.512 ± 0.167	4.352	3.654 ± 0.025	$0.969^{+0.322}_{-0.159}$
NGC 4593	2.152 ± 0.130	$0.388^{+2.061}_{-0.293}$	1.764 ± 0.084	1.041	2.067 ± 0.124	$0.220^{+1.196}_{-0.171}$
NGC 5506 Obs 1	17.800 ± 0.153	$6.279^{+0.227}_{-0.220}$	9.755 ± 0.036	10.379	1.715 ± 0.015	$0.545^{+0.024}_{-0.023}$
NGC 5506 Obs 2	17.114 ± 0.210	$5.952^{+0.218}_{-0.218}$	9.375 ± 0.035	9.890	1.730 ± 0.021	$0.533^{+0.024}_{-0.024}$
NGC 5548	3.998 ± 0.087	$1.364^{+0.817}_{-0.483}$	2.624 ± 0.060	1.841	2.172 ± 0.047	$0.518^{+0.350}_{-0.207}$
NGC 7213	3.477 ± 0.109	$0.208^{+0.397}_{-0.126}$	3.269 ± 0.054	2.410	1.443 ± 0.045	$0.064^{+0.222}_{-0.039}$
NGC 7314	1.427 ± 0.110	0	1.427 ± 0.110	0.879	1.623 ± 0.125	–
NGC 7469	3.478 ± 0.102	$0.923^{+0.076}_{-0.158}$	$2.555^{+0.179}_{-0.269}$	2.102	1.655 ± 0.049	$0.361^{+0.035}_{-0.007}$
PDS 456	0.249 ± 0.062	0	0.130 ± 0.006	0.353	0.795 ± 0.176	–
PG 1211+143	0.498 ± 0.249	0	0.498 ± 0.249	0.391	1.274 ± 0.637	–
RBS 1124	0.905 ± 0.057	$0.211^{+2.862}_{-0.138}$	0.694 ± 0.058	0.494	1.832 ± 0.115	$0.304^{+4.310}_{-0.209}$
SWIFT J2127.4+5654	3.533 ± 0.095	$1.276^{+0.207}_{-0.621}$	$2.257^{+0.059}_{-0.074}$	3.348	1.055 ± 0.028	$0.565^{+0.108}_{-0.317}$
TON S180	0.773 ± 0.129	$0.052^{+0.016}_{-0.147}$	0.328 ± 0.014	0.564	1.371 ± 0.229	$0.072^{+0.026}_{-0.072}$

Publications

- Patrick A.R., Reeves J.N., Porquet D., Markowitz A.G., Lobban A.P., Ter-shima Y., 2011, MNRAS, 411, 2353
‘Iron line profiles in *Suzaku* spectra of bare Seyfert galaxies’
- Patrick A.R., Reeves J.N., Lobban A.P., Porquet D., Markowitz A.G., 2011, MNRAS, 416, 2725
‘Assessing black hole spin in deep *Suzaku* observations of Seyfert 1 AGN’
- Tatum M.M., Turner T.J., Sim S.A., Miller L., Reeves J.N., Patrick A.R., Long K.S., 2012, ApJ, 752, 94
‘Modelling the Fe K line profiles in type 1 AGN with a Compton-thick disk wind’
- Patrick A.R., Reeves J.N., Porquet D., Markowitz A.G., Braitto V., Lobban A.P., 2012, MNRAS, 426, 2522
‘A *Suzaku* survey of Fe K lines in Seyfert 1 AGN’

Bibliography

Abdo A.A., et al., 2011, ApJ, 733, 26

Allen D.A., 1976, ApJ, 207, 367

Alloin D., et al., 1995, A&A, 293, 293

Alonso-Herrero A., et al., 2012, MNRAS, 425, 311

Antonucci R., 1993, ARA&A, 31, 473

Arnaud K.A., Branduardi-Raymont G., Culhane J.L., Fabian A.C., Hazard C., 1985, MNRAS, 217, 105

Arnaud K.A., 1996, *Astronomical Data Analysis Software and Systems V*, eds. Jacoby G., Barnes J., pg17, ASP Conf. Series Volume 101

Arnaud K.A., Ingham J., 2006, heasarc.gsfc.gov/docs/software/lheasoft/ftools/xselect/index.html

Anders E., Grevesse N., *Geochimica et Cosmochimica Acta*, 1989, 53, 197

Antonucci R.R.J., Miller J.S., 1985, ApJ, 297, 621

Bahcall J.N., Kirhakos S., Schneider, D.P., 1995, ApJ, 457, 557

Baldwin J.A., Phillips M.M., Terlevich R., 1981, PASP, 93, 5

Ballantyne D.R., Vaughan S., Fabian A.C., 2003, MNRAS, 342, 239

Bania T., et al, 1991, ApJ, 101, 2147

Barr R., White N.E., Sanford P., Ives J.C., 1977, MNRAS, 181, 43

Barthlemy S.D., et al., 2005, SSRv, 120, 143

Barvainis R., 1993, ApJ, 412, 513

- Baumgartner W.H., Tueller J., Markwardt C.B., Skinner G.K., 2010, *HEAD*, 11, 1305
- Beckwith K., Done C., 2004, *MNRAS*, 352, 353
- Berti E., Volonteri M., 2008, *ApJ*, 684, 822
- Bevington P.R., 1969, *Data Reduction and Error Analysis for the Physical Sciences*, McGraw-Hill: New York
- Bianchi S., Matt G., 2002, *A&A*, 387, 76
- Bianchi S., Matt G., Balestra I., Guainazzi M., Perola G.C., 2004, *A&A*, 422, 65
- Bianchi S., Guainazzi M., Matt G., Fonseca Bonilla N., Ponit G., 2009, *A&A*, 495, 421
- Blandford R.D., Znajek R.L., 1977, *MNRAS*, 179, 433
- Blandford R.D., McKee C.F., 1982, *ApJ*, 255, 419
- Blustin A.J., Branduardi-Raymont G., Behar E., Kaastra J.S., Kahn S.M., Page M.J., Sako M., Steenbrugge K.C., 2002, *A&A*, 392, 453
- Blustin A.J., Page M.J., Fuerst S.V., Branduardi-Raymont G., Ashton C.E., 2005, *A&A*, 431, 111
- Blustin A.J. et al., 2007, *A&A*, 466, 107
- Boldt E., Leiter D., 1986, in *Structure and Evolution of Active Galactic Nuclei*, ed. G. Giuricin et al. (Dordrecht, Holland: D. Reidel Publishing Co.), p. 383
- Boldt E., 1987, *IAUS*, 124, 611
- Boroson T.A., Green R.F., 1992, *ApJs*, 80, 109
- Braitto V., et al., 2007, *ApJ*, 670, 978
- Brenneman L.W., Reynolds C.S., 2006, *ApJ*, 652, 1028

- Brenneman L.W., et al., 2011, ApJ, 736, 103
- Cappi M., et al., 2009, A&A, 504, 401
- Cash W., 1979, ApJ, 28, 939
- Cavaliere A., Morrison P., 1980, ApJ, 238, 63
- Chartas G., Brandt W.N., Gallagher S.C., 2003, ApJ, 595, 85
- Chartas G., Brandt W.N., Gallagher S.C., Garmire G.P., 2002, ApJ, 579, 169
- Cooke B., Ricketts M.J., Maccacaro T., Pye J.P., Elvis M., 1978, MNRAS, 182, 489
- Crummy J., Fabian A.C., Gallo L., Ross R.R., 2006, MNRAS, 365, 1067
- Cusumano G. et al., 2010, A&A, 510, 48
- Czerny B., Elvis M., 1987, ApJ, 321, 305
- Dadina M., Cappi M., Malaguti G., Ponti G., de Rosa A., 2005, A&A, 442, 461
- Dauser T., Wilms J., Reynolds C.S., Brenneman L.W., 2010, MNRAS, 409, 1534
- Davis S. W., Done C., Blaes O. M., 2006, ApJ, 647, 525
- de la Calle Pérez I., et al., 2010, A&A, 524, A50
- den Herder J.W., et al., 2001, A&A, 365, 7
- Dewangan G.C., Griffiths R.E., Dasgupta S., Rao A.R., 2007, ApJ, 671, 1284
- Done C., Madejski G.M., Zycki P.T., 2000, ApJ, 536, 213
- Done C., Gierliński M., Kubota A., 2007, A&ARv, 15, 1
- Dovčiak M., Karas V., Yaqoob T., 2004, ApJS, 153, 205
- Elvis M., Maccacaro T., Wilson A.S., Ward M.J., Penston M.V., Fosburg R.A.E.,
Perola G.C., 1978, MNRAS, 183, 129

- Emmanoulopoulos D., Papadakis I.E., McHardy I.M., Nicastro F., Bianchi S., Arévalo P., 2011, MNRAS, 415, 1895
- Fabian A.C., Rees M.J., Stella L., White N.E., 1989, MNRAS, 238, 729
- Fabian A.C., et al., 2012, MNRAS, 419, 116
- Fanaroff B.L., Riley J.M., 1974, MNRAS, 167, 31
- Fiore F., Matt G., Nicastro F., 1997, MNRAS, 284, 731
- Gallo L.C., Lehmann I., Pietsch W., Boller Th., Brinkmann W., Friedrich P., Grupe D., 2006, MNRAS, 365, 688
- Gallo L.C., Miniutti G., Miller J.M., Brenneman L.W., Fabian A.C., Guainazzi M., Reynolds C.S., 2011, MNRAS, 411, 607
- Gallo L.C., et al., 2013, MNRAS, 428, 1191
- Gammie C.F., Shapiro S.L., McKinney J.C., 2004, ApJ, 602, 312
- Garafalo D., 2009, ApJ, 699, 400
- George I.M., Fabian A.C., 1991, MNRAS, 249, 352
- Ghosh K.K., Soundararajaperumal S., 1991, ApJ, 383, 574
- Giacconi R., Kellogg E., Gorenstein P., Gursky H., Tananbaum H., 1971, ApJ, 165, 27
- Giacconi R., et al., 1979, ApJ, 230, 540
- Gierliński M., Done C., 2004, MNRAS, 349, L7
- Gofford J., Reeves J.N., Tombesi F., Braito V., Turner T.J., Miller L., Cappi M., 2013, 430, 60
- Gondoin P., Lumb D., Siddiqui H., Guainazzi M., Schartel N., 2001, A&A, 373, 805

- Gondoin P., Orr A., Lumb D., Santos-Lleo M., 2002, *A&A*, 388, 74
- Greenhill L.J., Moran J.M., Herrnstein J.R., 1997, *ApJ*, 481, 23
- Grupe D., Komossa S., Gallo L.C., Fabian A.C., Larsson J., Pradhan A.K., Xu D., Miniutti G., 2008, *ApJ*, 681, 982
- Guainazzi M., Bianchi S., Dovčiak M., 2006, *Astron. Nachr.*, 10, 1032
- Guilbert P.W., Rees, M.J., 1988, *MNRAS*, 233, 475
- Haardt F., Maraschi, L., 1993, *ApJ*, 413, 507
- Halpern J.P., 1984, *ApJ*, 281, 90
- Harrison, F.A. et al. 2010, *SPIE*, 7732, 27
- Hill G.J., Goodrich R.W., Depoy D.L., 1996, *ApJ*, 462, 163
- Holt S.S., 1976, *Ap&SS*, 42, 123
- Hughes S. A., Blandford R. D., 2003, *ApJ*, 585, 101
- Ives J.C., Sanford P.W., Penston M.V., 1976, *ApJ*, 207, L159
- Iwasawa et al., 1996, *MNRAS*, 282, 1038
- Jansen F., et al., 2001, *A&A*, 365, 1
- Kaastra J.S., Mewe R., Liedahl D.A., Komossa S., Brinkman A.C., 2000, *A&A*, 354, L83
- Kalberla P.M.W., et al., 2005, *A&A*, 440, 775
- Kallman T.R., Palmeri P., Bautista M. A., Mendoza C., Krolik J. H., 2004, *ApJS*, 155, 675
- Kaspi S., Brandt W.N., Netzer H., Sambruna R., Chartas G., Garmire G.P., Nousek J.A., 2000, *ApJ*, 535, 17

- Kaspi S., et al., 2001, ApJ, 554, 216
- Kaspi S., et al., 2002, ApJ, 574, 643
- Kataoka J. et al., 2007, PASJ, 59, 279
- Kelley R.L., et al., 2007, PASJ, 59, 77
- Kelley R.L. et al., 2010, American Astronomical Society, HEAD meeting 11, Bulletin of the American Astronomical Society, Vol. 41, p.738
- King A.R., Kolb U., 1999, MNRAS, 305, 654
- King A.R., Pounds K.A., 2003, MNRAS, 345, 657
- King A.R., Lubow A.H., Ogilvie G.I., Pringle J.E., 2005, MNRAS, 363, 49
- King A.R., Pringle J.E., 2007, MNRAS, 377, 25
- King A.R., Pringle J.E., Hofmann J.A., 2008, 385, 1621
- Kolehmainen M., Done C., Diaz Trigo M., 2011, MNRAS, 416, 311
- Koyama K. et al., 2007, PASJ, 59S, 23
- Krolik J.H., Kallman T.R., 1987, ApJ, 320, 5
- Krolik J.H., Begelman M.C., 1988, ApJ, 329, 702
- Krolik J.H., 1999, *Active Galactic Nuclei: From the Central Black Hole to the Galactic Environment*, Princeton Series in Astrophysics
- Krongold Y., Nicastro F., Elvis M., Brickhouse N., Binette L., Mathur S., Jiménez-Bailón E., 2007, ApJ, 659, 1022
- Laor A., 1991, ApJ, 376, 90
- Larsson J., Miniutti G., Fabian A.C., Miller J.M., Reynolds C.S., Ponti G., 2008, MNRAS, 384, 1316

- Lightman A.P., White, T.R., 1988, ApJ, 335, 57
- Lira P., Arévalo P., Uttley P., McHardy I., Breedt E., 2010, IAUS, 267, 90
- Lobban A.P., Reeves J.N., Porquet D., Braito V., Markowitz A.G., Miller L., Turner T.J., 2010, MNRAS, 508, 551
- Lobban A.P., Reeves J.N., Miller L., Turner T.J., Braito V., Kraemer S.B., Crenshaw D.M., 2011, MNRAS, 414, 1965
- Lohfink A.M., Reynolds C.S., Mushotzky R.F., Nowak M.A., 2013, arXiv1301.4997
- Longinotti A.L., Sim S.A., Nandra K., Cappi M., 2007, MNRAS, 374, 237
- Lu Y., Wang T., 2000, ApJ, 537, 103
- Magdziarz P., Zdziarski A.A., 1995, MNRAS, 273, 837
- Maiolino R. et al., 2010, A&A, 517, 47
- Makino F., 1987, ApL, 29, 223
- Malizia A., et al., 2008, MNRAS, 389, 1360
- Malkan M.A., Sargent W.L.W., 1982, ApJ, 254, 22
- Markowitz A.G., Reeves J.N., Braito V., 2006, ApJ, 646, 783
- Markowitz A.G. et al., 2008, PASJ, 60S, 277
- Markowitz A.G., Reeves J.N., 2009, ApJ, 705, 496
- Markwardt C.B., Tueller J., Skinner J.K., Gehrels N., Barthelmy S.D., Mushotzky R.F., 2005, ApJ, 633, 77
- Mason K.O., et al., 2001, A&A, 365, 36
- Matsuoka M., Piro L., Yamauchi M., Murakami T., 1990, ApJ, 361, 440

- Matt G., 1994, MNRAS, 267, L17
- Matt G., Brandt W.N., Fabian A.C., 1996, MNRAS, 280, 823
- Matt G., Guainazzi M., Perola G.C., Fiore F., Nicastro F., Cappi M., Piro L., 2001, A&A, 377, 31
- Matt G., 2002, MNRAS, 337, 147
- McHardy I.M., Czerny B., 1987, Nature, 325, 696
- McHardy I.M., 1990, In *Proc. 23rd ESLAB Symp.*
- McKernan B., Yaqoob T., Reynolds C.S., 2007, MNRAS, 379, 1359
- Middleton M., Done C., Gierliński M., Davis S.W., 2006, MNRAS, 373, 1004
- Miley G.K., Miller J.S., 1979, ApJ, 228, 55
- Miller J.M., et al., 2008, ApJ, 679, 113
- Miller J.M., Reynolds C.S., Fabian A.C., Miniutti G., Gallo L.C., 2009, ApJ, 697, 900
- Miller L., Turner T.J., Reeves J.N., 2008, A&A, 483, 437
- Miller L., Turner T.J., Reeves J.N., 2009, MNRAS, 399, 69
- Miller L., Turner T.J., 2009, A&A Review, 17, 47
- Miller L., Turner T.J., 2013, submitted to ApJ Letters, arXiv:1303.4309
- Miniutti G., Fabian A.C., Goyder R., Lasenby A.N., 2003, MNRAS, 344, L22
- Miniutti G., Fabian A.C., 2004, MNRAS, 349, 1435
- Miniutti G., et al., 2007, PASJ, 59S, 315
- Miniutti G., Panessa F., De Rosa A., Fabian A.C., Malizia A., Molina M., Miller J.M., Vaughan S., 2009, MNRAS, 398, 255

- Miniutti G., Piconcelli E., Bianchi S., Vignali C., Bozzo E., 2010, MNRAS, 401, 1315
- Mitsuda K., et al., 2007, PASJ, 59, 1
- Miyoshi M., Moran J.M., Herrnstein J.R., Greenhill L.J., Nakai N., Diamond P., Inoue M., 1995, Nature, 373, 127
- Morrison R., McCammon D., 1983, ApJ, 270, 119
- Murray S.S., et al., 2000, SPIE, 4012, 68
- Mushotzky R.F., Serlemitsos, P.J., Beecker, R.H., Boldt, E.A., Holt, S.S., 1978a, ApJ, 220, 790
- Mushotzky R.F., Holt, S.S., Serlemitsos, P.J., 1978b, ApJ, 225, L115
- Mushotzky R.F., Marshall F.E., Boldt E.A., Holt S.S., Serlemitsos P.J., 1980, ApJ, 235, 377
- Mushotzky R.F., Fabian A.C., Iwasawa K., Kunieda H., Matsuoka A., Nandra K., Tanaka Y., 1995, MNRAS, 272, 9
- Nandra K., Pounds K.A., Stewart G.C., George I.M., Hayashida K., Makino F., Ohashi T., 1991, MNRAS, 248, 760
- Nandra K., Pounds K.A., 1994, MNRAS, 268, 405
- Nandra K., 2006, MNRAS, 368, 62
- Nandra K., O'Neill P.M., George I.M., Reeves J.N., 2007, MNRAS, 382, 194
- Nardini E., Fabian A.C., Reis R.C., Walton D.J., 2011, MNRAS, 410, 1251
- Nardini E., Fabian A.C., Walton D.J., 2012, MNRAS, 423, 3299
- Noda H., Makishima K., Nakazawa K., Uchiyama H., Yamada S., Sakurai S., 2013, PASJ, 65, 4

- O'Neill P.M., Nandra K., Cappi M., Longinotti A.L., Sim S.A., 2007, MNRAS, 381, 94
- Osterbrock D.E., 1978, PNAS, 75, 540
- Osterbrock D.E., 1989, *Astrophysics of Gaseous Nebulae and Active Galactic Nuclei* (Mill Valley CA: University Science Books)
- Pan H.C., Stewart G.C., Pounds K.A., 1990, MNRAS, 242, 177
- Patrick A.R., Reeves J.N., Porquet D., Markowitz A.G., Lobban A.P., Terushima Y., 2011a, MNRAS, 411, 2353
- Patrick A.R., Reeves J.N., Lobban A.P., Porquet D., Markowitz A.G., 2011b, MNRAS, 416, 2725
- Patrick A.R., Reeves J.N., Porquet A.P., Markowitz A.G., Braito V., Lobban A.P., 2012, MNRAS, 426, 2522
- Peterson B.M., 1993, PASP, 105, 247
- Peterson B.M., 1997, *An Introduction to Active Galactic Nuclei*, Cambridge University Press
- Peterson B.M., Wilkes B., 2000, *Active Galaxies: Unified Model*, Encyclopedia of Astronomy and Astrophysics
- Piro L., Yamauchi M., Matsuoka M., 1990, ApJ, 360, 35
- Porquet D., 2006, A&A, 445, L5
- Pounds K.A., McHardy I.M., 1988, In *Physics of Neutron Stars and Black Holes* ed. Y. Tanaka, pg 285, Tokyo: Universal Academy
- Pounds K.A., Reeves J.N., O'Brian P., Page K., Turner M.J.L., Nayakshin S., 2001, ApJ, 559, 181

- Pounds K.A., Reeves J.N., King A.R., Page K.L., O'Brien P.T., Turner M.J.L., 2003, MNRAS, 345, 705
- Proga D., Stone J.M., Kallman T.R., 2000, ApJ, 543, 686
- Reeves J.N., Turner M.J.L., Pounds K.A., O'Brien P.T., Boller Th., Ferrando P., Kendziorra E., Vercellone S., 2001, A&A, 365, 134
- Reeves J.N., Nandra K., George I.M., Pounds K.A., Turner T.J., Yaqoob T., 2004, ApJ, 602, 648
- Reeves J.N. et al., 2009, ApJ, 701, 493
- Reis R.C., Fabian A.C., Miniutti G., Miller J.M., Reynolds C.S., 2008, MNRAS, 387, 1489
- Reynolds C.S., Brenneman L.W., Garofalo D., 2005, Ap&SS, 300, 71
- Reynolds C.S., Brenneman, L.W., Lohfink A.M., Trippe M.L., Miller J.M., Reis R.C., Nowak M.A., Fabian A.C., 2012a, AIPC, 1427, 157
- Reynolds C. S., Brenneman, L. W., Lohfink A. M., Trippe M. L., Miller J. M., Fabian A. C., Nowak M. A., 2012b, ApJ, 755, 88
- Rezzolla L., Barausse E., Dorband E.N., Pollney D., Reisswig C., Seiler J., Husa S., 2008, Phys. Rev. D, 78, 044002
- Risaliti G., 2002, A&A, 386, 379
- Risaliti G., et al., 2013, Nature, 494, 449
- Rivers E., Markowitz A.G., Rothschild R., 2011a, ApJS, 193, 3
- Rivers E., Markowitz A.G., Rothschild R., 2011b, ApJ, 742, 29
- Ross R.R., Fabian A.C., Young A.J., 1999, MNRAS, 306, 461

- Ross R.R., Fabian A.C., Ballantyne D.R., 2002, MNRAS, 336, 315
- Rosswog, S., Bruggen, M., 2007, *Introduction to High Energy Astrophysics*, Cambridge University Press
- Ross R.R., Fabian A.C., 2005, MNRAS, 358, 211
- Schmoll S., et al., 2009, ApJ, 703, 2171
- Scott J.E., Kriss G.A., Lee J.C., Quijano J.K., Brotherton M., Canizares C.R., Green R.F., Hutchings J., et al, 2005, ApJ, 634, 193
- Serlemitsos P.J., et al., 2007, PASJ, 59, 9
- Seyfert C.K., 1943, ApJ, 97, 28
- Sim S.A., Long K.S., Miller L., Turner T.J., 2008, MNRAS, 388, 611
- Sim S.A., Miller L., Long K.S., Turner T.J., Reeves J.N., 2010, ApJ, 703, 2171
- Stark J.P., Davidson P.J.N., Culhane L., 1976, MNRAS, 174, 35
- Steidel C.C., Sargent W.L.W., 1991, ApJ, 382, 433
- Strüder L., et al., 2001, A&A, 365, 18
- Svoboda J., Guainazzi M., Karas V., 2010, A&A, 512, 62
- Takahashi T. et al., 2007, PASJ, 59S, 35
- Takahashi T., et al., 2010, SPIE, 7732, 27
- Tanaka Y., Inoue H., Holt S.S., 1994, PASJ, 46, 37
- Tanaka Y., et al., 1995, Nature, 375, 659
- Tatum M.M., Turner T.J., Sim S.A., Miller L., Reeves J.N., Patrick A.R., Long K.S., 2012, ApJ, 752, 94

- Taylor B.G., Andresen R.D., Peacock A., Zobl, R., 1981, *SSRv*, 30, 479
- Thorne, K.S., 1974, *ApJ*, 191, 507
- Titarchuk L., 1994, *ApJ*, 434, 313
- Tombesi F., Sambruna R.M, Reeves J.N., Braito V., Ballo L., Gofford J., Cappi M., Mushotzky R.F., 2010a, *ApJ*, 719, 700
- Tombesi F., Cappi M., Reeves J.N., Palumbo G.G.C., Yaqoob T., Braito V., Dadina M., 2010b, *A&A*, 521, 57
- Tsuruta S., Kellen M., 1995, *ApJ*, 453, 9
- Tueller J., Mushotzky R.F., Barthelmy S., Cannizzo J.K., Gehrels N., Markwardt C.B., Skinner G.K., Winter L.M., 2008, *ApJ*, 681, 113
- Tueller J., et al., 2010, *ApJS*, 186, 378
- Turner M.J.L., et al., 2001, *A&A*, 365, 27
- Turner T.J., Pounds K.A., 1989, *MNRAS*, 240, 833
- Turner T.J., Miller L., 2009, *The Astronomy and Astrophysics Review*, 17, 47
- Turner T.J., Miller L., Kraemer S.B., Reeves J.N., 2011, *ApJ*, 733, 48
- Veilleux, S., Osterbrock, D.E., 1987, *ApJ*, 63, 295
- Voges W., et al., 1999, *A&A*, 349, 389
- Volonteri M., Madau P., Quataert E., Rees M.J., 2005, *ApJ*, 620, 69
- Volonteri M., Sikora M., Lasota J-P., 2007, *ApJ*, 667, 704
- Walton D.J., Nardini E., Fabian A.C., Gallo L.C., Reis R.C., 2013, *MNRAS*, 428, 2901

- Ward J., Wilson A.S., Disney M.J., Elvis M., Maccacaro T., 1977, *A&A*, 59, 19
- Wilms J., Allen A., McCray R., 2000, *ApJ*, 542, 91
- Wilkins D.R., Fabian A.C., 2011, *MNRAS*, 414, 1269
- Wilson, A.S., Colbert, E.J.M., 1995, *ApJ*, 438, 62
- Yaqoob T., George I.M., Nandra K., Turner T.J., Serlemitsos P.J., Mushotzky R.F., 2001, *ApJ*, 546, 759
- Yaqoob T., Reeves J. N., Markowitz A., Serlemitsos P. J., Padmanabhan U., 2005, *ApJ*, 627, 156
- Younes G., Porquet D., Sabra B., Grosso N., Reeves J.N., Allen M.G., 2010, *A&A*, 517, 33
- Young A.J., Lee J.C., Fabian A.C., Reynolds C.S., Gibson R.R., Canizares C.R., 2005, *ApJ*, 631, 733
- Zheng W., et al., 2012, *Nature*, 489, 406
- Zoghbi A., Fabian A.C., Uttley P., Miniutti G., Gallo L.C., Reynolds C.S., Miller J.M., Ponti G., 2010, *MNRAS*, 401, 2419
- Zycki P.T., Ebisawa K., Niedzwiecki A., Miyakawa T., 2010, *PASJ*, 62, 1185